Arnau Sala Cadellans

Exchange-only, nuclear spin-free qubits in semiconductor quantum dots

Arnau Sala Cadellans

Doctoral thesis

NTNU
Norwegian University of Science and Technology
Thesis for the Degree of
Philosophiae Doctor
Faculty of Natural Sciences
Department of Physics

NTNU
Norwegian University of
Science and Technology

NTNU
Norwegian University of
Science and Technology

NTNU

Arnau Sala Cadellans

Exchange-only, nuclear spin-free qubits in semiconductor quantum dots

Thesis for the Degree of Philosophiae Doctor

Trondheim, September 2020

Norwegian University of Science and Technology
Faculty of Natural Sciences
Department of Physics

NTNU
Norwegian University of
Science and Technology

Abstract

There are many successful proposals for using electron spins in quantum dots as qubits: From the original single-spin qubit proposed by Loss and DiVincenzo to multi-electron qubits. However, despite the considerable progress in the past two decades, a semiconductor quantum dot-based qubit that is scalable, reliable and robust enough for actual quantum information applications has not been realized yet. Common problems in semiconductor quantum dot-based spin qubits are (i) the manipulation and coupling of spin states in a scalable way and (ii) the extension of the coherence time of the qubit to allow for enough qubit operations before the quantum state decoheres.

The first problem has been overcome with the so-called exchange-only qubit. In this qubit the spin state of few coupled electrons in neighboring quantum dots can be fully controlled using electric fields only, and these electric fields can be easily localized on the scale of single dots. The second problem, however, is still hindering the progress towards large-scale quantum computation using quantum dot-based spin qubits.

In this regard, we propose a feasible and scalable exchange-only spin qubit composed of four quantum dots that is, to leading order, intrinsically insensitive to randomly fluctuating magnetic noise, while still offering a full electric control [1]. Motivated by our findings, we then analyze in full detail the main relaxation mechanisms in exchange-only spin qubits composed of three and four dots, and find the regimes where the coherence time of the qubit can be extended by several orders of magnitude [2]. We then explore the possibility of implementing our proposal from Ref. [1] in a device composed of three quantum dots—which would offer an unprecedented degree of tunability [3]—and in an already existing device with five quantum dots, proving that the straightforward implementation of our proposal is feasible.

We conclude this project with a thorough analysis of a common electric dipole spin resonance (EDSR) experiment in a system composed of two quantum dots with intrinsic spin-mixing mechanisms. EDSR is a broadly used tool for spectroscopy of quantum dots, yet a detailed theoretical analysis of the physics of an electrically driven system of quantum dots at resonance is still lacking. We thus investigate this system with the aim to find an explanation to many of the features observed in an EDSR experiment that are, up to date, unexplained.

List of publications

Paper [1]

Exchange-only singlet-only spin qubit
Arnau Sala and Jeroen Danon
Physical Review B, **95**, 241303(R) (2017)

Paper [2]

Leakage and dephasing in ^{28}Si-based exchange-only spin qubits
Arnau Sala and Jeroen Danon
Physical Review B, **98**, 245409 (2018)

Paper [3]

Highly tunable exchange-only singlet-only qubit in a GaAs triple quantum dot
Arnau Sala, Jørgen Holme Qvist and Jeroen Danon
Physical Review Research, **2**, 012062(R) (2020)

My contribution to the papers

I made substantial contributions to all three publications in this thesis. In Paper [1] I did most of the calculations and produced most of the results. In Paper [2] I carried all the numerical calculations and I also derived most of the analytical expressions. I contributed substantially in writing the manuscripts in [1, 2]. In Paper [3] the second author and I contributed equally. We both carried all the calculations and derived all the expressions. We both participated equally in writing the manuscript.

Preface

This thesis is submitted in partial fulfillment to the requirements for the degree of Philosophiae Doctor at the Norwegian University of Science and Technology (NTNU), Trondheim, Norway. The work was performed at the Department of Physics under the supervision of Jeroen Danon, with Prof. Jacob Linder as a cosupervisor. In addition to the thesis, the doctoral program included 30 ECTS of coursework, corresponding to the workload of one semester, as well as teaching undergraduate physics courses during six semesters, also corresponding to the full workload of one semester.

This text is meant to supplement the papers that we have published during these four years at NTNU, attached at the end of the thesis, and provide an extensive description of unpublished work that is still not in the form of a paper.

In Chapter 1 we provide the motivation for the project and introduce some basic concepts about quantum computation and quantum dots. Chapter 2 contains the theoretical framework that we need to understand the physics of quantum-dot based spin qubits and reproduce all the results from the papers. Chapters 3, 4 and 5 contain the results from Papers I, II and III, plus some additional work that is not yet published. In Chapter 3 we introduce the exchange-only singlet-only spin qubits and show its properties. In addition, we also explain how our proposal can be implemented in devices that already exist. In Chapter 4 we present a simplified version of the qubit from Chapter 3 that is much more tunable. In Chapter 5 we study the most relevant mechanisms of decoherence in triple- and quadruple-dot exchange-only qubits and explore mechanisms to mitigate their effects on the coherence time of the qubit. Finally, in Chapter 6 we

study in rigorous analytical detail the electric dipole spin resonance on a system composed of two quantum dots with intrinsic spin-mixing mechanisms. The contents of this chapter will eventually result in a publication that is now in preparation.

Acknowledgments

First of all I want to start by thanking my supervisor Jeroen Danon. Not only for introducing me to this fascinating field, but also for his guidance, good advice and for making me see the light on my darkest (research-wise) moments. Working with you has been a pleasant experience.

I also want to thank my coauthor and colleague Jørgen Holme Qvist. It has been a pleasure to work with you.

During the last four years I have met wonderful people and great friends, here at QuSpin and beyond the outer rim of the university. I want to thank, without a particular order Longfei, Martin, Andreas, Morten, Vetle, Øyvind, Jonas, Payel, Sol, Justin, and well... many others. Some people deserve a special consideration, though. These are the ones I spent most time with, and those with whom I have had the most interesting physics (or not) discussions. Thank you Lina, Jonas Ghini, Matthias, Max, Vasil, Akash, Atousa, Eirik and Håvard. I need also thank Even and Nicolai for all the Fridays (and some Mondays) at "beatz". Thank you Even and Vasil also for all the lunch-over-Teams we have had together during the home-office period.

And from outside QuSpin I cannot forget about Tonje, May Lise, Corinna, Tengzhi, Sophia, and most specially Nastasia. You have been one of my greatest friends and I am very grateful for all the hikes, dinners, drinks, movies, chess matches, (infinitely) long talks, and everything we have done together.

I also want to thank my family and most especially my brother Xavier, with whom I have spent some of my most memorable moments. Next time you get stuck in a foreign country call me!

Working from home during a world pandemic is not easy. Social distancing is hard. And writing a thesis on these conditions is tough. But Marion was there to have regular coffee breaks with me, do sports together and have dinner with me. I am extremely grateful to you for all the time

we have spent together, all the dinners we have had, all the gin&tonics and our weekends away from Trondheim. Thank you for giving me comfort when I was stressed about my project and my thesis. You are an angel!

Contents

1

Introduction

This chapter is only an appetizer. We will not go into details here, but we will introduce some concepts that we use in the rest of this thesis.

1.1 Quantum computation

It seems that with a computer we can calculate anything: We just need enough memory and enough time. Yet every time we write a code to run some calculations we have to think how to optimize it because we never have enough memory or time. A quantum computer is not much different. We will not be able to solve *any* problem instantaneously with a quantum laptop (if such a thing ever exists), but if we are smart enough we can use the extra toolbox that quantum mechanics provide to solve some problems very efficiently.

Take for example Shor's algorithm. Everyone has studied (or heard about) this algorithm in undergraduate courses. If you want to factorize a large number N in your laptop you can take the naive approach and try dividing it by all prime numbers between 2 and $\sqrt{N}$, but that can take some time. There are more efficient algorithms to do that, but in the best case the computational time that takes to solve this problem scales exponentially with the number of digits of N and becomes intractable for
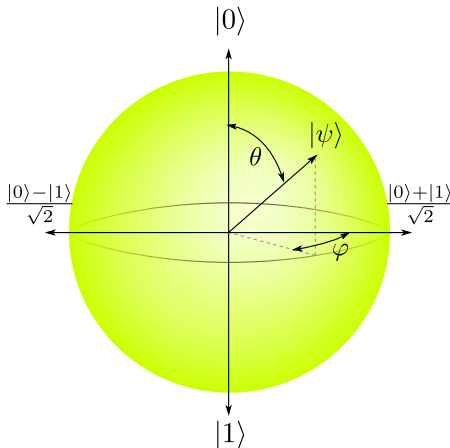
Figure 1.1: A quantum state $|\psi\rangle$ is represented as a point in the surface of the Bloch sphere. The angle theta contains information about the overlap between the state $|\psi\rangle$ and the basis states $|0\rangle$ and $|1\rangle$, whereas the angle φ describes a phase.

large enough N [4]. Shor's algorithm [4–6] may look inefficient too because it requires calculating Fourier transforms, which are typically slow (and also require a large amount of memory). But there is a twist: In a quantum computer we can calculate Fourier transforms in a polynomial time rather than exponential, as is the case in classic computers. Shor's algorithm can thus be implemented in a quantum computer to solve the problem of factorization of large numbers efficiently in a polynomial time.

We will not go into details about quantum computation and quantum algorithms. This is just an example of the powerful capabilities of a quantum computer, but it is not in the scope of this thesis to convince anyone why we need quantum computers and what can they do for us. A quick Google search will already mention some of its applications in Internet security, research, etc. We will instead focus on the most essential part of quantum computers: the qubit. A qubit is a quantum bit. It is the analog of a bit in a classic computer but it is not limited to be either in the state 0 or 1. A qubit can be in any quantum superposition of the states $|0\rangle$ and $|1\rangle$. Qubits are often represented as points in the surface of a sphere: the Bloch sphere. Indeed, any qubit can be expressed as

$$|\psi(\theta, \varphi)\rangle = \cos\frac{\theta}{2}|0\rangle + e^{i\varphi}\sin\frac{\theta}{2}|1\rangle, \tag{1.1}$$
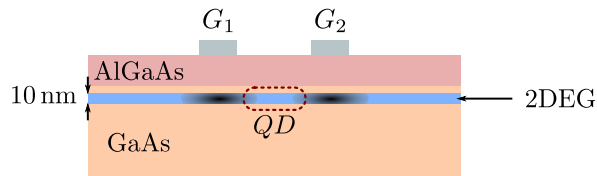
Figure 1.2: A 2DEG is formed e.g., close to the interface between a GaAs/AlGaAs heterojunction [9]. It consists of a thin layer ($\sim$ 10nm) where electrons can have a high mobility. Top gates (G_1 and G_2), lithographically grown, can create a depletion zone in the 2DEG (dark areas), isolating a small region where we can trap one or a few excess electrons (the region enclosed by the dashed red curve). This is a quantum dot.

up to an overall phase, where θ and φ are the polar and azimuthal angles in the Bloch sphere of Fig. 1.1. The states $|0\rangle$ and $|1\rangle$ denote the north and south poles, respectively, of the sphere.

A qubit is thus a quantum mechanical two-level system, and we need to find a physical implementation of this two-level system if we want to create a quantum computer. When one thinks about two-level quantum systems the first thing that comes to mind is probably the spin of an electron. That is text-book physics. And that is (maybe) what Daniel Loss and David DiVincenzo thought when they wrote their seminal paper on quantum computation using quantum dots [7].

The idea is very simple: If we can localize one electron and manipulate its spin, we can use the spin states $|\uparrow\rangle$ and $|\downarrow\rangle$ as the qubit states. We also need a mechanism to initialize the qubit into any desired quantum state, read out the output state after running a quantum algorithm and we must also be able to couple this qubit to, at least, another qubit to perform two-qubit gates [4, 8]. In Ref. [7] the authors address all these issues and propose to localize the electrons in *quantum dots*.

1.2 Quantum dots

A quantum dot is a potential well that can trap one or a few electrons (or holes). They are typically fabricated in semiconductors, in a two-dimensional electron gas (2DEG). We can think of a 2DEG as a surface in a semiconductor where electrons occupy the conduction band and, thus, can move relatively freely. A 2DEG can be created in Si MOSFETs, in
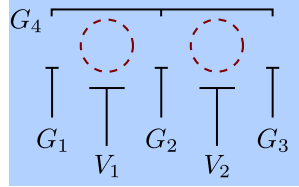
Figure 1.3:   Negative voltages applied to the metallic gates G_1, G_2, G_3 and G_4 create a depletion zone in the 2DEG (blue surface). This results in two small isolated islands, the quantum dots, where electrons can be trapped (red circles). The electrochemical potential in the dots can be controlled by the gates V_1 and V_2.

Si/Ge heterostructures, in GaAs/AlGaAs, etc, and in all cases the electrons are confined in a triangular potential along the z direction only, but are unbounded in the x-y plane [9, 10].

On top of the heterostructure we can put metallic gates. These can be used to apply a localized electric field and create a depletion zone in the 2DEG (see Fig. 1.2). These depletion zones can be engineered to create a whole closed area in the 2DEG where we can trap one or a few electrons. This artificial potential well is a quantum dot.

Once we have a quantum dot we can couple it to a reservoir (by letting electrons tunnel in and out of the quantum dot) and trap one electron. Then we can use the spin of this localized electron for quantum computation.

1.3   Making a spin qubit (using quantum dots)

To understand how a quantum dot-based spin qubit works it is better to see a top view of the device. Fig. 1.3 shows a schematic illustration of a system composed of two quantum dots.

The blue surface represents the 2DEG. On top of the device several metallic gates can be individually addressed to create and manipulate the quantum dots: By applying a negative potential on the gates G_i, the resulting electric field creates a depletion zone on the 2DEG where electrons are not allowed and a small island where the electrons can be trapped. In Fig. 1.3 we show two of such islands, indicated by red dashed circles. These are the quantum dots. We can control the coupling between the two dots by detuning of the gate G_2. The gates G_1 and G_3 can be

used to allow electrons in and out of the quantum dots, while the gates V_1 and V_2 control the electrochemical potential in the dots.

If we now trap one electron in each of the dots we can control its spin with magnetic fields. In fact, with such a simple device, composed of only two quantum dots, it is possible to implement a quantum algorithm [11].

But in this thesis we are not interested in single-spin qubits. The goal of our project is to study decoherence mechanisms in exchange-only spin qubits and mitigate their effects.

2

Spin qubits in quantum dots

This chapter serves as an introduction to the concepts presented in the following chapters and in the papers. Here we also introduce most of the theoretical framework that we need to understand the physics of quantum dot-based, exchange-only spin qubits.

While a two-level system such as the spin of the electron confined in a quantum dot seems the ideal implementation for a qubit, there are many practical issues that make it unfeasible. The two most dramatic obstacles are (*i*) the problem of manipulating a single spin and (*ii*) the limited coherence of the quantum state [9, 10, 12].

Since Loss and DiVincenzo's proposal for a spin qubit based on quantum dots, the field has advanced significantly. Major obstacles that would made quantum dot-based spin qubits impractical have been overcome. The first problem mentioned above is not an issue anymore if we use exchange-only (XO) spin qubits. These are quantum dot-based spin qubits that can be fully manipulated solely by electrostatic gates built on the top surface of the nanostructure [13, 14].

The second problem, on the other hand, is still hindering the progress in the field of semiconductor spin qubits and constitutes the motivation of this thesis. Quantum coherence can be lost if the spin couples to randomly fluctuating magnetic fields, such as those produced by the ensemble of

(a)

$V(x)$

Dot 1   Dot 2 x

(b)

$V(x)$

Dot 1   Dot 2 x
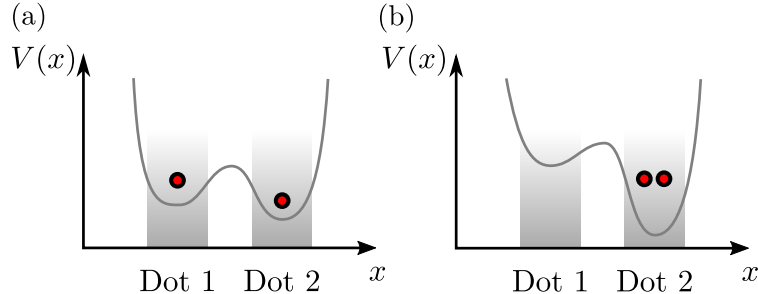
Figure 2.1:   Diagram of the electric potential in a system of two quantum dots along the x direction, within the 2DEG. (a) The system is initialized in a configuration where each quantum dot (gray areas) is occupied by one electron (red dots). (b) Electrons can tunnel to neighboring quantum dots when the tunnel barrier is low enough.

nuclear spins in the spin-full atoms of the material that host the quantum dot. These atoms are typically Ga and As, or even natural silicon, and in all cases nuclear spins have a dramatic effect on the coherence time of the qubits. On top of that, electric noise and electron-phonon coupling, together with other spin-mixing mechanisms such as spin-orbit interaction, also contribute substantially to decoherence [15–18].

2.1   The singlet-triplet qubit

We already mentioned that manipulating a single spin is challenging, although not impossible. It can be achieved by using localized magnetic fields on the quantum dot that contains the single electron [19] or via an on-chip microwave antenna [20], but the complexity of the resulting system would make scalability virtually impossible, since a full control of the qubit requires a control over two perpendicular directions of the fields. Lots of research has therefore been devoted to achieve an *electric* control of the qubit, and very soon some devices capable of a partial electric control were built and tested. One of them is the singlet-triplet (S-T) qubit [21–23]. This device is composed of two quantum dots with one excess electron on each of the dots. The two quantum dots are tunnel coupled. This means that the potential barrier between the two quantum dots, schematically represented in Fig. 2.1, is low enough so that one of the electrons can jump from one quantum dot into the other.

When the two electrons are confined in different quantum dots, the spin of the system can be in four possible states: the spins can either form a singlet or a triplet with different spin projections,

$$|S\rangle = \frac{1}{\sqrt{2}}\left(|\uparrow\downarrow\rangle - |\downarrow\uparrow\rangle\right), \tag{2.1}$$

$$|T^{(0)}\rangle = \frac{1}{\sqrt{2}}\left(|\uparrow\downarrow\rangle + |\downarrow\uparrow\rangle\right), \tag{2.2}$$

$$|T^{(+)}\rangle = |\uparrow\uparrow\rangle, \tag{2.3}$$

$$|T^{(-)}\rangle = |\downarrow\downarrow\rangle. \tag{2.4}$$

The system can then be tuned in the spin blockade regime (or Pauli spin blockade regime) [9]. In this regime two electrons can occupy the same quantum dot only if they form a singlet state, but doubly occupancy is forbidden if they form a triplet.

We model the quantum dots as a parabolic potential in the x and y directions but we assume a very strong potential on the z direction. If we consider only one electron, integrating out the z component leaves us with the single-particle Hamiltonian

$$H = \frac{1}{2m^*}(\mathbf{p} + e\,\mathbf{A}(\mathbf{r}))^2 + \frac{1}{2}m^*\omega_0^2\mathbf{r}^2, \tag{2.5}$$

where $\mathbf{p}$ is the momentum of the electron, $\mathbf{r}$ is its coordinates vector, $\mathbf{A}$ is the vector potential, ω_0 sets the effective radius of the dot $\sigma_0 = \sqrt{\hbar/(m^*\omega_0)}$ and m^* is the effective mass of the electron. The solutions of the Schrödinger equation for an electron confined in such a potential are the Fock-Darwin states [24], with eigenenergies equally spaced by $E_{\mathrm{orb}} = \hbar^2/(m^*\sigma_0^2)$. Let us consider a quantum dot with size σ_0 and with one electron, as we show in the diagram in Fig. 2.2(a). If we add a second electron and they form a singlet state, then the electrons can occupy the same orbital state and the only cost in energy will be given by an electrochemical potential V_g and a Coulomb potential U [Fig. 2.2(b)]; but if the two electrons from a triplet state instead, Pauli's exclusion principle states that the electrons must occupy different orbital states and, therefore, the energy cost will be further incremented by E_{orb} [Fig. 2.2(c)]. If σ_0 is small enough, doubly occupancy of the dot by a pair of electrons in a triplet state will be, in practice, forbidden. This is the Pauli spin blockade regime, and it has some implications: In a double dot with a finite tunnel barrier between the dots and with one electron on each quantum dot, as in Fig. 2.1, if the electrons form a singlet state then one of the electrons can
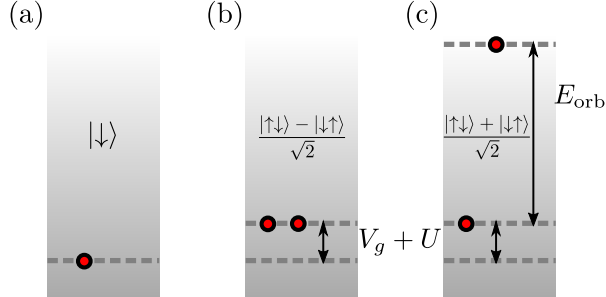
Figure 2.2:   Schematic representation of the orbital states in a quantum dot in the Pauli spin blockade regime. (a) The system contains one electron that occupies the lowest state. (b) If two electrons are added into the dot and they both occupy the lowest orbital state, the energy of the system is increased by an electrochemical potential V_g and a Coulomb potential U. This is only possible if the two electrons form a singlet state. (c) If the two electrons form a triplet state, the energy will be further increased by E_{orb}, an energy that is typically orders of magnitude larger than any other energy scale in the system.

tunnel into the neighboring dot, but if they form a triplet state they cannot. The S-T spin qubit takes advantage of this spin-selective tunneling.

A typical energy spectrum for a S-T qubit is shown in Fig. 2.3 [9]. In the presence of an external magnetic field the polarized triplet states ($|T^{(+)}\rangle$ and $|T^{(-)}\rangle$) split out, while the singlet and the unpolarized triplet ($|S\rangle$ and $|T^{(0)}\rangle$) remain degenerate. If the tunnel barrier between the two dots is low enough then the singlet state hybridizes with the state $|S_{02}\rangle$—this is the state with zero electrons in one dot and two electrons forming a singlet state in the other dot. This results in an exchange energy splitting J between the singlet and triplet states. One can then use these two states as the qubit states: we can define $|0\rangle \equiv |S\rangle$ and $|1\rangle \equiv |T^{(0)}\rangle$. The effective Hamiltonian for such a qubit, with a fixed tunnel barrier, is given by[1]

$$H_{\mathrm{eff}} = \frac{1}{2}J\sigma^z + \frac{1}{2}g\mu_{\mathrm{B}}\Delta B_z\sigma^x, \tag{2.6}$$

---

[1]We will not go into full detail here. The effective Hamiltonian for a triple quantum dot spin qubit will instead be derived below, since triple dot spin qubits are more relevant for this thesis. For more details about the S-T qubit please refer to Ref. [9].
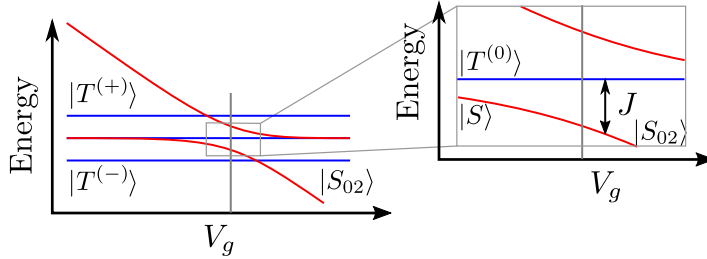
Figure 2.3: Typical energy spectrum of a S-T qubit as a function of the gate-induced offset V_g in one of the dots, keeping the electrochemical potential in the other dot fixed. Red lines show singlet states and blue lines triplet states. When the tunnel barrier is small enough, the states $|S\rangle$ and $|S_{02}\rangle$ hybridize and an emerging exchange energy J splits out the singlet and triplet states. The vertical gray line indicates a possible operating point of the qubit.

with a qubit splitting J that depends on the gate offset potential V_g that we apply to one of the quantum dots. This potential can thus be used to achieve an electric control of the z axis in the Bloch sphere, while for the detuning along a perpendicular axis (for qubit rotations) we still need localized magnetic fields in the form of a magnetic field gradient ΔB_z between the two dots. The remaining two parameters, g and μ_B, are the g-factor and the Bohr magneton.

The S-T spin qubit thus limits the need for localized magnetic fields to only gradients of fields in one direction, and opens the path to a full electric control of spin qubits. Indeed, the work of the authors in Ref. [21] indicate that a full electric control can be achieved if the origin of all the detuning axis is an exchange interaction.

2.2 The exchange-only qubit

As in the S-T qubit, the exchange-only (XO) qubit also uses multi-spin states as qubit states. In this chapter we focus on the triple quantum dot XO spin qubit. This qubit is composed of three quantum dots with one electron each. The dots are placed in a linear array and are tunnel coupled to each other, as we show in Fig. 2.4. The system is tuned into the spin blockade regime, allowing each dot i to contain $N_i \in \{0, 1, 2\}$ excess
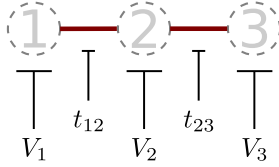
Figure 2.4:   We consider three quantum dots in a linear array. The dots are tunnel coupled to the nearest neighbor only, and the strength of this tunneling interaction can be controlled by gate electrodes on the semiconductor. The electrochemical potential on each quantum dot can be controlled by the gate-induced offsets V_1, V_2 and V_3.

electrons. We model the system with a Hubbard-like Hamiltonian [25–28]:

$$H_{\mathrm{Hubb}} = \sum_i \left[\frac{U}{2} n_i (n_i - 1) - V_i n_i \right] + \sum_{\langle i,j \rangle} U_c n_i n_j + \sum_{\langle i,j \rangle, \alpha} \frac{t_{ij}}{\sqrt{2}} c_{i,\alpha}^\dagger c_{j,\alpha}.$$

$$(2.7)$$

In this expression the operator $n_i = \sum_\alpha c_{i,\alpha}^\dagger c_{i,\alpha}$ is the particle number operator for the dot i, with $c_{i,\alpha}^\dagger$ the creation operator for an electron with spin α in the orbital ground state of dot i. The first two terms describe the electrostatic energy of the system. The energy U is the responsible for the Coulomb interaction between two electrons in the same quantum dot. When only one electron (or none) is present in the quantum dot this term vanishes. The next term, with V_i, accounts for the electrochemical potential on each quantum dot when it contains at least one excess electron. This is controlled by electric fields coming from the electrostatic gates that are lithographically placed on top of the device. Lastly, the term with U_c accounts for the Coulomb repulsion between two electrons in neighboring quantum dots. This energy U_c is typically smaller than the on-site Coulomb repulsion U. We will assume throughout (unless otherwise specified) that the orbital level splitting on the dots, E_{orb}, is the largest energy scale in the system (larger than U), so we will only include states involving double occupation ($N_i = 2$) if the two electrons are in a singlet state.

With three electrons, each in one different quantum dot, there are *eight* possible spin states—four doublets and four quadruplets—, all degenerate:

$$|0_{-1/2}\rangle = \frac{1}{\sqrt{6}} \left(|\downarrow\downarrow\uparrow\rangle + |\uparrow\downarrow\downarrow\rangle - 2|\downarrow\uparrow\downarrow\rangle \right), \qquad (2.8)$$

$$|1_{-1/2}\rangle = \frac{1}{\sqrt{2}}\left(|\downarrow\downarrow\uparrow\rangle - |\uparrow\downarrow\downarrow\rangle\right), \tag{2.9}$$

$$|Q_{-1/2}\rangle = \frac{1}{\sqrt{3}}\left(|\downarrow\downarrow\uparrow\rangle + |\uparrow\downarrow\downarrow\rangle + |\downarrow\uparrow\downarrow\rangle\right), \tag{2.10}$$

$$|Q_{-3/2}\rangle = |\downarrow\downarrow\downarrow\rangle, \tag{2.11}$$

$$|0_{+1/2}\rangle = \frac{1}{\sqrt{6}}\left(|\uparrow\uparrow\downarrow\rangle + |\downarrow\uparrow\uparrow\rangle - 2|\uparrow\downarrow\uparrow\rangle\right), \tag{2.12}$$

$$|1_{+1/2}\rangle = \frac{1}{\sqrt{2}}\left(|\uparrow\uparrow\downarrow\rangle - |\downarrow\uparrow\uparrow\rangle\right), \tag{2.13}$$

$$|Q_{+1/2}\rangle = \frac{1}{\sqrt{3}}\left(|\uparrow\uparrow\downarrow\rangle + |\downarrow\uparrow\uparrow\rangle + |\uparrow\downarrow\uparrow\rangle\right), \tag{2.14}$$

$$|Q_{+3/2}\rangle = |\uparrow\uparrow\uparrow\rangle. \tag{2.15}$$

The states $|0_{-1/2}\rangle$, $|1_{-1/2}\rangle$ and $|Q_{-1/2}\rangle$ have a spin projection $S_z^{\text{tot}} = -\frac{1}{2}$, whereas the states $|0_{+1/2}\rangle$, $|1_{+1/2}\rangle$ and $|Q_{+1/2}\rangle$ have a spin projection $S_z^{\text{tot}} = \frac{1}{2}$. The states $|Q_{-3/2}\rangle$ and $|Q_{+3/2}\rangle$ have a spin projection $S_z^{\text{tot}} = -\frac{3}{2}$ and $S_z^{\text{tot}} = \frac{3}{2}$, respectively. A magnetic field along the z direction will thus split out some states, adding an energy E_Z between them. However, some degeneracies will remain.

The last term in the Hamiltonian (2.7) describes the tunneling interaction between quantum dots. Electrons can tunnel from one dot to the other via a process that preserves the spin of the tunneling electron. This interaction lifts the remaining degeneracies. Let us focus on the subspace formed by the doublet states $|0_{-1/2}\rangle$, $|1_{-1/2}\rangle$ and the spin-$\frac{1}{2}$ quadruplet $|Q_{-1/2}\rangle$: because of the magnetic field, the other states will be further apart in the spectrum. These states can also be written as:

$$|0\rangle \equiv |0_{-1/2}\rangle = \frac{1}{\sqrt{3}}\left(|S_{12}\rangle|\downarrow_3\rangle - |S_{23}\rangle|\downarrow_1\rangle\right), \tag{2.16}$$

$$|1\rangle \equiv |1_{-1/2}\rangle = -|S_{13}\rangle|\downarrow_2\rangle, \tag{2.17}$$

$$|Q_1\rangle \equiv |Q_{-1/2}\rangle = \frac{1}{2\sqrt{3}}\left(|T_{12}^{(0)}\rangle|\downarrow_3\rangle + |T_{13}^{(0)}\rangle|\downarrow_2\rangle + |T_{23}^{(0)}\rangle|\downarrow_1\rangle\right), \tag{2.18}$$

Where $|S_{ij}\rangle$ indicates a singlet pairing between electrons in dots i and j and $|\downarrow_i\rangle$ indicates a spin-down electron in dot i. Similarly, $|T_{ij}^{(0)}\rangle$ indicates an unpolarized triplet pairing between electrons in dots i and j.

The qubit will be manipulated by a modulation of the potentials V_i, but since an equal shift of all three potentials only adds an offset to the Hamiltonian we only need to consider two independent detuning parameters [28]. For these we choose $\epsilon = (V_3 - V_1)/2$ and $V_m = (V_1 + V_3)/2 - V_2$.
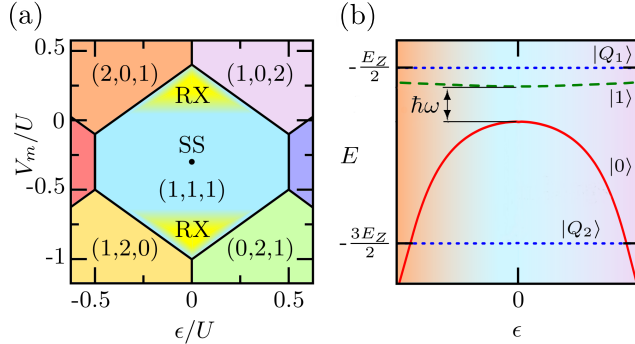
Figure 2.5:   (a) Charge stability diagram as a function of the detuning parameters ϵ and V_m. We show the position of the sweet spot, at the center of the (1,1,1) region, and the RX regimes. (b) Schematic representation of the lowest part of the energy spectrum of an XO qubit within the RX regime as a function of ϵ (in arbitrary units), with $t_{12} = t_{23}$. For completeness we have included the state $|Q_2\rangle = |Q_{-3/2}\rangle$ in the spectrum. In both panels we have used $U_c = 0.3U$ and $V_2 = 2U_c - V_1 - V_3$.

Recall that the system is tuned into the spin blockade regime. Since the state $|Q_1\rangle$ is formed by triplet pairings only, the electrons in this state cannot tunnel from one quantum dot to another. For the other two states, tunneling is possible. The three electrons can then be in different charge states. We have started this discussion with the electrons in the charge state (1,1,1), where (N_1, N_2, N_3) indicates the number of electrons in each quantum dot. Because of the finite tunneling interaction, other states are possible. We can, in fact, use the electrostatic part of the Hamiltonian in Eq. (2.7) to find out which charge states are relevant. For that we evaluate the energy of different charge states and construct a diagram that shows the lowest energetic charge state for different values of the detuning parameters ϵ and V_m. The result is the charge stability diagram (CSD) in Fig. 2.5(a).

In the following we will consider the charge states (2,0,1), (1,0,2), (1,2,0) and (0,2,1)[2]. Given that doubly-occupied quantum dots can only host singlet states, all the spin states that we need after including these extra charge states take the form $|S_{11}\rangle \otimes |\uparrow_3\rangle$, $|S_{11}\rangle \otimes |\downarrow_3\rangle$, etc. That is,

---

[2]Other charge states are also possible, but we want to keep it simple and consider only states that are coupled to (1,1,1) by only one tunneling event. At the same time, we only consider states with no more than two electrons per quantum dot.

two spin states per charge state.

Let us summarize what we have so far: We have a list of eight states in the (1,1,1) charge region, but we also have a strong magnetic field that splits the states, so we can focus on the subspace formed by the states with $S_z = -\frac{1}{2}$; There are other charge states that are coupled to the states in (1,1,1), and these need also to be considered. For simplicity we will consider an XO qubit operated at the resonant-exchange (RX) regime—top of the (1,1,1) charge region in Fig. 2.5. To study a system in this regime we only need three charge states: the states (1,1,1), (2,0,1) and (1,0,2), with the spin states $|0\rangle$, $|1\rangle$, $|Q_1\rangle$, $|D_{201}\rangle \equiv |S_{11}\rangle \otimes |{\downarrow}_3\rangle$ and $|D_{102}\rangle \equiv |S_{33}\rangle \otimes |{\downarrow}_1\rangle$. We subsequently use the basis $\{|0\rangle, |1\rangle, |Q_1\rangle, |D_{201}\rangle, |D_{102}\rangle\}$. Using this basis the Hamiltonian in Eq. (2.7) takes the form:

$$
H_{\text{Hubb}} = \begin{pmatrix}
0 & 0 & 0 & \frac{\sqrt{3}}{2}t_{12} & -\frac{\sqrt{3}}{2}t_{23} \\
0 & 0 & 0 & -\frac{1}{2}t_{12} & -\frac{1}{2}t_{23} \\
0 & 0 & 0 & 0 & 0 \\
\frac{\sqrt{3}}{2}t_{12} & -\frac{1}{2}t_{12} & 0 & U - 2U_c + \epsilon - V_m & 0 \\
-\frac{\sqrt{3}}{2}t_{23} & -\frac{1}{2}t_{23} & 0 & 0 & U - 2U_c - \epsilon - V_m
\end{pmatrix}.
$$
(2.19)

In order to arrive to this expression we have subtracted an energy offset $E_{\text{off}} = 2U_c - V_1 - V_2 - V_3 - \frac{1}{2}E_z$. Note the block structure of the Hamiltonian. We can identify a first 3×3 block, where all the matrix elements are zero; a second 2×2 block, with non-zero elements in the diagonal; and the tunnel elements coupling the two blocks. By writing the Hamiltonian in this way we can see that the states in the (1,1,1) region will hybridize with the states in the other charge regions. This hybridization provides an additional exchange energy that lifts the degeneracy of the states in the (1,1,1) region. For a small enough tunneling $t_{ij} \ll (U - 2U_c \pm \epsilon - V_m)$, this exchange energy can be evaluated perturbatively. We chose to apply a Schrieffer-Wolff (SW) transformation to the Hamiltonian (2.19) to separate the two blocks. A SW transformation is a very useful method to do a perturbation expansion of a Hamiltonian when some of the states are degenerate, as the first block of the Hamiltonian above[3].

After the transformation, the first block contains a shift in the energies due to the exchange interaction between the quantum dots. The SW transformation also results in an effective coupling, whose origin is also the exchange interaction, that couples the two qubit states. The quadruplet

---

[3]See the Appendix A for more details about the SW transformation.

state remains unmodified and decoupled from the other states because there are no tunnel coupling elements between this state and any other state in a different charge region. To simplify the notation further we define $\Delta \equiv U - 2U_c - Vm$, and write the transformed Hamiltonian into the (1,1,1) subspace:

$$H_{\mathrm{SW}} = \begin{pmatrix} -\frac{3}{4}\left(\frac{t_{12}^2}{\Delta+\epsilon} + \frac{t_{23}^2}{\Delta-\epsilon}\right) & \frac{\sqrt{3}}{4}\left(\frac{t_{12}^2}{\Delta+\epsilon} - \frac{t_{23}^2}{\Delta-\epsilon}\right) & 0 \\ \frac{\sqrt{3}}{4}\left(\frac{t_{12}^2}{\Delta+\epsilon} - \frac{t_{23}^2}{\Delta-\epsilon}\right) & -\frac{1}{4}\left(\frac{t_{12}^2}{\Delta+\epsilon} + \frac{t_{23}^2}{\Delta-\epsilon}\right) & 0 \\ 0 & 0 & 0 \end{pmatrix} \tag{2.20}$$

If we now project this Hamiltonian onto the qubit subspace and subtract an energy offset we can write the effective qubit Hamiltonian as

$$H_{\mathrm{qb}} = \frac{1}{2}J_z\sigma^z + J_x\sigma^x, \tag{2.21}$$

with the exchange energies J_z and J_x given by

$$J_z = \frac{1}{2}\left(\frac{t_{12}^2}{\Delta+\epsilon} + \frac{t_{23}^2}{\Delta-\epsilon}\right), \qquad J_x = \frac{\sqrt{3}}{4}\left(\frac{t_{12}^2}{\Delta+\epsilon} - \frac{t_{23}^2}{\Delta-\epsilon}\right), \tag{2.22}$$

and σ^x and σ^z the first and third Pauli matrices. This is the Hamiltonian of a triple quantum dot XO qubit in the RX regime. For equal tunneling between quantum dots $\tau \equiv t_{12} = t_{23}$, at zero detuning, defined as $\epsilon = 0$, the exchange energies reduce to $J_z = \tau^2/\Delta$ and $J_x = 0$. The qubit splitting J_z can thus be controlled via the gate potentials by changing Δ, thus providing an electric control over the z axis in the Bloch sphere.

2.2.1 Manipulation of the qubit

Let us go back to the Hamiltonian (2.19). The matrix element coupling the state $|0\rangle$ to the state $|D_{201}\rangle$ is larger than the matrix element coupling the state $|1\rangle$ to the state $|D_{201}\rangle$ by a factor $\eta_{201} = \sqrt{3}$, but they are both non-zero. There is, therefore, another state $|\psi_{201}\rangle$ that will couple with a larger matrix element to the state $|D_{201}\rangle$. If we take the states $|0\rangle$ and $|1\rangle$ as opposite states in the Bloch sphere, the state $|\psi_{201}\rangle$ that maximally couples to the state $|D_{201}\rangle$ is at an angle $\theta_{201} = 2\arctan(\eta_{201}) = 2\pi/3$ in the Bloch disk (a vertical cut of the Bloch sphere). Similarly, the state $|\psi_{102}\rangle$ that maximally couples to the state $|D_{102}\rangle$ is at an angle $\theta_{102} = 2\arctan(\eta_{102}) = -2\pi/3$ in the Bloch disk. We show this in Fig. 2.6.
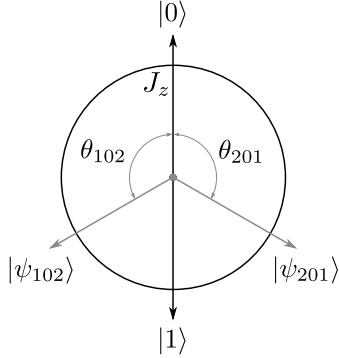
Figure 2.6:   Vertical cut of the Bloch sphere. Here we can see the detuning axes that result from the exchange interaction. At zero detuning, with $J_x = 0$ and $J_z = \tau^2/\Delta$, the Bloch field points towards the north pole, but pulsing into the neighboring charge states results in a detuning axis along $\theta_{201} = 2\pi/3$ and $\theta_{102} = -2\pi/3$.

The ratio $J_x/J_z = -\sqrt{3}\epsilon/(2\Delta)$ additionally shows that we can achieve any rotation angle continuously from 0 to $2\pi/3$. This function is continuous in ϵ and vanishes at $\epsilon = 0$. At this point the Bloch field points towards the North pole, thus $\theta = 0$. Increasing theta will make the Block field tilt continuously up to its maximum angle $\theta_{\max} = 2\pi/3$ when ϵ is large enough to drive the system into the charge state (2,0,1). We thus have full control of the qubit by detuning of the gate-induced offsets V_i.

The qubit can also be manipulated via Rabi driving. A small perturbation of ϵ around zero detuning results in the Hamiltonian

$$H_{\mathrm{qb}} = \frac{1}{2}\frac{\tau^2}{\Delta}\sigma^z - \frac{\sqrt{3}}{2}\frac{\tau^2\epsilon}{\Delta^2}\sigma^x + \mathcal{O}(\epsilon^2). \qquad (2.23)$$

A small, periodic detuning on ϵ around $\epsilon = 0$ will thus not shift the qubit splitting substantially but it will provide rotation axis along the orthogonal direction that will induce fast periodic oscillations between the qubit states. Let us see this in more detail. Consider the qubit Hamiltonian in Eq. (2.23) but with a periodic detuning $\epsilon = A\cos\omega t$ oscillating around $\epsilon = 0$ with an amplitude A and a frequency ω. We can write this Hamiltonian as

$$H'_{\mathrm{qb}} = \frac{1}{2}\hbar\omega_z\,\sigma^z + \tilde{A}\cos(\omega t)\,\sigma^x, \qquad (2.24)$$

with $\tilde{A} = \sqrt{3}\tau^2 A/(2\Delta^2)$ and the qubit splitting $\hbar\omega_z = \tau^2/(2\Delta)$. We then move into a rotating frame via a unitary transformation

$$H_{\rm rf} = e^{i\omega_z t\sigma^z} H'_{\rm qb} e^{-i\omega_z t\sigma^z}. \tag{2.25}$$

Since we are interested in driving the system at resonance, with $\omega = \omega_z$, we use a rotating wave approximation to remove the fast oscillating terms (terms that oscillate with $\omega + \omega_z$) and keep only the terms that oscillate with $\omega - \omega_z$. At resonance, this Hamiltonian simplifies to

$$H'_{\rm rf} = \frac{1}{2}\tilde{A}\,\sigma^x. \tag{2.26}$$

Now we can solve the Schrödinger equation with this Hamiltonian and find the time evolution of an initial qubit state. Suppose that we prepare the system into the state $|0\rangle$ and after some time t we want to measure the probability of finding the system in the state $|1\rangle$. This probability is given by

$$P_1(t) = |\langle 1|0(t)\rangle|^2 = \sin^2\left(\frac{\tilde{A}t}{2\hbar}\right). \tag{2.27}$$

Via a detuning of the offset potentials V_i, we thus expect to see Rabi oscillations from one qubit state to the other with a frequency $\Omega = \tilde{A}/\hbar$.

2.3   Electron-phonon coupling

In quantum dot-based spin qubits where both qubit states have the same spin structure—*doublets* in the case of triple dot XO qubits or *singlets* in the case of the XO singlet-only spin qubit of Paper I, see Chapter 3—one of the main mechanisms of qubit relaxation is the coupling of phonons with the electrons in the quantum dots [27, 28]. This electron-phonon coupling is also responsible for the dissipation of energy during other relaxation processes [16–18, 29, 30]: An electron in an excited state $|\uparrow\rangle$ with energy $E_{\rm Z}/2$ under the presence of a Zeeman field and random magnetic noise $g\mu_{\rm B}\boldsymbol{\delta\mathbf{B}} \cdot \boldsymbol{\sigma}$, can relax into the lower energy state $|\downarrow\rangle$, with energy $-E_{\rm Z}/2$, with the consequent dissipation of energy $\delta_{\rm dis} = E_{\rm Z}$ by a phonon. It is thus utterly necessary to account for the effects of the electron-phonon coupling when studying the coherence time of a semiconductor spin qubit.

We estimate the coherence time by evaluating the relaxation rate from one initial state $|i\rangle$ to another state $|f\rangle$ using Fermi's golden rule and considering the electron-phonon interaction perturbatively. The relaxation

rate to lowest order in perturbation is

$$\Gamma_{i \to f} = \frac{2\pi}{\hbar} |\langle f|H'|i\rangle|^2 \delta(E_f - E_i),\qquad(2.28)$$

with $|i\rangle$ and $|f\rangle$ two eigenstates of the unperturbed Hamiltonian, with energies E_i and E_f, respectively; H' would be the Hamiltonian that describes the electron-phonon interaction. We model this interaction as

$$H_{\text{e-ph}} = \sum_{\mathbf{k},p} \lambda_{\mathbf{k},p} \rho_{\mathbf{k}} \left(a_{\mathbf{k},p} + a^\dagger_{-\mathbf{k},p} \right),\qquad(2.29)$$

where $\lambda_{\mathbf{k},p}$ are the matrix elements of the electron-phonon coupling, $\rho_{\mathbf{k}}$ is the Fourier transform of the electronic density operator and $a^\dagger_{\mathbf{k},p}$ is a ladder operator that creates a phonon with momentum $\mathbf{k}$ and polarization p. In a system with n quantum dots, the Fourier transform of the density operator in second quantization formalism, is

$$\rho_{\mathbf{k},\alpha} = \sum_{i,j=1}^{n} \int_{-\infty}^{\infty} d\mathbf{r} e^{-i\mathbf{k}\cdot\mathbf{r}} \psi_i^*(\mathbf{r})\psi_j(\mathbf{r}) c^\dagger_{i,\alpha} c_{j,\alpha},\qquad(2.30)$$

with the electron wave function $\psi_i(\mathbf{r})$ (now accounting for spin as well, indicated by the index α). For circular quantum dots defined by the parabolic potential from Eq. (2.5), these wave function are given by the Fock-Darwin states [16] $\psi_i(\mathbf{r}) = \exp[-(\mathbf{r} - \mathbf{d}_i)^2/4\sigma_0^2]/\sqrt{\pi\sigma_0^2}$, where $\mathbf{d}_i$ labels the position of the dot i. For simplicity we will assume that the wave functions of two electrons in different quantum dots do not overlap, such that $\int d\mathbf{r} e^{-i\mathbf{k}\cdot\mathbf{r}} \psi_i^*(\mathbf{r})\psi_j(\mathbf{r}) = 0$ if $i \neq j$, and we instead include this overlap in the Hubbard Hamiltonian only as a phenomenological parameter[4]: the tunneling elements t_{ij}. We impose a strong confinement along the z direction (perpendicular to the plane of the 2DEG) and set the origin of coordinates to one of the quantum dots (i.e., $\mathbf{d}_1 = 0$). The matrix elements of the electronic density operator will then be

$$\int_{-\infty}^{\infty} d\mathbf{r} e^{-i\mathbf{k}\cdot\mathbf{r}} \psi_i^*(\mathbf{r})\psi_i(\mathbf{r}) = e^{-i\mathbf{k}\cdot\mathbf{d}_i} F_{\mathbf{k}}\qquad(2.31)$$

with $F_{\mathbf{k}} = \exp[-k_\parallel^2 \sigma_0^2/4]$, where $k_\parallel$ is the projection of the vector $\mathbf{k}$ into the plane of the quantum dots, σ_0 is the size of the quantum dot.

---

[4]The tunneling t_{ij} accounts for the overlap of wave functions and also for the Coulomb exchange interaction between two electrons in different quantum dots.

There is one remaining element in Eq. (2.29) that we have not talked about: the matrix elements of the electron-phonon coupling. These matrix elements are given by

$$\lambda_{\mathbf{k},p} = \left(M_{\text{pe}}^{(p)} + M_{\text{def}}^{(p)} \right) \sqrt{\frac{\hbar}{2\rho \mathcal{V} v_p k}}. \tag{2.32}$$

$M_{\text{pe}}^{(p)}$ and $M_{\text{def}}^{(p)}$ describe the coupling to piezoelectric and deformation phonons, respectively, ρ is the mass density of the semiconductor, $\mathcal{V}$ is a normalization volume and v_p is the sound velocity for the phonons with polarization p. In the rest of the text we will consider quantum dots in GaAs and Si only. We will therefore describe these couplings for the two materials. For GaAs, we have both piezoelectric and deformation phonons, and the couplings $M_{\text{pe}}^{(p)}$ and $M_{\text{def}}^{(p)}$ are given by

$$M_{\text{pe}}^{(p)} = ieh_{14}A_{\mathbf{k},p}, \qquad\qquad M_{\text{def}}^{(p)} = \Xi k \delta_{pl}, \tag{2.33}$$

where e is the elementary electric charge, h_{14} is the piezoelectric constant, Ξ is the deformation potential and $A_{\mathbf{k},p}$ are the anisotropy factors, which depend only on the phonon polarization $p = \{l, t_1, t_2\}$ and the direction of the vector $\mathbf{k}$. For GaAs they read [16]:

$$(A_{\mathbf{k},l})^2 = 9\cos^2(\theta)\sin^4(\theta)\sin^2(2\phi), \tag{2.34}$$

$$(A_{\mathbf{k},t1})^2 = \frac{1}{4}\left[1 + 3\cos(2\theta)\right]^2\sin^2(\theta)\sin^2(2\phi), \tag{2.35}$$

$$(A_{\mathbf{k},t2})^2 = \sin^2(2\theta)\cos^2(2\phi), \tag{2.36}$$

where the polar direction $\theta = 0$ is taken to be perpendicular to the plane of the 2DEG and the azimuthal angle ϕ is the in-plane angle. We assumed that the direction $\{\theta, \phi\} = \{\pi/2, 0\}$ points along the [100] crystallographic direction. For Si quantum dots these expressions are simpler because there are no piezoelectric phonons in this semiconductor [31]:

$$M_{\text{def}}^{(l)} = \left(\Xi_d + \Xi_u \cos^2\theta\right) k, \qquad M_{\text{def}}^{(t_1)} = \Xi_u \sin\theta\cos\theta\, k, \tag{2.37}$$

and the coupling for one of the transversal polarizations is zero $M_{\text{def}}^{(t_2)} = 0$. With these ingredients we can calculate relaxation rates from an initial state $|i; \text{vac}\rangle \equiv |i\rangle \otimes |\text{vac}\rangle$ to a final state $|f; 1_{\mathbf{k},p}\rangle \equiv |f\rangle \otimes |1_{\mathbf{k},p}\rangle$, where $|\text{vac}\rangle$ is the phonon vacuum and $|1_{\mathbf{k},p}\rangle$ describes a phonon with momentum $\mathbf{k}$ and polarization p. More specifically, we evaluate

$$\Gamma_{i \to f} = \sum_{\mathbf{k},p} \frac{2\pi}{\hbar} \left| \langle f; 1_{\mathbf{k},p} | H_{\text{e-ph}} | i; \text{vac} \rangle \right|^2 \delta(E_f - E_i), \tag{2.38}$$

where we summed over all possible final states, i.e., all phonon momenta and polarizations. If we want to study other relaxation processes that combine the electron-phonon interaction with another mechanism then we will need to include other terms in the perturbation expansion. We will see that when we study spin-mixing mechanisms of relaxation in the section 2.5 below.

2.4 Electric noise and sweet spots

Another important source of decoherence is the electric noise. The coupling strength between the spin of an electron and electric fields produced by random electric noise is not strong enough to be relevant. However, in XO qubits, where we have full control of the quantum states by electric fields only, the system is very susceptible to electric noise in the form of electric field fluctuations in the gate offsets V_i [32–34]. It is thus necessary to investigate any forms to limit the consequences of this noise. Let us start first by quantifying the effects of electric noise. We have previously seen, in Eq. (2.21), that the effective Hamiltonian of the qubit subspace has the form $H_{\mathrm{qb}} = \frac{1}{2}J_z\sigma^z + J_x\sigma^x$, with the exchange energies J_z and J_x that depend on some or all the gate-induced offsets V_i. A small fluctuation in the electric field on these V_i will result in

$$H_{\mathrm{qb}}^{(1)} = \frac{1}{2}(J_z + \delta_z)\sigma^z + (J_x + \delta_x)\sigma^x, \tag{2.39}$$

where $\delta_z = \sum[dJ_z(V_i)/dV_i]\delta V_i$ is responsible of dephasing of the qubit and $\delta_x = \sum[dJ_x(V_i)/dV_i]\delta V_i$ is responsible of relaxation or mixing between the qubit states. We focus on pure dephasing in this qubit basis, i.e., we investigate how the phase of a quantum state is randomized due to fluctuations in the qubit splitting $\hbar\delta\omega_z(t)$, and assume the noise δV_i to be quasistatic Gaussian noise with zero mean [32]. For simplicity we only consider noise in J_z, since the effects of noise in J_x will be much smaller[5] and study the dephasing time of the qubit at zero detuning ($J_x = 0$).

We prepare the system in the state $|+\rangle = \frac{1}{\sqrt{2}}(|0\rangle + |1\rangle)$. After some time t, we expect the system to have evolved into the state $|\psi(t)\rangle =$

---

[5]We can actually show that at zero detuning ($J_x = 0$) the Hamiltonian $H_{\mathrm{qb}}^{(1)}$ can be diagonalized and we can obtain a new set of qubit states. In this new basis the Hamiltonian will then read $H_{\mathrm{qb}}^{(1)} = \frac{1}{2}(J_z + \delta_z')\sigma_z$, with $\delta_z' \simeq \delta_z + 2\delta_x^2/J_z$. Since we expect the two energy variations δ_z and δ_x to be of the same order of magnitude, it is reasonable to consider only the effects of noise in J_z and drop out δ_x.

$\frac{1}{\sqrt{2}}(|0\rangle + e^{i\phi(t)}|1\rangle)$, where $\phi(t) = \omega_0 t + \delta\phi(t)$, and the unknown part of the phase being $\delta\phi(t) = \int_0^t \delta\omega_z(t')dt'$. To quantify the dephasing time we have to evaluate $\langle e^{i\delta\phi(t)}\rangle$. We can do that by evaluating $\log\langle e^{i\delta\phi(t)}\rangle$ and using

$$\delta\phi(t) = \frac{t}{\hbar}\sum_i \frac{\partial J_z}{\partial V_i}\delta V_i + \mathcal{O}(\delta V^2). \tag{2.40}$$

To leading order, $\delta\phi(t)$ is linear in the fluctuations δV_i, and thus Gaussian. Then we can do a cumulant expansion of the logarithm,

$$\log\langle e^{i\delta\phi(t)}\rangle = \sum_{n=1}^{\infty} \kappa_n \frac{(it)^n}{n!}, \tag{2.41}$$

with κ_n the n-th cumulant of the distribution of $\delta\omega_z$, and use that, for Gaussian variables with zero mean, only the second cumulant of the expansion $\kappa_2 = \sum_i (\partial J_z/\partial V_i)^2\langle \delta V_i^2\rangle/\hbar^2$ is non-zero. This yields $\log\langle e^{i\delta\phi(t)}\rangle = -\frac{1}{2}t^2\kappa_2$, from where we can extract an approximate dephasing time T_φ by using $\log\langle e^{i\phi(t)}\rangle = -t^2/T_\varphi^2$ [15]. Once we have an analytical expression for the pure dephasing time T_φ we can proceed to find a way to minimize it. Note that the on-site potentials V_i enter into the expression for T_φ via Eq. (2.40). If we can find a set of detuning potentials—that is, a point in the charge stability diagram—that makes $\partial J_z/\partial V_i = 0$ for all or some i, then the dephasing time would be substantially extended. Such point is called *Sweet Spot* (SS) and, from Eq. (2.40), we can see that this point maximizes the dephasing time of the qubit [15, 32, 34–36].

At the SS we cannot use the same procedure to calculate the dephasing time. Here the first derivative of the qubit splitting J_z vanish, and we are left with

$$\delta\phi(t) = \frac{t}{2\hbar}\sum_{i,j} \frac{\partial^2 J_z}{\partial V_i\partial V_j}\delta V_i\delta V_j + \mathcal{O}(\delta V^3). \tag{2.42}$$

The phase $\delta\phi(t)$ is not Gaussian anymore, causing $\log\langle e^{i\phi(t)}\rangle \neq -\frac{1}{2}t^2\kappa_2$ [37]. In the cumulant expansion we would have to consider more (or all) terms, especially if we want to consider long times, leaving us with expressions that are not possible to evaluate. One can only use that method as long as $\frac{\partial\omega_z}{\partial V_i} \gg \frac{\partial^2\omega_z}{\partial V_i\partial V_j}$, a condition that is not satisfied at the SS. We can instead estimate the dephasing time in a different way: We can calculate the probability that a state initially prepared in $|+\rangle$ remains in the state $|+\rangle$ after a time t. That is, evaluate $|\langle +|\psi(t)\rangle|^2$. And then calculate the average of the probability over the random noise $\langle P_+(t)\rangle = \langle|\langle +|\psi(t)\rangle|^2\rangle_{\text{noise}}$. We start by

solving the Schrödinger equation with the Hamiltonian $H_{\text{qb}}^{(1)} = \frac{1}{2}(J_z + \delta_z)\sigma^z$ in a rotating frame, as we did in Section 2.2.1, from which we obtain $|\psi(t, \delta V_i)\rangle$. Then we evaluate

$$\langle P_+(t)\rangle = \int \prod_i \left(\frac{d(\delta V_i)}{\sqrt{2\pi\sigma_e^2}} \exp\left[-\frac{\delta V_i^2}{2\sigma_e^2} \right] \right) |\langle +|\psi(t, \delta V_i)\rangle|^2, \qquad (2.43)$$

where σ_e is the standard deviation of the noise in the offset potentials. We then extract a dephasing time from the resulting expression (we will see this in Chapter 5).

2.5 Spin-mixing mechanisms

Besides the electron-phonon interaction and the electric noise-induced dephasing described above, the remaining main sources of decoherence in Xo qubits are spin-mixing mechanisms. The two most common are the spin-orbit (SO) interaction and the hyperfine coupling between the spin of an electron confined in a quantum dot and the nuclear spins of the host material in the semiconductor. These two mechanisms, combined with the electron-phonon coupling as a mechanism to dissipate energy, can lead to relaxation between the qubit states or out of the qubit subspace. One of the goals of this thesis is to mitigate the effects of these decoherence mechanisms and we will thus study them in detail.

2.5.1 Hyperfine interaction

High quality III-V semiconductors such as GaAs consist of atoms carrying randomly oscillating, non-zero nuclear spins. These nuclear spins couple to the electrons confined in the quantum dotscausing spin relaxation and decoherence. We model the ensemble of nuclear spins in each quantum dot (estimated to be around $\sim 10^6$ spins) as a randomly fluctuating effective magnetic field $\mathbf{K}_i$ (the Overhauser field) that acts on the electrons localized in the dot i [9, 12, 38]. The dynamics of the Overhauser field is typically slower than a single qubit operation time of an XO qubit, so we can threat the effective field $\mathbf{K}_i$ as quasistatic.

However, like any other magnetic moment, the magnetic moments of the nuclei will also couple to the orbital degrees of freedom of nearby electrons, but this coupling is weak and can be safely neglected [9, 38–41]. We thus model the electron-nuclei interaction as a Fermi contact

interaction and describe this hyperfine interaction between nuclear spins and the electron spins with the Hamiltonian

$$H_{\text{hf}} = \frac{g\mu_{\text{B}}}{2} \sum_{i,\alpha,\beta} c_{i,\alpha}^{\dagger} \mathbf{K}_i \cdot \boldsymbol{\sigma}_{\alpha\beta} c_{i,\beta}, \qquad (2.44)$$

where $\boldsymbol{\sigma}$ is the Pauli matrices vector and $c_{i,\alpha}^{\dagger}$ is the ladder operator that creates an electron with spin α in the quantum dot i. The hyperfine interaction can cause relaxation via a spin flip or via dephasing due to random shifts of the qubit splitting. We study this in more detail in the following chapters, where we consider the effects of this interaction on specific devices.

2.5.2 Spin-orbit interaction

The spin-orbit interaction couples the motion of an electron in a crystal to its spin. Within a 2DEG in the x-y plane, this coupling is described by the Hamiltonian [29, 30]

$$H_{\text{SO}} = \alpha(-p_y\sigma^x + p_x\sigma^y) + \beta(-p_x\sigma^x + p_y\sigma^y). \qquad (2.45)$$

In quantum dots, where the electrons are localized in a small region of space, the average motion $\langle \mathbf{p} \rangle$ of the electron vanishes. However, a spin flip is still possible via three mechanisms: (*i*) a virtual tunneling of the electron from one quantum dot to the nearest; (*ii*) a virtual excitation of a higher orbital state[6] within the same dot; (*iii*) a virtual excitation of a valley state (in Si-based qubits) within the same dot as well.

We can then calculate relaxation rates out of the qubit subspace using a second-order Fermi's golden rule and considering both the electron-phonon and the SO interactions as perturbation:

$$\Gamma_{i \to f} = \sum_{\mathbf{k},p} \frac{2\pi}{\hbar} \left| \sum_v \frac{\langle f; 1_{\mathbf{k},p}|H'|v\rangle\langle v|H'|i; \text{vac}\rangle}{E_v - E_i} \right|^2 \delta(E_f - E_i), \qquad (2.46)$$

where $H' = H_{\text{SO}} + H_{\text{e-ph}}$, the initial state $|i\rangle$ is a qubit state combined with the phonon vacuum, the final state $|f\rangle$ is a lower energy state out of the qubit subspace combined with a phonon with momentum $\mathbf{k}$ and polarization p, and the sum runs over all possible virtual states $|v\rangle$.

---

[6]Even though quantum dot-based spin qubits are usually operated in the spin block-ade regime, where excited orbitals are not accessible, we will allow for a virtual excitation of these high energy states to make this section comprehensive.
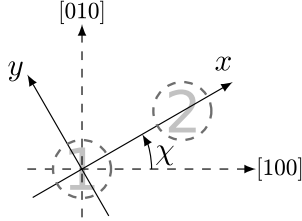
Figure 2.7: Reference frame of the system. We use two quantum dots as an example. The quantum dots are located in the (001) crystallographic plane, and the tunneling direction is along the x axis, which forms an angle χ with the [100] crystallographic direction.

In the XO qubits that we consider in this thesis both quit states have the same spin structure. Qubit relaxation—that is, from the state $|1\rangle$ to the state $|0\rangle$—does therefore not require a spin-mixing mechanism. The SO interaction is only relevant for relaxation (or leakage) out of the qubit subspace. In this section we will focus of leakage processes, since qubit relaxation has been treated in Sec. 2.3 above.

We consider a system of a few quantum dots with the 2DEG in the (001) plane of the crystal, and choose the axis of the tunneling direction to be along the x direction, forming an angle χ with the [100] direction of the crystal, as we illustrate in Fig. 2.7. Then we model the spin-flip mechanism of the SO coupling (terms with σ^x only) for each electron as

$$H_{\mathrm{SO}} = A_{xx}p_x\sigma^{x'} + A_{xy}p_y\sigma^{x'} \tag{2.47}$$

where $\mathbf{p}$ is the momentum of the electron, which we consider strongly confined along the z direction. The Pauli matrices $\boldsymbol{\sigma}$ act on the spin states and we consider the z' direction to be aligned with the external magnetic field which, in turn, points along the x direction (see Fig. 2.7). The two coupling constants A_{xx} and A_{xy} contain information about the angle χ and the Rashba and Dresselhaus coupling amplitudes α and β:

$$A_{xx} = \alpha + \beta\sin 2\chi, \qquad\qquad A_{xy} = \alpha + \beta\cos 2\chi. \tag{2.48}$$

The derivation of the matrix elements of the SO Hamiltonian and the electron-phonon coupling is quite tedious and is also device-specific: The geometry of the system as well as the material of the host semiconductor play an important role. We will therefore not derive them in this chapter, but we provide below the recipe for obtaining the matrix elements, which

we took mainly from Refs. [16, 18, 36, 42]. The full expressions will be presented in Chapter 5.

In the following we use the basis $\{|nvs\rangle\}$, where n denotes the orbital state (we only consider the ground and first excited states, 0 and 1), v is the valley state (either $-$ or $+$, and only relevant for quantum dots defined in Si) and s is the spin state ($\uparrow$ or $\downarrow$).

(*i*) Charge sates

In order to evaluate the matrix elements of the SO interaction for a spin-flip tunneling process we need to find an expression for the momentum operator $\mathbf{p}$. For this we use $\mathbf{p} = \frac{i}{\hbar}m^*[H_{\text{Hubb}}, \mathbf{r}]$, with H_{Hubb} the Hamiltonian from Eq. (2.7) and m^* the effective electron mass [16, 43]. Phonon emission is then governed by the matrix elements that we calculated in Section 2.3. The matrix element that describes the emission of a phonon by an electron in quantum dot j and in the lowest orbital ($n = 0$) and valley ($v = $"$-$") states reads, for any spin s:

$$\langle 0-s; 1_{\mathbf{k},p}|H_{\text{e-ph}}|0-s; \text{vac}\rangle = \lambda_{\mathbf{k},p}e^{-i\mathbf{k}\cdot\mathbf{d}_j}e^{-(k_x^2+k_y^2)\sigma_0^2/4}. \tag{2.49}$$

(*ii*) Orbital states

So far we have only considered the lowest orbital state in the quantum dots, but the parabolic potential that confines the electrons in the quantum dots [see the Hamiltonian in Eq. (2.5)] results in Fock-Darwin states with energy splitting $E_{\text{orb}} = \hbar^2/(m^*\sigma_0^2)$. And, even though the energy separation E_{orb} is, by far, the largest energy scale in the system, the first orbital state can, in principle, be virtually excited. The electron can then undergo a spin flip during this virtual excitation. Since the SO interaction couples the orbital ground state to the first excited state with opposite spin [9], we need to evaluate the matrix element

$$\langle 1^{\alpha}-\bar{s}|p_{\alpha}\sigma^{x'}|0-s\rangle = \frac{i\hbar}{\sqrt{2}\sigma_0}, \tag{2.50}$$

where $\bar{s}$ is the spin state opposite to s and the superscript α denotes the component of the wave function is in the excited state [43]. The electron-phonon Hamiltonian also couples these two orbital states [18], with the matrix elements

$$\langle 1^{\alpha}-s; 1_{\mathbf{k},p}|H_{\text{e-ph}}|0-s; \text{vac}\rangle = -\frac{i}{\sqrt{2}}k_{\alpha}\sigma_0\lambda_{\mathbf{k},p}e^{-i\mathbf{k}\cdot\mathbf{d}_j}e^{-(k_x^2+k_y^2)\sigma_0^2/4}. \tag{2.51}$$

(*iii*) Valley states

Silicon-based quantum dots have the advantage that the most abundant isotope of Si is nuclear spin-free, hence reducing the effects of hyperfine noise. On the other hand, the band gap in bulk Si is indirect and the conduction band has six minima. In most Si-based heterostructures strain splits off four of these minima, but we are still left with two of them. Localized electrons in the conduction band thus have an extra "valley" degree of freedom, which we describe by the wave function

$$\psi^{(v)} = F^{(v)}(\mathbf{r})\left[\alpha_1^{(v)} u_1(\mathbf{r})e^{ik_z z} + \alpha_2^{(v)} u_2(\mathbf{r})e^{-ik_z z}\right], \qquad (2.52)$$

where $F^{(v)}(\mathbf{r})$ is the envelope wave function corresponding to valley v and $u_{1,2}(\mathbf{r})$ are the periodic Bloch functions at the minima of the conduction band.

Both SO and electron-phonon interaction can couple opposite valley states [18], in a similar they couple orbital states. However, the relevant matrix elements of both the SO and the electron-phonon Hamiltonians depend sensitively on details of the confinement along the z direction, and these are hard to predict. To simplify the calculations and obtain a qualitative expression we use the dipole approximation $e^{-i\mathbf{k}\cdot\mathbf{r}} \approx 1 - i\mathbf{k}\cdot\mathbf{r}$ in the electron-phonon Hamiltonian of Eq. (2.29). This approximation is valid if the wave length of the emitted phonon—with momentum $\mathbf{k}$, proportional to the energy difference between the initial and final states, dissipated by the phonon—is much larger than the confinement length σ_0. That is, $\Delta E^2 \ll (\hbar v_t/\sigma)^2$, where ΔE is the energy difference between the initial and final states. This is indeed the case in typical XO qubits. By employing this approximation we can write

$$\langle 0+s; 1_{\mathbf{k},p}|H_{\text{e-ph}}|0-s; \text{vac}\rangle \approx \lambda_{\mathbf{k},p} e^{-i\mathbf{k}\cdot\mathbf{d}_j}(\mathbf{k}\cdot\mathbf{r}_{+-}), \qquad (2.53)$$

with $\mathbf{r}_{+-} = \langle 0+s|\mathbf{r}|0-s\rangle$ the valley dipole matrix element. If we use again that $\mathbf{p} = \frac{i}{\hbar}m^*[H_{\text{Hubb}}, \mathbf{r}]$, then we can obtain the matrix elements of the SO Hamiltonian in terms of the dipole matrix elements. For simplicity we will use that $|z_{+-}| \ll |x_{+-}|, |y_{+-}|$ and assume equal dipole matrix elements along the x and y directions, with $x_{+-} = y_{+-} \equiv r_d$ [44, 45].

With all these ingredients we can investigate all the major mechanisms of relaxation and decoherence in XO qubits and find mechanisms to minimize their effects, suitable for each implementation of the XO qubit.

3

The exchange-only singlet-only spin qubit

We propose a new, exchange-only singlet-only spin qubit of unprecedented quality. The qubit is scalable and offers full electrical control and a large coherence time. We additionally explain how to implement our proposal into already existing devices. Some of the contents of this chapter are included in Paper I.

Exchange-only qubits are easy to manipulate and fabricate, and scalability is indeed one of their main advantages. Nevertheless, the XO qubit that we have introduced in the previous chapter works with qubit states that have non-zero spin. This non-zero spin can couple to magnetic noise and provide a channel for relaxation outside the qubit subspace, thus limiting substantially the coherence time of the qubit [27, 32, 39, 40]. It is especially concerning the magnetic field gradients set up by the ensemble or randomly fluctuating nuclear spins in the materials that host the quantum dots. Especially in III-IV semiconductors such as GaAs, since this is a broadly used material to fabricate state-of-the-art semiconductor-based quantum devices [46–50]. Many approaches have been proposed to overcome this problem, such as devising hyperfine-induced feedback cycles, optimizing complex echo pulsing schemes, etc [51–59]. These approaches

lead indeed to prolonged coherence times, although complicating the manipulation of the qubit. But we will not discuss them here.

Quantum-dot-based spin qubits can also be fabricated in isotopically purified ^{28}Si, which can be nearly nuclear-spin-free. The down side of this approach is that the stronger charge noise in silicon-based devices and the extra valley degree of freedom complicate the qubit operation. This will be further analyzed in Chapter 5.

We want a simple XO device that can be easily fabricated in GaAs. But we also want a qubit that does not decohere in the presence of magnetic field gradients of any nature. If we look back at the (short) history of quantum dot-based spin qubits we can get a hint on how to proceed. *One* electron offers the quantum two-level system that we need, but it is is hard to control and decoheres fast. *Two* electrons are easier to control since two-electron spin qubits allow for electric control of the qubit along one axis of the Bloch sphere, but still require localized magnetic fields for full control; also the coherence time is smaller. *Three* electrons offer a promising alternative, and decoherence, although it is still a problem, can be overcome by implementing some of the protocols aforementioned. *Four* electrons... What about four electrons? With four electrons we can construct a qubit subspace where both qubit states are singlet (spin-less) states. Since singlet states do not couple to each other by any external or intrinsic magnetic fields, the coherence time of the qubit will, in principle, be very large. Indeed, a singlet-only subspace is known to be a "decoherence-free" subspace for spin qubits [60, 61].

3.1   The singlet-only spin qubit

We propose a system composed of four quantum dots arranged in a T-like geometry, as shown in Fig. 3.1, with one electron on each dot. Our calculations show that a linear array of four quantum dots would also display a similar non-degenerate spectrum, but the arising exchange interaction will only allow for control of axis along one hemisphere of the Bloch sphere. This is in principle enough for a full qubit manipulation if this is done via a pulsing scheme (see Sec. 3.2) but qubit operations via Rabi driving would be challenging. We thus want to design a qubit that has at least the same features as the triple dot XO qubit, and the T-like design offers exactly what we need, as we show below.

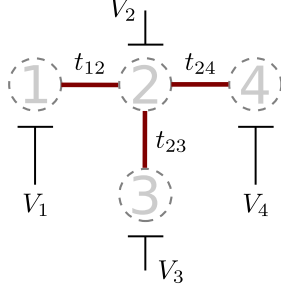With four electrons—independently of the geometry—we have *sixteen*

Figure 3.1: The XO singlet-only spin qubit is composed of four quantum dots in a T-like geometry. The dots are tunnel coupled to their nearest neighbor only, indicated by red lines and the tunnel coupling energies t_{ij}. Gate electrodes control the potentials V_i in the dots.

spin states, out of which two are singlets[1]. These two singlet states, that we will conveniently label $|0\rangle$ and $|1\rangle$ are:

$$|0\rangle = \frac{1}{2\sqrt{3}} \left[|\uparrow\uparrow\downarrow\downarrow\rangle + |\downarrow\downarrow\uparrow\uparrow\rangle + |\uparrow\downarrow\uparrow\downarrow\rangle + |\downarrow\uparrow\downarrow\uparrow\rangle - 2|\uparrow\downarrow\downarrow\uparrow\rangle - 2|\downarrow\uparrow\uparrow\downarrow\rangle \right], \quad (3.1)$$

$$|1\rangle = \frac{1}{2} \left[|\uparrow\uparrow\downarrow\downarrow\rangle - |\uparrow\downarrow\uparrow\downarrow\rangle - |\downarrow\uparrow\downarrow\uparrow\rangle + |\downarrow\downarrow\uparrow\uparrow\rangle \right]. \quad (3.2)$$

We use the two singlet states as the qubit states. These can also be expressed in terms of singlet or triplet couplings between pairs of electrons:

$$|0\rangle = \frac{1}{\sqrt{3}} \left[|S_{13}S_{24}\rangle + |S_{12}S_{34}\rangle \right], \quad (3.3)$$

$$|1\rangle = |S_{14}S_{23}\rangle, \quad (3.4)$$

but it is even more interesting if we write the state $|0\rangle$ in terms of couplings of the electrons in quantum dots 1 and 4 and the electrons in the quantum dots 2 and 3, as we do with the state $|1\rangle$:

$$|0\rangle = \frac{1}{\sqrt{3}} \left[|T_{14}^{(0)}T_{23}^{(0)}\rangle - |T_{14}^{(+)}T_{23}^{(-)}\rangle - |T_{14}^{(-)}T_{23}^{(+)}\rangle \right]. \quad (3.5)$$

---

[1]There are several ways to see this. The simplest is to construct the four-particle spin operator $\mathbf{S}^2$ and diagonalize it. But the most beautiful way is to count on one's fingers: we know that there are only five quintuplet states (the state $|\uparrow\uparrow\uparrow\uparrow\rangle$ has $S_z = 2$, and quintuplets come in groups of five) and we also know that there are $\binom{4}{2} = 6$ states with $S_z = 0$; the only possible combination is five quintuplets, three three-fold (nine in total) triplets and two singlets.

The state $|0\rangle$ is formed by triplet pairings only, even though it has $\mathbf{S}^2 = 0$, whereas the state $|1\rangle$ is composed of singlet pairings only. Since we tune the system into the spin blockade regime we expect to see a different exchange energy associated to each of the two states. The other fourteen states within the (1,1,1,1) charge region are

$$|Q^{(+2)}\rangle = |\uparrow\uparrow\uparrow\uparrow\rangle, \tag{3.6}$$

$$|Q^{(+1)}\rangle = \frac{1}{2}[|\uparrow\uparrow\uparrow\downarrow\rangle + |\uparrow\uparrow\downarrow\uparrow\rangle + |\uparrow\downarrow\uparrow\uparrow\rangle + |\downarrow\uparrow\uparrow\uparrow\rangle], \tag{3.7}$$

$$|Q^{(0)}\rangle = \frac{1}{2}[|\uparrow\uparrow\downarrow\downarrow\rangle + |\uparrow\downarrow\uparrow\downarrow\rangle + |\downarrow\uparrow\uparrow\downarrow\rangle + |\uparrow\downarrow\downarrow\uparrow\rangle + |\downarrow\uparrow\downarrow\uparrow\rangle + |\downarrow\downarrow\uparrow\uparrow\rangle], \tag{3.8}$$

$$|Q^{(-1)}\rangle = \frac{1}{\sqrt{6}}[|\downarrow\downarrow\downarrow\uparrow\rangle + |\downarrow\downarrow\uparrow\downarrow\rangle + |\downarrow\uparrow\downarrow\downarrow\rangle + |\uparrow\downarrow\downarrow\downarrow\rangle], \tag{3.9}$$

$$|Q^{(-2)}\rangle = |\downarrow\downarrow\downarrow\downarrow\rangle, \tag{3.10}$$

$$|T_\alpha^{(+)}\rangle = \frac{1}{\sqrt{6}}[2|\uparrow\uparrow\downarrow\uparrow\rangle - |\downarrow\uparrow\uparrow\uparrow\rangle - |\uparrow\uparrow\uparrow\downarrow\rangle], \tag{3.11}$$

$$|T_\alpha^{(0)}\rangle = \frac{1}{2\sqrt{3}}[2|\uparrow\downarrow\downarrow\uparrow\rangle - 2|\downarrow\uparrow\uparrow\downarrow\rangle - |\uparrow\downarrow\uparrow\downarrow\rangle + |\downarrow\uparrow\downarrow\uparrow\rangle + |\uparrow\uparrow\downarrow\downarrow\rangle - |\downarrow\downarrow\uparrow\uparrow\rangle], \tag{3.12}$$

$$|T_\alpha^{(-)}\rangle = \frac{1}{\sqrt{6}}[|\downarrow\downarrow\downarrow\uparrow\rangle + |\uparrow\downarrow\downarrow\downarrow\rangle - 2|\downarrow\downarrow\uparrow\downarrow\rangle], \tag{3.13}$$

$$|T_\beta^{(+)}\rangle = \frac{1}{\sqrt{2}}[|\uparrow\uparrow\uparrow\downarrow\rangle - |\downarrow\uparrow\uparrow\uparrow\rangle], \tag{3.14}$$

$$|T_\beta^{(0)}\rangle = \frac{1}{2}[|\uparrow\downarrow\uparrow\downarrow\rangle - |\downarrow\uparrow\downarrow\uparrow\rangle + |\uparrow\uparrow\downarrow\downarrow\rangle - |\downarrow\downarrow\uparrow\uparrow\rangle], \tag{3.15}$$

$$|T_\beta^{(-)}\rangle = \frac{1}{\sqrt{2}}[|\uparrow\downarrow\downarrow\downarrow\rangle - |\downarrow\downarrow\downarrow\uparrow\rangle], \tag{3.16}$$

$$|T_\gamma^{(+)}\rangle = \frac{1}{2\sqrt{3}}[3|\uparrow\downarrow\uparrow\uparrow\rangle - |\downarrow\uparrow\uparrow\uparrow\rangle - |\uparrow\uparrow\downarrow\uparrow\rangle - |\uparrow\uparrow\uparrow\downarrow\rangle], \tag{3.17}$$

$$|T_\gamma^{(0)}\rangle = \frac{1}{\sqrt{6}}[|\uparrow\downarrow\uparrow\downarrow\rangle - |\downarrow\uparrow\downarrow\uparrow\rangle - |\uparrow\uparrow\downarrow\downarrow\rangle + |\downarrow\downarrow\uparrow\uparrow\rangle + |\uparrow\downarrow\downarrow\uparrow\rangle - |\downarrow\uparrow\uparrow\downarrow\rangle], \tag{3.18}$$

$$|T_\gamma^{(-)}\rangle = \frac{1}{2\sqrt{3}}[|\downarrow\downarrow\downarrow\uparrow\rangle + |\downarrow\downarrow\uparrow\downarrow\rangle + |\uparrow\downarrow\downarrow\downarrow\rangle - 3|\downarrow\uparrow\downarrow\downarrow\rangle]. \tag{3.19}$$

Besides the two singlet states from above, there are nine triplet states T and five quintuplet states Q. Note, though, that the choice of the basis is not random. We have chosen a basis that knows about the total spin, but any other basis that is formed by e.g., a rotation of the qubit states would be an equally valid basis.
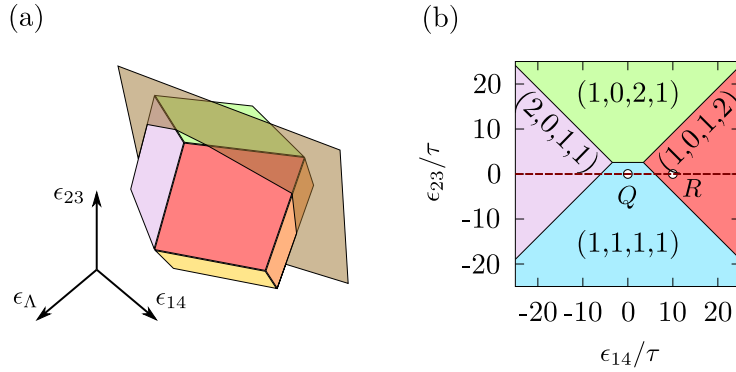
Figure 3.2: (a) Three-dimensional CSD. The figure shows the borders of each charge region as a function of ϵ_{14}, ϵ_{23} and ϵ_Λ. (b) We fix $\epsilon_\Lambda = 0$ and focus on the RX regime, close to the charge regions (2,0,1,1), (1,0,2,1) and (1,0,1,2). The qubit is operated along the read dashed line, with the points Q and R showing the qubit operation point and the readout point.

After introducing a finite, spin-conserving tunneling interaction between quantum dots the system will no longer be in the charge state (1,1,1,1). The wave function of the electrons will extend to neighboring quantum dots and other charge states will then be accessible.

We model the system as we did in section 2.2: with a Hubbard-like Hamiltonian. Recall that the system we study is composed of four quantum dots in a T-like geometry with nearest-neighbor tunneling, on-site gate offset potentials and an external, in-plane and homogeneous magnetic field that produces a Zeeman splitting of the states with non-zero spin. The Hamiltonian is then

$$H_{\text{Hubb}} = \sum_i \left[\frac{U}{2} n_i(n_i - 1) - V_i \, n_i \right] + \sum_{\langle i,j \rangle} U_c \, n_i n_j$$
$$- \sum_{\langle i,j \rangle, \alpha} \frac{t_{ij}}{\sqrt{2}} \, c_{i,\alpha}^\dagger c_{j,\alpha} + \sum_{i,\alpha} \frac{E_{\text{Z}}}{2} \, c_{i,\alpha}^\dagger \sigma_{\alpha\alpha}^z c_{i,\alpha}, \quad (3.20)$$

The first line of Eq. (3.20) describes the electrostatic energy of the system and the second line contains the spin-conserving tunnel coupling and the Zeeman splitting of the electronic spin states, with $E_{\text{Z}} = g\mu_{\text{B}}B_z$.

We can use the electrostatic part of H to find the charge ground state as a function of the gate-induced offsets V_i and obtain a charge stability

diagram as a function of V_1, but for convenience we introduce four different tuning parameters

$$\epsilon_{14} = (V_4 - V_1), \tag{3.21}$$

$$\epsilon_{23} = \frac{1}{2}(V_3 - V_2), \tag{3.22}$$

$$\epsilon_\Lambda = \frac{1}{4}(-V_1 + V_2 + V_3 - V_4), \tag{3.23}$$

$$\epsilon_\Sigma = \frac{1}{4}(V_1 + V_2 + V_3 + V_4). \tag{3.24}$$

and we fix $\epsilon_\Sigma = \frac{3}{4}U_c$, so that the $(1,1,1,1)$ state $|Q^{(0)}\rangle$ has zero energy. The CSD is thus three-dimensional [see Fig. 3.2(a)] but in this chapter we restrict ourselves to the plane $\epsilon_\Lambda = 0$ and focus on the RX regime, close to the charge states $(2,0,1,1)$, $(1,0,2,1)$ and $(1,0,1,2)$, where exchange effects due to the vicinity of these charge regions can be significant. Fig. 3.2(b) shows the relevant part of the charge stability diagram as a function of ϵ_{14} and ϵ_{23}, with $\epsilon_\Lambda = 0$, $U = 50\,\tau$, and $U_c = 15\,\tau$ (τ being our unit of energy, of the order of the tunnel coupling energies).

We now introduce the finite tunnel coupling energies t_{ij} and the Zeeman energy E_Z, and investigate the spectrum of H in more detail, defining the qubit operation point Q to have the tuning $\epsilon_{14} = \epsilon_{23} = \epsilon_\Lambda = 0$, corresponding to setting $V_1 = V_2 = V_3 = V_4$.

Along the red dashed line in Fig. 3.2(b) ϵ_{14} parametrizes a "linear tilt" of the potential of the dots 1, 2, and 4, equivalent to the triple-dot detuning parameter ϵ that we used in Chapter 2 to operate the XO qubit (see Refs. [27, 28, 62]). In Fig. 3.3 we plot the energy spectrum of the six lowest-energy states with $S_z = 0$ as a function of ϵ_{14} along the red line. For this plot we set $t_{12} = t_{24} = \frac{4}{3}t_{23} = \tau$ and use a Zeeman energy $E_Z = 1.875\,\tau$ (corresponding to $E_Z = 30\,\mu$eV, for $\tau = 16\,\mu$eV [27]). We only show the part of the plot that corresponds to the top of the $(1,1,1,1)$ region. Other charge states are higher up in energy and thus not shown, but the exchange effects are nevertheless evident. In the plot we can identify a quintuplet state, labeled $|Q^{(0)}\rangle$, three triples that we label $|T_{1,2,3}\rangle$ (blue curves), and the two qubits states (in green and red) that split out by an energy $\hbar\omega_z$. The other spin states in the $(1,1,1,1)$ region, with $S_z = \pm1, \pm2$, are split off by multiples of E_Z and not shown.
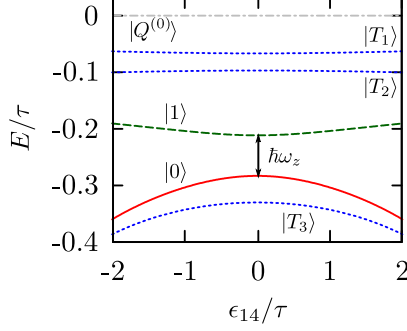
Figure 3.3: Energy spectrum of the subspace spanned by the states with $S_z = 0$. We plot the eigenenergies along the red line in Fig. 3.2, with $t_{12} = t_{24} = \frac{4}{3}t_{23} = \tau$.

3.1.1 Effective Hamiltonian

Close to the qubit operation point Q, in Fig. 3.2, with $\epsilon_{14} = 0$, the exchange effects are significant but still small enough to allow us to treat the system perturbatively and derive an effective qubit Hamiltonian. We tune the system such that $\Delta \equiv U - 3U_c > 0$. In this situation, around the qubit operation point Q lowest-lying excited states are the charge states (2,0,1,1), (1,0,2,1), and (1,0,1,2), all with an excitation energy Δ. We additionally assume that the energy scale of the tunnel coupling τ is much smaller than this excitation energy, $\tau \ll \Delta$, and proceed as in Section. 2.2, performing a SW transformation of the Hamiltonian. The resulting Hamiltonian has a block structure, with the singlet states being, in the basis $\{|1\rangle, |0\rangle\}$:

$$H_S = \begin{pmatrix} -\frac{1}{4}(J_{12} + J_{24} + 4J_{23}) & \frac{\sqrt{3}}{4}(J_{12} - J_{24}) \\ \frac{\sqrt{3}}{4}(J_{12} - J_{24}) & -\frac{3}{4}(J_{12} + J_{24}). \end{pmatrix} \quad (3.25)$$

In this expression we have used the exchange energies

$$J_{12} = \frac{t_{12}^2}{\Delta + 2\epsilon_\Lambda + \epsilon_{14} - \epsilon_{23}}, \quad (3.26)$$

$$J_{24} = \frac{t_{24}^2}{\Delta + 2\epsilon_\Lambda - \epsilon_{14} - \epsilon_{23}}, \quad (3.27)$$

$$J_{23} = \frac{t_{23}^2}{\Delta - 2\epsilon_{23}}. \quad (3.28)$$

We find similar expressions for the triplets block, whereas for the quintuplets block we simply have $H_Q = 0$. Moreover, since the Hamiltonian H_{Hubb} commutes with the total spin projection operator S_{tot}^z, none of the states with $S_{\text{tot}}^z = 0$ is coupled to any other state with $S_{\text{tot}}^z \neq 0$, not only to this order in perturbation, but to all orders in the t_{ij}.

For the case where $t_{12} = t_{24}$, the singlet and triplet Hamiltonians, H_S and H_{T^0}, simplify considerably at the point Q, resulting in

$$H_S = \begin{pmatrix} -\frac{1}{2}(J + 2J_{23}) & 0 \\ 0 & -\frac{3}{2}J \end{pmatrix}, \tag{3.29}$$

$$H_{T^0} = \begin{pmatrix} -\frac{1}{6}(J + 2J_{23}) & 0 & \frac{2}{3\sqrt{2}}(J - J_{23}) \\ 0 & -\frac{1}{2}J & 0 \\ \frac{2}{3\sqrt{2}}(J - J_{23}) & 0 & -\frac{2}{3}(2J + J_{23}) \end{pmatrix}, \tag{3.30}$$

where for the triplets we used the basis $\{|T_\alpha^{(0)}\rangle, |T_\beta^{(0)}\rangle, |T_\gamma^{(0)}\rangle\}$. Ignoring corrections to the wave functions of the order τ/Δ, the states $|1\rangle$, $|0\rangle$ and $|T_2\rangle \equiv |T_\beta^{(0)}\rangle$ are eigenstates of the Hamiltonians H_S and H_{T^0}, respectively, at the qubit operation point. The two remaining unpolarized triplet eigenstates being

$$|T_1^{(0)}\rangle = \cos\frac{\theta}{2}|T_\alpha^{(0)}\rangle + \sin\frac{\theta}{2}|T_\gamma^{(0)}\rangle, \tag{3.31}$$

$$|T_3^{(0)}\rangle = \sin\frac{\theta}{2}|T_\alpha^{(0)}\rangle - \cos\frac{\theta}{2}|T_\gamma^{(0)}\rangle, \tag{3.32}$$

where we have introduced an angle θ, defined as $\tan\theta = 4\sqrt{2}(J - J_{23})/(7J + 2J_{23})$, with $J = \tau^2/\Delta$ and $J_{23} = t_{23}^2/\Delta$. We again used $t_{12} = t_{24} = \tau$. The first order corrections in τ/Δ to these basis states read

$$|1\rangle^{(1)} = \frac{1}{2}\frac{\tau}{\Delta}(|S_{11}S_{34}\rangle - |S_{13}S_{44}\rangle) - \frac{t_{23}}{\Delta}|S_{14}S_{33}\rangle, \tag{3.33}$$

$$|0\rangle^{(1)} = -\frac{\sqrt{3}}{2}\frac{\tau}{\Delta}(|S_{11}S_{34}\rangle + |S_{13}S_{44}\rangle), \tag{3.34}$$

$$|T_1\rangle^{(1)} = -\left(\frac{\cos\frac{\theta}{2}}{2\sqrt{3}} + \frac{2\sin\frac{\theta}{2}}{\sqrt{6}}\right)\frac{\tau}{\Delta}(|S_{11}T_{34}^{(0)}\rangle - |T_{13}^{(0)}S_{44}\rangle)$$

$$\qquad - \left(\frac{\cos\frac{\theta}{2}}{\sqrt{3}} - \frac{2\sin\frac{\theta}{2}}{\sqrt{6}}\right)\frac{t_{23}}{\Delta}|T_{14}^{(0)}S_{33}\rangle, \tag{3.35}$$

$$|T_2\rangle^{(1)} = -\frac{1}{2}\frac{\tau}{\Delta}(|S_{11}T_{34}^{(0)}\rangle + |T_{13}^{(0)}S_{44}\rangle), \tag{3.36}$$

$$|T_3\rangle^{(1)} = -\left(\frac{\sin\frac{\theta}{2}}{2\sqrt{3}} - \frac{2\cos\frac{\theta}{2}}{\sqrt{6}}\right)\frac{\tau}{\Delta}\left(|S_{11}T_{34}^{(0)}\rangle - |T_{13}^{(0)}S_{44}\rangle\right)$$

$$-\left(\frac{\sin\frac{\theta}{2}}{\sqrt{3}} + \frac{2\cos\frac{\theta}{2}}{\sqrt{6}}\right)\frac{t_{23}}{\Delta}|T_{14}^{(0)}S_{33}\rangle. \tag{3.37}$$

3.1.2   The singlet-only qubit subspace

We define the qubit Hamiltonian as the singlet-only Hamiltonian in Eq. (3.25) after subtracting a constant energy offset. This results in

$$H_{\mathrm{qb}} = \frac{1}{4}(J_{12} + J_{24} - 2J_{23})\sigma^z + \frac{\sqrt{3}}{4}(J_{12} - J_{24})\sigma^x, \tag{3.38}$$

where σ^z and σ^x denote the Pauli matrices, and the two qubit states, to lowest order in τ/Δ are

$$|1\rangle = |S_{14}S_{23}\rangle + \frac{1}{2}\frac{\tau}{\Delta}\left(|S_{11}S_{34}\rangle - |S_{13}S_{44}\rangle\right) - \frac{t_{23}}{\Delta}|S_{14}S_{33}\rangle \tag{3.39}$$

$$|0\rangle = \frac{1}{\sqrt{3}}\left(|S_{13}S_{24}\rangle + |S_{12}S_{34}\rangle\right) - \frac{\sqrt{3}}{2}\frac{\tau}{\Delta}\left(|S_{11}S_{34}\rangle + |S_{13}S_{44}\rangle\right), \tag{3.40}$$

up to some normalization constant. We observe that: (*i*) All the terms of this qubit Hamiltonian can be controlled by detuning of the (electric only) tuning parameters ϵ_{14}, ϵ_{23} and ϵ_{Λ}. Therefore, the singlet-only spin qubit that we propose here is indeed an XO qubit. (*ii*) The structures of both this Hamiltonian and its eigenstates are fully equivalent to that of the triple-dot XO qubit [cf. Eq. (5) in Ref. [28]. See also Eq. (2.20) and Section 2.2.1]. This qubit can, thus, be operated in the same way as the XO qubit: either by static pulsing [62] or via resonant driving [27]. (*iii*) At the qubit operation point Q, the qubit splitting $\hbar\omega_z = (t_{12}^2 + t_{24}^2 - 2t_{23}^2)/2\Delta$, vanishes if all three tunnel couplings are equal. We therefore choose $t_{12} = t_{24} \neq t_{23}$. We can see this behavior in Fig. 3.4: The qubit state $|0\rangle$ couples the electrons in dots 2 and 3 in a triplet state, but the state $|1\rangle$ couples these electrons in a singlet state. Changing t_{23} thus cannot have any effect on $|0\rangle$, but it must change the energy of the state $|1\rangle$ because of the exchange effects that go as t_{23}^2/Δ. In Fig. 3.4(b) we show that indeed the energy of the state $|1\rangle$ changes as a function of t_{23} and for $t_{23} = \tau$ the qubit subspace becomes degenerate.

Manipulation of the qubit

At the RX regime, close to the nearby charge states, the exchange interaction is significant. This results in two symmetric detuning axis readily
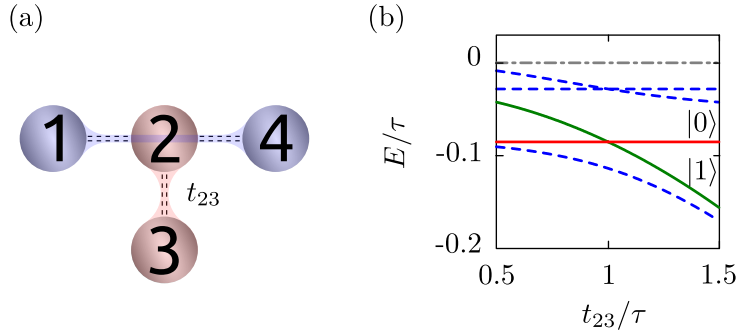
Figure 3.4: (a) We can express the qubit states in terms of couplings between the electrons in dots 1 and 4 and the electrons in dots 2 and 3. (b) Energy spectrum of the six states with $S_z = 0$ at the point Q as a function of t_{23}, with $t_{12} = t_{24} = \tau$.

available by detuning of ϵ_{14}. Proceeding as in Section 2.2.1, for small detuning, $|\epsilon_{14}| \ll \Delta$, we can expand the effective qubit Hamiltonian H_{qb} to linear order in ϵ_{14}, yielding

$$H_{\mathrm{qb}} = \frac{1}{2}\hbar\omega_z\sigma^z - \frac{\sqrt{3}}{2}\frac{\tau^2\epsilon_{14}}{\Delta^2}\sigma^x, \qquad (3.41)$$

A harmonic modulation of the detuning, of the form $\epsilon_{14} = A\cos(\omega\tau)$, will, as we saw in Section 2.2.1, induce Rabi rotations with a period $T_{\mathrm{Rabi}} = 4\pi\hbar\Delta^2/(\sqrt{3}\tau^2 A)$. Using $\Delta = 5\tau$, and a small driving amplitude of $A = 0.15\tau$, this would yield a rotation time $T_{\mathrm{Rabi}} \approx 50$ ns.

Decoherence

We mentioned before that the reason for choosing a singlet-only spin qubit was to avoid relaxation and decoherence produced by gradients (fluctuating or static) of magnetic fields across the quantum dots. An example of these being the gradients of magnetic fields arising from the fluctuating bath of nuclear spins in GaAs nanostructures, which couple to the qubit states through the hyperfine interaction [9, 27, 40].

To analyze the effect of the hyperfine interaction on the XO singlet-only qubit, we use the effective Hamiltonian that we introduced in Section 2.5.1

$$H_{\mathrm{hf}} = \frac{g\mu_{\mathrm{B}}}{2}\sum_{i,\alpha,\beta} c_{i,\alpha}^\dagger \mathbf{K}_i \cdot \boldsymbol{\sigma}_{\alpha\beta} c_{i,\beta}, \qquad (3.42)$$

where $\mathbf{K}_i$ is the local Overhauser field acting on an electron in dot i, and project this Hamiltonian onto the qubit subspace:

$$\langle 1|H_{\mathrm{hf}}|1\rangle = \langle 0|H_{\mathrm{hf}}|0\rangle = \langle 1|H_{\mathrm{hf}}|0\rangle = 0 \qquad (3.43)$$

To leading order, the nuclear fields do not affect the qubit subspace and, therefore, do not cause any decoherence. However, this hyperfine Hamiltonian couple both qubit states to the other four-electron triplet states. Transitions to states with $S_z = \pm 1$ are strongly suppressed by the large Zeeman energy E_{Z}. We thus focus on the coupling to the triplet states with $S_z = 0$, via $K_{z,i}$. This component of the nuclear fields thus couple $|0\rangle$ and $|1\rangle$ to the triplets $|T_1\rangle$, $|T_2\rangle$ and $|T_3\rangle$, and the small energy difference between these states, which is of the order of J, J_{23}, favors a hybridization of the singlets and triplets. We see that by evaluating the Hyperfine Hamiltonian in the basis $\{|1\rangle, |0\rangle, |T_1\rangle, |T_2\rangle, |T_3\rangle\}$:

$$H_{\mathrm{hf}} = \frac{g\mu_{\mathrm{B}}}{9} \begin{pmatrix} 0 & 0 & \mathrm{h.c.} & & \\ 0 & 0 & & & \\ 3\sqrt{3}\kappa_{14}u & \kappa_{23}u - 6\sqrt{2}\kappa_\Lambda v & 0 & 0 & 0 \\ 3\kappa_{23} & 3\sqrt{3}\kappa_{14} & 0 & 0 & 0 \\ 3\sqrt{3}\kappa_{14}v & 6\sqrt{2}\kappa_\Lambda u + \kappa_{23}v & 0 & 0 & 0 \end{pmatrix}, \qquad (3.44)$$

where "h.c." stands for hermitian conjugate. Here we have introduced the field gradients

$$\kappa_{14} = g\mu_{\mathrm{B}} \frac{K_{z,1} - K_{z,4}}{2}, \qquad (3.45)$$

$$\kappa_{23} = g\mu_{\mathrm{B}} \frac{K_{z,2} - K_{z,3}}{2}, \qquad (3.46)$$

$$\kappa_\Lambda = g\mu_{\mathrm{B}} \frac{K_{z,1} - K_{z,2} - K_{z,3} + K_{z,4}}{4}, \qquad (3.47)$$

and we used the notation

$$u = \cos\frac{\theta}{2} - \sqrt{2}\sin\frac{\theta}{2}, \qquad (3.48)$$

$$v = \sqrt{2}\cos\frac{\theta}{2} + \sin\frac{\theta}{2}, \qquad (3.49)$$

with the angle θ as defined above. This coupling can cause leakage out of the qubit subspace, as in the triple-dot XO qubit. On the other hand, it does not affect the qubit splitting to linear order in $\mathbf{K}_i$. However, this coupling can contribute to qubit decoherence by producing a higher-order shift in the qubit splitting.

A second-order perturbation expansion in the nuclear fields yields an energy shift in the qubit splitting $\delta_{\rm hf} = \delta E_1 - \delta E_0$

$$\delta_{\rm hf} = \frac{\Delta}{\tau^2} \left(\frac{89\kappa_{14}^2}{72} - \frac{688\kappa_{23}^2}{2187} - \frac{928\kappa_{23}\kappa_\Lambda}{729} - \frac{112\kappa_\Lambda^2}{243} \right). \tag{3.50}$$

This energy shift, of the order of magnitude $\sim K^2\Delta/\tau^2$, is smaller by a factor $\sim K\Delta/\tau^2$ as compared to the shift induced by the hyperfine coupling in other semiconductor-based spin qubits. We estimate the resulting decoherence time of the qubit to be $T_2^* \sim \hbar J/(g\mu_{\rm B}K)^2$. This is the coherence time that we would expect from a Ramsey experiment. For typical parameters (that is, for $J = 2~\mu$eV and $K = 1$ mT) this amounts to an improvement of two orders of magnitude over other spin qubits in GaAs, where $T_2^* \sim \hbar/(g\mu_{\rm B}K)$.

Let us now analyze the main effect of the higher-order correction to the qubit splitting set by the random nuclear noise. We proceed as in Section 2.2.1 but now with a random shift $\delta_{\rm hf}$ in the qubit splitting, and study the evolution of a qubit state when the system is driven at resonance with an amplitude $\tilde{A} = \sqrt{3}\tau^2 A/(2\Delta^2)$. We thus use the effective Hamiltonian:

$$H_{\rm eff} = \frac{1}{2}(\hbar\omega_z + \delta_{\rm hf})\sigma^z + \tilde{A}\cos(\omega_z t)\sigma^x, \tag{3.51}$$

and using a rotating wave approximation, we write the Hamiltonian in a rotating frame,

$$H_{\rm rf} = \frac{1}{2}\delta_{\rm hf}\sigma^z + \frac{1}{2}\tilde{A}\sigma^x. \tag{3.52}$$

We then prepare the system in the initial state $|0\rangle$ and assume a fixed $\delta_{\rm hf}$. The Schrödinger equation can then be solved analytically, yielding Rabi oscillations on the probability of finding the system in $|1\rangle$ after a time t,

$$P_1(t, \delta_{\rm hf}) = |\langle 1|\psi(t)\rangle|^2 = \frac{1}{2}\frac{\tilde{A}^2}{\tilde{A}^2 + \delta_{\rm hf}^2} \left[1 - \cos\left(\frac{t}{\hbar}\sqrt{\tilde{A}^2 + \delta_{\rm hf}^2} \right) \right]. \tag{3.53}$$

We consider the fluctuations in $K_{z,i}$ to be quasistatic, i.e., constant for each operation cycle, and average over many cycles, with a different configuration of $K_{z,i}$ each time. This leads to a suppression of the Rabi oscillations, described as

$$\langle P_1(t)\rangle = \int \frac{dK_{z,1}dK_{z,2}dK_{z,3}dK_{z,4}}{8\pi^2\sigma_{K_z}^4} \frac{\tilde{A}^2}{\tilde{A}^2 + \delta_{\rm hf}^2} \left[1 - \cos\left(\frac{t}{\hbar}\sqrt{\tilde{A}^2 + \delta_{\rm hf}^2} \right) \right]$$
$$+ \exp\left(-\frac{K_{z,1}^2 + K_{z,2}^2 + K_{z,3}^2 + K_{z,4}^2}{2\sigma_{K_z}^2} \right), \tag{3.54}$$
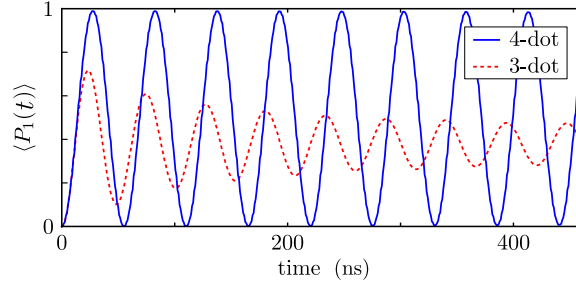
Figure 3.5: This is time-dependent expectation value of the probability $P_1(t)$ (blue curve) after initializing in $|0\rangle$ and driving resonantly with $\epsilon_{14} \propto \cos(\omega_z t)$. We calculated this probability numerically, averaging over 2500 random configurations of the nuclear fields. We also compare the results with an equivalent calculation for a triple-dot XO qubit (red curve), using the same parameters.

where all the nuclear fields $K_{z,i}$ are assumed to be Gaussian-distributed with zero mean and a standard deviation σ_{K_z} [32]. At large times $t \gg \hbar\tilde{A}/\delta_{\mathrm{hf}}^2$, this integral suggests that the hyperfine coupling in the XO singlet-only spin qubit leads to a power-law decay in the Rabi oscillations, $\langle P_1(t)\rangle \propto t^{-\alpha}$ with $\alpha \approx 1$.

We also complement the analytical calculations by performing numerical simulations of resonant driving of the qubit. We project the Hamiltonian in Eq. (3.20) to the $S_z = 0$ subspace of all relevant charge states and diagonalize the resulting Hamiltonian at the point Q (see Fig. 3.2). This yields the eigenstates at $\epsilon_{14} = 0$ as well as the qubit splitting $\hbar\omega_z$. Then we initialize the system into the singlet state $|0\rangle$ and let it evolve under the Hamiltonian $H_{\mathrm{Hubb}} + H_{\mathrm{hf}}$, with $\epsilon_{14} = A \cos(\omega_z t)$ and four random nuclear fields $\mathbf{K}_i$. We repeat these steps many times, with a different set of $\mathbf{K}_i$ each time, and calculate the average time-dependent probability $\langle P_1(t)\rangle$. In Fig. 3.5 we show the probability $\langle P_1(t)\rangle$ (blue curve), evaluated with $A = 2.5\ \mu\mathrm{eV}$ and averaged over 2500 random nuclear field configurations. We considered $\mathbf{K}_i$ as Gaussian-distributed noise with $\sigma_{K_z} = 0.07\ \mu\mathrm{eV}$. In the figure we observe several Rabi oscillations in ~ 500 ns without any significant decay. At much longer times, nevertheless, we expect to see a suppression in the oscillations.

As a comparison, we also show equivalent simulations of a resonant driving of the triple-dot XO qubit, using the same parameters. The result is plotted with a red curve in Fig. 3.5, together with the Rabi oscillations
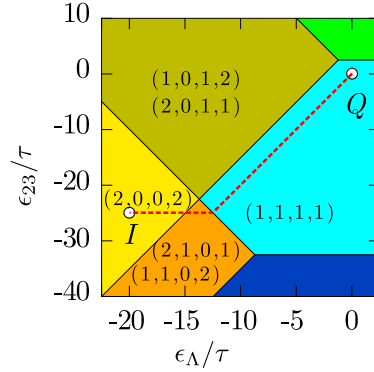
Figure 3.6: This is the initialization scheme that we propose. The qubit is prepared in the only singlet state available in (2,0,0,2) and pulsed adiabatically from the point I to the qubit operation point Q, without entering in the charge regions (1,0,1,2) and (2,0,1,1) to avoid possible level crossings.

in the XO singlet-only qubit. In this case the probability $\langle P_1(t) \rangle$ decays significantly in the first few Rabi periods. The clear contrast between the two curves shows the improvement, regarding the coherence of the qubit, that offers the XO singlet-only spin qubit that we propose in this chapter.

3.1.3   Initialization and readout of the qubit states

One important ingredient of every quantum computation protocol is the ability to reliably initialize a qubit in one of its basis states and read out the output quantum state after running an algorithm.

Readout of the qubit can be performed by spin-to-charge conversion, in a similar way as in the *S-T* [21] and triple-dot XO [27, 62] qubits. In our setup this can be done by pulsing into the point R in Fig. 3.2 via detuning of ϵ_{14}. Only the singlet state $|0\rangle$, couples adiabatically to the singlet state in this charge region. A protective measurement of the qubit state can be achieved by simply measuring the charge configuration of the system at this point.

Initialization can be carried in a similar way. We prepare the system in a ground state that couples adiabatically to only one of the qubit states. For that we choose the charge state (2,0,0,2), which has a singlet structure because of Pauli's spin blockade. This state couples adiabatically to the
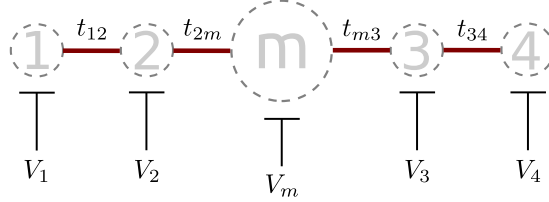
Figure 3.7: This XO singlet-only spin qubit is composed of five quantum dots in a linear array. The dots are tunnel coupled to their nearest neighbor only, indicated by red lines and the tunnel coupling energies t_{ij}. Gate electrodes control the potentials V_i in the dots.

state $|0\rangle$ when the system is pulsed back to Q along the red dashed line in Fig. 3.6.

One requirement for successful initialization and readout of the qubit is that all possible level crossings during the initialization and readout paths are swept through fast enough so that the chance for spin-flip transition to a different spin state is strongly suppressed. This exact same condition holds for the triple-dot XO qubit, where the qubit state $|0\rangle$ crosses a spin-$\frac{3}{2}$ state during readout [27].

3.2 A straightforward implementation

We now want to study the possibility of implementing this qubit into an existing device. We believe that the qubit can be straightforwardly implemented in the device in Ref. [48]. This device consists of five tunnel coupled quantum dots in a linear arrangement, as we show in Fig. 3.7, with the central dot being substantially larger than the other four dots and hosting a large (between 50 and 100) even number of electrons. The system can be tuned into a configuration where the two lowest energy states in the central dot are a singlet and a triplet multi-electron spin states. We further assume that the energy separation between them is small enough so that a transition from a singlet to a triplet ground state [2] is possible via electric or magnetic tuning with reasonable electric and magnetic fields [48, 63].

---

[2]This is similar to what we showed in Fig. 3.4, where via a modulation of t_{23} the ground state of the system changes from the qubit state $|0\rangle$ to $|1\rangle$.

The system is prepared in a state $(1, 1, m, 1, 1)$ with m such that the ground state of the multielectron dot is a singlet state but the ground state for $m + 2$ is a triplet state [48]. An orbital excitation within the quantum dot m is, in this system, possible when it contains $m + 2$ electrons with a small cost in energy. With $m + 2$ electrons the first excited state will then be a singlet state [48]. Within the charge state (1,1,m,1,1), and taking the middle dot to be always in a singlet state, there are up to 16 different spin configurations, two of which are singlet states (see Section 3.1). We call the lowest energy singlet state $|0\rangle$ and the higher energy singlet state $|1\rangle$, defined as:

$$
\begin{aligned}
|0\rangle &= |S_{14} S_m S_{23}\rangle \\
&= \frac{1}{2} \left(|\uparrow\uparrow\, S_m\, \downarrow\downarrow\rangle - |\uparrow\downarrow\, S_m\, \uparrow\downarrow\rangle - |\downarrow\uparrow\, S_m\, \downarrow\uparrow\rangle + |\downarrow\downarrow\, S_m\, \uparrow\uparrow\rangle \right),
\end{aligned} \tag{3.55}
$$

$$
\begin{aligned}
|1\rangle &= \frac{1}{\sqrt{3}} \left(-|T_{14}^+ S_m T_{23}^-\rangle - |T_{14}^- S_m T_{23}^+\rangle + |T_{14}^0 S_m T_{23}^0\rangle \right) \\
&= \frac{1}{2\sqrt{3}} \left(|\uparrow\uparrow\, S_m\, \downarrow\downarrow\rangle + |\downarrow\downarrow\, S_m\, \uparrow\uparrow\rangle + |\uparrow\downarrow\, S_m\, \uparrow\downarrow\rangle \right. \\
&\qquad\qquad \left. + |\downarrow\uparrow\, S_m\, \downarrow\uparrow\rangle - 2\, |\uparrow\downarrow\, S_m\, \downarrow\uparrow\rangle - 2\, |\downarrow\uparrow\, S_m\, \uparrow\downarrow\rangle \right).
\end{aligned} \tag{3.56}
$$

With this notation, S_m denotes a singlet configuration in the central dot. We use the state $|0\rangle$ as the north pole of the Bloch sphere and its orthogonal singlet state $|1\rangle$ as the south pole. See Fig. 3.8(a). The system can be unambiguously initialized in a state $|i\rangle = |S_{12} S_m S_{34}\rangle$, more conveniently expressed as:

$$
|i\rangle = -\frac{1}{2}|0\rangle + \frac{\sqrt{3}}{2}|1\rangle. \tag{3.57}
$$

This is achieved by preparing the system into the initialization charge state $(2, 0, m, 0, 2)$, where due to a large orbital energy splitting in the lateral dots the electrons in the two external quantum dots can only be in a singlet state, and then pulsing into $(1, 1, m, 1, 1)$, the region I in Ref. [48] (see also Fig. 3.10 below). The state $|i\rangle$ has an angle of 120 degrees with respect to $|0\rangle$. Qubit manipulation is achieved by electrostatic tuning of the gate voltages V_i. Either via the external quantum dot potentials V_1 and V_4 or the central dot potential V_m. Close to the charge state $(2, 0, m, 0, 2)$, but still in region I, the external quantum dots are strongly coupled, while the exchange interaction between them and the central dot is smaller [see Fig. 3.8(b)] this results in an axis at 120 degrees in the Bloch sphere, parallel to $|i\rangle$. In region I, increasing V_m towards regions II$_a$/II$_b$
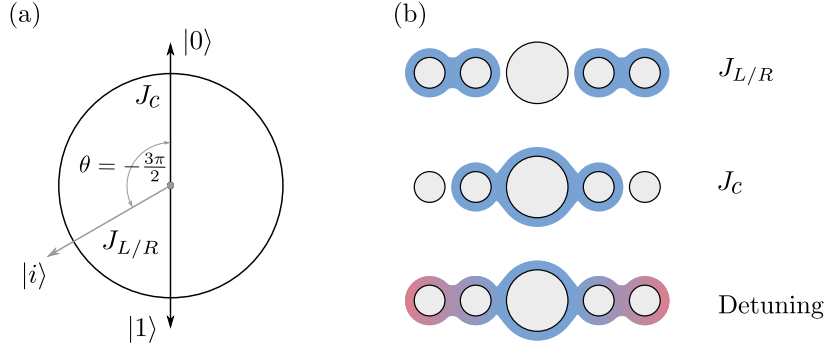
Figure 3.8: (a) Vertical cut of the Bloch sphere showing the initialization state $|i\rangle$ in the basis $\{|0\rangle, |1\rangle\}$ and (b) quantum dot couplings and detuning.

(Fig. 3.10), effectively couples the dots 2 and 3 to the central dot m and results in an exchange energy J_c. This is represented in the Bloch sphere by an axis pointing towards the north pole (see also Fig. 3.9). Increasing V_m further, into the region III, brings the system into the charge state $(1, 0, m+2, 0, 1)$, where the sign of J_c is reversed, i.e., the field now points towards $|1\rangle$, at 180 degrees.

Since the Bloch angle θ in Fig. 3.9 is rather step-like and angles beyond 180 are not accessible (as opposed to what we saw in Section 2.2, where any rotation in the Bloch sphere is possible), full rotations between the states $|0\rangle$ and $|1\rangle$ are challenging: in this figure we can only reach precisely the angles 0, 120 and 180 degrees, as reported in Ref. [48]. An angle $\theta = 90^o$ lays in the sharp, step-like, transition and is therefore experimentally difficult to achieve. Manipulating the qubit at close proximity to other charge states can, on the other hand, produce a "richer" set of detuning tools. To study the effects of the charge states $(2, 0, m, 1, 1)$, $(1, 1, m, 0, 2)$, $(2, 0, m+1, 0, 1)$ and $(1, 0, m+1, 0, 2)$ we use the Hamiltonian [48, 63]

$$
H = -\sum_i V_i n_i + \frac{U_i}{2} n_i(n_i - 1) + \sum_{i \neq j} \frac{K_{i,j}}{2} n_i n_j
$$
$$
+ \sum_{\langle i,j \rangle, \sigma} \frac{t_{ij}}{\sqrt{2}} c^\dagger_{i,\sigma} c_{j,\sigma} - \frac{\xi}{2} \mathbf{S}^2 + \frac{1}{2} g \mu_B B_{\parallel} (n_\uparrow - n_\downarrow), \quad (3.58)
$$

with U_i the on-site Coulomb interaction in dot i and $K_{i,j}$ the cross-capacitance between neighboring dots. The Coulomb interaction between
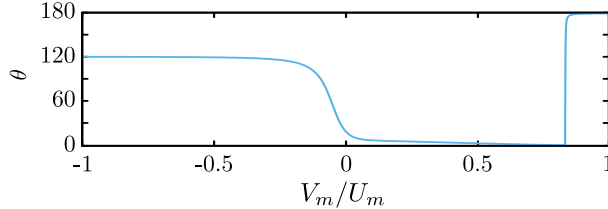
Figure 3.9:   Bloch angle θ as a function of the gate potential V_m for $V_1 = V_2 = V_4 = 0$ and $V_3 = 2\,\mu\text{eV}$. Other parameters as in Ref. [48]

two electrons in different orbitals in the middle dot is also accounted for via $K_{i,j}$. We study the magnitude of the exchange field and the Bloch angle as a function of V_m and V_1, while keeping $V_4 = V_1$ and fixing V_2 and $V_3 > V_3$ close to zero, as in the model used in Ref. [48]. This is shown in Fig. 3.10, where we used the same parameters as in their text. In this Hamiltonian, the spin operator $\mathbf{S}^2$ acts only on the two higher-orbital electrons in the central quantum dot when it is occupied by $m+2$ electrons. This term enforces a triplet ground state in the region III, where the charge state is $(1, 0, m+2, 0, 1)$. The last term describes the Zeeman splitting between states with different spin projection.

We study in more detail two special cases, both very close to the charge states $(2, 0, m+1, 0, 1)$ and $(1, 0, m+1, 0, 2)$: (i) the vertical dashed line in Fig. 3.10, at $V_1 = V_4 = 4.6U_m$, and (ii) the tilted dotted line $V_m = 10U_m - 2V_1$, also with $V_1 = V_4$. In both cases initialization and readout is performed at the i/r point (white star), where the ground state couples adiabatically to $|i\rangle$.

Fig. 3.11(a) shows the lowest part of the spectrum along the line (i), centered at the charge region $(1, 0, m+1, 1, 1)/(1, 0, m+1, 1, 1)$. The two lowest singlet states are shown in blue and green. At the center of the spectrum, the lowest state points towards $|0\rangle$ in the Bloch sphere and the excited state to $|1\rangle$. Other singlet states are shown in gray. Fig. 3.11(b) shows the strength of the exchange field (relative to its maximum in the domain) and the angle in the Bloch sphere along the same line. Close to $V_m = U_m$, where the system goes from the charge states $(1, 0, m+1, 1, 1)/(1, 0, m+1, 1, 1)$ to $(1, 0, m+2, , 1)$, the exchange energy changes sign. This is indicated by the abrupt change in the angle θ that goes from nearly 0 to 180. Moving towards the opposite direction produces a smoother change of θ (and also a smooth variation of $|J|$) from 0 to 120 degrees. This enables a precise control of the angle in the Bloch sphere
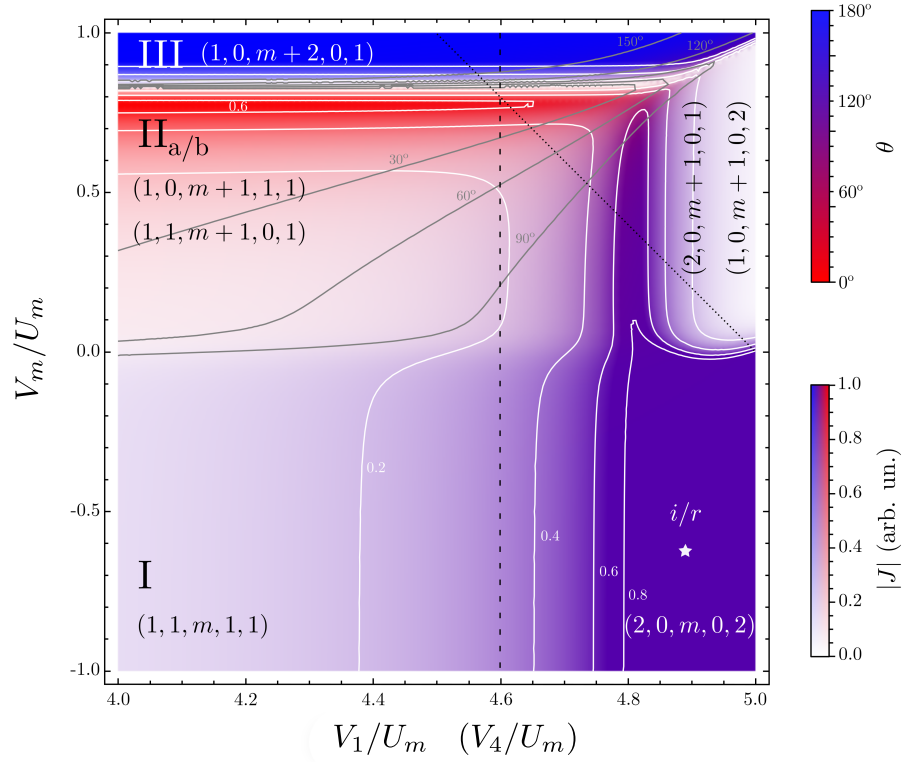
Figure 3.10: Bloch angle θ and exchange magnitude $|J|$ as a function of V_m and V_1 (keeping $V_4 = V_1$) with $V_2 = 0$ and $V_3 = 2\,\mu$eV. Different charge regions are indicated. We also show curves along which the exchange field magnitude is constant (white curves) and curves along which the Bloch angle is constant (gray curves). The color gradient indicates the angle θ and the transparency shows the strength of the exchange field $|J|$. Two lines (dashed and dotted) indicate two possible paths for manipulation of the qubit. The white star marks a region where initialization and readout would be most successful.
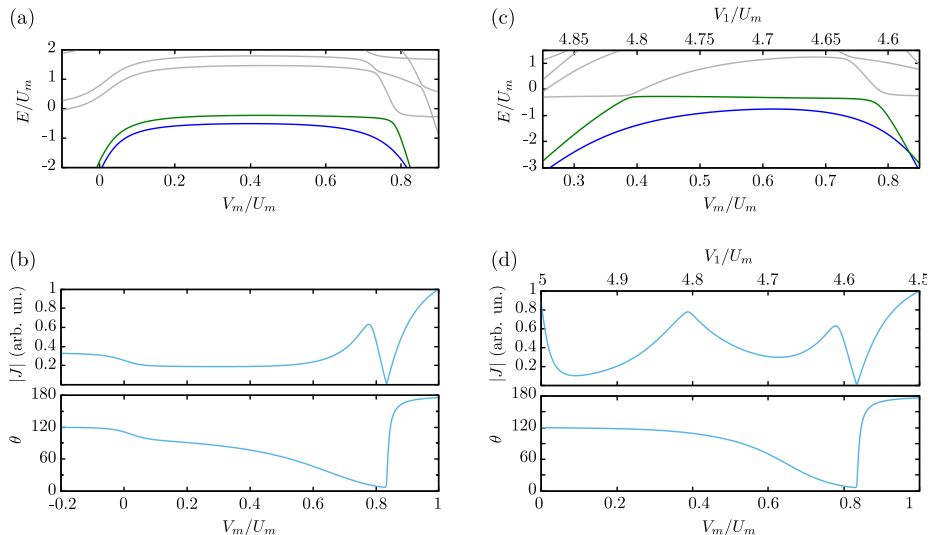
Figure 3.11: Singlet states spectrum along (a) the dashed line in Fig. 3.10 and (c) the tilted dotted line. The two lowest singlet states, which we use as qubit states, are colored. (b,d) Magnitude of the strength of the exchange field $|J|$ and Bloch angle θ along the same lines, respectively. The exchange field $|J|$ is given in arbitrary units, with $|J| = 1$ being the maximum value of $|J|$ within the domain we consider in each panel.

and makes possible full rotations by electrostatic pulsing of the gates.

Similar features are observed if the detuning is along the tilted line (*ii*), with a similar spectrum [Fig. 3.11(c)] but with more and larger peaks in $|J|$ [Fig. 3.11(d)]. Note, however, that initializing in the charge states $(2, 0, m+1, 0, 1)$ and $(1, 0, m+1, 0, 2)$ does not necessarily result in a singlet state (see Fig. 3.10 as well), and readout may result inefficient if there are spin mixing mechanisms that couple singlet and triplet states, since not all quantum dots are doubly occupied.

3.2.1   Qubit manipulation

Let us, for simplicity, introduce an effective two-level Hamiltonian to investigate possible mechanisms to manipulate the qubit. This effective Hamiltonian results from the projection of the Hamiltonian in Eq. (3.58)

into the two-level qubit subspace:

$$H_{\mathrm{qb}} = \frac{1}{2}|J(V_i)| \cos\left[\frac{\theta(V_i)}{2}\right] \sigma^z + |J(V_i)| \sin\left[\frac{\theta(V_i)}{2}\right] \sigma^x. \qquad (3.59)$$

If the exchange field $|J|$ close to $\theta = 0$ is large enough, a small modulation of the field along V_m can induce Rabi rotations with a period h/A, where $A = \delta V_m \left|\frac{d}{dV_m}(|J|\sin\frac{\theta}{2})\right|$. δV_m is the amplitude of the oscillations in the potential and $|J|$ and θ the magnitude of the exchange field and the angle in the Bloch sphere.

Detuning of the qubit via pulsing is also possible: The smoothnes of the curve $\theta(V_m)$ allow us to precisely select any rotation angle in one side of the Bloch sphere [see Figs.3.11(b,d)]. Nevertheless, since we do not have control over the full Bloch sphere, the qubit rotations will be challenging.

<div style="text-align: right; font-size: 3em; color: #cccccc; font-weight: bold;">4</div>

Higher tunability

We propose a novel implementation of an XO singlet-only qubit in GaAs that can be straightforwardly implemented in existing triple-dot devices and with a qubit splitting that can be tuned over several tens of μeV. The contents of this chapter are included in Paper III.

In the XO singlet-only spin qubit proposed in Chapter 3, the coherence time of the qubit is substantially extended by eliminating the leading effects of magnetic noise. However, the long coherence time of the qubit comes at the cost of a relatively small qubit splitting. This is a common problem with XO qubits [50, 64–66]. To overcome this problem, we propose a new GaAs-based singlet-only spin qubit that can be implemented in triple-dot devices. This qubit will have a simpler design and a substantially larger (and tunable) qubit splitting. Fig. 4.1 shows the device that we propose. It consists of three quantum dots with a middle dot that can allocate several electrons.

We tune the triple quantum dot to a (1,4,1) charge configuration and apply an out-of-plane magnetic field. On the central dot, the interplay between the magnetic field and the Coulomb interaction between the electrons results in a rich energy spectrum with many crossings between levels with different total spin and orbital angular momentum. As we will see below, when the central dot is occupied by four electrons, the ground state
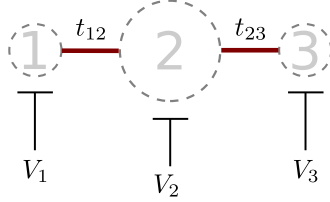
Figure 4.1: The system is composed of three quantum dots, with a central dot that can allocate several electrons and two outer dots in the spin blockade regime. The dots are tunnel coupled to their nearest neighbors and the electrochemical potential in each dot can be controlled by the gate-induced offsets V_1, V_2 and V_3.

changes from a triplet to a singlet character, typically at a moderate field of ~ 100 mT [67], in a similar way as we saw in the last chapter. We prepare the system close to this singlet-triplet crossing, and couple the central dot to two singly-occupied outer dots via a tunneling interaction. This yields an XO singlet-only qubit where the singlet-triplet splitting on the central dot, and thus the qubit splitting, can be tuned over a large range of energies by adjusting the external magnetic field. The qubit is equivalent to the XO singlet-only qubit presented in Chapter 3, but now the singlet/triplet nature of the electrons in the dots 2 and 3 in Fig. 3.4(a) is replaced by singlet/triplet couplings of two electrons in the middle dot in Fig. 4.1. This yields a GaAs-based XO singlet-only qubit that is not more complicated to create or operate than existing triple-dot devices. Moreover, this has a qubit splitting that can be straightforwardly tunable through a wide range of energies, from zero to several μeV. Conceptually similar qubits have been proposed in Refs. [66] and [68]. Probably the most promising one is a proposal for a singlet-only qubit in Si, taking advantage of valley states [66]. Our proposal differs from this in that our qubit is more tunable[1], is easy to manipulate and can be implemented both in GaAs but also in Si quantum dots.

─────────────────────

[1]In Si-based quantum dots the magnitude of the valley splitting, as well as the phase differences between valley couplings on different dots, are hard to control or predict in practice [10], severely affecting the qubit operation and its coherence time [69].

4.1 A singlet-only spin qubit in three dots

The only substantial difference between this qubit and the XO qubits that we talked about in Chapters 2 and 3 is the multi-electron central quantum dot. Until now we have considered small quantum dots in the spin blockade regime, but for this proposal we have to consider a slightly larger dot that can accommodate more electrons and produce an electron orbital spectrum with seizable energies. The physics of multi-electron quantum dots has been studied before, but we will now do it in more detail and derive some expressions that we will need later to construct an effective Hamiltonian that governs the dynamics of the qubit. For this we will mostly follow the method used in Ref. [67].

4.1.1 Multi-electron quantum dots

The physics of a multi-electron quantum dot is qualitatively different from that of the quantum dots in the spin blockade regime that we have seen previously. Here we have to account for other orbital states, as well as for the Coulomb interaction between the many electrons that occupy the dot. Moreover, in this system we also include a magnetic field perpendicular to the plane of the quantum dots that squeezes the wave function of the electrons. Let us consider each of these new ingredients, one at a time.

A perpendicular magnetic field

Consider a quantum dot defined by a circularly symmetric parabolic potential in the x-y plane (the plane of the 2DEG) and a very strong confinement along the z direction. Consider also an out-of-plane magnetic field. We saw in Chapter 2 that the Hamiltonian of a single electron in such a potential is given by

$$H_0^{(i)} = \frac{1}{2m^*}[\mathbf{p}_i + e\mathbf{A}(\mathbf{r}_i)]^2 + \frac{1}{2}m^*\omega_0^2\mathbf{r}_i^2 + \frac{1}{2}g\mu_{\mathrm{B}}B\sigma_i^z, \qquad (4.1)$$

where ω_0 defines the strength of the in-plane confinement of the electrons and thus define the quantum dot. The effective radius of the dots in the absence of a magnetic field is given by $\sigma_0 = \sqrt{\hbar/(m^*\omega_0)}$. The vector potential $\mathbf{A}(\mathbf{r}) = \frac{1}{2}B(x\hat{y} - y\hat{x})$ describes the magnetic field along the z (out of plane) direction, and last term couples the magnetic field to the spin of the electrons.

The eigenstates of this Hamiltonian are the Fock-Darwin states [24],

$$\psi_{n,l,\eta}(\mathbf{r}_i) = \sqrt{\frac{n!}{\pi\sigma^2(n+|l|)!}}\,\rho_i^{|l|}e^{-\rho_i^2/2}L_n^{|l|}\left(\rho_i^2\right)e^{-il\theta_i}, \qquad (4.2)$$

where we used the polar coordinates $\rho_i = r_i/\sigma$ and θ_i. Here, $\sigma = \sqrt{\hbar/m^*\Omega}$ is the effective, magnetic field-dependent dot radius, with a magnetic-field-dependent oscillator frequency $\Omega = \sqrt{\omega_0^2 + \omega_c^2/4}$, and $\omega_c = eB/m^*$ the cyclotron frequency. $L_a^b(x)$ is the associated Laguerre polynomial. The quantum number $n = 0, 1, 2, \ldots$ in the expression above labels the radial orbital degree of freedom of the electron, and the quantum number $l \in \mathbb{Z}$ labels the orbital angular momentum. We use $\eta = \pm 1$ for the spin of the electron. The corresponding eigenenergies are

$$E_{n,l,\eta}^{(i)} = \hbar\Omega(2n + |l| + 1) - \frac{1}{2}\hbar\omega_c l + \frac{1}{4}g\frac{m^*}{m_e}\hbar\omega_c\eta, \qquad (4.3)$$

where m_e is the mass of the electron at rest. The first term describes the two-dimensional harmonic-oscillator energies, now with a magnetic-field-dependent frequency Ω. The second term comes from the direct coupling of the angular momentum l to the out-of-plane magnetic field. Finally, the last term accounts for the Zeeman effect.

This produces the text-book Fock-Darwin spectrum of Fig. 4.2. In this figure we show the single-particle energies as a function of the ω_c for different quantum numbers n and l. The levels plotted in red are the ones we used in our analytic and numerical calculations.

Many-particle interactions

Next we want to find the expressions for the eigenenergies of the multi-electron states and their spin structure, in the presence of electron-electron interactions. For this we follow the method used in [67, 70]. We describe the electron-electron interaction with the Hamiltonian

$$V = \sum_{i<j}\frac{e^2}{4\pi\varepsilon|\mathbf{r}_i - \mathbf{r}_j|}, \qquad (4.4)$$

where ε is the effective dielectric constant of the surroundings of the quantum dot. For a system with two electrons analytical diagonalization of the Hamiltonian $H_1 = \sum_i H_0^{(i)} + V$ is possible [43], but for more than two electrons there is no obvious solution. We thus treat this many-body problem
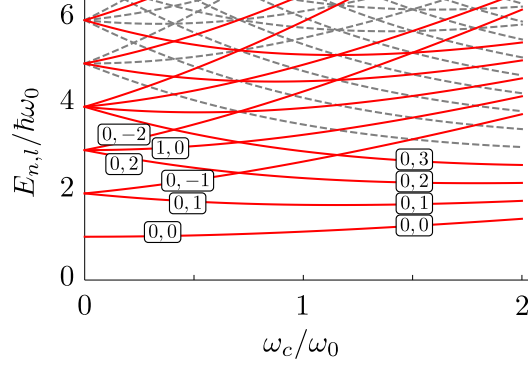
Figure 4.2: Fock-Darwin spectrum as a function of ω_c, where the boxed labels indicate the orbital and angular momentum quantum numbers (n, l). For simplicity we have omitted the Zeeman effect and all the lines are thus two-fold degenerate. In red we plotted the levels that we include in our calculations.

perturbatively and work in a restricted configuration space. We construct a basis of many-particle states from products of single-particle states and impose a cutoff on the quantum numbers n and l as was done in Ref. [67]. Working in this basis allow us to find explicit expressions for the matrix elements of the Hamiltonian in Eq. (4.4)

Let us start by constructing a basis from antisymmetrized products of Fock-Darwin states. We denote these states $|s\rangle$. For a system of M electrons, the states $|s\rangle$ are characterized by a set of quantum numbers $s = \{n_{s_1}, l_{s_1}, \eta_{s_1}; \ldots; n_{s_M}, l_{s_M}, \eta_{s_M}\}$. We then write the antisymmetrized wave function in position space $\langle \mathbf{r}_1, \ldots \mathbf{r}_M | s \rangle = \phi_s(\mathbf{r}_1, \ldots \mathbf{r}_M)$ as

$$\phi_s(\mathbf{r}_1, \ldots \mathbf{r}_M) = \mathcal{A}[\psi_{n_{s_1}, l_{s_1}, \eta_{s_1}}(\mathbf{r}_1) \ldots \psi_{n_{s_M}, l_{s_M}, \eta_{s_M}}(\mathbf{r}_M)], \quad (4.5)$$

where $\mathcal{A}$ is the antisymmetrization operator. Since $\sum_i H_0^{(i)}$ is diagonal in the basis of these product states, we can write the full Hamiltonian as

$$H_1 = \sum_s \left[\hbar\Omega(2N_s + K_s + M) - \frac{1}{2}\hbar\omega_c L_s + \frac{1}{2}g\frac{m^*}{m_e}\hbar\omega_c S_s + V_{ss} \right] |s\rangle \langle s|$$
$$+ \sum_{s \neq r} V_{sr}|s\rangle \langle r|, \quad (4.6)$$

where $N_s = \sum_i n_{s_i}$, $K_s = \sum_i |l_{s_i}|$, $L_s = \sum_i l_{s_i}$, $S_s = \frac{1}{2}\sum_i \eta_{s_i}$, and $V_{sr} = \langle s|V|r\rangle$. To write an explicit matrix form of this Hamiltonian we therefore

need to evaluate the integrals

$$V_{sr} = \sum_{i<j}^{M} \int d\mathbf{r}_1 \cdots d\mathbf{r}_M \, \phi_s^*(\mathbf{r}_1, \ldots \mathbf{r}_M) \frac{e^2}{4\pi\varepsilon|\mathbf{r}_i - \mathbf{r}_j|} \phi_r(\mathbf{r}_1, \ldots \mathbf{r}_M) \quad (4.7)$$

for all sets of quantum numbers s and r. However, since the Coulomb potential couples electrons pairwise, we only need to evaluate integrals of the form

$$\int d\mathbf{r}_1 d\mathbf{r}_2 \, \psi_{n_1,l_1,\eta}^*(\mathbf{r}_1) \psi_{n_2,l_2,\eta'}^*(\mathbf{r}_2) \psi_{n_3,l_3,\eta'}(\mathbf{r}_2) \psi_{n_4,l_4,\eta}(\mathbf{r}_1) \frac{e^2}{4\pi\varepsilon|\mathbf{r}_1 - \mathbf{r}_2|}. \tag{4.8}$$

Using the Fock-Darwin states from Eq. (4.2) and the results from Ref. [71] we can evaluate the integral analytically and find a closed form expression for all V_{sr} in Eq. (4.8) and thus H_1, from Eq. (4.6).

Multi-electron spectra

With these ingredients the eigenstates and eigenenergies of the full many-particle Hamiltonian $H_1 = \sum_i H_0^{(i)} + V$ can then be found from numerical diagonalization or, in the weak-interaction limit characterized by $\kappa \equiv e^2/(4\pi\hbar\varepsilon\sigma_0\omega_0) \ll 1$, from a perturbation expansion in κ.

We will use a charge configuration (1,4,1), which means that we will have four electrons in the middle quantum dot. Nevertheless, since we introduced as well a finite tunneling interaction that gives rise to exchange effects, we must also consider other charge states. For simplicity, in the following analytical calculations we will restrict ourselves to charge states that are only one tunneling event away from (1,4,1). This means that we need to consider the states (1,5,0), (0,5,1), (2,3,1), (1,3,2). We therefore need to study the spectra of quantum dots with *three*, *four* and *five* electrons. For the numeric evaluations we consider also other charge states that are close to the (1,4,1) region although not coupling to it directly by one single tunneling transition, such as the states (2,2,2) and (0,6,0).

We carry the analysis assuming a relatively small magnetic field, with $\omega_c/\omega_0 \leq 0.3$, and a not too strong electron-electron interaction $\kappa < 1$. Moreover, for the multi-electron dot, we use the 28 single-particle states with $n \in \{0,1\}$, $l \in \{0,\pm 1, \pm 2, \pm 3\}$ and $\eta = \pm 1$ from Fig. 4.2 to construct our basis of many-particle states.

The numerical analysis shows that, for up to five electrons and small $\kappa = 0.5$, the low-energy part of the spectrum of H_1 of the middle dot resembles the exact many-particle spectrum reported in Refs. [67, 72] with quite
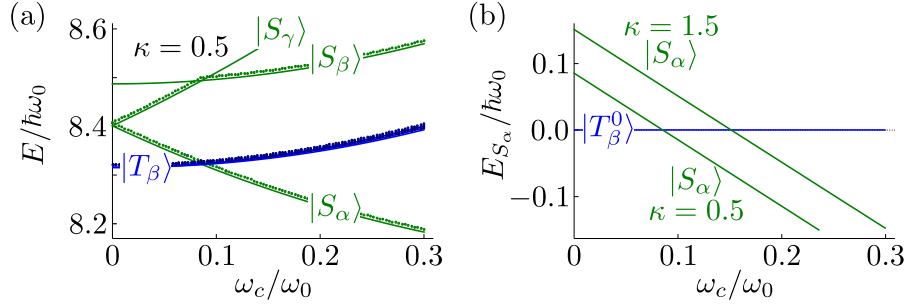
Figure 4.3: (a) Energy spectrum of a quantum dot with four electrons in a perpendicular magnetic field as a function of ω_c, with $\kappa = 0.5$ and $g = -0.4$. The dots show the results from a numerical diagonalization of the Hamiltonian. Solid lines show the analytic expressions for the magnetic field-dependent energies. Singlet states are plotted in green and triplet states in blue. (b) Numerically evaluated energy of the state $|S_\alpha\rangle$ relative to $|T_\beta^0\rangle$ for two values of κ.

high accuracy. In Fig. 4.3(a) we show the lowest part of the energy spectrum of a quantum dot with four electrons, where we used $g = -0.4$. The numerical results are shown by blue (states with a triplet character) and green (states with a singlet character) dots. In this plot we show only the six states with lowest energy. The three triplet states are labeled $|T_\beta\rangle$ and have the largest weight in the orbital configuration $(0,0)^2(0,1)^1(0,-1)^1$, where $(n,l)^m$ means m electrons in the orbital state (n,l) [67]. The three lowest singlet states are labeled $|S_{\alpha,\beta,\gamma}\rangle$, and their largest weights are in the orbital configurations $(0,0)^2(0,1)^2$, $(0,0)^2(0,1)^1(0,-1)^1$, and $(0,0)^2(0,-1)^2$, respectively. The magnitude of the Zeeman splitting is so small compared to the orbital energies that it is not possible to distinguish, visually, the three triplet states.

At zero magnetic field, exchange effects arising from the electron-electron Coulomb interaction favor a spin triplet ground state. When the field is increased, we observe that: (i) all orbital energies increase due to the magnetic compression of the wave functions, through an increase in $\Omega(\omega_c)$, (ii) the singlet states $|S_\alpha\rangle$ and $|S_\gamma\rangle$ split out due to the coupling of the magnetic field to their total projected orbital angular momentum $L_z = \pm 2\hbar$, and (iii) the Zeeman effect splits out the three triplet states as well.

This leads to a singlet-triplet crossing at $\omega_c/\omega_0 \sim 0.1$. At around this

point the four-particle ground state changes from a singlet to a triplet character in the same way as the quadruple dot XO qubit from Chapter 3, (cf. to Fig. 3.4). Close to this degeneracy the next excited state—one of the other two singlet states—is typically $\sim 0.2\,\hbar\omega_0$ higher in energy. This large energy difference allows us to disregard these excited states. Note also that the magnitude of the magnetic field, through ω_c, that forces a singlet-triplet crossing also depends on κ. Therefore, for larger quantum dots, with a smaller $E_{\mathrm{orb}} = \hbar\omega_0$, a smaller ω_c will be required.

Next we proceed to carry our analytical analysis. For a quantum dot with four electrons, and up to second order in κ, we find the energies for the three lowest triplet levels:

$$E_{T_\beta^{(S)}} = 6\hbar\Omega + \frac{S}{2}g\frac{m^*}{m_e}\hbar\omega_c + \gamma_T^{(1)}\kappa\hbar\sqrt{\Omega\omega_0} + \gamma_T^{(2)}\kappa^2\hbar\omega_0, \qquad (4.9)$$

where $S \in \{-1, 0, 1\}$ labels the total spin projection of the triplet states. The coefficients $\gamma_T^{(1)}$ and $\gamma_T^{(2)}$, given by

$$\gamma_T^{(1)} = 2\sqrt{2\pi}, \qquad \gamma_T^{(2)} = -\frac{195893509\pi}{805306368} \approx -0.764, \qquad (4.10)$$

determine the prefactor of the first- and second-order correction, respectively. The energy of the two lowest singlet levels is

$$E_{S_{\alpha,\gamma}} = 6\hbar\Omega - \frac{L}{2}\hbar\omega_c + \gamma_{S1}^{(1)}\kappa\hbar\sqrt{\Omega\omega_0} + \gamma_{S1}^{(2)}\kappa^2\hbar\omega_0, \qquad (4.11)$$

where L is the total orbital angular momentum projection of the state. That is, $L = 2$ for the lowest singlet $|S_\alpha\rangle$ and $L = -2$ for the first excited singlet $|S_\gamma\rangle$. Here we have also introduced the two coefficients

$$\gamma_{S1}^{(1)} = \frac{67}{16}\sqrt{\frac{\pi}{2}}, \qquad \gamma_{S1}^{(2)} = -\frac{38109479\pi}{134217728} \approx -0.892. \qquad (4.12)$$

Finally, for the singlet $|S_\beta\rangle$ we find

$$E_{S_\beta} = 6\hbar\Omega + \gamma_{S2}^{(1)}\kappa\hbar\sqrt{\Omega\omega_0} + \gamma_{S2}^{(2)}\kappa^2\hbar\omega_0, \qquad (4.13)$$

with the coefficients

$$\gamma_{S2}^{(1)} = \frac{35}{8}\sqrt{\frac{\pi}{2}}, \qquad \gamma_{S2}^{(2)} = -\frac{1391260025\pi}{4294967296} \approx -1.02. \qquad (4.14)$$

With these results we can write an expression for the singlet-triplet splitting $E_{ST} = E_{T_\beta^0} - E_{S_\alpha}$,

$$E_{ST} = \hbar\omega_c - \frac{3}{16}\sqrt{\frac{\pi}{2}}\kappa\hbar\sqrt{\Omega\omega_0} + \frac{32763365\pi}{805306368}\kappa^2\hbar\omega_0, \qquad (4.15)$$

which for small ω_c/ω_0 can be very well approximated by

$$E_{ST} \approx \hbar\omega_c + \left(-\frac{3}{16}\sqrt{\frac{\pi}{2}}\kappa + \frac{32763365\pi}{805306368}\kappa^2\right)\hbar\omega_0$$

$$\approx \hbar\omega_c + \left(-0.235\,\kappa + 0.128\,\kappa^2\right)\hbar\omega_0. \qquad (4.16)$$

Note that the splitting between $|S_\alpha\rangle$ and $|T_\beta^0\rangle$ is to good approximation linear in ω_c in the regime of interest, and the ground state changes from a spin triplet to a singlet around $\omega_c/\omega_0 \sim 0.1$. These two generic features are the key ingredients for our qubit proposal.

One could alternatively use levels that cross in this subsystem to construct a singlet-triplet qubit [68], but in this case qubit control would still rely on modulation of the magnetic field. If, instead, we add two more quantum dots with a single electron on each, then we can create a triple-dot exchange-only singlet-only qubit similar to the quadruple-dot qubit proposed in Chapter 3, where the tunability of the singlet-triplet splitting of the two central electrons, via detuning of t_{23} (see Fig. 3.4), is now replaced by tunability of the splitting through the external magnetic field.

4.1.2 The six-particle singlet-only qubit subspace

We construct our qubit using two *six*-electron spin states. We use the device sketched in Fig. 4.1, with a charge configuration (1,4,1), and proceed again as in Chapter 2. We model the system with the Hamiltonian

$$H = \sum_{i=1}^{3}\left(H_1^{(i)} - V_i n_i\right) + \sum_{\langle i,j\rangle} U_c n_i n_j - \sum_{\langle i,j\rangle,\eta} \frac{t_{ij}}{\sqrt{2}}c_{i\eta}^\dagger c_{j\eta}, \qquad (4.17)$$

where now we included $H_1^{(i)}$: the single-dot many-particle Hamiltonian for a quantum dot i described above in Eq. (4.6).

This is a very simple model where we assumed that: (*i*) The gate-induced potentials V_i are smooth enough so that they affect all electronic orbitals in the same way. (*ii*) The distance between the quantum dots dots is large enough to allow us to treat the interdot electrostatic energy (the
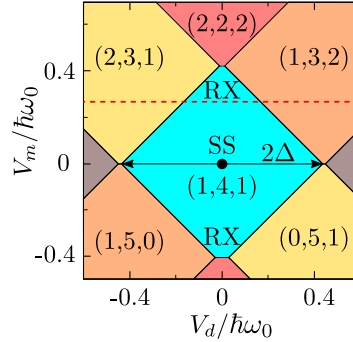
Figure 4.4:   Charge stability diagram of the six-electron XO qubit as a function of V_m and V_d, centered at the charge region (1,4,1). The figure shows the positions of the SS, at the center, and the RX regimes, on top of the (1,4,1) region. The red dotted line indicates where the qubit is manipulated, both for qubit operations and readout. For this figure we have used $\omega_c/\omega_0 = 0.1$, $U_c = 0.2\,\omega_0$, $\kappa = 0.5$ and $m^* = 0.067 m_e$.

second term in the Hamiltonian) as being dependent only on the number of electrons in the dots (n_i) and not on their exact orbital configuration. (*iii*) All tunneling processes we will consider below involve a (0,0)-orbital on the lateral quantum dots and a $(0, \pm 1)$-orbital on the central dot; since all $(0, \pm 1)$-orbitals have the same radial structure we take the tunneling coefficients t_{ij} to be independent of the electronic orbitals involved. We thus use t_l for the magnitude of the tunnel coupling between the quantum dots 1 and 2, regardless of the orbitals involved, and t_r for the tunnel coupling between the dots 2 and 3. Furthermore, the quantum dots that form the qubit have different sizes. We use $\sigma_0 = 30$ nm for the central dot and $\sigma_0 = 20$ nm for the lateral dots. This allows for spin blockade in the external dots and seizable charging and orbital energies in the middle dot, which are necessary for obtaining a qubit equivalent to the XO singlet-only qubit of Chapter 3.

From the electrostatic part of H we find the CSD of Fig. 4.4 as a function of the detuning $V_d = \frac{1}{2}\left(V_3 - V_1\right)$ and $V_m = \frac{1}{2}\left(V_1 + V_3\right) - V_2$. We study the qubit within the charge state (1,4,1), either at the RX regime or at the SS. Within the (1,4,1) region the four lowest-energy six-particle

states with spin $S^2 = 0$ can be written as

$$|0\rangle = |S_\alpha S_{13}\rangle, \tag{4.18}$$

$$|1\rangle = \frac{1}{\sqrt{3}} \left[|T_\beta^{(0)} T_{13}^{(0)}\rangle - |T_\beta^{(-)} T_{13}^{(+)}\rangle - |T_\beta^{(+)} T_{13}^{(-)}\rangle \right], \tag{4.19}$$

$$|2\rangle = |S_\beta S_{13}\rangle, \tag{4.20}$$

$$|3\rangle = |S_\gamma S_{13}\rangle, \tag{4.21}$$

where, as in the previous chapters, $|S_{13}\rangle$ and $|T_{13}\rangle$ indicate the pairing of two electrons in the outer dots in a singlet or triplet state. The states $|S_{\alpha,\beta,\gamma}\rangle$ and $|T_\beta\rangle$ are the lowest singlet and triplet states on the central dot, as defined above (see Fig. 4.3 and the text around). The qubit is thus defined in this singlet subspace, with the qubit states being $|0\rangle$ and $|1\rangle$.

We propose to tune the system close to the degeneracy of the states $|S_\alpha\rangle$ and $|T_\beta\rangle$ on the central dot. For a dot size of $\sigma_0 = 30$ nm, this happens at $B \approx 75$ mT (that is, $\omega_c/\omega_0 = 0.1$). Furthermore we use $U_c = 0.2\,\omega_0$ and $\kappa = 0.5$. Close to this point, the singlets $|2\rangle$ and $|3\rangle$ will be split off by an energy much larger than the qubit splitting.

We derive an effective qubit Hamiltonian by means of a SW transformation of the Hamiltonian in Eq. (4.17). For this we assume that $\tau/\Delta \ll 1$, with τ the magnitude of the tunnel couplings (typically $\tau \sim 10$ μeV) and 2Δ the width of the (1,4,1) region (see Fig. 4.4). This condition is satisfied across most of the (1,4,1) charge region, and allows us to treat the tunnel coupling perturbatively. We thus proceed as in Chapter 2 and project the resulting transformed Hamiltonian onto the qubit subspace, yielding to order τ^2

$$H_{\mathrm{qb}} = \frac{1}{2} \left(E_{ST} + J_z \right) \sigma^z + J_x \sigma^x. \tag{4.22}$$

From this expression we observe that the qubit splitting is dominated by the singlet-triplet splitting on the central dot E_{ST} which, from Eq. (4.16) we see that it is, to good approximation, linear in ω_c. We emphasize that through $\omega_c \propto B$ this term, and therefore the qubit splitting, can be easily tuned over tens of μeV.

The other two terms, the energies J_z and J_x read:

$$J_z = \frac{1}{2} \left(\frac{t_l^2 \Delta}{(V_d - V_m)^2 - \Delta^2} + \frac{t_r^2 \Delta}{(V_d + V_m)^2 - \Delta^2} \right.$$
$$\left. + \frac{3t_l^2 (\Delta + \omega_c)}{(V_d - V_m)^2 - (\Delta + \omega_c)^2} + \frac{3t_r^2 (\Delta + \omega_c)}{(V_d + V_m)^2 - (\Delta + \omega_c)^2} \right), \quad (4.23)$$

$$J_x = \sqrt{\frac{3}{2}} \left(\frac{t_r^2 \Delta}{(V_d + V_m)^2 - \Delta^2} - \frac{t_l^2 \Delta}{(V_d - V_m)^2 - \Delta^2} \right). \quad (4.24)$$

Close to the line where $V_d = 0$ and with $t_l \approx t_r$, the two exchange terms can be expressed as

$$J_z \approx -\tau^2 \left[\frac{\Delta}{\Delta^2 - V_m^2} + \frac{3(\Delta + \omega_c)}{(\Delta + \omega_c)^2 - V_m^2} \right], \quad (4.25)$$

$$J_x \approx \frac{\sqrt{6}\tau\Delta}{\Delta^2 - V_m^2} \left[\delta t + \frac{2tV_m}{\Delta^2 - V_m^2} V_d \right], \quad (4.26)$$

for Δ as defined in Fig. 4.4, and with $\tau = \frac{1}{2}(t_l + t_r)$ and $\delta t = t_l - t_r$. The exchange energy J_z gives only a small tuning-dependent correction to the qubit splitting, largely dominated by E_{ST}. On the other hand, J_x provides a coupling to σ^x, and its linear dependence in δt and V_d can be used to drive Rabi oscillations, either via a detuning of the tunneling asymmetry δt or via a detuning of V_d.

As we mentioned before, we are interested in studying the dynamics of the qubit at the RX regime and at the SS. At the RX regime, close to the top and bottom of the (1,4,1) region in Fig. 4.4, the strong coupling to the other charge states offers fast qubit control through V_d [27]. In Fig. 4.5(a) we show the lowest-energy states of the system as a function of V_d along the horizontal dashed line in Fig. 4.4 (along $V_m/\omega_0 = 0.27$) obtained from the Hamiltonian in Eq. (4.17). In this figure we have ignored the Zeeman splitting for clarity, which would add an energy splitting between the triplet (and quintuplet) states of $\sim 1.7\mu$eV for $\omega_c/\omega_0 = 0.1$. We used the same parameters as in Fig. 4.4 and further set $\tau = 25$ μeV and $\delta t = 0$. The green and blue curves show the qubit states $|0\rangle$ and $|1\rangle$, respectively. The three spin triplets $|T_{1,2,3}\rangle$, and a spin quintuplet $|Q\rangle$ is shown in gray.

At the SS the qubit is, to linear order, insensitive to electric noise in the potentials V_i, offering some protection against charge noise. Nevertheless, the spectrum at this point is qualitatively similar to the spectrum at the RX regime. We show the spectrum at the SS in Fig. 4.5(b), for the same set of parameters as in Fig. 4.5(a), but now as a function of the tunneling
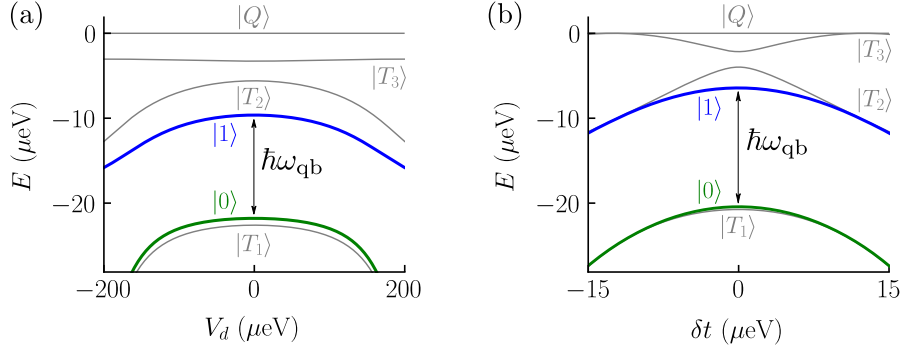
Figure 4.5: (a) Energy spectrum of the Hamiltonian in Eq. (4.17) at the RX regime as a function of the detuning V_d, showing only the lowest laying states and ignoring the Zeeman splitting. (b) Energy spectrum at the SS as a function of the tunneling asymmetry δt. The green and blue lines show the qubit states $|0\rangle$ and $|1\rangle$ respectively; the gray lines show the spin triplet and quintuplet states. In both panels we have used $\tau = 25\mu$eV and $\omega_c = 0.1\omega_0$.

asymmetry δt, with $V_d = 0$. The smaller exchange effects at the center of the CSD translate into a qubit splitting that is closer to E_{ST} ($\approx 18.3\ \mu$eV for $\omega_c/\omega_0 = 0.1$). Note, however, that both spectra are similar to the energy spectrum of the XO singlet-only qubit of Fig. 3.3, in Chapter 3. Furthermore, in both panels we show results for values of the magnetic field on the right-hand side of the singlet-triplet crossing (Fig. 4.3), but for smaller fields, on the left-hand side of the crossing, the qubit works similarly, except that the ground state would be the qubit state $|1\rangle$.

Let us now study in more detail the degree of tunability of the qubit. In Fig. 4.6(a) we show the qubit splitting $\hbar\omega_z$ as a function of the magnetic field, in terms of ω_c, both in the RX regime and at the SS. This confirms the high degree of tunability of our qubit: in a range of ω_c/ω_0 from 0.1 to 0.2 (equivalent to a magnetic field from ~ 70mT to ~ 140mT) the qubit splitting increases from nearly 0 to $\sim 130\mu$eV. This high degree of tunability, unprecedented in any other XO spin qubit, permits an efficient and adaptable coupling to other systems such as microwave cavities which can be used to couple distant qubits [15, 50, 73, 74].
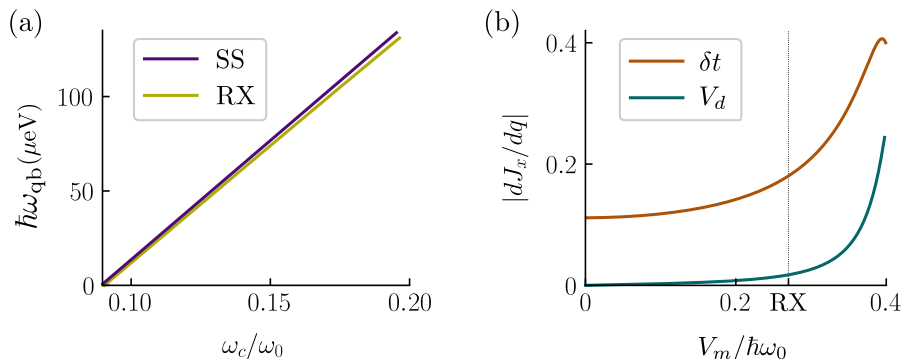
Figure 4.6: (a) Qubit splitting as a function of the magnetic field at the RX regime (yellow) and at the SS (purple), where $\omega_c/\omega_0 = 0.1$ corresponds to $B \approx 75$ mT. (b) This panel shows the derivative dJ_x/dq for $q \in \{\delta t, V_d\}$ as a function of V_m and at $V_d = 0$. This magnitude indicates the efficiency of δt and V_d as driving parameters. For (a) we used $V_m = 0.27$ and $V_d = 0$.

4.1.3 Manipulation of the qubit

This qubit has exactly the same detuning axis as the XO qubits presented in Chapters 2 and 3. Therefore, single-qubit rotations can be performed via resonant Rabi driving via a sinusoidal modulation of a tuning parameter q—we choose either $q = V_d$ or $q = \delta t$— with a small amplitude $\tilde{q}$ and frequency ω. For small enough $\tilde{q}$ the qubit Hamiltonian from Eq. (4.22) can be approximated as

$$H_{\mathrm{qb}} = \frac{1}{2}\hbar\omega_z\sigma^z + A_q \sin(\omega t)\sigma^x, \qquad (4.27)$$

where $A_q = \tilde{q}\,(dJ_x/dq)_{q=q_0}$. Similarly to the XO singlet-only qubit and the XO triple-dot qubit, driving this qubit resonantly, with a frequency $\omega = \omega_z$, induces Rabi oscillations with a period h/A_q. At the RX regime, we can use V_d as the driving parameter. With an amplitude of $\tilde{V}_d = 5$–10 μeV this will result in fast rotations with a Rabi period of $T_{\mathrm{Rabi}} \approx 20$–40 ns. At the SS, a resonant detuning of the qubit is more efficient via a driving on δt. A periodic driving on δt with an amplitude $\delta\tilde{t} = 2$ μeV will result in Rabi oscillations with a period of $T_{\mathrm{Rabi}} \approx 20$ ns. We can see this in Fig. 4.6(b), where we plot the "efficiency" dJ_x/dq of the two driving parameters $q \in \{\delta t, V_d\}$ as a function of V_m, along the line $V_d = 0$. Note

that at the SS, at $V_m = 0$, the sensitivity to V_d vanishes. At this point, and also throughout all V_m within the charge region (1,4,1), driving of δt is more effective. This behavior is in agreement with Eq. (4.26).

Fast qubit rotations can therefore be achieved both in the RX regime and at the SS. Qubit initialization and readout can be accomplished in the same way as in the XO triple-dot qubit or as in the XO singlet-only spin qubit of Chapter 3.

4.1.4 Electric and magnetic noise: Decoherence

We have previously seen that in singlet-only spin qubits there is no direct coupling between the qubit states via the hyperfine interaction, to lowest order. Higher-order effects, however, can give rise to energy shifts of the qubit splitting that may lead to qubit dephasing, in the same way as we saw in the previous chapter. The qubit that we presented in this chapter is not different in this regard. We thus need to study the effects of the hyperfine interaction in this qubit. We model the interaction between the electron spins and the spins of the nuclei in the same way as before[2].

We thus proceed as before and find that a rough estimate for the scale of the dephasing time caused by the higher-order effects of the hyperfine fields is $T_2^* \sim A_q \hbar (E_0 - E_{T_1^0})^2 / \sigma_K^4$, where E_0 and $E_{T_1^0}$ are the energies of the qubit state $|0\rangle$ and the triplet state $|T_1^{(0)}\rangle$. As expected, when the states $|T_1^{(0)}\rangle$ and $|0\rangle$ are very close in energy, the effective magnetic field-induced interaction between both states is larger and the dephasing time is thus shorter. At the SS, where the two states are closer, the dephasing time is thus shorter than in the RX regime.

To corroborate this, we evaluate the probability $\langle P_1(t) \rangle$ of finding the qubit in $|1\rangle$ after initializing in $|0\rangle$ and driving resonantly, as a function of time t. We carry this calculation numerically and focus on the two cases illustrated in Fig. 4.5. The results are shown in Fig. 4.7. In this figure we show the time-dependent probabilities for (a) driving via V_d in the RX regime, and (b) driving via δt at the SS. In both cases we evaluate the probability after averaging over 2500 random nuclear configurations of $\mathbf{K}_i$ and considering the nuclear noise as Gaussian-distributed with zero mean and $\sigma_K = 0.07$ μeV [32] (refer to Section 3.1.2). We used the driving amplitudes $\tilde{V}_d = 10$ μeV and $\delta\tilde{t} = 2$ μeV.

---

[2]The coupling between the nuclear magnetic moments and the *orbital* degrees of freedom of the electrons in the central dot is, on the other hand, negligible, and will therefore not be considered here.
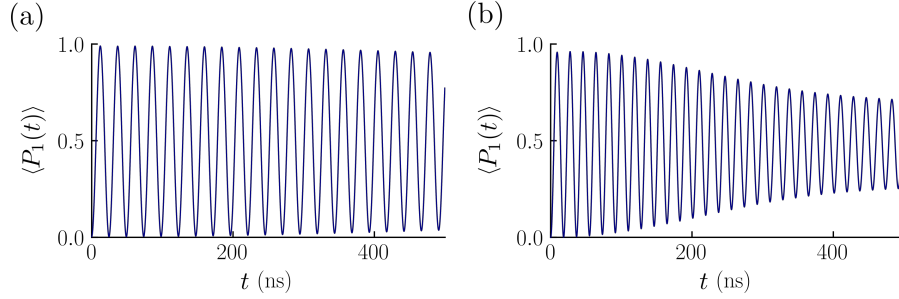
Figure 4.7: Time dependent probability $\langle P_1(t) \rangle$ (a) at the RX regime and (b) at the SS, after averaging over 2500 random nuclear field configurations. The decay of the Rabi oscillations at long times show a longer coherence time at the RX regime than at the SS.

The results show that the hyperfine-induced dephasing, even at the SS, is small compared to the Rabi period. Nevertheless, a longer coherence time is observed at the RX regime, where the energy difference between the lowest qubit state and the leakage states $|T_1^{(0,\pm)}\rangle$ is larger.

5

Relaxation, leakage and dephasing

We have seen a variety of XO qubits: From the triple-dot XO qubit from Chapter 2 to the singlet-only XO qubits from Chapters 3 and 4. Here we investigate the different mechanisms of decoherence on these specific devices and show an enhancement of the coherence time by several orders of magnitude when the qubit is operated at the SS. Some of the contents of this chapter are included in Paper II and partially also in Papers I and III.

In Chapter 2 we identified the main mechanisms of decoherence in XO qubits, and in Chapters 3 and 4 we proposed two novel devices that address some of these issues. Nevertheless, once the main mechanisms of decoherence have been disabled we have to quantify the remaining sources of decoherence in order to be able to predict the coherence time of the qubit, that is, the usable computational time. In this regard we study the remaining relaxation and decoherence mechanisms of two different systems: (*i*) An XO triple-dot spin qubit hosted in purified ^{28}Si, where the fraction of spin-full nuclei in the bulk semiconductor is negligible, and (*ii*) the XO singlet-only spin qubit of Chapter 3, which is intrinsically insensitive, to leading order, to the effects of any random magnetic noise.

We argued before that one of the main mechanisms of decoherence in triple-dot XO spin qubits hosted in high quality III-V semiconductors is a relaxation out of the qubit subspace due to the coupling between the electrons confined in the quantum dots and the ensemble of fluctuating nuclear spins in the semiconductor. To solve this problem we presented a proposal for an XO singlet-only spin qubit, but another straightforward solution, already investigated by many [10, 23, 32, 33, 75, 76], consist on hosting the qubit in highly purified ^{28}Si, which is the most abundant and a nuclear spin-free isotope of silicon[1]. Indeed, when it comes to its fabrication, GaAs has been proven to be a very successful material [9, 13], and although the fabrication of quantum dots in Si is more challenging it also has many advantages. Certainly, the valley degeneracy in Si adds more degrees of freedom, but this degeneracy can be efficiently lifted resulting in a ground-state gap [10, 77]. One can then fabricate a triple-dot spin qubit, with the advantage that there are (almost) no nuclear spins and the qubit can be operated by means of electric fields only [33]. But these two solutions—the XO singlet-only spin qubit of chapters 3 and 4 and the Si-based XO triple-dot spin qubit—albeit eliminating the major source of decoherence, are not decoherence-free. The remaining sources of decoherence are: (*i*) electric noise in the metallic gates that control and define the quantum dots, leading to qubit dephasing [13, 34], also at the SS, (*ii*) an electron-phonon coupling that can cause spin-conserving qubit relaxation [28] within the qubit subspace, and (*iii*) the SO interaction that can enable spin-flip transitions out of the qubit subspace when combined with a mechanism of energy dissipation [9, 13].

In the this chapter we study the effects of electric noise, electron-phonon coupling and the SO interaction for the XO qubit from Chapter 2 and the XO singlet-only qubit from Chapter 3, with some brief comments on the highly tunable XO singlet-only qubit from Chapter 4. We thus identify decoherence-free regions in the parameter space that extend substantially the coherence time of the qubits.

---

[1]Let us note, though, that perfect purification in Si is not possible, hence there is always a weak random magnetic field gradient between dots. Moreover an effective Zeeman noise has been reported in Si quantum dots [33]. This Zeeman noise has been shown to be one of the main sources of decoherence, together with electric noise, in triple QDs.
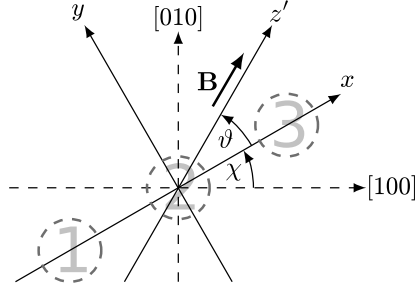
Figure 5.1: Reference frame of the system. The quantum dots lie in the x-y plane which, in turn, lies in the (001) crystallographic plane. An in-plane magnetic field $\mathbf{B}$ is applied at an angle ϑ with respect to the interdot axis to induce a Zeeman splitting of spin states. We consider an interdot axis x at an angle χ with respect to the crystallographic [100] direction.

5.1 Model of the system

We model both qubits with the Hubbard-like Hamiltonian that we introduced before. Nevertheless, since the geometry of the two qubits and the properties of the host materials are different, we will briefly explain the different peculiarities of the devices that we need to consider for the further analysis.

The triple-dot XO qubit

Here we consider a linear array of three circular quantum dots, hosted in ^{28}Si, in the (001) crystallographic plane, as schematically depicted in Fig. 5.1. The dots have radius σ_0 and interdot distance d (center-to-center). We assume a large orbital level splitting E_{orb} on the dots, and hence tune the system into the spin blockade regime.

We model the system as in Chapter 2, including all possible three-particle charge states that are coupled to the charge state (1,1,1) by only one tunneling transition. These charge states are (2,0,1), (1,0,2), (1,2,0) and (0,2,1). The full charge stability diagram is shown in Fig. 5.2. As we did before, we included a nearest-neighbor, spin-conserving, interdot tunnel coupling and an in-plane external magnetic field that adds a Zeeman splitting between states with different spin projection S_z. The tunnel coupling parameters t_{12} and t_{23} are renormalized to include the effects of

(a)   (b)

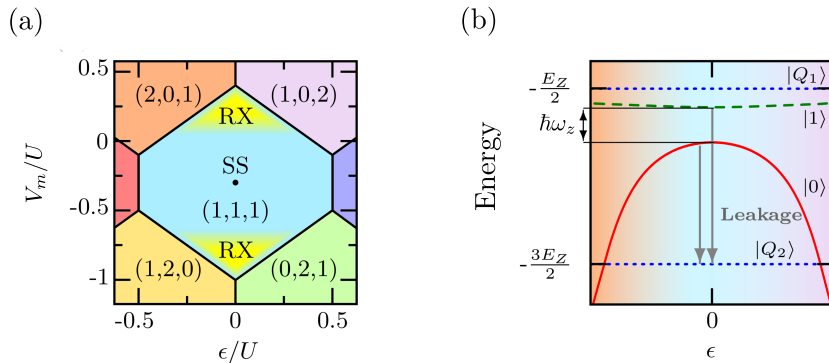Figure 5.2:   (a) Charge stability diagram as a function of the detuning ϵ and V_m. In the region (1,1,1) we indicate the position of the SS and the RX regimes. (b) Qualitative sketch showing the lower-energy part of spectrum of the XO triple-dot qubit as a function of ϵ (in arbitrary units) within the RX regime. (refer to Section 2.2). The gray arrows indicate the leakage processes investigated here. In both panels we used $U_c = 0.3\,U$, $V_2 = 2U_c - V_1 - V_3$ and for the spectrum we further used $t_{12} = t_{23}$.

the phase differences between the valley states on neighboring dots [9]. From here onward we will use $t_{12} = t_{23} \equiv \tau$.

We are interested in the RX regime, at the top and bottom of the (1,1,1) charge region, where a small modulation of ϵ with frequency ω induces Rabi oscillations and allows for fast qubit operations [27, 62]; and we are also interested in the SS, at the center of the (1,1,1) region, where the qubit offers a similar control [32, 35, 78], and has also the benefit that electric noise in the gate potentials does not influence, to leading order, the qubit splitting. This results in a dephasing time T_2^* that is orders of magnitude larger than in the RX regime [15, 36].

At $\epsilon = 0$, for any V_m, the qubit splitting to lowest order in τ reads:

$$\hbar\omega_z = \tau^2 \left(\frac{1}{U - 2U_c - V_m} + \frac{1}{U + V_m} \right). \tag{5.1}$$

The qubit splitting can be controlled through τ and V_m and, as we saw earlier in Section 2.2, a small ϵ yields a term $\propto \epsilon\,\sigma^x$ in the projected qubit Hamiltonian.

Since phonon-mediated relaxation of the triple-dot XO qubit has been studied elsewhere [13, 28, 65] and ^{28}Si is nuclear-spin-free, we will focus
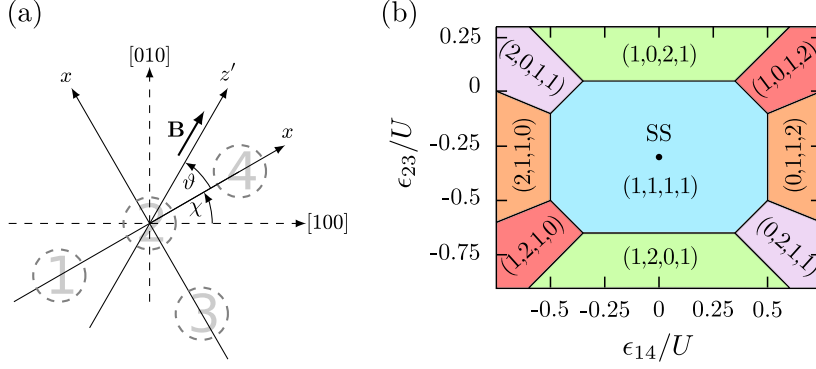
Figure 5.3: (a) Four quantum dots are placed on the (001) plane of the semiconductor at an angle χ from the [100] crystallographic direction in a T-like geometry. (b) CSD of this setup with $U_c = 0.3U$. We show only the section of the CSD with $\epsilon_\Lambda = U_c/2$. This plane contains a SS at the center of the (1,1,1,1) charge region.

here on leakage processes caused by the SO interaction. These are indicated in the spectrum of Fig. 5.2(b) with gray arrows, and are defined as transitions from one of the qubit states $|0\rangle$ or $|1\rangle$ to the quadruplet state $|Q_2\rangle$ that lays below the qubit subspace. We will additionally study the dephasing of the qubit states as a consequence of electric noise in the gate-induced offsets V_i.

The XO singlet-only qubit

We model the XO singlet-only qubit in a similar way, as we did in Chapter 3. Before we studied, for simplicity, the plane defined by $\epsilon_\Lambda = 0$. The choice of the plane is not much relevant, but choosing this plane helps to reduce the complexity of the calculations and incidentally contains enough features to make the problem at hand interesting enough. Now we will consider the plane $\epsilon_\Lambda = U_c/2$, since this is the plain that contains the SS.

At zero detuning, with $\epsilon_{14} = 0$ and in the plane $\epsilon_\Lambda = U_c/2$, the qubit splitting goes as (to lowest order in t_{ij}):

$$\hbar\omega = \tau^2 \left(\frac{1}{U - 2U_c - \epsilon_{23}} + \frac{1}{U + \epsilon_{23}} \right)$$
$$- t_{23}^2 \left(\frac{1}{U - 3U_c - 2\epsilon_{23}} + \frac{1}{U + U_c + 2\epsilon_{23}} \right), \quad (5.2)$$

where we again used $t_{12} = t_{24} = \tau$, and kept $t_{23} \neq \tau$.

Usually, in multi-dot qubits, a magnetic field is applied to the system to break degeneracies within the qubit subspace. This is indeed what we did in Chapter 3, but for the quadruple-dot XO qubit this field is not be necessary. The absence of a magnetic field has some benefits:

1.—Due to the complexity of the fabrication of the quantum dots, these may come with different sizes and different g-factors. This can give rise to a magnetic field gradient between quantum dots when a magnetic field is applied [33]. Suppressing the magnetic field thus eliminates this problem.

2.—A magnetic field will split the triplet states with different S_z, and some of them will lay lower down in the energy spectrum. This shift in the energy difference between the qubit states and the triplet states makes the relaxation rates out of the qubit subspace much larger and, therefore, limit the coherence time of the system. Additionally, if we look at the energy spectrum in Fig 3.3, from Chapter 3 we can see three triplet states around the qubit states. If we include a magnetic field that is large enough to sweep away the polarized triplets from the qubit subspace there will be three polarized triplet states $|T_{1,2,3}^{(+)}\rangle$ far below the qubit states, plus one unpolarized the triplet state $|T_3^{(0)}\rangle$ close to the qubit state $|0\rangle$. Thus a total of four triplet states below the qubit subspace. Without the magnetic splitting only three triplet states lay below $|0\rangle$. Reducing the number of states the qubit can leak to also increases the coherence time of the qubit.

3.—In absence of magnetic fields the system becomes time-reversal symmetric and that gives rise to a further reduction of the relaxation rates via a mechanism similar to a Van Vleck cancellation [30, 79] but with a system of integer spin instead, as we will see below.

On the other hand, since the XO singlet-only spin qubit is intrinsically insensitive to any magnetic noise or gradients, the downsides of applying a magnetic field are not significant.

We will investigate the effects of electric noise on the coherence time of the qubit and also leakage processes from the qubit states $|0\rangle$ and $|1\rangle$ to the triplet states $|T\rangle_3^{(\pm,0)}$.
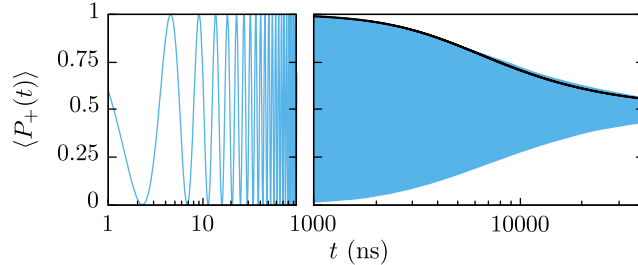
Figure 5.4: Time-dependent return probability $|\langle+|\psi(t)\rangle|^2$ after initializing in $|+\rangle$, averaged over 10^5 configurations of δV_i taken from a normal distribution with $\langle\delta V_i\rangle = 0$ and a standard deviation $\sigma_e = 5\mu$eV (blue line). The black line shows the envelope function predicted in Eq. (5.5).

5.2 Electric noise and sweet spots

In a triple-dot XO qubit there is a sweet spot at $V_m = -U_c$, the center of the charge stability diagram. At this point the qubit splitting is minimal:

$$\hbar\omega_z = \frac{2\tau^2}{U - U_c},\tag{5.3}$$

with $d\omega_z/dV_i = 0$ for all V_i, and the effects of electric noise in the gates on the coherence time of the qubit are also minimal. Nevertheless we want to investigate the next-order correction to the dephasing time T_φ due to electric noise. We do that by evaluating the probability $P_+(t)$ of finding the system in the initial state $|+\rangle = \frac{1}{\sqrt{2}}(|0\rangle + |1\rangle)$ after it has been freely evolving under the influence of electric noise in the gate offsets only. The average of this probability over noise should display several oscillations between 0 and 1, with a period $2\pi/\omega_z$, that decay in time to $\langle P_+(t \to \infty)\rangle = 0.5$. We evaluate this expression both analytically and numerically. We tune the system to the SS and add random offsets δV_i to all the gate-induced offsets V_i, taken from a normal distribution with $\sigma_e = 5$ μeV [32]. By diagonalizing the Hamiltonian, we identify the two qubit states $|1\rangle$ and $|0\rangle$, and create an initial state $|+\rangle = \frac{1}{\sqrt{2}}(|0\rangle + |1\rangle)$. We then evaluate numerically the time-dependent qubit state $|\psi(t)\rangle = \exp\{-\frac{i}{\hbar}Ht\}|+\rangle$, and from this we calculate $P_+(t)$ for this specific set of δV_i. We repeat this process 10^5 times and calculate the average $\langle P_+(t)\rangle$. The result is the blue curve in Fig. 5.4, where we can see an oscillating probability that decays to $1/2$ over time.

An analytical evaluation of the average $\langle P_+(t)\rangle$, yields

$$\langle P_+(t)\rangle = \frac{1}{2} + \frac{\cos\left(t\frac{2\tau^2}{\hbar(U-U_c)} - \arctan\left[t\frac{4\tau^2\xi^2}{\hbar(U-U_c)^3}\right]\right)}{2\sqrt{1 + t^2\frac{16\tau^4\sigma_e^4}{\hbar^2(U-U_c)^6}}}. \qquad (5.4)$$

This expression has been obtained by following the recipe outlined in Section 2.4. This probability oscillates with a frequency $2\tau^2/\hbar(U-U_c)$, while additionally acquiring a phase shift that goes to $-\pi/2$ for large times. From this we extract a simple expression for the envelope function of the oscillations

$$P_{\text{env}} = \frac{1}{2} + \frac{1}{2\sqrt{1 + t^2\frac{16\tau^4\sigma_e^4}{\hbar^2(U-U_c)^6}}}. \qquad (5.5)$$

The oscillations will thus decay as a power law with $P_{\text{env}} \propto T_\varphi/t$, and a dephasing time of $T_\varphi = \hbar(U-U_c)^3/(4\tau^2\sigma_e^2)$. This is in clear contrast with the exponential decay $\propto e^{-t^2/T_\varphi^2}$ that is encountered elsewhere in the CSD, and predicted by the "cumulant expansion method" [15, 73]. Fig. 5.4 shows a good match between the envelope function, in black, and the numerical simulations, in blue.

In the XO singlet-only qubit the sweet spot is also located at the center of the charge stability diagram, with $\epsilon_{14} = 0$, $\epsilon_{23} = -U_c$ and $\epsilon_\Lambda = U_c/2$, and the qubit splitting at this point is

$$\hbar\omega_z = \frac{2\tau^2}{U - U_c} - \frac{2t_{23}^2}{U - U_c}. \qquad (5.6)$$

Here, the average of the probability over the noise δV_i can also be evaluated analytically, although the calculation is more tedious. Nonetheless, one can still obtain the envelope function of the oscillations:

$$P_{\text{env}} = \frac{1}{2}\left[1 + \left(1 + \frac{64\,t_{23}^4\sigma_e^4\,t^2}{(U-U_c)^6\hbar^2}\right)^{-1/4}\left(1 + \frac{16\,\tau^4\sigma_e^4\,t^2}{(U-U_c)^6\hbar^2}\right)^{-1/2}\right]. \qquad (5.7)$$

We show this result together with a numerical study of the probability $\langle P_+(t)\rangle$ for an XO singlet-only qubit in Fig. 5.5, where we proceeded in the same way as before. At long times we observe that the probability decays as a power law $P_{\text{env}}(t) \sim t^{-3/2}$. We can then extract, from Eq. (5.7) a characteristic time $T_\varphi = \hbar(U-U_c)^3\left(128\,t_{23}^2\tau^4\sigma_e^6\right)^{-1/3}$.
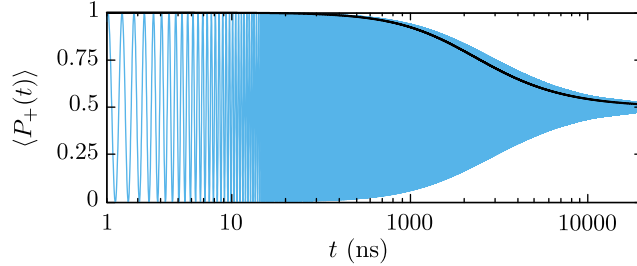
Figure 5.5: Time-dependent return probability $\langle P_+(t) \rangle$ as a function of time for the quadruple-dot XO qubit, averaged over 10^5 configurations of δV_i taken from a normal distribution with $\langle \delta V_i \rangle = 0$ and a standard deviation $\sigma_e = 5\mu\text{eV}$ (blue line). The black line shows the envelope of this probability, estimated in Eq. (5.7).
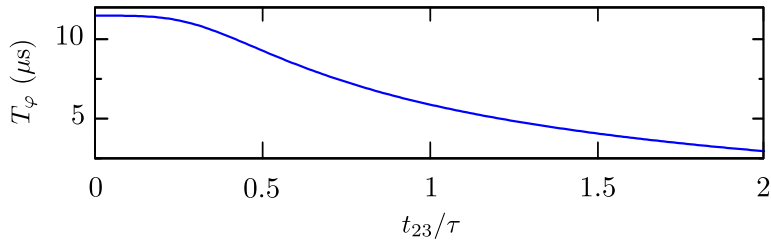
Figure 5.6: Dephasing time as a function of t_{23} at the sweet spot, obtained from Eq. (5.7). The dephasing time of the qubit is maximal when the dots 2 and 3 are decoupled, i.e., $t_{23} = 0$

The dependence of the probability on the tunneling amplitude t_{23} is noteworthy. In Fig. 5.6 we plot the envelope probability P_{env} as a function of t_{23} at the SS with zero detuning. Here, and also in Eq. (5.7), we see that the dephasing time goes as $T\varphi \sim t_{23}^{-2/3}$, signaling a better performance for smaller t_{23}. This should motivate the choice $t_{23} < \tau$. If one sets $t_{23} = 0$, the dephasing time is maximal and so is the qubit splitting at the SS. Nevertheless we still need to be able to couple the dots 2 and 3 (and thus have a finite t_{23}) for qubit initialization and readout (see Section 3.1.3).

We also investigate the effects of electric noise in the highly tunable XO qubit from Chapter 4. In this case we analyze the coherence time T_2^* of the qubit *away* from the SS, since he wave already seen in Section 4.1.4 that the magnetic noise set by the environmental nuclear spins is more

efficient at dephasing the qubit at the SS than at the RX regime.

Proceeding as before we find a shift in the qubit splitting in the RX regime given by:

$$\hbar\delta\omega_z = \sqrt{6}t^2 V_m \delta V \left[-\frac{\Delta}{(V_m^2 - \Delta^2)^2} - \frac{3(\Delta + \omega_c)}{(V_m^2 - (\Delta + \omega_c)^2)^2} \right], \qquad (5.8)$$

where δV is the random fluctuation in the gates. We then estimate the dephasing induced by the electric noise at the RX regime as

$$T_2^* \simeq \frac{A_q \hbar}{6t^4 V_m^2 \sigma_e^2} \left[\frac{\Delta}{(V_m^2 - \Delta^2)^2} + \frac{3(\Delta + \omega_c)}{(V_m^2 - (\Delta + \omega_c)^2)^2} \right]^{-2}. \qquad (5.9)$$

At the SS, where $\hbar\delta\omega_z = 0$ the qubit splitting is thus insensitive to fluctuations in the potentials V_i to leading order. Here we find, via a numerical evaluation of the coherence time, a dephasing time of $T_2^* \gg 10~\mu$s.

5.3   Spin-conserving qubit relaxation

The coupling between the electrons confined in the quantum dots and the phonons present in the host semiconductor is unavoidable. Nevertheless the effects of this interaction can be mitigated. In Si-based triple-dot XO qubits the direct qubit relaxation rate, from the state $|1\rangle$ to $|0\rangle$ is

$$\Gamma_{1\to 0} = \frac{1}{70\pi} \frac{\tau^4}{\Delta_3^4} \frac{d^2 \Xi_u^2 (\hbar\omega_z)^5}{\hbar^6 v_t^7 \rho}, \qquad (5.10)$$

where $\hbar\omega_z$ is the qubit splitting and Δ_3 is defined as $\Delta_3^{-2} = (U - 2U_c - V_m)^{-2} - (U + V_m)^{-2}$. The variables d, Ξ_u, v_t and ρ are the distance between dots, the deformation potential, the sound velocity (along a transversal direction) and the electron density in Si, all defined in Section 2.3. We will not spend too much time discussing about this expressions because it has already been studied before in other publications (see, e.g., Refs. [13, 28, 65]; the derivation of this expression is also sketched in Section 2.3). But we can observe that the dependence of the rate on τ^4/Δ_3^4 suggest that, to this order of perturbation, the relaxation rate vanishes at the SS, where $1/\Delta_3 = 0$, thus extending substantially the coherence time of the qubit.

When studying the coherence properties of the XO singlet-only qubit we found something very similar. Following the recipe from Chapter. 2,

yields to leading order in τ

$$\Gamma_{1\to 0} = \frac{2\pi}{\hbar} \sum_{\mathbf{k},p} |\lambda_{\mathbf{k},p}|^2 \frac{3}{4} \frac{\tau^4}{\Delta_4^4} \sin^2(k_x d)$$

$$\times \exp\left(-\frac{k^2\sigma_0^2}{2}\right) \delta(E_0 - E_1 + \hbar\omega_{-\mathbf{k},p}), \quad (5.11)$$

where the energies E_0 and E_1 correspond to the states $|0\rangle$ and $|1\rangle$, and we have used

$$\Delta_4^{-2} = \frac{1}{(U - 2U_c - \epsilon_{23})^2} - \frac{1}{(U + \epsilon_{23})^2}$$

$$- \frac{\tau^2/t_{23}^2}{(U - 3U_c - 2\epsilon_{23})^2} + \frac{\tau^2/t_{23}^2}{(U + U_c + 2\epsilon_{23})^2}. \quad (5.12)$$

For qubit splittings of the order $\sim \mu$eV, the coupling to piezoelectric phonons dominates [16], so we will not consider the contribution from the deformation potential. The relaxation rate can be evaluated by converting the sum over $\mathbf{k}$ to an integral. After substituting $\hbar\omega_z = E_1 - E_0$ and introducing the dimensionless coupling constant

$$g_{\text{pe}}^{(p)} \equiv \frac{(eh_{14})^2}{2\pi^2\hbar\rho v_p^3}. \quad (5.13)$$

we can obtain the simpler expression

$$\Gamma_{1\to 0} \approx \frac{\tau^4}{\Delta^4} \frac{\omega_z^3 d^3}{v^3} \frac{(eh_{14})^2}{10\pi\hbar\rho v^2 d}, \quad (5.14)$$

with v a phonon velocity that, for convenience, we now assume to be equal for all three polarizations, $v_t = v_l \equiv v$. To arrive here we have further used a dipole approximation and expanded the sine and the exponential functions in powers of $\omega_z d/v_p, \omega_z\sigma_0/v_p$ which are typically $\lesssim 10^{-2}$.

Here, again, the relaxation rate depends on Δ_4, signaling a large relaxation rate (and thus short coherence time) at the RX regime, where Δ_4 is smaller. At the SS, on the other hand, the relaxation rate vanishes as well (to this order of τ/Δ_4), showing that the electron-phonon coupling becomes ineffective as a form of qubit relaxation at the sweet spot.

Similar results are found, as we expected, for the highly tunable XO qubit of Chapter 4. In the RX regime, where the qubit splitting can be extensively tuned through ω_c, we estimate relaxation rates from $\Gamma_{1\to 0} \sim$ 1 GHz for $\hbar\omega_z \sim 50$ μeV to $\Gamma_{1\to 0} \sim 1$ MHz for $\hbar\omega_z \sim 10$ μeV, while is strongly suppressed as we approach the SS.

5.4   Spin-flip mechanisms

We now investigate the SO-mediated leakage mechanisms that we saw in Section 2.5.2, applied onto the triple-dot XO qubit and the XO singlet-only qubit, in more detail. For the first case we evaluate the leakage rates Γ_1 and Γ_0 from qubit states $|1\rangle$ and $|0\rangle$ to the ground state $|Q_2; 1_{\mathbf{k},p}\rangle$, that is, the ground state $|Q_2\rangle$ [see Fig. 5.2(b)] combined with one phonon with momentum $\mathbf{k}$ and polarization p. For simplicity we will evaluate these rates at $\epsilon = 0$ and with a symmetric tunnel coupling, $t_{12} = t_{23} = \tau$. For the XO singlet-only qubit the initial state would be either $|1\rangle$ or $|0\rangle$, and and the final state $|T_3^{(\pm,0)}; 1_{\mathbf{k},p}\rangle$. In all cases we proceed as in Section 2.5.2 and calculate the rates using a second-order Fermi's golden rule, treating the SO interaction and the electron-phonon coupling as perturbations.

5.4.1   Virtual spin-flip tunneling

As we discussed earlier, electrons can undergo a spin-flip transition while virtually tunneling to another quantum dot. This is equivalent to a transition from a three-electron spin state in the (1,1,1) region to another three-electron spin state in (1,1,1) via a virtual excitation of another charge state. This exchange-enabled mechanism produces the relaxation rates, to leading order in τ/Δ_3

$$\Gamma_1 \approx \frac{1}{16\pi} \frac{d^2}{l_{\mathrm{so}}^2} \frac{\tau^4}{\Delta_3^4} \frac{\Xi_u^2 E_Z^3}{\hbar^4 v_t^5 \rho} f_1^{\mathrm{ex}}\left(\frac{dE_Z}{\hbar v_t}\right), \tag{5.15}$$

$$\Gamma_0 \approx \frac{3}{16\pi} \frac{d^2}{l_{\mathrm{so}}^2} \frac{\tau^4}{\Delta_3^4} \frac{\Xi_u^2 E_Z^3}{\hbar^4 v_t^5 \rho} f_0^{\mathrm{ex}}\left(\frac{dE_Z}{\hbar v_t}\right), \tag{5.16}$$

with the SO length $l_{\mathrm{so}} = \hbar/(m^* A_{xx})$ containing the constants:

$$A_{xx} = \alpha \cos\vartheta + \beta(\cos\vartheta \sin 2\chi + \sin\vartheta \cos 2\chi), \tag{5.17}$$

$$A_{xy} = \alpha \sin\vartheta + \beta(\cos\vartheta \cos 2\chi - \sin\vartheta \sin 2\chi), \tag{5.18}$$

as given in Section 2.5.2 but now with a magnetic field pointing at an angle ϑ from the x axis (see Fig. 5.1). The dimensionless functions $f_{1,0}^{\mathrm{ex}}(x)$ are given in the Appendix C, and for $x \gtrsim 1$ they go as $f_{1,0}^{\mathrm{ex}}(x) \sim 1$. For small $E_Z^2 \ll (\hbar v_t/d)^2$ we can expand the functions $f_{1,0}^{\mathrm{ex}}(x)$ in small x, yielding

$$\Gamma_1 \approx \frac{1}{840\pi} \frac{d^2}{l_{\mathrm{so}}^2} \frac{\tau^4}{\Delta_3^4} \frac{d^4 \Xi_u^2 E_Z^7}{\hbar^8 v_t^9 \rho}, \tag{5.19}$$

$$\Gamma_0 \approx \frac{1}{35\pi} \frac{d^2}{l_{\mathrm{so}}^2} \frac{\tau^4}{\Delta_3^4} \frac{d^2 \Xi_u^2 E_Z^5}{\hbar^6 v_t^7 \rho}. \tag{5.20}$$
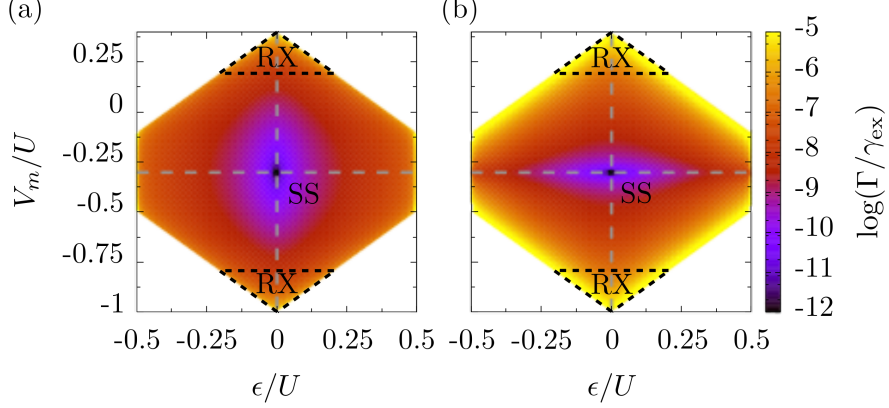
Figure 5.7: Exchange-enable leakage rates across the whole $(1,1,1)$ charge region, from the state (a) $|1\rangle$ and (b) $|0\rangle$ to $|Q_2\rangle$ in units of $\gamma_{ex} \equiv d^2 \Xi_u^2 E_Z^3 / (l_{so}^2 \hbar^4 v_t^5 \rho) = 960$ kHz. For these plots we used We used $\tau = 16\ \mu$eV, $U = 50\ \tau$, $U_c = 15\ \tau$, $E_Z = 2\ \tau$ [31, 36, 80–82], and we set the angles $\vartheta = \chi = 0$

At this order of perturbation the rates scale as $\Gamma_1 \propto E_Z^7$ and $\Gamma_0 \propto E_Z^5$, and Γ_1 is smaller than Γ_0 by a factor $(dE_Z/\hbar v_t)^2$. This only holds in case of equal tunneling amplitudes. Otherwise we find that both rates scale as $\Gamma \propto E_Z^5$. We can compare these two rates with the direct, spin-conserving, qubit relaxation rate $\Gamma_{1\to0}$, from Eq. (5.10), which comes, mainly, via electron-phonon coupling [28, 30]. In all cases the rates cancel when $1/\Delta_3 = 0$, that is, at the SS. At this point qubits are highly insensitive to (*i*) dephasing due to electric noise, (*ii*) spin-conserving relaxation from (mainly) an electron-phonon coupling and (*iii*) leakage via a tunneling-assisted SO interaction. Additionally, we observe a strong angular dependence of SO-mediated relaxation rates, via the dependence of A_{xx} on the angles χ and ϑ. This allows for a further reduction of these rates by varying the device orientation (χ) and the direction of the magnetic field (ϑ). This feature has already been predicted and observed in other qunatum dot-based devices [17, 77, 83, 84].

We also perform a numerical analysis of the leakage rates across the entire $(1,1,1)$ charge region. For the numerical calculations we diagonalize the Hamiltonian $H = H_{\text{Hubb}} + H_{\text{SO}}$ [see Eqns. (2.7) and (2.47)], disregarding the excited orbital and valley states and evaluate the relaxation rates using Fermi's golden rule, considering the electron-phonon interaction as
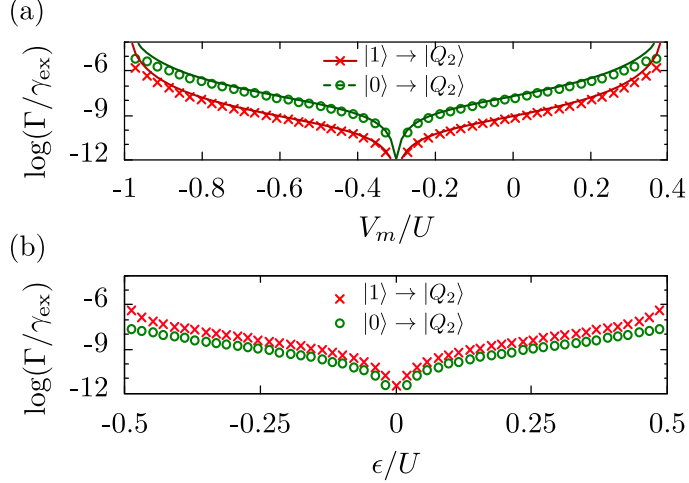
(a)

(b)

Figure 5.8: Exchange-enable leakage rates $\Gamma_{1,0}$ across (a) the vertical dashed lines in Fig. 5.7 for $\epsilon = 0$ and (b) the horizontal dashed line in Fig. 5.7 for $V_m = -0.3\,U$. Circles and crosses show numerical results, whereas solid lines show the analytical rates from Eqns. (5.19) and (5.20).

a perturbation of the Hamiltonian H:

$$\Gamma_\alpha = \frac{2\pi}{\hbar} \sum_{\mathrm{k},p} |\langle Q_2; 1_{\mathbf{k},p}|H_{\mathrm{e\text{-}ph}}|\alpha; \mathrm{vac}\rangle|^2\, \delta(E_f - E_i). \qquad (5.21)$$

We show the results in Fig. 5.7, where we plot the leakage rates as a function of the detuning ϵ and V_m in units of $\gamma_{\mathrm{ex}} \equiv d^2\Xi_u^2 E_Z^3/(l_{\mathrm{so}}^2\hbar^4 v_t^5\rho)$. For this we assumed Si/SiGe quantum dots with size $\sigma_0 = 10$ nm and interdot distance $d = 100$ nm. Fig. 5.7(a) shows the rate Γ_1 and Fig. 5.7(b) the rate Γ_0. In both cases, the magnitude of the rates (from $\sim 10^{-12}\,\gamma_{\mathrm{ex}} \sim 10^{-9}\,$kHz to $\sim 10^{-5}\,\gamma_{\mathrm{ex}} \sim 10^{-2}\,$kHz), is typically much smaller than the magnitude of the relaxation rate due to phonon-mediated qubit relaxation, of the order of $\sim 1\,$kHz.

We conclude the numerical analysis with Figs. 5.8(a,b). This figure shows line cuts of the plots in Fig. 5.7 along the vertical and horizontal dashed lines. In Fig. 5.8(a) we plot the leakage rates as a function of V_m for $\epsilon = 0$, and in Fig. 5.8(a) we plot the same rates as a function of ϵ for $V_m = -0.3\,U$. Circles and crosses show the numerical results, while the solid lines in (a) show the rates from Eqs. (5.19, 5.20) that we obtained

analytically. The plots show a good agreement between the numerical and the analytical analysis.

At the SS, where the relaxation rates are strongly suppressed, the qubit can also be operated via a modulation of the tunneling amplitudes, without the need of leaving this point of low decoherence [13, 78].

Let us now study the leakage mechanisms in the XO singlet-only spin qubit from Chapter 3. This qubit is hosted in GaAs, which is a material with a weak spin-orbit interaction. Nevertheless we want to quantify the effects of the SO interaction and compare them with those of the electron-phonon coupling and the hyperfine interaction. Unfortunately, for a system composed of four quantum dots, with 16 different spin states in the (1,1,1,1) charge region, the analytical calculation of the relaxation rates can become cumbersome and simple expressions can only be obtained at certain special points, such at the sweet spot, up to the lowest order of perturbation. We therefore prefer to show numerical results instead, since it is possible to calculate the relaxation rates numerically without further approximations.

We have proceeded in the following way: We calculated the matrix elements of the Hubbard Hamiltonian [in Eq. (3.20)], the SO Hamiltonian [in Eq. (2.47)] and the Hyperfine interaction Hamiltonian [in Eq. (2.44)] for this device and evaluated the relaxation rates using the electron-phonon Hamiltonian of Eq. (2.29) as the perturbation of the full Hamiltonian $H = H_{\text{Hubb}} + H_{\text{SO}} + H_{\text{hf}}$. We have first studied each spin-flip mechanism independently, starting with the SO interaction. In this case the SO interaction lifts the degeneracy of the triplet states and makes possible the numerical evaluation of the rates. We found unusually low relaxation rates at all points in the charge region (1,1,1,1). These are shown in Fig. 5.9. The left panel shows the relaxation rates from the qubit state $|0\rangle$ to the triplets that lay underneath (see Fig. 3.11) and the panel on the right shows the relaxation rates from the qubit state $|1\rangle$ to the triplets.

A more detailed analysis shows that when the system we consider is free of nuclear fields, and therefore time-reversal symmetric, the relaxation rates experience a significant reduction, similar to that produced by the Van Vleck cancellation in half-integer spin systems [30, 79]. In Fig. 5.10 we show that by treating the SO interaction as a perturbation, together with the electron-phonon coupling, the relaxation rates calculated via Fermi's golden rule (numerically) up to second order are exactly zero (left side, with $B_z \to 0$).

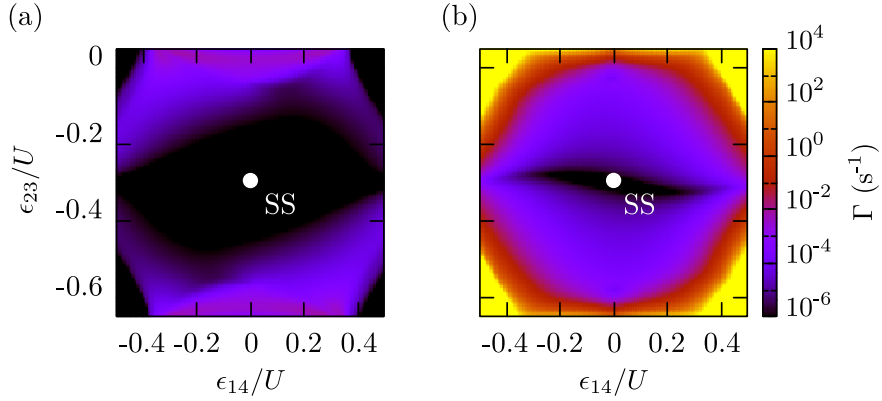When an external magnetic field is applied to the system, splitting the

Figure 5.9: Relaxation rates across the whole (1,1,1,1) region from (a) the qubit state $|0\rangle$ to the triplet states and (b) from the qubit state $|1\rangle$ to the triplet states. Both panels account for all the possible channels of leakage out of the qubit subspace via SO interaction together with the electron-phonon coupling in the absence of external magnetic fields. These rates have been calculated using $U = 800\,\mu\text{eV}$, $U_c = 0.3U$, $t_{12} = t_{24} = 24\,\mu\text{eV}$, $t_{23} = 16\,\mu\text{eV}$ and $\chi = 0$. The anisotropy of the figure is a consequence of the T-like structure of the system and the dependence of the SO Hamiltonian on the geometry of the system. Changing the third dot from the bottom to the top results in a mirror reflection of the figure with respect to an horizontal axis that goes through the center of the charge stability diagram.

triplet states, the relaxation rates increase gradually and the SO interaction becomes a relevant mechanism of relaxation, although less significant than direct qubit relaxation via the electron-phonon interaction only.

In this figure the relaxation rates have been calculated in the regions where we can define qubits states, that is, when we can distinguish two states with total spin $S = 0$ that have sufficiently different energies and are not too close, to the triplet states [red solid and green dashed lines in panel (a)]. In the lower panel the solid lines show the exact relaxation rates calculated numerically by diagonalizing H (with $H_{\text{hf}} = 0$), and the thick dashed lines are the same relaxation rates when the SO Hamiltonian is treated as a perturbation. It is here where we see the Van Vleck-like cancellation. The vertical dashed gray line shows an estimate of the upper limit of the magnitude of the nuclear fields that each electron feels in the
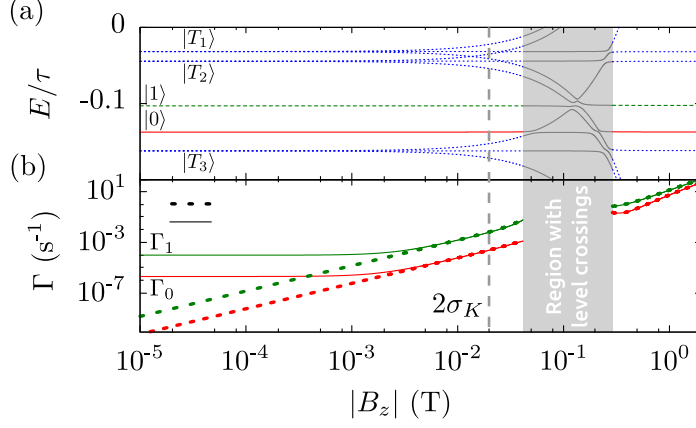
Figure 5.10: (a) Energy spectrum of the system as a function of an external magnetic field at a random point in the parameter space: $\epsilon_{14} = 0$, $\epsilon_{23} = -100\,\mu\text{eV} = -0.125U$, with $U = 800\,\mu\text{eV}$, $U_c = 0.3U$, $t_{12} = t_{24} = 24\,\mu\text{eV}$, $t_{23} = 16\,\mu\text{eV}$ and $\chi = 0$. A qubit can be defined wherever there is a significant level splitting that allows us to distinguish two states with total spin $S = 0$ (solid red and dashed green lines). In (b) the relaxation rates are calculated at the same point as a function of the external magnetic field. We show the rates from the state $|1\rangle$ (green) and $|0\rangle$ (red) calculated via an exact diagonalization of the Hamiltonian $H_{\text{Hubbard}} + H_{\text{SO}}$ (solid lines) and using H_{SO} as a perturbation (dashed lines). In both cases the hyperfine interaction is not considered, but we show the expected largest magnitude of the effective nuclear fields with the vertical dashed gray line.

quantum dots—since the nuclear spin noise is assumed to be Gaussian, about 95% of the measurements of the random fields will yield a field smaller than $2\sigma_K$.

For small or zero magnetic fields these relaxation rates are negligible, and what will determine the coherence time of the exchange-only singlet-only spin qubit is the dephasing due to electric noise and the qubit relaxation via the electron-phonon coupling. Note, nevertheless, that at the SS, at the center of the CSD in Fig. 5.3, any relaxation process involving an electron-phonon interaction cancels (to lowest order in Fermi's golden rule, treating the electron-phonon interaction as a perturbation) because of the isotropic symmetry of the charge stability diagram.

5.4.2   Virtual orbital excitation

The effective mass of electrons in Si is larger than in GaAs and, therefore, the energy splitting $E_{\mathrm{orb}} = \hbar^2/(m^*\sigma_0^2)$ in Si is much smaller than in GaAs for two quantum dots of the same size. In order to tune a quantum-dot-based qubit into the spin blockade regime one then has to make the quantum dots in silicon smaller, but this can result in quantum dots with an orbital splitting smaller than in GaAs [10]. In this section we will assume that the orbital splitting is seizable and we will therefore consider the possibility that an electron in a Si-based quantum dot can virtually excite an orbital level during the qubit operation. Nevertheless, because of the smaller effective electron mass in GaAs and also the weaker SO interaction in this semiconductor, we will not consider this possibility for the XO singlet-only spin qubit.

Under the same assumptions as before we evaluate the relaxation rates out of the qubit subspace for the triple-dot XO qubit:

$$\Gamma_1 \approx \frac{1}{4\pi} \frac{E_Z^4}{E_{\mathrm{orb}}^4} \frac{\Xi_u^2 E_Z^3}{\hbar^4 v_t^5 \rho} f_1^{\mathrm{orb}} \left(\frac{dE_Z}{\hbar v_t} \right), \tag{5.22}$$

$$\Gamma_0 \approx \frac{1}{12\pi} \frac{E_Z^4}{E_{\mathrm{orb}}^4} \frac{\Xi_u^2 E_Z^3}{\hbar^4 v_t^5 \rho} f_0^{\mathrm{orb}} \left(\frac{dE_Z}{\hbar v_t} \right), \tag{5.23}$$

where the dimensionless functions $f_{1,0}^{\mathrm{orb}}(x)$ are, again, in Appendix C. The first thing that we notice is that these rates come with large powers of E_Z/E_{orb} instead of the powers of τ/Δ_3 that we see in the exchange-enabled rates. For typical device parameters these rates are thus much smaller. We can again expand the functions $f_{1,0}^{\mathrm{orb}}(x)$ and obtain a simplified expression for the rates:

$$\Gamma_1 \approx \frac{2}{315\pi} \frac{3A_{xx}^2 + A_{yx}^2}{v_t^2} \frac{E_Z^4}{E_{\mathrm{orb}}^4} \frac{d^2 \Xi_u^2 E_Z^5}{\hbar^6 v_t^7 \rho}, \tag{5.24}$$

$$\Gamma_0 \approx \frac{2}{10395\pi} \frac{5A_{xx}^2 + A_{yx}^2}{v_t^2} \frac{E_Z^4}{E_{\mathrm{orb}}^4} \frac{d^4 \Xi_u^2 E_Z^7}{\hbar^8 v_t^9 \rho}. \tag{5.25}$$

Note that these "orbital-assisted" rates do not depend on any of the detuning parameters, and thus survive at the SS, as opposed to those in Eqns. (5.19, 5.20). Also, in this case Γ_1 is larger than Γ_0 by $(dE_Z/\hbar v_t)^{-2}$, opposite to the exchange-enabled rates from above.

5.4.3 Virtual valley excitation

Similarly, the valley-enabled relaxation rates are only calculated for the Si-based qubit. Proceeding as we described in Chapter 2 we find

$$\Gamma_1 \approx \frac{1}{\pi} \frac{A^2}{v_t^2} \frac{|r_d|^4}{l_Z^4} \frac{E_Z^2}{E_v^2} \frac{\Xi_u^2 E_Z^3}{\hbar^4 v_t^5 \rho} f_1^{\text{val}} \left(\frac{dE_Z}{\hbar v_t} \right), \qquad (5.26)$$

$$\Gamma_0 \approx \frac{1}{3\pi} \frac{A^2}{v_t^2} \frac{|r_d|^4}{l_Z^4} \frac{E_Z^2}{E_v^2} \frac{\Xi_u^2 E_Z^3}{\hbar^4 v_t^5 \rho} f_0^{\text{val}} \left(\frac{dE_Z}{\hbar v_t} \right), \qquad (5.27)$$

where E_v denotes the splitting between the two valley states and we introduced the Zeeman length $l_Z = \hbar/\sqrt{m^* E_Z}$. The strength of the SO interaction is given by $A \sim \alpha, \beta$ (see Section 2.5.2). We again make use of two dimensionless functions $f_{1,0}^{\text{val}}(x)$, given in Appendix C, and expanded them in small x (small $E_Z^2 \ll (\hbar v_t/d)^2$), giving

$$\Gamma_1 \approx \frac{32}{315\pi} \frac{A^2}{v_t^2} \frac{|r_d|^4}{l_Z^4} \frac{E_Z^2}{E_v^2} \frac{d^2 \Xi_u^2 E_Z^5}{\hbar^6 v_t^7 \rho}, \qquad (5.28)$$

$$\Gamma_0 \approx \frac{16}{3465\pi} \frac{A^2}{v_t^2} \frac{|r_d|^4}{l_Z^4} \frac{E_Z^2}{E_v^2} \frac{d^4 \Xi_u^2 E_Z^7}{\hbar^8 v_t^9 \rho}. \qquad (5.29)$$

We find again that the rates do not depend on any of the detuning parameters, and thus survive at the SS. Comparing all the expressions, we see that the valley-assisted rates are typically smaller than the orbital-assisted ones by a factor $\sim |r_d|^4 E_{\text{orb}}^2/(\sigma_0^4 E_v^2)$, given that $|r_d| \sim 1$–2 nm and $\sigma_0 \sim 10$–30 nm.

Even though both orbital- and valley-enabled relaxation rates are constant throughout the whole (1,1,1) charge region, and thus surviving at the SS, the electron-phonon coupling, the electric noise and the hyperfine noise are the dominant mechanisms of decoherence (albeit weak) at this point. The SO interaction at the SS should thus not be a concern.

<div style="text-align: right; font-size: 4em; color: #999;">6</div>

Electric dipole spin resonance

In this chapter we study in full theoretical detail many of the features observed in the results of an electric dipole spin resonance experiment that, up to date, are still unexplained. A paper with the contents of this chapter is now in preparation.

In the previous chapters we have studied many aspects of the physics of quantum dot-based spin qubits, but here we will instead focus on one of the fundamental aspects needed to consider *before* setting up a spin qubit: the characterization of the quantum dots. In a system with quantum dots within the few-electron regime, as is the case for the systems that we have studied so far, spectroscopy of the dots is usually carried out via electric dipole spin resonance (EDSR) [54, 85–94]. However, despite being a widely used tool, there are still many features in the outcome of an EDSR experiment that still lack a thorough theoretical description.

We will thus investigate a common implementation of an EDSR experiment, consisting of two quantum dots, tunnel coupled, in a material with a strong SO coupling. The quantum dots are also coupled to external source and drain leads, as it is schematically depicted in Fig. 6.1(a). A voltage bias between the dots allows for a current through the system. The dots are then tuned into the spin blockade regime, allowing electrons
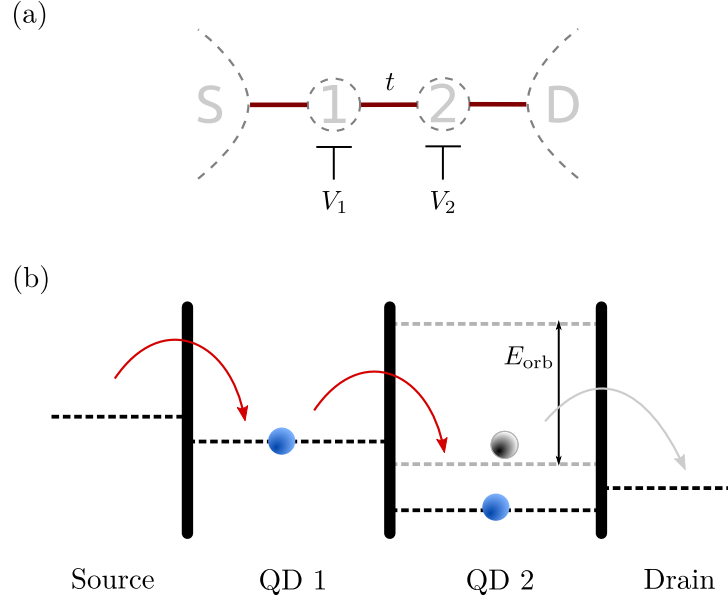
(a)

(b)

Figure 6.1:   (a) The system is composed of two quantum dots, tunnel coupled. The dots are also coupled to external source (S) and drain (D) leads. Two metallic gates control the electrochemical potentials V_1 and V_2 in the dots. (b) Electrons flow from the source to the drain leads. When only one electron occupies the second quantum dot, the chemical potential on the dot is not enough to let the electron tunnel to the drain lead. When a second electron enters the system it can tunnel from the first to the second dot only if both electrons occupy the lowest orbital state, and thus are paired in a singlet state. Then one of the electrons can tunnel to the drain lead.

to tunnel out of the system only if the spin selection rules set by the interplay between the spin blockade and the SO coupling allow it. That is, only when the dot closest to the drain lead can be occupied by two electrons in the lowest electronic orbital in a singlet state [see Fig. 6.1(b)]. Therefore, when tunneling is not allowed the current is blocked. To come out of the blockade, a periodically oscillating electric field is applied to the quantum dots through detuning of V_2. This external drive does not couple directly to the spin of the electrons, but the interplay between the oscillating potential and the SO coupling can induce spin rotations (as we saw in Chapters 2 and 5). These spin flips occur whenever the frequency of the

driving is in resonance with the level splitting of different spin states, set up, in this case, by a Zeeman splitting. This resonant response can thus lift the spin blockade and give rise to an increase in the current through the double dot. Since this increase of the current occurs when the drive frequency is at resonance with the Zeeman splitting, a measurement of the resonance frequency as a function of the magnetic field will thus yield the effective *g*-factor of the electron that couples to the driving.

In the following, we identify the different spin-orbit-mediated spin mixing mechanisms that could play a role in an EDSR experiment. We investigate the resulting differences in the shape of the resonances as they appear in the current as a function of the drive frequency.

6.1 The model of the system

We model the subsystem formed by the two tunnel-coupled quantum dots with the Hubbard-like Hamiltonian that we saw in the previous chapters:

$$H_{\text{Hubb}} = \sum_i \left[\frac{U}{2} \, n_i(n_i - 1) - V_i \, n_i \right] + \sum_{\langle i,j \rangle} U_c \, n_i n_j$$
$$- \sum_{\langle i,j \rangle, \alpha} \frac{t_{ij}}{\sqrt{2}} \, c^\dagger_{i,\alpha} c_{j,\alpha} + \sum_{i,\alpha,\beta} \frac{1}{2} g_i \mu_B \, c^\dagger_{i,\alpha} (\mathbf{B} \cdot \boldsymbol{\sigma})_{\alpha\beta} \, c_{i,\beta}, \quad (6.1)$$

with the last line describing a spin-conserving tunneling and the coupling of the spin of the electrons to an external magnetic field, with a different g-factor g_i for each dot. The difference in the g factors across dots is due to the strong SO coupling in the material. For simplicity we will consider this field to be in-plane. The SO interaction gives rise to an effective spin-flip tunnel coupling t_{so} between the states in the (1,1) charge region and the states in other charge configurations, given by [16, 95]

$$t_{\text{so}}^{(x,y,z)} = \frac{i \, d \, t_{12}}{l_{\text{so}}^{(x,y,z)}}, \quad (6.2)$$

where d is the distance between the quantum dots and $l_{\text{so}}^{(x,y,z)}$ is the relevant SO length, as defined in Chapter 5 (see also Ref. [95]). The quantum dots are initially occupied by two electrons in the charge configuration (1,1). A tilt in the electrochemical potential in the dots $V_2 - V_1 > 0$ results in the transition $(1,1) \rightarrow (0,2)$ if the two electrons can occupy the lowest electronic orbital of the quantum dot in the right, forming a singlet

state. A further bias voltage between the source and drain leads allows the transition $(0,2) \to (0,1)$, and this then produces a measurable current. The system is then subsequently refilled into the state (1,1), by an addition of one electron coming from the source lead. With this picture in mind it is clear that we only need to consider the (1,1) spin states $|\uparrow\uparrow\rangle$, $|\uparrow\downarrow\rangle$, $|\downarrow\uparrow\rangle$, $|\downarrow\downarrow\rangle$ and the (0,2) singlet state $|S_{02}\rangle$. In the basis set by these five states, and with a magnetic field along the z direction only, the Hubbard Hamiltonian reads

$$
H_5 = \begin{pmatrix}
g\mu_{\mathrm{B}}B_z & 0 & 0 & 0 & t_1 \\
0 & \delta g\mu_{\mathrm{B}}B_z & 0 & 0 & t_2 \\
0 & 0 & -\delta g\mu_{\mathrm{B}}B_z & 0 & t_2^* \\
0 & 0 & 0 & -g\mu_{\mathrm{B}}B_z & t_1^* \\
t_1^* & t_2^* & t_2 & t_1 & -E_{02}
\end{pmatrix}.
\tag{6.3}
$$

In order to arrive to this expression we have set the energy of the five states in the (1,1) region to 0 and we used $g \equiv (g_1 + g_2)/2$ and $\delta g \equiv (g_1 - g_2)/2$. The coupling elements t_1 and t_2 (and their complex conjugate t_1^* and t_2^*) now account for both tunneling and SO coupling:

$$
t_1 = \frac{t_{12} + t_{\mathrm{so}}^{(z)}}{\sqrt{2}}, \qquad\qquad t_2 = t_{\mathrm{so}}^{(x)} - it_{\mathrm{so}}^{(y)}.
\tag{6.4}
$$

The electrostatic energy difference between the first four states and the state $|S_{02}\rangle$ is $E_{02} = V_2 - V_1 - U + U_c > 0$. We model the source and drain leads as a bath of electrons that couples to the quantum dots via an escape rate Γ out of the state $|S_{02}\rangle$. Additionally, the other four (1,1) states are refilled with equal probability with the same state Γ as soon as one of the electrons leaves the system into the drain lead.

At zero magnetic field, where the first four states are degenerate, one can always find a different basis where the Hamiltonian H_5 takes the form

$$
\tilde{H}_5 = \begin{pmatrix}
0 & 0 & 0 & 0 & 0 \\
0 & 0 & 0 & 0 & 0 \\
0 & 0 & 0 & 0 & 0 \\
0 & 0 & 0 & 0 & \sqrt{2}\,\tau \\
0 & 0 & 0 & \sqrt{2}\,\tau & -E_{02}
\end{pmatrix},
\tag{6.5}
$$

with $\tau = \sqrt{|t_1|^2 + |t_2|^2}$. In this situation, if the two electrons that occupy the dots in the charge configuration (1,1) form a state that is not coupled to $|S_{02}\rangle$ (a *dark* state), the current will be blocked. On the other hand,

if the only (*bright*) state that couples to $|S_{02}\rangle$ is occupied, a current can be measured and the whole process can start again. As the magnetic field is increased, the different spin states split out and we can no longer write the Hamiltonian in this form. More bright states will appear and thus the probability of having a blocked current will be smaller.

Adding an external driving changes substantially the dynamics of the system. When the driving is applied as a periodic detuning of one of the on-site gate offsets, this effectively produces an oscillating exchange coupling, via t_1 and t_2, inside the (1,1) subspace that results in spin rotations. Additionally, the periodic change in the potential landscape in the quantum dots results in a periodic change of the wave functions of both localized electrons. The SO interaction then translates this change in the wave functions into a periodic effective magnetic field coupling to the spin of the electrons [86–88, 91]. We thus need to consider the effects of (*i*) an electric driving in the on-site potentials and (*ii*) a driving through a magnetic field.

When the electrons are in a dark state, a periodic detuning of the offset potentials will help the system out of the blockade. With a driving of the form $E_{02}(t) = E_0 + A\cos(\omega t)$, a small amplitude around zero detuning can induce coherent Rabi oscillations when the system is driven at resonance [86]. We have seen this behavior in the previous chapters. For large amplitudes, of the order of $A \sim \hbar\omega$, the coherent oscillations are then suppressed. We then observe resonances at different harmonics in the form of peaks or dips in the current profile as a function of the driving frequency or the magnitude of the Zeeman splitting [91].

With our model we want to reproduce both behaviors but also study the intermediate case, when we have an intermediate amplitude and the system is driven far from zero detuning. We therefore consider a time dependence into E_{02} but also in the magnetic field **B** arising from the strong SO couplings.

An analytical investigation of such a complex system is not easy, but our model can be further simplified: The systems that we want to study are typically characterized by having substantially different effective g-factors on each quantum dot [86–88, 91]. In this case the different energy levels are well separated and we can therefore study each of the resonances independently. We can thus reduce the dimensionality of the system from a 5×5 Hamiltonian to a 3×3 Hamiltonian where the only three levels that need to be considered are the two (1,1) spin states that are at resonance and the *escape* state $|S_{02}\rangle$ [85, 91, 96, 97]. We thus make our

analysis valid for the four subspaces $\{|\uparrow\uparrow\rangle, |\uparrow\downarrow\rangle, |S_{02}\rangle\}$, $\{|\uparrow\downarrow\rangle, |\downarrow\downarrow\rangle, |S_{02}\rangle\}$, $\{|\uparrow\uparrow\rangle, |\downarrow\uparrow\rangle, |S_{02}\rangle\}$, and $\{|\downarrow\uparrow\rangle, |\downarrow\downarrow\rangle, |S_{02}\rangle\}$. For simplicity, we will further restrict our analytic investigations to the first harmonic, i.e., where the driving frequency matches the Zeeman splitting on one of the two dots, $\hbar\omega \approx g_{1,2}\,\mu_{\mathrm{B}}B$.

6.2 Resonances

We study the different forms of driving separately, focusing on the resulting shape of the 1-photon resonance in the current (the first harmonic). In all cases the 3×3 Hamiltonian that we consider takes the form

$$H_3^{(\alpha)} = \begin{pmatrix} B & 0 & q_1 \\ 0 & -B & q_2 \\ q_1^* & q_2^* & -E_0 \end{pmatrix} + A\,\cos(\omega t)\,V_{\mathrm{drive}}^{(\alpha)}, \qquad (6.6)$$

where the parameters B, q_1 and q_2 that we have introduced in this Hamiltonian will be different for each of the subspaces that we consider. Let us anticipate, though, that in all the following results the couplings q_i will always appear as $|q_i|^2$. In order to simplify further the notation we thus take them as real. Regarding the energy B, here we use $B = g_i\mu_{\mathrm{B}}B_z/2$, where g_i corresponds to the electron that couples to the driving and thus undergoes a spin flip.

The external driving enters into the Hamiltonian via the matrix $V_{\mathrm{drive}}^{(\alpha)}$, where $\alpha \in \{\mathrm{d}, \mathrm{z}, \mathrm{x}\}$ indicates driving of the detuning, via B_z or via B_x, respectively,

$$V_{\mathrm{drive}}^{(\mathrm{d})} = \begin{pmatrix} 0 & 0 & 0 \\ 0 & 0 & 0 \\ 0 & 0 & 1 \end{pmatrix}, \qquad (6.7)$$

$$V_{\mathrm{drive}}^{(\mathrm{z})} = \begin{pmatrix} 1 & 0 & 0 \\ 0 & -1 & 0 \\ 0 & 0 & 0 \end{pmatrix}, \qquad (6.8)$$

$$V_{\mathrm{drive}}^{(\mathrm{x})} = \begin{pmatrix} 0 & 1 & 0 \\ 1 & 0 & 0 \\ 0 & 0 & 0 \end{pmatrix}, \qquad (6.9)$$

for the three mechanisms mentioned above.

6.2.1 Driving of the detuning

We have mentioned before that the current through the quantum dots is only possible when the electrons can occupy the state $|S_{02}\rangle$. Indeed, the current will be given by $I = \Gamma p_s$, with p_s being the probability of finding the system in the state $|S_{02}\rangle$, and Γ is the escape rate from the state $|S_{02}\rangle$ into the drain lead. If we set up a master equation of the form

$$\frac{d\rho}{dt} = -\frac{i}{\hbar}\left[\tilde{H}(t),\rho\right], \qquad (6.10)$$

for a density matrix ρ and some Hamiltonian $\tilde{H}(t)$ that accounts for both the quantum dots subsystem and the external source and drain leads, then we can obtain the current by evaluating the element of the density matrix $\rho_{ss} = |S_{02}\rangle\langle S_{02}|$.

We are interested in a steady state solution of this master equation. To find this solution with a time-dependent Hamiltonian we consider two options: (i) we expand the master equation in Fourier modes and find the solution that corresponds to the zeroth mode, which will give us the time-averaged ρ_{ss}; or (ii) we first evaluate the transition rates Γ_{ij} from all the states $|i\rangle \rightarrow |j\rangle$ using the time-dependent Fermi's golden rule and then set up a classical master equation and find a steady state solution.

For the case where the driving is in the detuning we opt for the latter. Upon imposing the normalization condition on the probabilities $p_1 + p_2 + p_s = 1$, the master equation yields the set of equations

$$\begin{cases} \Gamma_{21}p_2 + \Gamma p_s/2 - (\Gamma_{12} + \Gamma_{1s})p_1 = 0 \\ \Gamma_{12}p_1 + \Gamma p_s/2 - (\Gamma_{21} + \Gamma_{2s})p_2 = 0 \\ p_1 + p_2 + p_s = 1 \end{cases}, \qquad (6.11)$$

where p_i is the probability of measuring the system in the state $|i\rangle$, with $|i\rangle$ one of the three states of the subspaces that we consider. The current is then

$$I = \Gamma p_s = \frac{2\Gamma(\Gamma_{1s}\Gamma_{2s} + \Gamma_{12}(\Gamma_{1s} + \Gamma_{2s}))}{2\Gamma_{1s}\Gamma_{2s} + 2\Gamma_{12}(\Gamma_{1s} + \Gamma_{2s}) + \Gamma(4\Gamma_{12} + \Gamma_{1s} + \Gamma_{2s})}. \qquad (6.12)$$

For the evaluation of the rates Γ_{ij}, using the time-dependent Fermi's golden rule, see Appendix B, where we proceed as in Ref. [96]. We thus

obtain the rates (setting $\hbar = 1$ and using $\Gamma \gg A$)

$$
\Gamma_{12} = \frac{q_1^2 q_2^2}{\left((B + E_0)^2 + (\gamma + \Gamma)^2/4\right)\left((B - E_0)^2 + (\gamma + \Gamma)^2/4\right)}
$$
$$
\times \left(\frac{(\gamma + \Gamma)^2}{\Gamma} + \frac{\gamma\left(E_0^2 + (\gamma + \Gamma)^2/4\right)}{4B^2 + \gamma^2} + \frac{A^2\gamma}{2((2B - \omega)^2 + \gamma^2)}\right), \quad (6.13)
$$

$$
\Gamma_{1s} = \frac{(\gamma + \Gamma)q_1^4}{(B + E_0)^2 + (\gamma + \Gamma)^2/4} - \frac{4BE_0(\gamma + \Gamma)q_1^2 q_2^2}{(4B^2 + \gamma^2)\left(E_0^2 + (\gamma + \Gamma)^2/4\right)^2}
$$
$$
+ \frac{\gamma(\gamma + \Gamma)^2 q_1^2 q_2^2}{(4B^2 + \gamma^2)\left(E_0^2 + (\gamma + \Gamma)^2/4\right)^2}
$$
$$
- \frac{E_0^2 A^2 \gamma(\gamma + \Gamma)^2 q_1^2 q_2^2}{((2B - \omega)^2 + \gamma^2)\left(E_0^2 + (\gamma + \Gamma)^2/4\right)^4}
$$
$$
+ \frac{E_0 A^2 (\gamma + \Gamma)\left(E_0^2 + (\gamma + \Gamma)^2/4\right)(2B - \omega)q_1^2 q_2^2}{((2B - \omega)^2 + \gamma^2)\left(E_0^2 + (\gamma + \Gamma)^2/4\right)^4}, \quad (6.14)
$$

and a similar rate for Γ_{2s}. Additionally we found $\Gamma_{21} = \Gamma_{12}$. In these expressions we introduced γ, an effective, exchange-enabled escape rate from the states in (1,1) into the drain leads, defined as

$$
\gamma = \frac{1}{2}\left(\frac{\Gamma q_1^2}{(B + E_0)^2 + \Gamma^2/4} + \frac{\Gamma q_2^2}{(B - E_0)^2 + \Gamma^2/4}\right). \quad (6.15)
$$

Putting all together, and after some approximations that amount to assume $E_0 \gg B$ and $\Gamma \gg A$, we obtain the current

$$
I \approx 2\gamma\left(\frac{2q_1 q_2}{q_1^2 + q_2^2}\right)^2
$$
$$
+ \left(\frac{2q_1 q_2}{q_1^2 + q_2^2}\right)^2 \frac{8\gamma A^2}{[4E_0^2 + \Gamma^2]^2} \frac{(q_1^2 - q_2^2)^2 - 2\Gamma^2(\epsilon_1^2 + \epsilon_2^2)}{4\gamma^2 + \frac{16A^2}{[4E_0^2 + \Gamma^2]^2}\left(\frac{4E_0^2 - \Gamma^2}{4E_0^2 + \Gamma^2}\right)^2 q_1^2 q_2^2 + \delta^2}
$$
$$
+ \left(\frac{2q_1 q_2}{q_1^2 + q_2^2}\right)^2 \frac{8\gamma A^2}{[4E_0^2 + \Gamma^2]^2} \frac{(4E_0^2 - \Gamma^2)(\epsilon_1 - \epsilon_2)\delta}{4\gamma^2 + \frac{16A^2}{[4E_0^2 + \Gamma^2]^2}\left(\frac{4E_0^2 - \Gamma^2}{4E_0^2 + \Gamma^2}\right)^2 q_1^2 q_2^2 + \delta^2}. \quad (6.16)
$$

The first line describes the background current. This is the current that we would observe in absence of a driving, when $A \to 0$. In the next two terms we describe the exchange-induced level shift with $\epsilon_{1,2}$, given by

$$
\epsilon_{1,2} = \frac{4E_{02}q_{1,2}^2}{4E_{02}^2 + \Gamma^2}. \quad (6.17)
$$

We also characterize the detuning from the 1-photon resonance as

$$\delta = 2B - \omega. \tag{6.18}$$

The second line in Eq. (6.16) describes a peak or dip in the current. For typical parameters ($q_1, q_2 \ll \Gamma, E_0$ and $\Gamma > E_0$) the sign of this term is negative and it results in a dip in the current. As the energy $E_0 \to 0$ the dip will become a peak. Note that this term resembles a Lorentzian curve. Indeed the peak/dip has a maximum/minimum at $\delta = 0$, which corresponds to $\omega = 2B$, and a width given mostly by γ when the driving amplitude is small. We can observe all these features in Fig. 6.2, where we further compare the analytical findings with numerical results.

The last term accounts for an asymmetry in the shape of the peak or dip. This term is also Lorentzian-like but it comes with a factor of δ on the numerator. For equal couplings $q_1 = q_2$ (equivalent to $\epsilon_1 = \epsilon_2$), that is for a transition from $|\uparrow\uparrow\rangle$ to $|\downarrow\downarrow\rangle$ or from $|\uparrow\downarrow\rangle$ to $|\downarrow\uparrow\rangle$, this term vanishes, but for the four other cases that we are interested in, this last term tilts substantially the current around the peak and makes it asymmetric. The sign of this tilting depends on the sign of $q_1^2 - q_2^2$ via $\epsilon_1 - \epsilon_2$.

Note that the peak or dip will always occur at $\delta = 0$, that is, for $\omega \simeq 2B = g_i \mu_B B_z$. It is then possible, in an EDSR experiment, to measure and distinguish two different g-factors in two quantum dots: The current profile as a function of the magnetic field and the driving frequency will show a line (a peak or a dip) with two different slopes.

6.2.2 Driving via a magnetic field

Since the oscillations in the magnetic field are expected to be a consequence of the driving in the detuning we expect the amplitude of this driving to be small compared to the amplitude that we considered previously. Here we will thus investigate the current profile for a driving via a magnetic field, both along the z and x directions, with a driving amplitude $A \ll B$.

Driving via B_z

The current profile for a driving via a magnetic field can be obtained in a simpler way. We describe the time evolution of the system with a Lindblad master equation and find a steady-state solution by expanding the master equation in Fourier modes. Setting again $\hbar = 1$, the Lindblad master
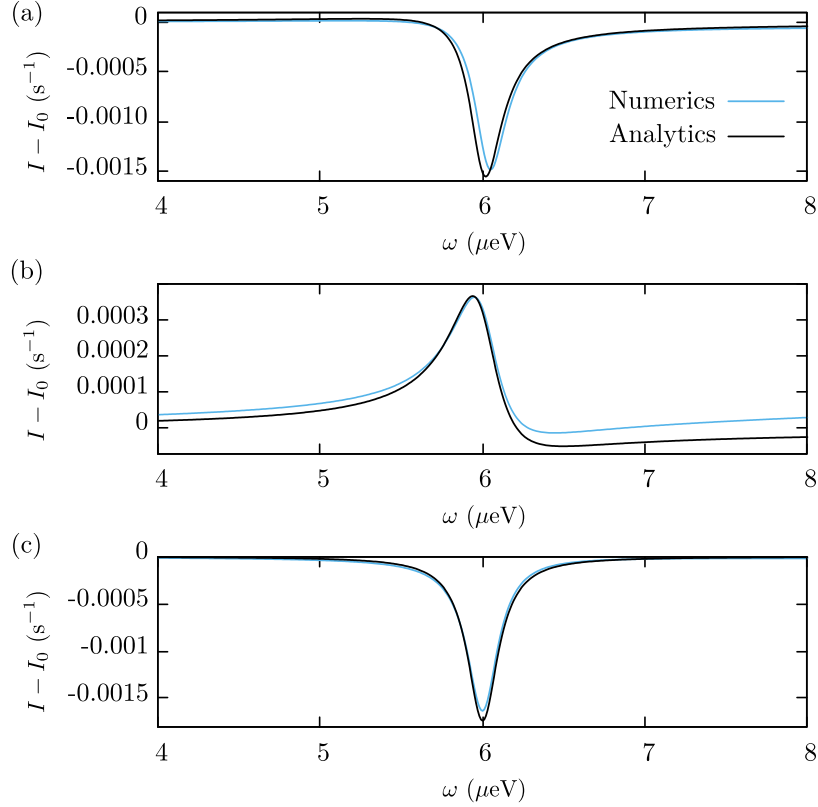
Figure 6.2:   Current profile as a function of the frequency when the driving is via the detuning. We subtracted an offset for clarity. Blue lines show the analytical results from Eq. (6.16). Black lines show the numerical results. (a) For large $E_0 \gg A$ we always observe a dip in the current. If, additionally, the couplings q_1 and q_2 are different, the dip in the current is asymmetric. (b) As $E_0 \to 0$ the dip becomes a peak instead. (c) For equal couplings $q_1 = q_2$, the dip is symmetric. In all cases we focus on the 1-photon resonances. In (a) we used $E_0 = 50\,\mu\text{eV}$, $q_1 = 3\,\mu\text{eV}$ and $q_2 = 2\,\mu\text{eV}$; for (b) we used $E_0 = 5\,\mu\text{eV}$, and the same q_1 and q_2; in (c) we used $E_0 = 50\,\mu\text{eV}$ and $q_1 = q_2 = 2.5\,\mu\text{eV}$. For the remaining parameters we used $A = 20\,\mu\text{eV}$, $\Gamma = 150\,\mu\text{eV}$ and $B = 3\,\mu\text{eV}$, together with $\hbar = 1$.

equation for the system that we consider in this section reads

$$
\frac{d\rho}{dt} = -i[H_3^{(z)}, \rho] + \frac{1}{2}\Gamma \begin{pmatrix} \rho_{ss} & 0 & -\rho_{1s} \\ 0 & \rho_{ss} & -\rho_{2s} \\ -\rho_{s1} & -\rho_{s2} & -2\rho_{ss} \end{pmatrix}, \qquad (6.19)
$$

where we included decay of the state $|S_{02}\rangle$ to the drain lead with rate Γ, and assumed that immediately after such a decay process the system is initialized again in one of the (1,1) states, as we discussed before.

Since now Γ is, by far, the largest energy scale of the system we can separate time scales and assume that all dynamics induced by Γ reach (quasi-)equilibrium instantaneously on the time scale of the rest of the dynamics. We will then have a subsystem formed by the first 2×2 block of the master equation, with slow dynamics; and another subsystem, described by the escape state $|S_{02}\rangle$ and its coupling to the other two sates, with fast dynamics. Under this assumption we can focus on the dynamics of the (1,1) subspace. We first find a steady-state solution of the Lindblad equation as a function of the matrix elements in the (1,1) subspace (the first 2×2 block). Since the time dependence is included only in this block, and we assumed the dynamics of this block to be very slow compared to the time scale of the dynamics of ρ_{ss}, we can take the matrix elements in the (1,1) subspace as constant.

We thus obtain the matrix elements ρ_{1s}, ρ_{2s}, ρ_{s1}, ρ_{s2} and ρ_{ss} as a function of the matrix elements of the first block, ρ_{11}, ρ_{12}, ρ_{21} and ρ_{22}. With this we can write a reduced master equation for the first block only. If we "vectorize" this expression [1] the resulting master equation reads

$$
\frac{d\rho^{(2)}}{dt} = \begin{pmatrix} -\frac{2\Gamma q_1^2}{4E_0^2+\Gamma^2} & \frac{4iE_0 q_1 q_2}{4E_0^2+\Gamma^2} & -\frac{4iE_0 q_1 q_2}{4E_0^2+\Gamma^2} & \frac{2\Gamma q_2^2}{4E_0^2+\Gamma^2} \\ -\frac{2q_1 q_2}{\Gamma+2iE_0} & \mathcal{B} & 0 & \frac{2q_1 q_2}{-\Gamma+2iE_0} \\ \frac{2q_1 q_2}{-\Gamma+2iE_0} & 0 & \mathcal{B}^* & -\frac{2q_1 q_2}{\Gamma+2iE_0} \\ \frac{2\Gamma q_1^2}{4E_0^2+\Gamma^2} & -\frac{4iE_0 q_1 q_2}{4E_0^2+\Gamma^2} & \frac{4iE_0 q_1 q_2}{4E_0^2+\Gamma^2} & -\frac{2\Gamma q_2^2}{4E_0^2+\Gamma^2} \end{pmatrix} \cdot \begin{pmatrix} \rho_{11} \\ \rho_{12} \\ \rho_{21} \\ \rho_{22} \end{pmatrix},
$$
$$(6.20)$$

with $\mathcal{B} = -2iB(t) + \frac{2q_1^2}{2iE_0-\Gamma} - \frac{2q_2^2}{2iE_0+\Gamma}$. Once we find a solution for this equation we can calculate the current as $I = \Gamma\rho_{ss}$, with the ρ_{ss} as a

---

[1]An equation of the form $A \cdot B = C$, with A, B and C three different $n \times n$ matrices can be written as $\mathcal{A} \cdot \mathbf{b} = \mathbf{c}$, with $\mathcal{A}$ an $n^2 \times n^2$ matrix and $\mathbf{b}$ and $\mathbf{c}$ two vectors of length n^2. Writing a matrix equation in this form allows us to use the tools from linear algebra to solve it.

function of ρ_{11}, ρ_{12}, ρ_{21} and ρ_{22} that we obtained before. However, since the energy $B(t)$ is time-dependent we cannot solve the master equation straightforwardly. We instead expand the density operator and the master equation in Fourier modes using

$$\rho(t) = \sum_{n=-\infty}^{\infty} \rho_n e^{in\omega t}. \tag{6.21}$$

With this transformation, a master equation in the form of Eq. (6.19) transforms as

$$\sum_n e^{in\omega t} \frac{d}{dt} \rho_n = \sum_n \left\{ -i[H_3^{(z)}(t), \rho_n] e^{in\omega t} + \Gamma[\rho_n] e^{in\omega t} - in\omega \rho_n e^{in\omega t} \right\}, \tag{6.22}$$

where $\Gamma[\rho_n]$ is the escape/refill term from Eq. (6.19) now written in terms of the Fourier modes. A similar expression can be found as well for the reduced master equation from Eq. (6.20),

Next we write the detuning as $B(t) = B_0 + A\cos\omega t$, expanding the cosine using exponential functions, $B(t) = B_0 + A(\exp[i\omega t] + \exp[-i\omega t])/2$, and use these exponential functions as the basis states in the Fourier space. This results in a high dimensional master equation matrix with a block structure, where each block corresponds to a Fourier mode. The elements with $\rho_n \exp[in\omega t]$ are in the diagonal blocks, and the elements with $\rho_n \exp[i(n+1)\omega t]$ and $\rho_n \exp[i(n-1)\omega t]$ are in the upper and lower diagonals, coupling the block matrices in the main diagonal.

Numerical simulations guarantee that, for small amplitude $A \lesssim \omega$, expanding the master equation in only the modes $n = 0, \pm 1$ is enough to describe with high accuracy all the features of the current profile around the 1-photon resonance.

After this Fourier expansion, the master equation above becomes a 12-dimensional time-*independent* object, and the steady state solution of the elements of the zeroth Fourier mode, combined with the solution that we found for ρ_{ss} gives the current

$$I \approx 2\gamma \left(\frac{2q_1 q_2}{q_1^2 + q_2^2} \right)^2 \frac{A^2[(\epsilon_1 + \epsilon_2)^2 + 4\gamma^2] + 16B^2\gamma^2 + (A^2 - 2B\delta)^2}{4A^2(\epsilon_1\epsilon_2 + 2\gamma^2) + 16\tilde{B}^2\gamma^2 + (A^2 - 2\tilde{B}\delta)^2}, \tag{6.23}$$

where, again, we have made some simplifications assuming that $B \gg \epsilon_{1,2}, \gamma$. Additionally, to shorten the notation, we have introduced $\tilde{B} = B + (\epsilon_1 - \epsilon_2)/2 = -\text{Im}[\mathcal{B}]/2$.
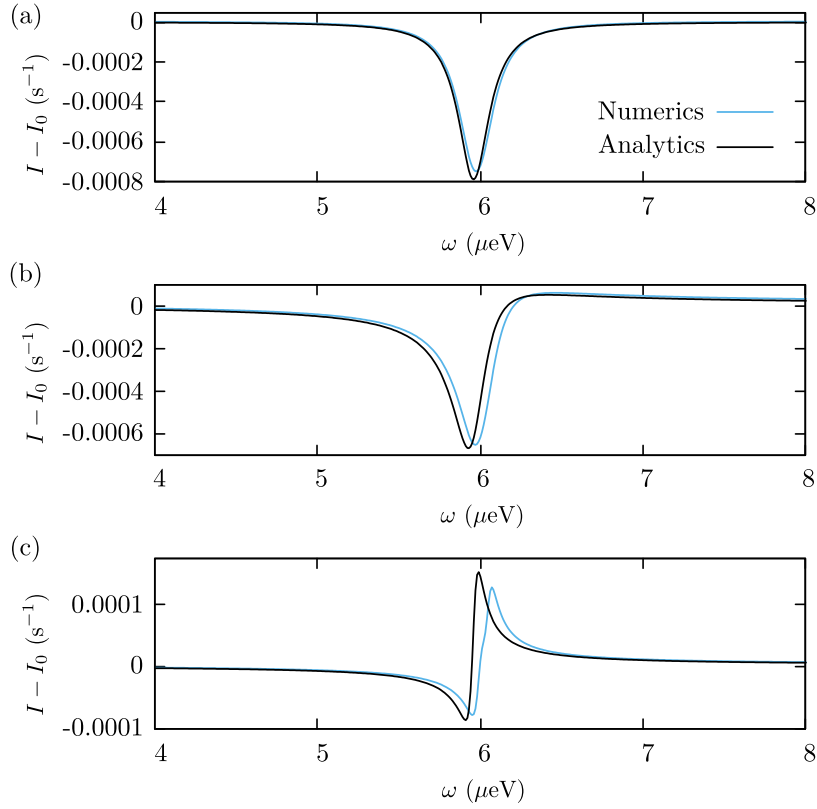
Figure 6.3: Current profile (minus an offset) as a function of the frequency with a SO-mediated driving via B_z. Blue lines show the analytical results from Eq. (6.23), and black lines show the numerical results. (a) For equal couplings $q_1 = q_2 = 2.5\,\mu\text{eV}$ and a moderate-large amplitude $A = 0.5\,\mu\text{eV}$ we observe a symmetric dip in the current. (b) Changing the magnitude of the couplings to $q_1 = 3\,\mu\text{eV}$ and $q_2 = 2\,\mu\text{eV}$ makes the dip asymmetric. (c) For a very large $E_0 = 120\mu\text{eV}$ and very asymmetric couplings $q_1 = 3\,\mu\text{eV}$ and $q_2 = 1\,\mu\text{eV}$, the dip starts a transition towards becoming a peak. The other parameters are the same as before.

In this expression we observe similar features as before. To investigate this let us write the current in a simplified form, by dropping a factor $2\gamma(B^2/\tilde{B}^2)[q_1q_2/(q_1^2+q_2^2)]^2$ and writing the resulting expression as

$$f = \frac{a^2 + (b-\delta)^2}{c^2 + (d-\delta)^2}, \tag{6.24}$$

with the parameters a, b, c and d given by

$$a^2 = \frac{A^2}{4B^2}[(\epsilon_1+\epsilon_2)^2 + 4\gamma^2] + 4\gamma^2 \tag{6.25}$$

$$b = \frac{A^2}{2B} \tag{6.26}$$

$$c^2 = \frac{A^2}{\tilde{B}^2}(\epsilon_1\epsilon_2 + 2\gamma^2) + 4\gamma^2 \tag{6.27}$$

$$d = \frac{A^2}{2\tilde{B}}. \tag{6.28}$$

For any non-zero couplings q_1 and q_2, and finite E_0, the parameters above satisfy $a^2 \lesssim c^2$. Then, depending on the value of each exchange energies, we can have $b = d$ if $q_1 = q_2$, $b > d$ if $q_1 > q_2$ or $b < d$ if $q_1 < q_2$. At resonance, when $\delta = d$, the function f becomes

$$f = \frac{a^2 + \frac{1}{4}(\epsilon_1-\epsilon_2)^2}{c^2}. \tag{6.29}$$

We show in Fig. 6.3 that for equal couplings $q_1 = q_2$, we end up with $f = a^2/c^2 < 0$ and we thus observe a decrease in the current, i.e., a dip. But in the case where $c^2 < a^2 + \frac{1}{4}(\epsilon_1-\epsilon_2)^2$, then we observe a peak. Note also that the term $(b-\delta)^2$ cancels either before or after the resonance point, depending on the sign of $(\epsilon_1-\epsilon_2)$. This produces an asymmetry in the peak/dip similar to the one observed before.

Driving via B_x

We calculate the current profile for a driving via a SO-induced effective magnetic field along the x direction, B_x, in exactly the same way. In this case, we obtain the current

$$I \approx 2\gamma\left(\frac{2q_1q_2}{q_1^2+q_2^2}\right)^2\left(1 + \frac{A^2\left(\frac{q_1^2-q_2^2}{2q_1q_2}\right)^2}{4\gamma^2+\delta^2}\right), \tag{6.30}$$
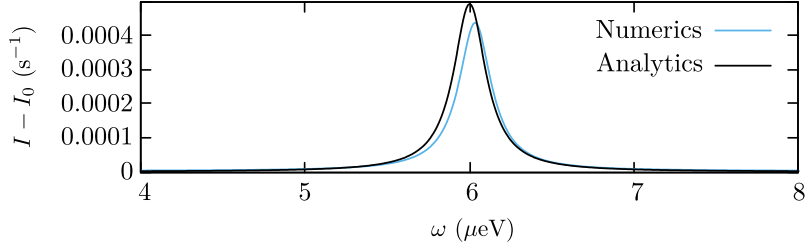
Figure 6.4:   Current as a function of the frequency with a SO-mediated driving via B_x, where we subtracted an offset. The blue line shows the analytical result from Eq. (6.30), and the black line shows the numerical results. For this figure we used a reasonably small amplitude $A = 0.1\,\mu\text{eV}$ and asymmetric couplings $q_1 = 3\,\mu\text{eV}$ and $q_2 = 2\,\mu\text{eV}$. The remaining parameters are the same as before.

which displays only peaks when the system is driven at resonance (see Fig. 6.4). Note also that the peak disappears when the couplings q_1 and q_2 are the same.

6.2.3   A numerical analysis

We study the validity of our expressions with a numerical analysis. For this we find a steady state solution of Eq. (6.22) for all three types of driving. We found that using six Fourier modes (that is, for $n \in [-6, 6]$) the solution converges. Nevertheless, we considered ten modes instead. The results shown in Figs. 6.2, 6.3 and 6.4 show a quite good agreement with the analytical calculations.

A

Schrieffer-Wolff transformation

A Schrieffer-Wolff transformation is a unitary transformation that is often used to diagonalize a Hamiltonian of the form $H_0 + \lambda V$ perturbatively, treating the term with λV as the perturbation. This transformation is particularly useful when the Hamiltonian has a block structure, as is the case in the Hubbard-like Hamiltonians that we have seen in this thesis, and some of the eigenvalues of the unpetrurbed Hamiltonian H_0 are degenerate.

One usually starts with a Hamiltonian $H = H_0 + \lambda V$, where H_0 is a diagonal Hamiltonian of the form

$$H_0 = \begin{pmatrix} H_1 & 0 \\ 0 & H_2 \end{pmatrix}, \tag{A.1}$$

where H_1 and H_2 can be degenerate but the eigenenergies $E_1^{(i)}$ of H_1 must, in general, differ from the eigenenergies $E_2^{(i)}$ of H_2. The perturbation V, with $\lambda \ll |E_1^{(i)} - E_2^{(j)}|$, then couples the blocks of H_0:

$$V = \begin{pmatrix} 0 & V_{12} \\ V_{21} & 0 \end{pmatrix}. \tag{A.2}$$

We can diagonalize the Hamiltonian H with the unitary operator $U = e^{S(\lambda)}$, for some operator $S(\lambda)$, using $H' = e^{S(\lambda)}He^{-S(\lambda)}$.

Suppose now that we want to find the eigenvalues of H up to $\mathcal{O}(\lambda^2)$ while, at the same time, decoupling the blocks H_1 and H_2 from H up to order $\mathcal{O}(\lambda^2)$. For this we can expand the operator $S(\lambda)$ in powers of λ:

$$S(\lambda) = \sum_{n=0}^{\infty} \lambda^n S_n. \tag{A.3}$$

For $\lambda = 0$ the Hamiltonian is already diagonal, therefore the unitary transformation should read $H_0 = e^{S_0}H_0e^{-S_0}$. We thus choose $S_0 = 0$. Since we want to find an expansion to order $\mathcal{O}(\lambda^2)$, we can use $S(\lambda) = \lambda S_1$.

Next we perform a series expansion on the transformed Hamiltonian H' for small λ around $\lambda = 0$. For this we use the Baker-Campbell-Hausdorff formula and write

$$\begin{aligned}
H' &= e^{\lambda S_1}(H_0 + \lambda V)e^{-\lambda S_1} \\
&= H_0 + \lambda V + \lambda\,[S_1, H_0 + \lambda V] + \frac{\lambda^2}{2}\,[S_1, [S_1, H_0 + \lambda V]] + \mathcal{O}(\lambda^3) \\
&\approx H_0 + \lambda\,(V + [S_1, H_0]) + \lambda^2\left([S_1, V] + \frac{1}{2}\,[S_1, [S_1, H_0]]\right). \quad\text{(A.4)}
\end{aligned}$$

Recall that we want to uncouple the blocks H_1 and H_2 from the Hamiltonian to lowest order in λ. This amounts to find an operator S_1 that leaves only even powers of λ in the transformed Hamiltonian H'. We can then find the operator S_1 by solving the equation $V + [S_1, H_0] = 0$. This yields the effective Hamiltonian

$$H_{\text{eff}} = H_0 + \frac{\lambda^2}{2}\,[S_1, V]. \tag{A.5}$$

This Hamiltonian has a block structure

$$H_{\text{eff}} = \begin{pmatrix} \tilde{H}_1 & 0 \\ 0 & \tilde{H}_2 \end{pmatrix}, \tag{A.6}$$

where now $\tilde{H}_1$ and $\tilde{H}_2$ are not necessarily diagonal but the two blocks are decoupled and we can treat them independently.

It is very common to encounter this perturbation expansion in many publications, and indeed this is the perturbation expansion that we have used in all the previous chapters, but sometimes doing the expansion to order $\mathcal{O}(\lambda^2)$ is not enough, and the generalization to the next order $\mathcal{O}(\lambda^4)$

is not straightforward. We thus decided to include this Appendix in the thesis hopping that some may find it useful.

We thus want to find a unitary transformation that, after a perturbation expansion, decouples the two blocks of the Hamiltonian $H_0 + \lambda V$ up to order $\mathcal{O}(\lambda^4)$. For this we need to expand the operator $S(\lambda)$ up to a higher power of λ. Since we want expressions with λ^4 we need to consider $S(\lambda) = \lambda S_1 + \lambda^2 S_2 + \lambda^3 S_3 + \lambda^4 S_4$. The transformed Hamiltonian then reads

$$H' = H + [S, H] + \frac{1}{2}[S, [S, H]]$$
$$+ \frac{1}{6}[S, [S, [S, H]]] + \frac{1}{24}[S, [S, [S, [S, H]]]] + \mathcal{O}(\lambda^5). \quad \text{(A.7)}$$

We now expand S and write $H = H_0 + \lambda V$. This gives:

$$H' \approx H_0 + \lambda(V + [S_1, H])$$
$$+ \lambda^2 \left([S_1, V] + [S_2, H_0] + \frac{1}{2}[S_1, [S_1, H_0]]\right)$$
$$+ \lambda^3 \left([S_2, V] + \frac{1}{2}[S_1, [S_1, V]] + [S_3, H_0] + \frac{1}{2}[S_1, [S_2, H_0]]\right.$$
$$\left. + \frac{1}{2}[S_2, [S_1, H_0]] + \frac{1}{6}[S_1, [S_1, [S_1, H_0]]]\right)$$
$$+ \lambda^4 \left([S_3, V] + \frac{1}{2}[S_1, [S_2, V]] + \frac{1}{2}[S_2, [S_1, V]]\right.$$
$$+ \frac{1}{6}[S_1, [S_1, [S_1, V]]] + [S_4, H_0] + \frac{1}{2}[S_1, [S_3, H_0]]$$
$$+ \frac{1}{2}[S_2, [S_2, H_0]] + \frac{1}{2}[S_3, [S_1, H_0]] + \frac{1}{6}[S_1, [S_1, [S_2, H_0]]]$$
$$+ \frac{1}{6}[S_1, [S_2, [S_1, H_0]]] + \frac{1}{6}[S_2, [S_1, [S_1, H_0]]]$$
$$\left. + \frac{1}{24}[S_1, [S_1, [S_1, [S_1, H_0]]]]\right) \quad \text{(A.8)}$$

Now we proceed as before and eliminate the therms with odd powers of λ. For the term proportional to λ we have the same equation we found previously: $[S_1, H_0] = -V$. Also, since S_4 appears only once we are free to set it to $S_4 = 0$. We have two more unknowns, S_2 and S_3, but only the term proportional to λ^3 is left to be canceled. We are thus free to choose a relation between S_2 and S_3. For simplicity we use $S_2 = 0$. After some

simplifications we arrive at the expression

$$
\begin{aligned}
H' \approx H_0 &+ \frac{\lambda^2}{2} [S_1, V] \\
&+ \lambda^3 \left(\frac{1}{3} [S_1, [S_1, V]] + [S_3, H_0] \right) \\
&+ \frac{\lambda^4}{2} \left([S_3, V] + \frac{1}{4} [S_1, [S_1, [S_1, V]]] + [S_1, [S_3, H_0]] \right),
\end{aligned}
\tag{A.9}
$$

which, for

$$
[S_1, H_0] = -V, \qquad [S_3, H_0] = -\frac{1}{3} [S_1, [S_1, V]], \quad S_2 = S_4 = 0, \tag{A.10}
$$

reduces to the effective Hamiltonian

$$
H_{\text{eff}} = H_0 + \frac{\lambda^2}{2} [S_1 + S_3, V] - \frac{\lambda^4}{24} [S_1, [S_1, [S_1, V]]]. \tag{A.11}
$$

This Hamiltonian is again block-diagonal and the matrix elements contain terms of the order $\mathcal{O}(\lambda^4)$. To construct this Hamiltonian we only need to find the solution of Eqns. (A.10).

B

Time-dependent Fermi's golden rule

For the evaluation of the transition rates Γ_{ij} from Chapter 6 we follow, partially, Ref. [96]. Consider the Hamiltonian in a basis $\{|1\rangle, |2\rangle, |S\rangle\}$:

$$H = \begin{pmatrix} B_1 & 0 & q_1 \\ 0 & B_2 & q_2 \\ q_1 & q_2 & -E_0 + A\cos(\omega t) \end{pmatrix}, \tag{B.1}$$

We can split this Hamiltonian in two terms $H = H_0(t) + H_1$, with

$$H_0(t) = \begin{pmatrix} B_1 & 0 & 0 \\ 0 & B_2 & 0 \\ 0 & 0 & -E_0 + A\cos(\omega t) \end{pmatrix}, \tag{B.2}$$

$$H_1 = \begin{pmatrix} 0 & 0 & q_1 \\ 0 & 0 & q_2 \\ q_1 & q_2 & 0 \end{pmatrix} \tag{B.3}$$

As we did in Section 6.2.1, we introduce an effective decay rate out of the states in the (1,1) charge configuration,

$$\gamma \approx \frac{\Gamma(q_1^2 + q_2^2)}{4E_0^2 + \Gamma^2}. \tag{B.4}$$

We now proceed by doing a perturbation expansion on the eigenstates of H using H_1 as the perturbation. Let $|n\rangle$ be the instantaneous eigenstates of $H_0(t)$ at time t, with eigenvalues $E_n(t)$. Then, any state $|\psi(t)\rangle$ can be written as (for simplicity we set $\hbar = 1$)

$$|\psi(t)\rangle = \sum_n c_n(t) e^{-i \int_0^t dt' E_n(t')} |n\rangle, \tag{B.5}$$

with $c_n(-\infty) = 1$ if n is the initial state and 0 otherwise. Using the Schrödinger equation

$$i \frac{d}{dt}|\psi(t)\rangle = H|\psi(t)\rangle \tag{B.6}$$

we can find an equation for $c_n(t)$:

$$\frac{d}{dt} c_n(t) = -i \sum_k c_k(t) \langle n|H_1|k\rangle e^{-i \int_0^t dt' (E_k(t') - E_n(t'))}, \tag{B.7}$$

which can be integrated (now from $-\infty$ to t), yielding

$$c_n(t) = c_n(-\infty) - i \int_{-\infty}^t dt' \sum_k c_k(t') \langle n|H_1|k\rangle$$
$$\times e^{-i \int_0^{t'} dt'' (E_k(t'') - E_n(t''))}. \tag{B.8}$$

The transition rate can then be evaluated as $\Gamma_{i,n} = \frac{d}{dt}|c_n(t)|^2$. Using $c_k(-\infty) = \delta_{k,i}$ and Eq. (B.8), we can find an expression for $\Gamma_{i,n}$ up to $\mathcal{O}(q)^4$. Let us start by calculating the rate $\Gamma_{1,2}$, that is, the rate from the state $|1\rangle$ to $|2\rangle$ via $|S\rangle$. For this we need:

$$c_n(t) = c_n(-\infty) - i \int_{-\infty}^t dt_1 \sum_k c_k(-\infty) \langle n|H_1|k\rangle e^{-i \int_0^{t_1} dt_2 (E_k(t_2) - E_n(t_2))}$$
$$- \int_{-\infty}^t dt_1 \int_{-\infty}^{t_1} dt_2 \sum_{k,l} c_l(-\infty) \langle k|H_1|l\rangle \langle n|H_1|k\rangle$$
$$\times e^{-i \int_0^{t_2} dt_3 (E_l(t_3) - E_k(t_3))} e^{-i \int_0^{t_1} dt_4 (E_k(t_4) - E_n(t_4))} + \mathcal{O}(q)^3. \tag{B.9}$$

In this case we have $n = 2$ and $c_l = \delta_{l,1}$. The only possible value for $|k\rangle$ is $|S\rangle$. This expression then becomes

$$c_2(t) = -q_1 q_2 \int_{-\infty}^t dt_1 \int_{-\infty}^{t_1} dt_2 e^{-i(B_1 + E_0)t_1} e^{i(B_2 + E_0)t_2}$$
$$\times e^{-i \frac{A}{\omega} \sin(\omega t_1)} e^{i \frac{A}{\omega} \sin(\omega t_2)}, \tag{B.10}$$

But we are interested in the modulo squared of this expression:

$$|c_2(t)|^2 = q_1^2 q_2^2 \int_{-\infty}^{t} dt_4 \int_{-\infty}^{t_4} dt_3 \int_{-\infty}^{t} dt_2 \int_{-\infty}^{t_2} dt_1$$
$$\times e^{-i(B_1+E_0)(t_1-t_3)} e^{i(B_2+E_0)(t_2-t_4)}$$
$$\times e^{-i\frac{A}{\omega}(\sin(\omega t_1)-\sin(\omega t_2)-\sin(\omega t_3)+\sin(\omega t_4))}, \quad \text{(B.11)}$$

We introduce the escape rates out of the states by hand, following the diagrams in Fig. B.1 (see also Ref. [96]). For the diagram (a) we need to include in the integral the terms $\exp(-\gamma(t_4 - t_1 + t_3 - t_2)/2) \exp(-\Gamma(t_2 - t_1)/2) \exp(-\Gamma(t_4 - t_3)/2)$ and change the integration limits accordingly. We do the same for all the diagrams and put everything together to obtain an expression for $\Gamma_{1,2}$:

$$\Gamma_{1,2} = \frac{q_1^2 q_2^2}{((B_1 + E_0)^2 + (\gamma + \Gamma)^2/4)((B_2 - E_0)^2 + (\gamma + \Gamma)^2/4)}$$
$$\times \left(\frac{(\gamma + \Gamma)^2}{\Gamma} + \frac{\gamma(E_0^2 + (\gamma + \Gamma)^2/4)}{(B_1 - B_2)^2 + \gamma^2} + \frac{A^2\gamma}{2((B_1 - B_2 - \omega)^2 + \gamma^2)} \right).$$
$$\text{(B.12)}$$

In these expressions we show only the terms with a positive frequency (that is, the terms that come with an expression such as $B_1 - B_2 - \omega$ that cancels with a positive frequency ω). The terms with the negative frequency are small and will not be considered.

All the other transition rates are obtained in a similar fashion. For these we need to use the diagrams in Fig. B.2.
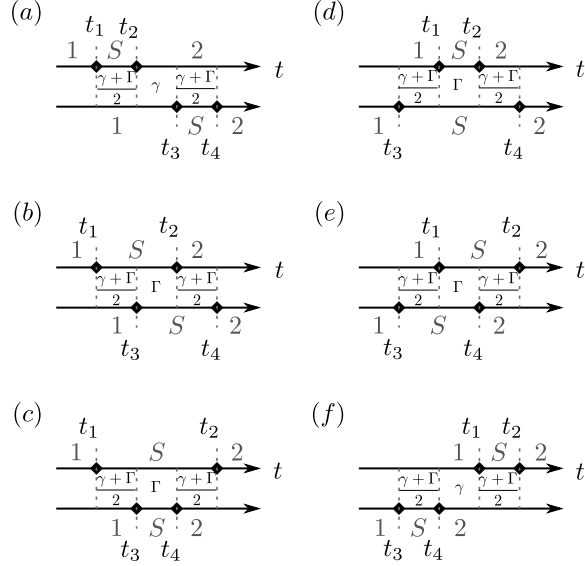
Figure B.1:   The escape rates need to be included considering all possible paths from the state $|1\rangle$ to the state $|2\rangle$ via the state $|S\rangle$ to order $\mathcal{O}(q^4)$. The addition of the contribution from all these paths will give us the transition rate $\Gamma_{1,2}$.

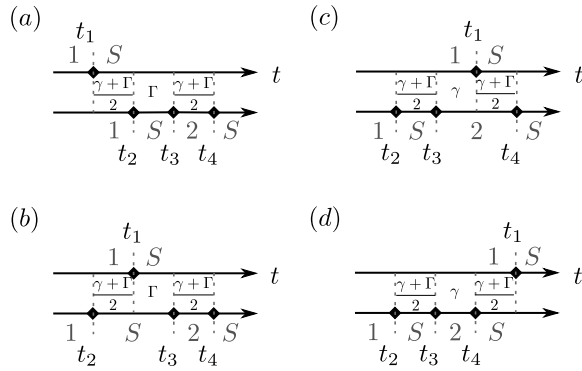Figure B.2:   To calculate the transition rate $\Gamma_{1,s}$, we need to consider all possible paths from the state $|1\rangle$ to the state $|2\rangle$ to order $\mathcal{O}(q^4)$.

C

Special functions for the relaxation rates

Upon calculating a relaxation rate mediated by the electron-phonon interaction, such as the rates given in Eqns. (2.38) and (2.46), one has then to integrate over all possible final states. In Si quantum dots, where the deformation potential depends on the momentum of the emitted phonon, it is still possible to evaluate these integrals, but the result is rather cumbersome. To simplify the notation in Chapter 5 and make it more readable, we introduced some dimensionless functions $f_{0,1}^{\text{ex}}(x)$, $f_{0,1}^{\text{orb}}(x)$, $f_{0,1}^{\text{val}}(x)$ that we define here. These function are used in Section 5.4.

For exchange-enabled transitions we have:

$$
\begin{aligned}
f_1^{\text{ex}}(x) = {}& \frac{4}{5} + \frac{1}{16x^5}\big[128x(x^2 - 9)\cos x \\
& - 2(4x^2 - 9)(x\cos 2x + 64\sin x) + (16x^2 - 9)\sin 2x\big], \quad \text{(C.1)} \\
f_0^{\text{ex}}(x) = {}& \frac{4}{15} + \frac{1}{16x^5}\big[2x(4x^2 - 9)\cos 2x - (16x^2 - 9)\sin 2x\big]. \quad \text{(C.2)}
\end{aligned}
$$

We encounter similar integrals when we evaluate the relaxation rate via a

virtual excitation of an orbital state. In this case we need to use:

$$f_1^{\text{orb}}(x) = \frac{8}{105}\left(\left(\frac{A_{xx}}{v_t}\right)^2 + \left(\frac{A_{yx}}{v_t}\right)^2\right) + \frac{1}{32x^6}\left[3\left(\frac{A_{yx}}{v_t}\right)^2(8x^2 - 15)\right.$$

$$+ 2\left(\frac{A_{yx}}{v_t}\right)^2(8x^4 - 78x^2 + 135)\bigg]\cos 2x$$

$$+ \frac{1}{64x^7}\left[\left(\frac{A_{yx}}{v_t}\right)^2(16x^4 - 84x^2 + 45)\right.$$

$$- 2\left(\frac{A_{xx}}{v_t}\right)^2(64x^4 - 258x^2 + 135)\bigg]\sin 2x, \quad \text{(C.3)}$$

$$f_0^{\text{orb}}(x) = \frac{8}{35}\left(\left(\frac{A_{xx}}{v_t}\right)^2 + \left(\frac{A_{yx}}{v_t}\right)^2\right)$$

$$+ \frac{1}{64x^7}\left\{512x\left[3\left(\frac{A_{yx}}{v_t}\right)^2(2x^2 - 15)\right.\right.$$

$$+ \left(\frac{A_{xx}}{v_t}\right)^2(x^4 - 39x^2 + 270)\bigg]\cos x$$

$$- 2x\left[3\left(\frac{A_{yx}}{v_t}\right)^2(8x^2 - 15)\right.$$

$$+ 2\left(\frac{A_{xx}}{v_t}\right)^2(8x^4 - 78x^2 + 135)\bigg]\cos 2x$$

$$+ 512\left[\left(\frac{A_{yx}}{v_t}\right)^2(x^4 - 21x^2 + 45)\right.$$

$$- \left(\frac{A_{xx}}{v_t}\right)^2(8x^4 - 129x^2 + 270)\bigg]\sin x$$

$$- \left[\left(\frac{A_{yx}}{v_t}\right)^2(16x^4 - 84x^2 + 45)\right.$$

$$- 2\left(\frac{A_{xx}}{v_t}\right)^2(64x^4 - 258x^2 + 135)\bigg]\sin 2x\right\}. \quad \text{(C.4)}$$

And finally, for virtual valley excitations we have:

$$f_1^{\text{val}}(x) = \frac{16}{105} + \frac{1}{64x^7}\left[2x(16x^4 - 132x^2 + 225)\cos 2x\right.$$

$$- (112x^4 - 432x^2 + 225)\bigg]\sin 2x, \quad \text{(C.5)}$$

$$f_0^{\text{val}}(x) = \frac{16}{35} + \frac{8}{x^7}\big[x(x^4 - 33x^2 + 225)\cos x$$
$$- (7x^4 - 108x^2 + 225)\sin x\big]$$
$$- \frac{1}{64x^7}\big[2x(16x^4 - 132x^2 + 225)\cos 2x$$
$$- (112x^4 - 432x^2 + 225)\sin 2x\big]. \quad \text{(C.6)}$$

Bibliography

[1] A. Sala and J. Danon, Physical Review B **95**, 241303(R) (2017).

[2] A. Sala and J. Danon, Physical Review B **98**, 245409 (2018).

[3] A. Sala, J. H. Qvist, and J. Danon, Physical Review Research **2**, 012062 (2020).

[4] M. A. Nielsen and I. L. Chuang, *Quantum Computation and Quantum Information* (Cambridge University Press, 2010).

[5] P. W. Shor, in *Proceedings 35th Annual Symposium on Foundations of Computer Science* (1994) pp. 124–134.

[6] A. Ekert and R. Jozsa, Reviews of Modern Physics **68**, 733 (1996).

[7] D. Loss and D. P. DiVincenzo, Physical Review A **57**, 120 (1998).

[8] D. P. DiVincenzo, Fortschritte der Physik **48**, 771 (2000).

[9] R. Hanson, L. P. Kouwenhoven, J. R. Petta, S. Tarucha, and L. M. K. Vandersypen, Reviews of Modern Physics **79**, 1217 (2007).

[10] F. A. Zwanenburg, A. S. Dzurak, A. Morello, M. Y. Simmons, L. C. L. Hollenberg, G. Klimeck, S. Rogge, S. N. Coppersmith, and M. A. Eriksson, Reviews of Modern Physics **85**, 961 (2013).

[11] T. F. Watson, S. G. J. Philips, E. Kawakami, D. R. Ward, P. Scarlino, M. Veldhorst, D. E. Savage, M. G. Lagally, M. Friesen, S. N. Coppersmith, M. A. Eriksson, and L. M. K. Vandersypen, Nature **555**, 633 (2018).

[12] W. A. Coish and J. Baugh, Physica Status Solidi (B) **246**, 2203 (2009).

[13] M. Russ and G. Burkard, Journal of Physics: Condensed Matter **29**, 393001 (2017).

[14] D. P. DiVincenzo, D. Bacon, J. Kempe, G. Burkard, and K. B. Whaley, Nature **408**, 339 (2000).

[15] M. Russ and G. Burkard, Physical Review B **91**, 235411 (2015).

[16] J. Danon, Physical Review B **88**, 075306 (2013).

[17] V. N. Golovach, A. Khaetskii, and D. Loss, Physical Review Letters **93**, 016601 (2004).

[18] C. Tahan and R. Joynt, Physical Review B **89**, 075302 (2014).

[19] F. H. L. Koppens, C. Buizert, K. J. Tielrooij, I. T. Vink, K. C. Nowack, T. Meunier, L. P. Kouwenhoven, and L. M. K. Vandersypen, Nature **442**, 766 (2006).

[20] R. Zhao, T. Tanttu, K. Y. Tan, B. Hensen, K. W. Chan, J. C. Hwang, R. C. Leon, C. H. Yang, W. Gilbert, F. E. Hudson, K. M. Itoh, A. A. Kiselev, T. D. Ladd, A. Morello, A. Laucht, and A. S. Dzurak, Nature Communications **10**, 5500 (2019).

[21] J. R. Petta, A. C. Johnson, J. M. Taylor, E. A. Laird, A. Yacoby, M. D. Lukin, C. M. Marcus, M. P. Hanson, and A. C. Gossard, Science **309**, 2180 (2005).

[22] B. M. Maune, M. G. Borselli, B. Huang, T. D. Ladd, P. W. Deelman, K. S. Holabird, A. A. Kiselev, I. Alvarado-Rodriguez, R. S. Ross, A. E. Schmitz, M. Sokolich, C. A. Watson, M. F. Gyure, and A. T. Hunter, Nature **481**, 344 (2012).

[23] K. Takeda, A. Noiri, J. Yoneda, T. Nakajima, and S. Tarucha, Physical Review Letters **124**, 117701 (2020).

[24] V. Fock, Zeitschrift für Physik **47**, 446 (1928).

[25] G. Burkard, D. Loss, and D. P. DiVincenzo, Physical Review B **59**, 2070 (1999).

[26] S. Das Sarma, X. Wang, and S. Yang, Physical Review B **83**, 235314 (2011).

[27] J. Medford, J. Beil, J. M. Taylor, E. I. Rashba, H. Lu, A. C. Gossard, and C. M. Marcus, Physical Review Letters **111**, 050501 (2013).

[28] J. M. Taylor, V. Srinivasa, and J. Medford, Physical Review Letters **111**, 050502 (2013).

[29] A. V. Khaetskii and Y. V. Nazarov, Physical Review B **61**, 12639 (2000).

[30] A. V. Khaetskii and Y. V. Nazarov, Physical Review B **64**, 125316 (2001).

[31] P. Yu and M. Cardona, *Fundamentals of Semiconductors: Physics and Materials Properties*, Graduate Texts in Physics (Springer Berlin Heidelberg, 2010).

[32] F. Martins, F. K. Malinowski, P. D. Nissen, E. Barnes, S. Fallahi, G. C. Gardner, M. J. Manfra, C. M. Marcus, and F. Kuemmeth, Physical Review Letters **116**, 116801 (2016).

[33] K. Eng, T. D. Ladd, A. Smith, M. G. Borselli, A. A. Kiselev, B. H. Fong, K. S. Holabird, T. M. Hazard, B. Huang, P. W. Deelman, I. Milosavljevic, A. E. Schmitz, R. S. Ross, M. F. Gyure, and A. T. Hunter, Science Advances **1**, e1500214 (2015).

[34] C. Zhang, X.-C. Yang, and X. Wang, Physical Review A **97**, 042326 (2018).

[35] F. K. Malinowski, F. Martins, P. D. Nissen, S. Fallahi, G. C. Gardner, M. J. Manfra, C. M. Marcus, and F. Kuemmeth, Physical Review B **96**, 045443 (2017).

[36] P. Huang and X. Hu, Physical Review B **89**, 195302 (2014).

[37] L. Cywiński, Physical Review A **90**, 042307 (2014).

[38] D. Paget, G. Lampel, B. Sapoval, and V. I. Safarov, Physical Review B **15**, 5780 (1977).

[39] A. V. Khaetskii, D. Loss, and L. Glazman, Physical Review Letters **88**, 186802 (2002).

[40] I. A. Merkulov, A. L. Efros, and M. Rosen, Physical Review B **65**, 205309 (2002).

[41] A. Abragam, *The principles of nuclear magnetism*, The International series of monographs on physics (Clarendon Press, Oxford, 1961).

[42] A. L. Saraiva, M. J. Calderón, R. B. Capaz, X. Hu, S. Das Sarma, and B. Koiller, Physical Review B **84**, 155320 (2011).

[43] V. N. Golovach, A. Khaetskii, and D. Loss, Physical Review B **77**, 045328 (2008).

[44] P. Huang and X. Hu, Physical Review B **90**, 235315 (2014).

[45] C. H. Yang, A. Rossi, R. Ruskov, N. S. Lai, F. A. Mohiyaddin, S. Lee, C. Tahan, G. Klimeck, A. Morello, and A. S. Dzurak, Nature Communications **4**, 2069 (2013).

[46] Y. P. Kandel, H. Qiao, S. Fallahi, G. C. Gardner, M. J. Manfra, and J. M. Nichol, Nature **573**, 553 (2019).

[47] J. P. Dehollain, U. Mukhopadhyay, V. P. Michal, Y. Wang, B. Wunsch, C. Reichl, W. Wegscheider, M. S. Rudner, E. Demler, and L. M. Vandersypen, Nature **579**, 528 (2020).

[48] F. K. Malinowski, F. Martins, T. B. Smith, S. D. Bartlett, A. C. Doherty, P. D. Nissen, S. Fallahi, G. C. Gardner, M. J. Manfra, C. M. Marcus, and F. Kuemmeth, Nature Communications **10**, 1196 (2019).

[49] T.-K. Hsiao, C. van Diepen, U. Mukhopadhyay, C. Reichl, W. Wegscheider, and L. Vandersypen, Physical Review Applied **13**, 054018 (2020).

[50] G. Burkard, M. J. Gullans, X. Mi, and J. R. Petta, Nature Reviews Physics **2**, 129 (2020).

[51] M. S. Rudner and L. S. Levitov, Physical Review Letters **99**, 036602 (2007).

[52] I. T. Vink, K. C. Nowack, F. H. L. Koppens, J. Danon, Y. V. Nazarov, and L. M. K. Vandersypen, Nature Physics **5**, 764 (2009).

[53] M. S. Rudner, L. M. K. Vandersypen, V. Vuletić, and L. S. Levitov, Physical Review Letters **107**, 206806 (2011).

[54] S. M. Frolov, J. Danon, S. Nadj-Perge, K. Zuo, J. W. W. van Tilburg, V. S. Pribiag, J. W. G. van den Berg, E. P. A. M. Bakkers, and L. P. Kouwenhoven, Physical Review Letters **109**, 236805 (2012).

[55] H. Bluhm, S. Foletti, D. Mahalu, V. Umansky, and A. Yacoby, Physical Review Letters **105**, 216803 (2010).

[56] H. Bluhm, S. Foletti, I. Neder, M. Rudner, D. Mahalu, V. Umansky, and A. Yacoby, Nature Physics **7**, 109 (2011).

[57] F. K. Malinowski, F. Martins, P. D. Nissen, E. Barnes, Ł. Cywiński, M. S. Rudner, S. Fallahi, G. C. Gardner, M. J. Manfra, C. M. Marcus, and F. Kuemmeth, Nature Nanotechnology **12**, 16 (2017).

[58] N. Rohling and G. Burkard, Physical Review B **93**, 205434 (2016).

[59] M. D. Shulman, S. P. Harvey, J. M. Nichol, S. D. Bartlett, A. C. Doherty, V. Umansky, and A. Yacoby, Nature Communications **5**, 5156 (2014).

[60] D. Bacon, J. Kempe, D. A. Lidar, and K. B. Whaley, Physical Review Letters **85**, 1758 (2000).

[61] D. A. Lidar and K. Birgitta Whaley, *Decoherence-Free Subspaces and Subsystems*, edited by F. Benatti and R. Floreanini, Irreversible Quantum Dynamics. Lecture Notes in Physics, Vol. 622 (Springer, Berlin, Heidelberg, 2003) pp. 83–120.

[62] J. Medford, J. Beil, J. M. Taylor, S. D. Bartlett, A. C. Doherty, E. I. Rashba, D. P. DiVincenzo, H. Lu, A. C. Gossard, and C. M. Marcus, Nature Nanotechnology **8**, 654 (2013).

[63] F. K. Malinowski, F. Martins, T. B. Smith, S. D. Bartlett, A. C. Doherty, P. D. Nissen, S. Fallahi, G. C. Gardner, M. J. Manfra, C. M. Marcus, and F. Kuemmeth, Physical Review X **8**, 011045 (2018).

[64] M. Russ and G. Burkard, Physical Review B **92**, 205412 (2015).

[65] V. Srinivasa, J. M. Taylor, and C. Tahan, Physical Review B **94**, 205421 (2016).

[66] M. Russ, J. R. Petta, and G. Burkard, Physical Review Letters **121**, 177701 (2018).

[67] M. Eto, Journal of the Physical Society of Japan **66**, 2244 (1997).

[68] L. Jacak, J. Krasnyj, D. Jacak, W. Salejda, and A. Mituś, Acta Physica Polonica A **99**, 277 (2001).

[69] D. Culcer, X. Hu, and S. Das Sarma, Physical Review B **82**, 205315 (2010).

[70] M. Rontani, F. Rossi, F. Manghi, and E. Molinari, Physical Review B **59**, 10165 (1999).

[71] M. Rontani, *Electronic States in Semiconductor Quantum Dots*, Ph.D. thesis, Università degli Studi di Modena e Reggio Emilia (1999).

[72] S. M. Reimann and M. Manninen, Reviews of Modern Physics **74**, 1283 (2002).

[73] M. Russ, F. Ginzel, and G. Burkard, Physical Review B **94**, 165411 (2016).

[74] A. J. Landig, J. V. Koski, P. Scarlino, C. Müller, J. C. Abadillo-Uriel, B. Kratochwil, C. Reichl, W. Wegscheider, S. N. Coppersmith, M. Friesen, A. Wallraff, T. Ihn, and K. Ensslin, Nature Communications **10**, 5037 (2019).

[75] M. Veldhorst, J. C. Hwang, C. H. Yang, A. W. Leenstra, B. De Ronde, J. P. Dehollain, J. T. Muhonen, F. E. Hudson, K. M. Itoh, A. Morello, and A. S. Dzurak, Nature Nanotechnology **9**, 981 (2014).

[76] J. T. Muhonen, J. P. Dehollain, A. Laucht, F. E. Hudson, R. Kalra, T. Sekiguchi, K. M. Itoh, D. N. Jamieson, J. C. McCallum, A. S. Dzurak, and A. Morello, Nature Nanotechnology **9**, 986 (2014).

[77] M. Raith, P. Stano, F. Baruffa, and J. Fabian, Physical Review Letters **108**, 246602 (2012).

[78] Y.-P. Shim and C. Tahan, Physical Review B **93**, 121410(R) (2016).

[79] J. H. Van Vleck, Physical Review **57**, 426 (1940).

[80] O. Malkoc, P. Stano, and D. Loss, Physical Review B **93**, 235413 (2016).

[81] O. Madelung, *Semiconductors: Data Handbook*, Data in Science and Technology (Springer Berlin Heidelberg, 2004).

[82] M. Raith, P. Stano, and J. Fabian, Physical Review B **83**, 195318 (2011).

[83] A. Hofmann, V. F. Maisi, T. Krähenmann, C. Reichl, W. Wegscheider, K. Ensslin, and T. Ihn, Physical Review Letters **119**, 176807 (2017).

[84] M. Raith, P. Stano, and J. Fabian, Physical Review B **86**, 205321 (2012).

[85] E. A. Laird, C. Barthel, E. I. Rashba, C. M. Marcus, M. P. Hanson, and A. C. Gossard, Semiconductor Science and Technology **24**, 064004 (2009).

[86] S. Nadj-Perge, S. M. Frolov, E. P. A. M. Bakkers, and L. P. Kouwenhoven, Nature **468**, 1084 (2010).

[87] M. D. Schroer, K. D. Petersson, M. Jung, and J. R. Petta, Physical Review Letters **107**, 176811 (2011).

[88] S. Nadj-Perge, V. S. Pribiag, J. W. G. van den Berg, K. Zuo, S. R. Plissard, E. P. A. M. Bakkers, S. M. Frolov, and L. P. Kouwenhoven, Physical Review Letters **108**, 166801 (2012).

[89] F. Pei, E. A. Laird, G. A. Steele, and L. P. Kouwenhoven, Nature Nanotechnology **7**, 630 (2012).

[90] V. S. Pribiag, S. Nadj-Perge, S. M. Frolov, J. W. G. van den Berg, I. van Weperen, S. R. Plissard, E. P. A. M. Bakkers, and L. P. Kouwenhoven, Nature Nanotechnology **8**, 170 (2013).

[91] J. Stehlik, M. D. Schroer, M. Z. Maialle, M. H. Degani, and J. R. Petta, Physical Review Letters **112**, 227601 (2014).

[92] R. Maurand, X. Jehl, D. Kotekar-Patil, A. Corna, H. Bohuslavskyi, R. Laviéville, L. Hutin, S. Barraud, M. Vinet, M. Sanquer, and S. De Franceschi, Nature Communications **7**, 3 (2016).

[93] A. Crippa, R. Maurand, L. Bourdet, D. Kotekar-Patil, A. Amisse, X. Jehl, M. Sanquer, R. Laviéville, H. Bohuslavskyi, L. Hutin, S. Barraud, M. Vinet, Y.-M. Niquet, and S. De Franceschi, Physical Review Letters **120**, 137702 (2018).

[94] F. N. M. Froning, L. C. Camenzind, O. A. H. van der Molen, A. Li, E. P. A. M. Bakkers, D. M. Zumbühl, and F. R. Braakman, arXiv:2006.11175 (2020).

[95] J. Danon and Y. V. Nazarov, Physical Review B **80**, 041301(R) (2009).

[96] J. Danon and M. S. Rudner, Physical Review Letters **113**, 247002 (2014).

[97] J. Stehlik, M. Z. Maialle, M. H. Degani, and J. R. Petta, Physical Review B **94**, 075307 (2016).

Paper I

Arnau Sala and Jeroen Danon

Exchange-only singlet-only spin qubit

Exchange-only singlet-only spin qubit

Arnau Sala and Jeroen Danon

Department of Physics, NTNU, Norwegian University of Science and Technology, 7491 Trondheim, Norway
(Received 9 February 2017; revised manuscript received 29 May 2017; published 19 June 2017)

We propose a feasible and scalable quantum-dot-based implementation of a singlet-only spin qubit which is to leading order intrinsically insensitive to random effective magnetic fields set up by fluctuating nuclear spins in the host semiconductor. Our proposal thus removes an important obstacle for further improvement of spin qubits hosted in high-quality III-V semiconductors such as GaAs. We show how the resulting qubit could be initialized, manipulated, and read out by electrical means only, in a way very similar to a triple-dot exchange-only spin qubit. Due to the intrinsic elimination of the effective nuclear fields from the qubit Hamiltonian, we find an improvement of the dephasing time T_2^* of several orders of magnitude as compared to similar existing spin qubits.

Spin qubits in semiconductor quantum dots are one of the more promising scalable qubit implementations put forward so far [1]. The original proposal almost two decades ago [2] was rapidly followed by early experimental successes, including demonstration of the principles of qubit initialization, manipulation, and readout [3,4]. At the same time, two main challenges for further progress were identified: (i) Single-qubit manipulation requires highly localized oscillating magnetic fields, which are very hard to realize in practice. (ii) All high-quality III-V semiconductors (such as GaAs) consist of atoms carrying nonzero nuclear spin, and the fluctuating ensemble of nuclear spins in each quantum dot couples to the spin of localized electrons through a hyperfine interaction. This coupling causes spin relaxation [5] and yields random effective local magnetic fields acting on the electron spins, which present an important source of qubit decoherence [6,7]. Most of the work in the field of semiconductor spin qubits in the past decades has been aimed at overcoming these two challenges.

One proposed way to overcome the requirement of oscillating magnetic fields is to use a material with a relatively strong spin-orbit interaction (such as InAs), in which coherent spin rotations could be achieved by the application of oscillating *electric* fields [8–10]. A drawback is that the spin-orbit interaction contributes to qubit relaxation [11] and also interferes with the spin-to-charge conversion commonly used for qubit initialization and readout [12]. Another approach is to encode the qubit in a *multielectron* spin state, which enables qubit control through (gate-tunable) exchange interactions [13]: Using two-electron spin states in a double quantum dot, one can define a qubit in the unpolarized singlet-triplet (S-T_0) subspace, which allows for electrical control of qubit rotations along one axis of the Bloch sphere [14,15]; recently it was realized that with one more quantum dot (and electron) one can use two three-electron spin states to define a qubit that has *two* such control axes [16]. The resulting triple-dot exchange-only (XO) qubit can thus be fully operated by electrical means only [16–18]. The downside of using exchange-operated spin qubits is their increased sensitivity to charge noise, either coming from environmental charge fluctuations or directly from the gates. However, recent work indicates that symmetric operation of such qubits could greatly reduce their sensitivity to charge noise [19–21].

These successes thus eliminated the need for highly localized oscillating magnetic fields, leaving the problem of the nuclear spins as the main intrinsic obstacle for further progress [22–25]. Common approaches to overcome this problem include devising hyperfine-induced feedback cycles, where driving the electronic spins out of equilibrium results in a suppression of the fluctuations of the nuclear spin ensemble [26–30], as well as optimizing complex echo pulsing schemes, where the dominating frequencies in the spectrum of the nuclear spin fluctuations are effectively filtered out [31–33], or via a Hamiltonian parameter estimation to operate the qubit with precise knowledge of the environment [34]. Although some of these ideas led to significantly prolonged coherence times, they all involve a large cost in overhead for qubit operation. Another promising approach is to host spin qubits in isotopically purified silicon, which can be (nearly) nuclear spin free [35–37], but the stronger charge noise and the extra valley degree of freedom complicate their operation.

Here, we propose a type of spin qubit that can be hosted in GaAs-based quantum dots, but (i) is intrinsically insensitive to the nuclear fields in the dots and (ii) can be operated fully electrically, similar to the triple-dot XO qubit. The idea is to encode the qubit in a *singlet-only* subspace, which is known to be "decoherence free" for spin qubits (in the sense that fluctuating Zeeman fields do not act inside the subspace) [38,39]. It turns out that a system of four spin-$\frac{1}{2}$ particles hosts such a subspace [40,41]: Among the 16 different four-particle spin states there are two singlets, thus providing a decoherence-free two-level subspace. Below, we present a feasible implementation of a qubit in this subspace, using four electrons in a quadruple quantum dot. We include a clearly outlined scheme for initialization, manipulation, and readout of this qubit, as well as an investigation of its performance in realistic circumstances. We find that, at the price of a slight increase in complexity beyond the triple-dot XO setup, our qubit has superior coherence properties, extending T_2^* by orders of magnitude, while still having a highly scalable design.

The qubit. We propose a setup in which four quantum dots are arranged in a T-like geometry, as shown in Fig. 1(a), where solid lines connect dots that are tunnel coupled. Nearby charge sensors, indicated by "M", can be used to monitor the charge state (N_1, N_2, N_3, N_4) of the quadruple dot, where N_i is
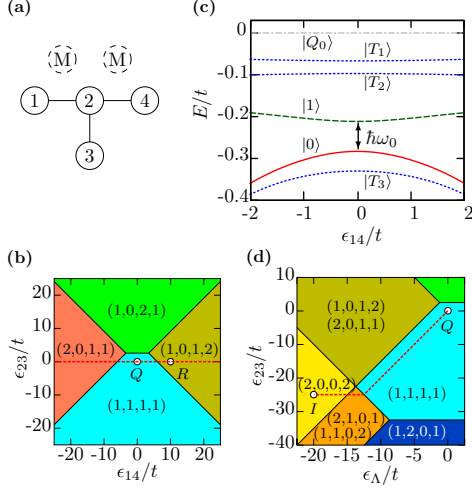
FIG. 1. (a) Schematic representation of the quadruple-dot geometry. The four dots are labeled 1–4 and solid lines indicate which dots are tunnel coupled. The dashed circles labeled "M" show suggested positions for charge sensors. (b) Charge stability diagram in the four-electron regime as a function of ϵ_{14} and ϵ_{23}, using $U = 50t$, $U_c = 15t$, and $\epsilon_\Lambda = 0$. The red dashed line shows the tuning axis along which the qubit is operated. (c) Spectrum of the subspace with $S_z = 0$ along the red dashed line in (b), with $t_{12} = t_{24} = \frac{4}{3}t_{23} = t$. Only the lowest part of the spectrum is shown. The red solid and green dashed lines correspond to the two singlet states that form the qubit. (d) Charge stability diagram as a function of ϵ_Λ and ϵ_{23} with $\epsilon_{14} = 0$ and further the same parameters as in (b). The red dashed line shows the path we suggest for qubit initialization.

the number of excess electrons on dot number i, as labeled in Fig. 1 [42]. To describe this system, we use a Hubbard-like Hamiltonian [43,44],

$$\hat{H} = \sum_i \left[\frac{U}{2} \hat{n}_i(\hat{n}_i - 1) - V_i \hat{n}_i \right] + \sum_{\langle i,j \rangle} U_c \hat{n}_i \hat{n}_j$$
$$- \sum_{\langle i,j \rangle, \alpha} \frac{t_{ij}}{\sqrt{2}} \hat{c}^\dagger_{i,\alpha} \hat{c}_{j,\alpha} + \sum_{i,\alpha} \frac{E_Z}{2} \hat{c}^\dagger_{i,\alpha} \sigma^z_{\alpha\alpha} \hat{c}_{i,\alpha}, \quad (1)$$

where $\hat{n}_i = \sum_\alpha \hat{c}^\dagger_{i,\alpha} \hat{c}_{i,\alpha}$ with $\hat{c}^\dagger_{i,\alpha}$ the creation operator for an electron with spin α on dot i. The first line of Eq. (1) describes the electrostatic energy of the system: The first term accounts for the on-site Coulomb interaction of two electrons occupying the same dot, the second term adds a local offset of the potential energy that can be controlled via gating, and the last term describes the cross capacitance between neighboring dots. To this we added (spin-conserving) tunnel couplings between neighboring dots, characterized by coupling energies t_{ij}, and a uniform Zeeman splitting of the electronic spin states induced by an external magnetic field applied along the z direction, where $E_Z = g\mu_B B$ is the Zeeman energy, with g the effective g factor ($g \approx -0.4$ in GaAs), μ_B the Bohr magneton, and B the magnitude of the applied field.

We can use the electrostatic part of $\hat{H}$ to find the charge ground state as a function of the gate-induced offsets V_i. For convenience, we introduce the tuning parameters $\epsilon_{14} = (V_4 - V_1)/2$, $\epsilon_{23} = (V_3 - V_2)/2$, $\epsilon_\Lambda = (-V_1 + V_2 + V_3 - V_4)/4$, and $\epsilon_\Sigma = (V_1 + V_2 + V_3 + V_4)/4$, where we fix $\epsilon_\Sigma = \frac{3}{4}U_c$. Focusing on the four-electron regime, we show a part of the resulting charge stability diagram as a function of ϵ_{14} and ϵ_{23} in Fig. 1(b), where we have set $\epsilon_\Lambda = 0$, $U = 50t$, and $U_c = 15t$ (t being our unit of energy, of the order of the tunnel coupling energies). Our region of interest is the "top" of the (1,1,1,1) charge region, where exchange effects due to the vicinity of the (2,0,1,1), (1,0,2,1), and (1,0,1,2) charge regions can be significant and are effectively tunable through the gate potentials V_i. We note here that we will assume throughout that the orbital level splitting on the dots is the largest energy scale in the system (larger than U), so we will only include states involving double occupation ($N_i = 2$) if the two electrons are in a singlet state.

We now include finite tunnel coupling energies t_{ij} and a Zeeman energy E_Z, and investigate the spectrum of $\hat{H}$ in more detail. The red dashed line in Fig. 1(b) indicates where $\epsilon_{23} = 0$, and along this line ϵ_{14} parametrizes a "linear tilt" of the potential of the three dots 1, 2, and 4, equivalent to the triple-dot detuning parameter that is used to operate the XO qubit (see Refs. [16,23,44]). In Fig. 1(c) we plot the resulting spectrum of the six lowest-lying states with $S_z = 0$ along this line, as a function of ϵ_{14}, where we have set $t_{12} = t_{24} = \frac{4}{3}t_{23} = t$ and $E_Z = 1.875t$. In the plot we can identify one quintuplet state $|Q_0\rangle$ (gray dotted dashed), three triplet states $|T_{1,2,3}\rangle$ (blue dotted), and two singlets (green dashed and red solid). The ten other spin states, having $S_z = \pm 1, \pm 2$, are split off by multiples of E_Z and not shown in the plot.

The two singlets we propose to use as qubit basis states are marked $|0\rangle$ and $|1\rangle$ in Fig. 1(c) and read to lowest (zeroth) order in the tunnel couplings t_{ij}

$$|1\rangle = |S_{14}S_{23}\rangle, \quad (2)$$

$$|0\rangle = \frac{1}{\sqrt{3}}\{|S_{13}S_{24}\rangle + |S_{12}S_{34}\rangle\}, \quad (3)$$

where S_{ij} denotes a singlet pairing of the two electrons in dots i and j. As an example, one can write explicitly $|1\rangle = \{|\uparrow\uparrow\downarrow\downarrow\rangle - |\uparrow\downarrow\uparrow\downarrow\rangle - |\downarrow\uparrow\downarrow\uparrow\rangle + |\downarrow\downarrow\uparrow\uparrow\rangle\}/2$.

Close to the central point $\epsilon_{14} = 0$, marked Q in Fig. 1(b), exchange effects are small in t/Δ, where $\Delta = U - 3U_c$ is the half width of the (1,1,1,1) charge region along the detuning axis ϵ_{14}, and we thus treat the tunnel couplings as perturbations. Including only the nearby charge states (2,0,1,1), (1,0,2,1), and (1,0,1,2), we can project $\hat{H}$ to the qubit subspace spanned by $|0\rangle$ and $|1\rangle$, yielding to second order in the t_{ij},

$$\hat{H}_{qb} = \frac{1}{4}(J_{12} + J_{24} - 2J_{23})\hat{\sigma}^z + \frac{\sqrt{3}}{4}(J_{12} - J_{24})\hat{\sigma}^x, \quad (4)$$

where we subtracted a constant offset. The $\hat{\sigma}^{x,z}$ denote Pauli matrices, and the relative magnitudes of the exchange energies $J_{12} = t^2_{12}/(\Delta + \epsilon_{14})$, $J_{24} = t^2_{24}/(\Delta - \epsilon_{14})$, and $J_{23} = t^2_{23}/\Delta$, can be controlled by the detuning parameter ϵ_{14} (note that we have set $\epsilon_{23} = 0$). We make two observations: (i) The qubit splitting at zero detuning, $\hbar\omega_0 = (t^2_{12} + t^2_{24} - 2t^2_{23})/2\Delta$,

vanishes if all three tunnel couplings are equal; ideally, one tunes $t_{12} = t_{24} \neq t_{23}$. (ii) The structure of this Hamiltonian is fully equivalent to that of the triple-dot XO qubit [cf. Eq. (5) in Ref. [44]], including its qualitative dependence on the detuning parameter. Thus, our qubit can be operated analogously to the XO qubit, i.e., by static pulsing [16] or resonant driving [23], and the point Q is a sweet spot where the qubit is to lowest order insensitive to noise in ϵ_{14}.

Qubit operation. Qubit rotations are most conveniently achieved using resonantly driven Rabi oscillations [23]. For small detuning, $|\epsilon_{14}| \ll \Delta$, we can expand $\hat{H}_{qb}$ to linear order in ϵ_{14}, yielding

$$\hat{H}_{qb} = \frac{1}{2}\hbar\omega_0\hat{\sigma}^z - \frac{\sqrt{3}}{2}\frac{t^2\epsilon_{14}}{\Delta^2}\hat{\sigma}^x, \tag{5}$$

where we used $t_{12} = t_{24} = t$. A harmonic modulation of the detuning, $\epsilon_{14} = A\cos(\omega\tau)$, will thus induce Rabi rotations of the qubit which at the resonance condition $\omega = \omega_0$ a Rabi period of $T_{Rabi} = 4\pi\hbar\Delta^2/(\sqrt{3}t^2A)$. Using again $\Delta = 5t$ (consistent with the realistic parameters $t = 20\ \mu$eV, $U = 1$ meV, and $U_c = 0.3$ meV), a moderate driving amplitude of $A = 2.5\ \mu$eV would yield a rotation time $T_{Rabi} \approx 50$ ns.

Readout of the qubit can be performed by spin-to-charge conversion, in a similar way as in the double-dot S-T_0 [14] and triple-dot XO [16,23] qubits. The detuning ϵ_{14} is quickly pulsed to the point marked R in Fig. 1(c), which lies in the (1,0,1,2) charge region. There are only two accessible (1,0,1,2) states with $S_z = 0$: The two electrons on dot 4 must be in a singlet state, but the electrons on dots 1 and 3 can form either a singlet S or unpolarized triplet T_0. Only the singlet-singlet configuration couples adiabatically to one of the qubit states (the state $|0\rangle$). After pulsing to R, the qubit state $|0\rangle$ will thus transition to a (1,0,1,2) charge configuration whereas the state $|1\rangle$ remains in a spin-blockaded (1,1,1,1) state. Subsequent charge sensing amounts to a projective measurement of the qubit state. One requirement is that the detuning pulse has to be fast enough so that spin-flip transitions from $|0\rangle$ to one of the lower-lying states with $S_z = 1,2$, which are crossed at $\epsilon_{14} \sim E_Z$, are very unlikely. (Note that exactly the same condition holds for the triple-dot XO qubit measurement scheme, where the spin-$\frac{1}{2}$ state connected to $|0\rangle$ crosses a spin-$\frac{3}{2}$ state [23].)

Initialization of the qubit can be achieved in a similar way. The simplest procedure is to pulse to a point in gate space where there is one unique singlet-only ground state, such as the point marked I in the (2,0,0,2) charge region [see Fig. 1(d)]. After waiting long enough, the system will have relaxed to this ground state, and a fast pulse back to the qubit tuning Q will yield a qubit prepared in $|0\rangle$. The path we propose for this pulse is marked in Fig. 1(d) by a red dashed line: First, ϵ_Λ is increased until the edge of the (1,1,1,1) charge region is reached, after which both ϵ_Λ and ϵ_{23} are increased simultaneously until the system reaches the point Q. For this pulse the same condition holds as for the readout pulse: It should be fast enough to not allow for spin-flip transitions into the lower-lying states with $S_z = 1,2$ [45].

Decoherence. The main source of decoherence in GaAs-based spin qubits is known to be the fluctuating bath of nuclear spins that couples to the qubit states through a hyperfine

interaction [1,6,23]. The effect of the ensemble of $\sim10^6$ nuclear spins in each quantum dot can, to good approximation, be modeled as a randomly and slowly fluctuating effective magnetic field $\mathbf{K}_i$ acting on the electrons localized in the dot i. The fluctuations are slow enough that the field can be considered as static on the time scale of a single qubit operation, but it varies randomly over the course of many measurement cycles. The rms value of these random fields was reported to be $K = 1$–3 mT in typical GaAs quantum dots [3,23,52]. The resulting uncertainty in the qubit level splitting translates to a decoherence time T_2^* of tens of ns, and forms at present the bottleneck for further improvement of the performance of GaAs-based spin qubits.

To understand the effect of hyperfine interaction on the singlet-only qubit, we write the effective Hamiltonian

$$\hat{H}_{hf} = \frac{g\mu_B}{2}\sum_{i,\alpha,\beta}\hat{c}_{i,\alpha}^\dagger\mathbf{K}_i\cdot\boldsymbol{\sigma}_{\alpha\beta}\hat{c}_{i,\beta}, \tag{6}$$

and project this Hamiltonian to the qubit subspace,

$$\hat{H}_{hf,qb} = 0. \tag{7}$$

This confirms that, to leading order, the nuclear fields do not affect the qubit and thus do not cause any decoherence. The hyperfine Hamiltonian does, however, couple both qubit states to all nine four-electron triplet states. Coupling to the triplet states with $S_z = \pm1$ is mediated by K_i^x and K_i^y, but transitions to these states are strongly suppressed by the large Zeeman energy E_Z. The z components of the nuclear fields couple $|0\rangle$ and $|1\rangle$ to $|T_{1,2,3}\rangle$, and this coupling (i) can cause leakage out of the qubit space, analogous to leakage to the spin-$\frac{1}{2}$ quadruplet state in the triple-dot XO qubit, and (ii) can yield a higher-order shift in the qubit splitting, contributing to qubit decoherence. Both effects are suppressed by the small factor $g\mu_B K/J$ (where J is the typical energy scale of the exchange energies J_{ij}), and the decoherence time resulting from the fluctuations of the qubit splitting [53] can be estimated as $T_2 \sim \hbar J/(g\mu_B K)^2$. For typical parameters ($J = 2\ \mu$eV and $K = 1$ mT) this would present an improvement of two orders of magnitude over other GaAs-based spin qubits, where $T_2^* \sim \hbar/g\mu_B K$.

To support these claims, we perform numerical simulations of resonant driving of the qubit. We project the Hamiltonian (1) to the 12-dimensional subspace of all (1,1,1,1), (2,0,1,1), (1,0,2,1), and (1,0,1,2) states with $S_z = 0$. We diagonalize the resulting Hamiltonian at the point Q [see Fig. 1(b)] using the same parameters as before and specifying $t = 16\ \mu$eV; this yields all eigenstates at $\epsilon_{14} = 0$ as well as the qubit splitting $\hbar\omega_0$. We initialize in the lowest-lying singlet state $|0\rangle$, and then let the system evolve under the Hamiltonian $\hat{H} + \hat{H}_{hf}$ where we include resonant driving $\epsilon_{14} = A\cos(\omega_0\tau)$ and four random nuclear fields $\mathbf{K}_i$. In Fig. 2 (solid blue) we show the resulting time-dependent probability to find the system in $|1\rangle$, where we used $A = 2.5\ \mu$eV and averaged over 2500 random nuclear field configurations with the $g\mu_B K_i^{x,y,z}$ drawn from a normal distribution with mean zero and $\sigma = 0.07\ \mu$eV. We observe eight Rabi oscillations in ~450 ns without any significant decay [54]. Of course, at longer
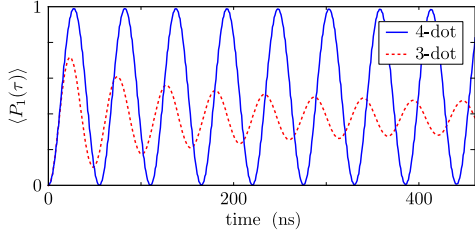
FIG. 2. Solid blue: Calculated time-dependent expectation value of $|1\rangle\langle 1|$ after initializing in $|0\rangle$ and driving resonantly with $\epsilon_{14} \propto \cos(\omega_0\tau)$, averaged over 2500 random configurations of the nuclear fields. Dashed red: Equivalent result for the triple-dot XO setup, using the same parameters.

times eventually leakage out of the qubit space as well as higher-order corrections due to the nuclear fields will suppress the oscillations in $\langle P_1(\tau)\rangle$.

As a comparison, we also performed equivalent simulations of resonant driving of a triple-dot XO qubit (cf. Ref. [23]), using exactly the same parameters (basically setting $t_{23} = 0$ and adjusting ω_0 to the new qubit splitting). The result is plotted with a red dashed line in Fig. 2; in this case the hyperfine-induced decay of $\langle P_1(\tau)\rangle$ is already significant in the first few Rabi periods. The clear contrast between the two curves illustrates the improvement presented by our quadruple-dot XO qubit.

Relaxation. Electron-phonon coupling can contribute to qubit relaxation, i.e., induce dissipative transitions from $|1\rangle$ to $|0\rangle$. The associated relaxation rate can be estimated using Fermi's golden rule, $\Gamma_{\text{rel}} = \frac{2\pi}{\hbar} \sum_f |\langle f|\hat{H}_{\text{e-ph}}|i\rangle|^2 \delta(E_f - E_i)$, where the initial state is $|1\rangle|\text{vac}\rangle$ (with $|\text{vac}\rangle$ denoting the phonon vacuum) and the sum runs over all possible final states $|0\rangle|1_{\mathbf{k},p}\rangle$ where one phonon has been created with wave vector

$\mathbf{k}$ and polarization p. We use an electron-phonon Hamiltonian

$$\hat{H}_{\text{e-ph}} = \sum_{\mathbf{k},p} \lambda_{\mathbf{k},p} \hat{\rho}_{\mathbf{k}}(\hat{a}_{\mathbf{k},p} + \hat{a}_{-\mathbf{k},p}^\dagger), \qquad (8)$$

where $\hat{a}_{\mathbf{k},p}^\dagger$ creates a phonon in mode $\{\mathbf{k},p\}$, $\hat{\rho}_{\mathbf{k}}$ is the Fourier transform of the electronic density matrix, and $\lambda_{\mathbf{k},p}$ are the coupling parameters (see, e.g., Ref. [55]). At typical qubit splittings the coupling to piezoelectric phonons dominates, in which case an explicit evaluation of Γ_{rel} yields to leading order in t/Δ the estimate [45]

$$\Gamma_{\text{rel}} \approx \frac{t^4}{\Delta^4} \frac{\omega_0^3 d^3}{v^3} \frac{(eh_{14})^2}{10\pi\hbar\rho v^2 d}, \qquad (9)$$

where v is the phonon velocity (for convenience now assumed equal for all three polarizations), d the distance between neighboring dots, h_{14} the piezoelectric constant, and ρ denotes the mass density of the semiconductor (for GaAs, $v \sim 4000$ m/s, $h_{14} \approx 1.45 \times 10^9$ V/m, and $\rho \approx 5300$ kg/m^3; see Ref. [56]). Setting $d = 100$ nm, this yields $\Gamma_{\text{rel}} = \omega_0^3(t/\Delta)^4(3 \times 10^{-23}$ Hz$^{-2})$, which for $\Delta = 5t$ and $\hbar\omega_0 = 1.5\ \mu$eV gives $\Gamma_{\text{rel}} = 0.57$ kHz.

Relaxation processes to $|T_3\rangle$ require a change of the spin state of the electrons [57] and are estimated to be smaller by a factor $\sim (g\mu_B K/J)^2$. Dissipative transitions to the lower-lying states with $S_z = 1,2$ require a spin flip and are suppressed by the large Zeeman energy E_Z.

Conclusions. We propose a quantum-dot-based singlet-only spin qubit which is to leading order intrinsically insensitive to randomly fluctuating nuclear fields. Our proposal thus removes the main obstacle for further improvement of spin qubits hosted in semiconductors with spinful nuclei, such as GaAs. Its scalability, full electrical control, and large coherence time make the singlet-only spin qubit one of unprecedented quality.

[1] R. Hanson, L. P. Kouwenhoven, J. R. Petta, S. Tarucha, and L. M. K. Vandersypen, Rev. Mod. Phys. **79**, 1217 (2007).

[2] D. Loss and D. P. DiVincenzo, Phys. Rev. A **57**, 120 (1998).

[3] F. H. L. Koppens, C. Buizert, K. J. Tielrooij, I. T. Vink, K. C. Nowack, T. Meunier, L. P. Kouwenhoven, and L. M. K. Vandersypen, Nature (London) **442**, 766 (2006).

[4] J. M. Elzerman, R. Hanson, L. H. Willems van Beveren, B. Witkamp, L. M. K. Vandersypen, and L. P. Kouwenhoven, Nature (London) **430**, 431 (2004).

[5] S. I. Erlingsson and Y. V. Nazarov, Phys. Rev. B **66**, 155327 (2002).

[6] I. A. Merkulov, A. L. Efros, and M. Rosen, Phys. Rev. B **65**, 205309 (2002).

[7] A. V. Khaetskii, D. Loss, and L. Glazman, Phys. Rev. Lett. **88**, 186802 (2002).

[8] V. N. Golovach, M. Borhani, and D. Loss, Phys. Rev. B **74**, 165319 (2006).

[9] C. Flindt, A. S. Sørensen, and K. Flensberg, Phys. Rev. Lett. **97**, 240501 (2006).

[10] S. Nadj-Perge, S. M. Frolov, E. P. A. M. Bakkers, and L. P. Kouwenhoven, Nature (London) **468**, 1084 (2010).

[11] A. V. Khaetskii and Y. V. Nazarov, Phys. Rev. B **64**, 125316 (2001).

[12] J. Danon and Y. V. Nazarov, Phys. Rev. B **80**, 041301(R) (2009).

[13] D. P. DiVincenzo, D. Bacon, J. Kempe, G. Burkard, and K. B. Whaley, Nature (London) **408**, 339 (2000).

[14] J. R. Petta, A. C. Johnson, J. M. Taylor, E. A. Laird, A. Yacoby, M. D. Lukin, C. M. Marcus, M. P. Hanson, and A. C. Gossard, Science **309**, 2180 (2005).

[15] J. M. Taylor, J. R. Petta, A. C. Johnson, A. Yacoby, C. M. Marcus, and M. D. Lukin, Phys. Rev. B **76**, 035315 (2007).

[16] J. Medford, J. Beil, J. M. Taylor, S. D. Bartlett, A. C. Doherty, E. I. Rashba, D. P. DiVincenzo, H. Lu, A. C. Gossard, and C. M. Marcus, Nat. Nanotechnol. **8**, 654 (2013).

[17] E. A. Laird, J. M. Taylor, D. P. DiVincenzo, C. M. Marcus, M. P. Hanson, and A. C. Gossard, Phys. Rev. B **82**, 075403 (2010).

[18] M. Russ and G. Burkard, arXiv:1611.09106.

[19] F. Martins, F. K. Malinowski, P. D. Nissen, E. Barnes, S. Fallahi, G. C. Gardner, M. J. Manfra, C. M. Marcus, and F. Kuemmeth, Phys. Rev. Lett. **116**, 116801 (2016).

[20] M. D. Reed, B. M. Maune, R. W. Andrews, M. G. Borselli, K. Eng, M. P. Jura, A. A. Kiselev, T. D. Ladd, S. T. Merkel, I. Milosavljevic, E. J. Pritchett, M. T. Rakher, R. S. Ross, A. E. Schmitz, A. Smith, J. A. Wright, M. F. Gyure, and A. T. Hunter, Phys. Rev. Lett. **116**, 110402 (2016).

[21] Y.-P. Shim and C. Tahan, Phys. Rev. B **93**, 121410(R) (2016).

[22] W. A. Coish and D. Loss, Phys. Rev. B **72**, 125337 (2005).

[23] J. Medford, J. Beil, J. M. Taylor, E. I. Rashba, H. Lu, A. C. Gossard, and C. M. Marcus, Phys. Rev. Lett. **111**, 050501 (2013).

[24] S. Mehl and D. P. DiVincenzo, Phys. Rev. B **87**, 195309 (2013).

[25] J.-T. Hung, J. Fei, M. Friesen, and X. Hu, Phys. Rev. B **90**, 045308 (2014).

[26] M. S. Rudner and L. S. Levitov, Phys. Rev. Lett. **99**, 036602 (2007).

[27] I. T. Vink, K. C. Nowack, F. H. L. Koppens, J. Danon, Y. V. Nazarov, and L. M. K. Vandersypen, Nat. Phys. **5**, 764 (2009).

[28] M. S. Rudner, L. M. K. Vandersypen, V. Vuletić, and L. S. Levitov, Phys. Rev. Lett. **107**, 206806 (2011).

[29] S. M. Frolov, J. Danon, S. Nadj-Perge, K. Zuo, J. W. W. van Tilburg, V. S. Pribiag, J. W. G. van den Berg, E. P. A. M. Bakkers, and L. P. Kouwenhoven, Phys. Rev. Lett. **109**, 236805 (2012).

[30] H. Bluhm, S. Foletti, D. Mahalu, V. Umansky, and A. Yacoby, Phys. Rev. Lett. **105**, 216803 (2010).

[31] H. Bluhm, S. Foletti, I. Neder, M. Rudner, D. Mahalu, V. Umansky, and A. Yacoby, Nat. Phys. **7**, 109 (2011).

[32] F. K. Malinowski, F. Martins, P. D. Nissen, E. Barnes, Ł. Cywiński, M. S. Rudner, S. Fallahi, G. C. Gardner, M. J. Manfra, C. M. Marcus, and F. Kuemmeth, Nat. Nanotechnol. **12**, 16 (2016).

[33] N. Rohling and G. Burkard, Phys. Rev. B **93**, 205434 (2016).

[34] M. D. Shulman, S. P. Harvey, J. M. Nichol, S. D. Bartlett, A. C. Doherty, V. Umansky, and A. Yacoby, Nat. Commun. **5**, 5156 (2014).

[35] F. A. Zwanenburg, A. S. Dzurak, A. Morello, M. Y. Simmons, L. C. L. Hollenberg, G. Klimeck, S. Rogge, S. N. Coppersmith, and M. A. Eriksson, Rev. Mod. Phys. **85**, 961 (2013).

[36] K. Eng, T. D. Ladd, A. Smith, M. G. Borselli, A. A. Kiselev, B. H. Fong, K. S. Holabird, T. M. Hazard, B. Huang, P. W. Deelman, I. Milosavljevic, A. E. Schmitz, R. S. Ross, M. F. Gyure, and A. T. Hunter, Sci. Adv. **1**, e1500214 (2015).

[37] M. Veldhorst, J. C. C. Hwang, C. H. Yang, A. W. Leenstra, B. de Ronde, J. P. Dehollain, J. T. Muhonen, F. E. Hudson,

K. M. Itoh, A. Morello, and A. S. Dzurak, Nat. Nanotechnol. **9**, 981 (2014).

[38] D. Bacon, J. Kempe, D. A. Lidar, and K. B. Whaley, Phys. Rev. Lett. **85**, 1758 (2000).

[39] D. A. Lidar and K. B. Whaley, in *Irreversible Quantum Dynamics*, edited by F. Benatti and R. Floreanini (Springer, Berlin, 2003), pp. 83–120.

[40] V. W. Scarola, K. Park, and S. Das Sarma, Phys. Rev. Lett. **93**, 120503 (2004).

[41] B. Antonio and S. Bose, Phys. Rev. A **88**, 042306 (2013).

[42] In fact, if sensitive enough, one charge sensor could suffice, as long as it is not placed equidistant from any pair of dots.

[43] G. Burkard, D. Loss, and D. P. DiVincenzo, Phys. Rev. B **59**, 2070 (1999).

[44] J. M. Taylor, V. Srinivasa, and J. Medford, Phys. Rev. Lett. **111**, 050502 (2013).

[45] See Supplemental Material at http://link.aps.org/supplemental/10.1103/PhysRevB.95.241303 for more detailed discussions and derivations of the equations presented in the main text, which includes Refs. [46–51].

[46] J. R. Schrieffer and P. A. Wolff, Phys. Rev. **149**, 491 (1966).

[47] J. Danon, Phys. Rev. B **88**, 075306 (2013).

[48] R. Thalineau, S. Hermelin, A. D. Wieck, C. Bäuerle, L. Saminadayar, and T. Meunier, Appl. Phys. Lett. **101**, 103102 (2012).

[49] T. Takakura, A. Noiri, T. Obata, T. Otsuka, J. Yoneda, K. Yoshida, and S. Tarucha, Appl. Phys. Lett. **104**, 113109 (2014).

[50] M. R. Delbecq, T. Nakajima, T. Otsuka, S. Amaha, J. D. Watson, M. J. Manfra, and S. Tarucha, Appl. Phys. Lett. **104**, 183111 (2014).

[51] D. M. Zajac, T. M. Hazard, X. Mi, E. Nielsen, and J. R. Petta, Phys. Rev. Appl. **6**, 054013 (2016).

[52] A. C. Johnson, J. R. Petta, J. M. Taylor, A. Yacoby, M. D. Lukin, C. M. Marcus, M. P. Hanson, and A. C. Gossard, Nature (London) **435**, 925 (2005).

[53] $K_i^{x,y}$ can cause a similar higher-order shift in the qubit splitting, but the resulting contribution to the dephasing rate $1/T_2^*$ is smaller by a factor J/E_Z .

[54] We note that these simulations include hyperfine-induced leakage out of the qubit space to other states with $S_z = 0$.

[55] P. Stano and J. Fabian, Phys. Rev. B **74**, 045320 (2006).

[56] O. Madelung, *Semiconductors: Data Handbook*, 3rd ed. (Springer, Berlin, 2004).

[57] Possible contributions from spin-orbit interaction to relaxation to $|T_3\rangle$ could be suppressed by applying the external magnetic field perpendicularly to the qubit plane.
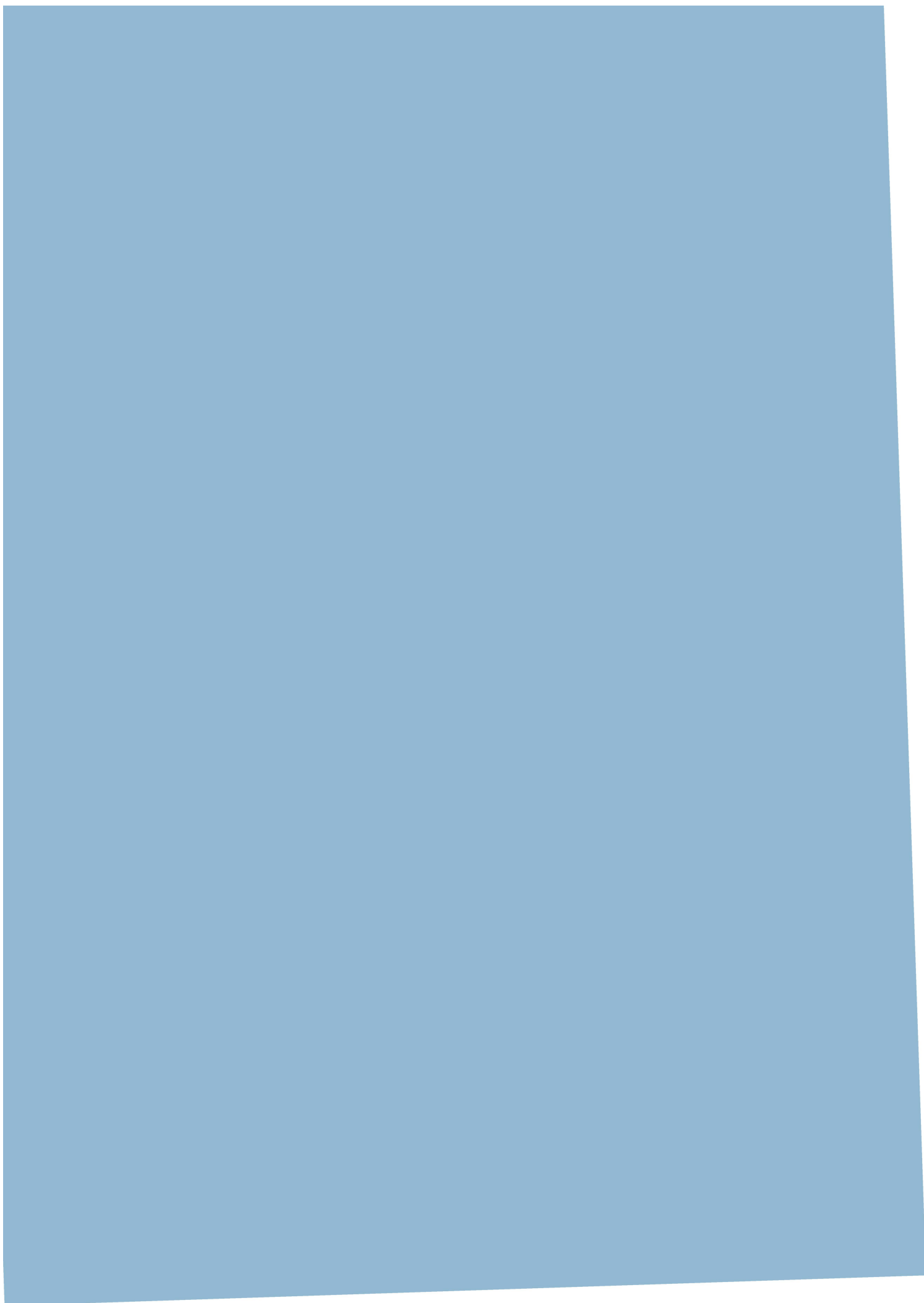
Paper II

Arnau Sala and Jeroen Danon

Leakage and dephasing in ^{28}Si-based exchange-only spin qubits

Leakage and dephasing in ^{28}Si-based exchange-only spin qubits

Arnau Sala and Jeroen Danon

Center for Quantum Spintronics, Department of Physics, Norwegian University of Science and Technology,
NO-7491 Trondheim, Norway

Exchange-only spin qubits hosted in ^{28}Si-based triple quantum dots do not suffer from decoherence caused by randomly fluctuating nuclear-spin ensembles and can be relatively robust against electrical noise when operated at a sweet spot. Remaining sources of decoherence are qubit relaxation, leakage out of the qubit subspace, and dephasing due to residual effects of charge noise, the latter two of which are the focus of this work. We investigate spin-orbit-mediated leakage rates to the three-spin ground state accompanied by virtual (i) tunneling, (ii) orbital excitation, and (iii) valley excitation of an electron. We find different power-law dependencies on the applied magnetic field B for the three mechanisms as well as for the two leakage rates, ranging from $\propto B^5$ to $\propto B^{11}$, and identify the sweet spot as a point of minimal leakage. We also revisit the role of electrical noise at the sweet spot and show that it causes a decay of coherent qubit oscillations that follows a power law $\propto 1/t$ (as opposed to the more common exponential decay) and introduces a $\pi/2$ phase shift.

I. INTRODUCTION

The development of semiconductor quantum-dot spin qubits seems to be a promising path towards the materialization of large-scale quantum computation [1]. In order to overcome the practical challenge of creating highly localized oscillating magnetic fields, implementations of such qubits have seen a development from single-dot single-spin systems to a more complicated triple-dot three-spin exchange-only (XO) qubit that can be fully operated by only electric fields [2–7]. Furthermore, hosting spin qubits in purified ^{28}Si, instead of the more traditional III-V materials, led to a significant improvement of observed qubit coherence times due to the negligible fraction of spinful nuclei in the material [8–14].

Remaining sources of decoherence for the ^{28}Si-based XO qubit are (i) electric noise in the environment of the qubit leading to qubit dephasing [15,16], (ii) electron-phonon coupling that can cause (spin-conserving) qubit relaxation [5], and (iii) spin-mixing mechanisms such as spin-orbit (SO) interaction that can enable leakage out of the qubit subspace to the three-spin ground state $|\downarrow \downarrow\downarrow\rangle$ [15,17]. Some of these mechanisms have already been studied: It was found that the effects of charge noise can be strongly suppressed by manipulating the qubit at a so-called sweet spot (SS), where the qubit splitting is, to leading order, insensitive to electric fluctuations [7,18], and electron-phonon coupling was shown to cause slow qubit relaxation (estimated as $\Gamma_{\rm rel} \lesssim 10$ Hz) that is proportional to the fifth power of the qubit splitting [19]; some effects of SO interaction can also be suppressed during gate operations in double quantum dots by shaping the pulse of the two-qubit coupling [20,21] or by using superexchange coupling in a triple-quantum-dot setup [22].

In this work we study some of the remaining questions. We first investigate the SO-induced leakage rates from the two qubit states to the ground state $|\downarrow \downarrow\downarrow\rangle$. Since a SO-assisted spin flip requires finite motion of the electron, such a leakage process must involve virtual excitation of a different orbital state [17]; here we consider the contributions from virtual tunneling, on-site orbital excitation, and valley excitation separately. For these three mechanisms we find different power laws for the dependence of the two rates on the applied magnetic field B, ranging from $\Gamma_{\rm leak} \propto B^5$ to $\Gamma_{\rm leak} \propto B^{11}$, and we also show that the SS is the point where both the qubit relaxation and leakage rates are minimal. Finally, we also revisit the role of charge noise at the SS, and we show that slow electric fluctuations in the qubit's environment cause a power-law decay $\propto 1/t$ of coherent qubit oscillations, as opposed to the exponential decay that is usually assumed [23,24].

The rest of this paper is organized as follows: In Sec. II we introduce our description of the system and the model Hamiltonians we use. In Sec. III we present our analytic results for the leakage rates based on the three mechanisms mentioned above. Then, in Sec. IV, we corroborate these results with a numerical evaluation of the dominating leakage rates, across the whole (1,1,1) charge region. In Sec. V we investigate charge-noise-induced dephasing, and in Sec. VI we finally present our conclusions.

II. MODEL

We consider a linear array of three circular quantum dots with radius σ and interdot distance d (center to center), as schematically depicted in Fig. 1(a). Assuming a large orbital level splitting on the dots, we allow each dot i to contain $n_i \in \{0, 1, 2\}$ excess electrons, and the triplet (n_1, n_2, n_3) will hereafter be used to label the different charge configurations. We model the system using a Hubbard-like Hamiltonian [5,6,25],

$$
\hat{H} = \sum_i \left[\frac{U}{2} \hat{n}_i (\hat{n}_i - 1) - V_i \hat{n}_i \right] + \sum_{\langle i,j \rangle} U_c \hat{n}_i \hat{n}_j
$$
$$
+ \sum_{\langle i,j \rangle, \alpha} \frac{t_{ij}}{\sqrt{2}} \hat{c}_{i,\alpha}^\dagger \hat{c}_{j,\alpha} + \sum_{i,\alpha} \frac{1}{2} g \mu_B B \hat{c}_{i,\alpha}^\dagger \sigma_{z'}^{\alpha\alpha} \hat{c}_{i,\alpha}, \quad (1)
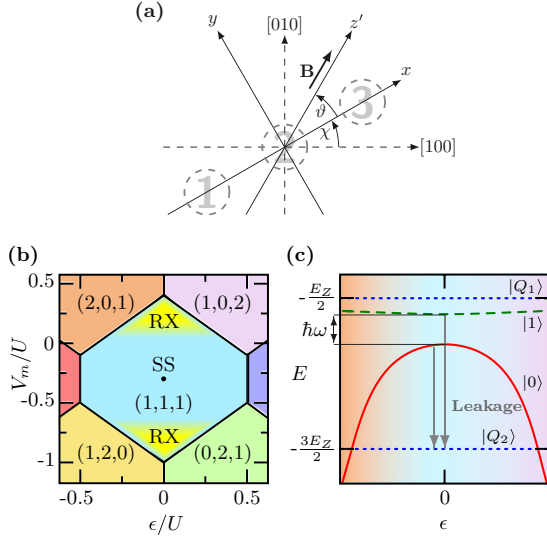$$

FIG. 1. (a) Reference frame of the system. The quantum dots (dashed gray circles) lie in the xy plane. An in-plane magnetic (Zeeman) field **B** is applied at an angle ϑ with the interdot axis, which, in turn, is at an angle χ with the crystallographic [100] direction. (b) Charge stability diagram, showing the charge ground state of the electrostatic part of the Hamiltonian (1) as a function of ϵ and V_m, using $U_c = 0.3U$ and $V_2 = 2U_c - V_1 - V_3$. (c) Qualitative sketch of the lower part of the spectrum of (1) as a function of ϵ in the regions labeled "RX" in (b), where we assumed $t_{12} = t_{23}$. The gray arrows indicate the leakage processes investigated here. In this plot all variables are in arbitrary units.

where $\hat{n}_i = \sum_\alpha \hat{c}_{i,\alpha}^\dagger \hat{c}_{i,\alpha}$, with $\hat{c}_{i,\alpha}^\dagger$ being the creation operator for an electron with spin α in the orbital ground state of dot i, and $\hat{\sigma}_{z'}$ is the diagonal Pauli matrix, acting in spin space. As in Refs. [5,26], the first line describes the electrostatic energy and includes an on-site charging energy U, gate-tunable local potentials V_i, and a nearest-neighbor charging energy U_c. The second line adds nearest-neighbor (spin-conserving) interdot tunnel couplings and a Zeeman splitting due to an externally applied magnetic field B, which we assume to be in plane. The tunnel coupling parameters could be effectively renormalized due to phase differences between the valley states on neighboring dots [27]; we assume such effects are included in the t_{ij} we use.

Figure 1(b) shows part of the charge stability diagram resulting from the first line of (1), where the regions with different charge (ground) states are indicated, as a function of $\epsilon = (V_3 - V_1)/2$ and $V_m = (V_1 + V_3)/2 - V_2$ for $U_c = 0.3\,U$ and $V_1 + V_2 + V_3 = 2U_c$. Within the $(1,1,1)$ region finite tunnel couplings t_{ij} lead to exchange effects that split the spectrum in a fourfold-degenerate spin quadruplet and two doubly degenerate doublets. The additional Zeeman field B further splits all states with different total spin projection S_z^{tot}, and in Fig. 1(c) we qualitatively sketch the resulting lower part of the spectrum of (1) in the $(1,1,1)$ region as a function of ϵ, where we assume that $t_{12} = t_{23} \equiv \tau$ and use $E_Z = g\mu_B B$.

At $\epsilon = 0$ the two spin doublet states with $S_z^{\text{tot}} = -\frac{1}{2}$ are $|0\rangle = (|\downarrow\downarrow\uparrow\rangle + |\uparrow\downarrow\downarrow\rangle - 2|\downarrow\uparrow\downarrow\rangle)/\sqrt{6}$ and $|1\rangle = (|\downarrow\downarrow\uparrow\rangle - |\uparrow\downarrow\downarrow\rangle)/\sqrt{2}$ and provide a basis for a qubit that can be controlled fully by electrical means [5–8,15,28]: The qubit splitting reads (to lowest order in τ) $\hbar\omega = 2\tau^2(U - U_c)/E_o E_i$, with $E_o = U - 2U_c - V_m$ and $E_i = U + V_m$, which can be controlled through τ and V_m, and a small ϵ yields a term $\propto \epsilon\,\hat{\sigma}_x$ in the projected qubit Hamiltonian [29]. Close to the borders of the $(1,1,1)$ region [the regimes labeled "RX" in Fig. 1(b)] a small modulation of ϵ with frequency ω thus induces Rabi oscillations. This so-called resonant-exchange (RX) regime has the advantage that the qubit operations can be fast [6,8]. At the center of the $(1,1,1)$ region (the sweet spot, labeled "SS") the qubit should be operated with larger pulses (resonant or static) [7,14,18], but here one has the benefit that the qubit splitting is, to leading order, insensitive to noise in the gate potentials. The qubit dephasing time T_2^* is thus predicted to be orders of magnitude larger at this point than in the RX regime [23,30]. Below we will investigate the remaining dephasing at the SS in more detail.

The leading effects of charge noise can thus be suppressed by operating the qubit at the SS, and since ^{28}Si is nuclear spin free, the hyperfine interaction that reduces the dephasing time in GaAs-based spin qubits to $\sim$10 ns [6,8,31,32] is not a concern here. That leaves as possibly dominating decoherence mechanisms (i) qubit relaxation (transitions from $|1\rangle$ to $|0\rangle$) due to electron-phonon coupling and (ii) leakage out of the qubit space (dissipative transitions to the ground state $|Q_2\rangle = |\downarrow\downarrow\downarrow\rangle$) enabled by SO interaction combined with electron-phonon coupling [see the gray arrows in Fig. 1(c)] [33–35]. Since phonon-mediated relaxation of the triple-dot XO qubit has been studied before [5,15,19], we will focus here on the leakage caused by SO interaction.

We model the SO coupling for each electron with the Hamiltonian [17,36]

$$\hat{H}_{\text{SO}} = A_{xx}\hat{p}_x\hat{\sigma}_{x'} + A_{yx}\hat{p}_y\hat{\sigma}_{x'}, \qquad (2)$$

where $\hat{\mathbf{p}}$ is the electron's momentum. We exclusively focus on the spin-flip terms $\propto\sigma_{x'}$ [see Fig. 1(a)] and use $A_{xx} = \alpha\cos\vartheta + \beta(\cos\vartheta\sin 2\chi + \sin\vartheta\cos 2\chi)$ and $A_{yx} = \alpha\sin\vartheta + \beta(\cos\vartheta\cos 2\chi - \sin\vartheta\sin 2\chi)$, where α and β are the amplitudes of the Rashba and Dresselhaus terms, respectively. Rashba SO coupling in Si-based quantum wells is predicted to come from structural inversion asymmetry arising from electric fields set up by interface effects [37,38]. Dresselhaus SO coupling is usually associated with inversion asymmetry of the crystal lattice, which is, in principle, absent in Si [10,39]. However, theoretical work predicted that microscopic details (such as the exact number of atomic Si layers in the well or roughness of the interfaces) can give rise to a Dresselhaus-like term that could be comparable to or even dominate over the Rashba term [40–42]; this was recently confirmed by several experiments [38,43,44].

For the electron-phonon coupling we use the Hamiltonian [37,45,46]

$$\hat{H}_{\text{e-ph}} = \sum_{\mathbf{k},p} \lambda_{\mathbf{k},p}\hat{\rho}_{\mathbf{k}}(\hat{a}_{\mathbf{k},p} + \hat{a}_{-\mathbf{k},p}^\dagger), \qquad (3)$$

with $\hat{\rho}_{\mathbf{k}} = \int d\mathbf{r} e^{-i\mathbf{k}\cdot\mathbf{r}} \hat{\rho}(\mathbf{r})$ being the Fourier transform of the electronic density operator, $\hat{a}^{\dagger}_{\mathbf{k},p}$ being the creation operator of a phonon with wave vector $\mathbf{k}$ and polarization p, and the coupling parameters $\lambda_{\mathbf{k},p}$ given by

$$|\lambda_{\mathbf{k},p}|^2 = \frac{\hbar}{2\rho_0 v_p k \mathcal{V}} \big[\Xi_d \mathbf{e}^p_k \cdot \mathbf{k} + \Xi_u \big(\mathbf{e}^p_k\big)_z k_z \big]^2, \qquad (4)$$

with v_p being the (polarization-dependent) sound velocity, ρ_0 being the electron density, $\mathcal{V}$ being the normalization volume, Ξ_u and Ξ_d being the uniaxial shear and dilatation deformation potentials [47], and $\mathbf{e}^l_k$ and $\mathbf{e}^t_k$ being unit vectors along the longitudinal and transversal directions of phonon propagation.

For localized electrons, such as in quantum dots, $\langle\hat{\mathbf{p}}\rangle$ vanishes, and therefore SO interaction does not directly couple states that have the same orbital wave function but opposite spin. Spin-flip transitions within the orbital ground state thus require the excitation of a virtual state which involves finite motion of the electrons. We will investigate three such mechanisms: (i) virtual tunneling to a neighboring dot (an "exchange-enabled" spin flip), (ii) virtual excitation of a higher orbital on the same dot, and (iii) virtual excitation of the other valley state, also on the same dot. All three mechanisms, in combination with the emission of a phonon to ensure energy conservation, can thus lead to a spin flip and thereby cause leakage out of the qubit space as discussed above.

We should note, however, that in realistic systems one often cannot treat the orbital or valley index of an excited state as a good quantum number, the actual states being of a mixed valley-orbital nature [10,48]. For clarity of presentation, we will first investigate the cases of pure virtual orbital and pure virtual valley excitation separately and then, at the end of Sec. III C, discuss how our results relate to the case of mixed valley-orbital states.

III. ANALYTIC RESULTS

We now investigate the three spin-orbit-mediated leakage mechanisms in more detail, and we evaluate the leakage rates $\Gamma_{1,0}$ from qubit states $|1\rangle$ and $|0\rangle$ to the ground state $|Q_2\rangle$, focusing on $\epsilon = 0$ and symmetric tunnel coupling, $t_{12} = t_{23} \equiv \tau$. In all cases we will calculate the rates using a second-order Fermi's golden rule,

$$\Gamma_\alpha = \sum_{\mathbf{k},p} \frac{2\pi}{\hbar} \left| \sum_v \frac{\langle f|\hat{H}'|v\rangle\langle v|\hat{H}'|i\rangle}{E_v - E_i} \right|^2 \delta(E_f - E_i), \qquad (5)$$

where $\hat{H}' = \hat{H}_{\text{SO}} + \hat{H}_{\text{e-ph}}$ and the second sum runs over all possible virtual states $|v\rangle$. The initial state $|i\rangle$ is $|\alpha; \text{vac}\rangle$ with $\alpha \in \{1, 0\}$ (one of the qubit states combined with the phonon vacuum), and the final state $|f\rangle$ is $|Q_2; 1_{\mathbf{k},p}\rangle$ (the ground state combined with one phonon with wave vector $\mathbf{k}$ and polarization p).

A. Virtual spin-flip tunneling

By using $\hat{\mathbf{p}} = \frac{i}{\hbar} m^* [\hat{H}, \hat{\mathbf{r}}]$, with $\hat{H}$ as in (1) and m^* being the effective electron mass, one can derive matrix elements of $\hat{H}_{\text{SO}}$ that couple states with different spin and charge configurations [45,49]. These "spin-flip tunneling" matrix

elements couple both $|1\rangle$ and $|0\rangle$ to $|Q_2\rangle$, and phonon emission is then governed by matrix elements that do not alter the spin or orbital state of the electrons. Assuming a parabolic confinement in the quantum dots, and thus a Gaussian ground-state envelope wave function, the matrix element describing the emission of a phonon by an electron in a quantum dot j at position x_j reads

$$\langle 0_j - s; 1_{\mathbf{k},p}|\hat{H}_{\text{e-ph}}|0_j - s; \text{vac}\rangle$$

$$= i\sqrt{\frac{\hbar}{2\rho_0 v_p k \mathcal{V}}} \big[\Xi_d \mathbf{e}^p_k \cdot \mathbf{k} + \Xi_u \big(\mathbf{e}^p_k\big)_z k_z \big] e^{-\frac{1}{4}(k_x^2 + k_y^2)\sigma^2 - ik_x x_j},$$

$$(6)$$

where $|0_j - s\rangle$ denotes the state of an electron in the ground state in dot j with spin s and in the lowest valley state (denoted by the $-$ symbol).

Taking into account all three electrons, we can arrive at analytic expressions for the leakage rates. Defining $\Delta^{-2} = E_o^{-2} - E_i^{-2}$, we find to leading order in τ/Δ

$$\Gamma_1 \approx \frac{1}{16\pi} \frac{d^2}{l_{\text{so}}^2} \frac{\tau^4}{\Delta^4} \frac{\Xi_u^2 E_Z^3}{\hbar^4 v_t^5 \rho_0} f_1^{\text{ex}}\left(\frac{dE_Z}{\hbar v_t}\right), \qquad (7)$$

$$\Gamma_0 \approx \frac{3}{16\pi} \frac{d^2}{l_{\text{so}}^2} \frac{\tau^4}{\Delta^4} \frac{\Xi_u^2 E_Z^3}{\hbar^4 v_t^5 \rho_0} f_0^{\text{ex}}\left(\frac{dE_Z}{\hbar v_t}\right), \qquad (8)$$

where $l_{\text{so}} = \hbar/m^* A_{xx}$ is the relevant spin-orbit length and the functions $f_{1,0}^{\text{ex}}(x) \sim 1$ for $x \gtrsim 1$; they are given explicitly in Appendix A. To arrive at these expressions, we assumed that $E_Z \gg \tau^2/E_{i,o}$ (which is typically satisfied if $B \gtrsim 10$ mT) and $E_Z^2 \ll (\hbar v_t/\sigma)^2$ (which, for $\sigma = 15$ nm, limits $B \lesssim 2$ T). Furthermore, we used the fact that in Si $v_l \approx 2v_t$, which makes $(v_t/v_l)^5 \ll 1$. For small $E_Z^2 \ll (\hbar v_t/d)^2$ we can expand the functions $f_{1,0}^{\text{ex}}(x)$ in small x, yielding

$$\Gamma_1 \approx \frac{1}{840\pi} \frac{d^2}{l_{\text{so}}^2} \frac{\tau^4}{\Delta^4} \frac{d^4 \Xi_u^2 E_Z^7}{\hbar^8 v_t^9 \rho_0}, \qquad (9)$$

$$\Gamma_0 \approx \frac{1}{35\pi} \frac{d^2}{l_{\text{so}}^2} \frac{\tau^4}{\Delta^4} \frac{d^2 \Xi_u^2 E_Z^5}{\hbar^6 v_t^7 \rho_0}. \qquad (10)$$

We see that $\Gamma_1 \propto E_Z^7$ and $\Gamma_0 \propto E_Z^5$ in this limit, and Γ_1 is smaller than Γ_0 by a factor of $(dE_Z/\hbar v_t)^2$. In the case of substantially asymmetric tunneling amplitudes (i.e., $t_{12} \neq t_{23}$) we find that both rates scale as $\Gamma \propto E_Z^5$.

These rates can be directly compared with the qubit relaxation rate, from $|1\rangle$ to $|0\rangle$, which comes mainly via electron-phonon coupling [5,34]

$$\Gamma_{\text{rel}} = \frac{1}{70\pi} \frac{\tau^4}{\Delta^4} \frac{d^2 \Xi_u^2 (\hbar\omega)^5}{\hbar^6 v_t^7 \rho_0}, \qquad (11)$$

where $\hbar\omega$ is the qubit splitting.

Note that all relaxation rates cancel when $1/\Delta = 0$, which happens at the SS. A qubit operated at this point will therefore be highly insensitive to both dephasing due to charge noise and relaxation and leakage. Additionally, the dependence of A_{xx} on the angles χ and ϑ allows for a reduction of the leakage rates by varying the device orientation and the direction of $\mathbf{B}$: In fact, for χ equal to a multiple of $\pi/2$, we see that there are angles $\vartheta = (n + \frac{1}{2})\pi$ for which $A_{xx} = 0$. Such

strong angular dependence of spin-orbit-mediated relaxation rates is already well known from theory and experiments on double quantum dots [50–53].

B. Virtual orbital excitation

The parabolic potential that confines the electrons in the quantum dots results in Fock-Darwin eigenstates with energy splitting $E_{\mathrm{orb}} = \hbar^2/m^*\sigma^2$. The SO interaction couples the orbital ground state to the first excited state with opposite spin [17],

$$\left\langle 1_j^{\alpha}-\bar{s}\middle|\hat{p}_{\alpha}\hat{\sigma}_{x'}\middle|0_j-s\right\rangle = \frac{i\hbar}{\sqrt{2}\sigma}, \quad (12)$$

where $\bar{s}$ denotes the spin state opposite to s and the superscript α indicates which component of the wave function is in the excited state [54]. The electron-phonon Hamiltonian also couples these two orbital states [37],

$$\left\langle 1_j^{\alpha}-s; 1_{\mathbf{k},p}\middle|\hat{H}_{\mathrm{e\text{-}ph}}\middle|0_j-s; \mathrm{vac}\right\rangle$$
$$= i\sqrt{\frac{\hbar}{2\rho_0 v_p k \mathcal{V}}}\left[\Xi_d \mathbf{e}_k^p \cdot \mathbf{k} + \Xi_u\left(\mathbf{e}_k^p\right)_z k_z\right]g_{10}^{(j,\alpha)}(\mathbf{k}), \quad (13)$$

with $g_{10}^{(j,\alpha)}(\mathbf{k})$ being the Fourier transform of the overlap between the ground and first excited states on dot j,

$$g_{10}^{(j,\alpha)}(\mathbf{k}) = -\frac{i}{\sqrt{2}}k_{\alpha}\sigma e^{-\frac{1}{4}(k_x^2+k_y^2)\sigma^2 - ik_x x_j}. \quad (14)$$

The resulting leakage rates, involving the virtual excitation of an orbital state, can straightforwardly be evaluated. Compared to the exchange-enabled rates, they come with large powers of $E_{\mathrm{Z}}/E_{\mathrm{orb}}$ instead of τ/Δ, which makes them typically much smaller. Under the same assumptions as before we find

$$\Gamma_1 \approx \frac{1}{4\pi}\frac{E_{\mathrm{Z}}^4}{E_{\mathrm{orb}}^4}\frac{\Xi_u^2 E_{\mathrm{Z}}^3}{\hbar^4 v_t^5 \rho_0}f_1^{\mathrm{orb}}\left(\frac{dE_{\mathrm{Z}}}{\hbar v_t}\right), \quad (15)$$

$$\Gamma_0 \approx \frac{1}{12\pi}\frac{E_{\mathrm{Z}}^4}{E_{\mathrm{orb}}^4}\frac{\Xi_u^2 E_{\mathrm{Z}}^3}{\hbar^4 v_t^5 \rho_0}f_0^{\mathrm{orb}}\left(\frac{dE_{\mathrm{Z}}}{\hbar v_t}\right), \quad (16)$$

where the dimensionless functions $f_{1,0}^{\mathrm{orb}}(x)$ are given in Appendix A. For $x \gtrsim 1$ they are of the order of $(A_{xx}^2 + A_{yx}^2)/v_t^2$, and for small $E_{\mathrm{Z}} \ll (\hbar v_t/d)^2$ we can again expand the functions, yielding

$$\Gamma_1 \approx \frac{2}{315\pi}\frac{3A_{xx}^2 + A_{yx}^2}{v_t^2}\frac{E_{\mathrm{Z}}^4}{E_{\mathrm{orb}}^4}\frac{d^2 \Xi_u^2 E_{\mathrm{Z}}^5}{\hbar^6 v_t^7 \rho_0}, \quad (17)$$

$$\Gamma_0 \approx \frac{2}{10395\pi}\frac{5A_{xx}^2 + A_{yx}^2}{v_t^2}\frac{E_{\mathrm{Z}}^4}{E_{\mathrm{orb}}^4}\frac{d^4 \Xi_u^2 E_{\mathrm{Z}}^7}{\hbar^8 v_t^9 \rho_0}. \quad (18)$$

In this case we thus find that $\Gamma_1 \propto E_{\mathrm{Z}}^9$ and $\Gamma_0 \propto E_{\mathrm{Z}}^{11}$ and that now Γ_1 is *larger* than Γ_0 by a factor of $(dE_{\mathrm{Z}}/\hbar v_t)^{-2}$ (on top of a rather large difference in numerical prefactors), opposite to the exchange-enabled rates. Comparing the two mechanisms qualitatively, we see that the factor $d^2\tau^4/l_{\mathrm{so}}^2\Delta^4$ in the exchange-enabled rates is replaced here by the factor $A^2 E_{\mathrm{Z}}^4/v_t^2 E_{\mathrm{orb}}^4$, which is typically much smaller [55]. Another qualitative difference is that the "orbital-assisted" rates (15)

and (16) do not depend on the tuning through Δ and thus survive at the SS.

We can compare these results with Eq. (12) in Ref. [37], where the authors calculated the ground-state spin relaxation rate in a *single* quantum dot via virtual excitation of an orbital state. We see that our results are fundamentally the same, apart from extra factors of $(dE_{\mathrm{Z}}/v_t\hbar)^2$, which result from the multielectron/multidot nature of our system and account for interference between spin-flip amplitudes on different dots. If we were to make the orbital energy splitting substantially different on each dot, we would also find $\Gamma \propto E_{\mathrm{Z}}^7$ for both relaxation rates.

C. Virtual valley excitation

The band gap in bulk Si is indirect, and the conduction band has six minima, away from $k = 0$. In most Si-based heterostructures strain splits off four of these minima, leaving two minima at $\mathbf{k} \approx \pm 0.85\,k_{\mathrm{max}}\hat{z}$, where $\hat{z}$ is the growth direction of the structure. Localized electrons in the conduction band thus have an extra "valley" degree of freedom and can be described by the wave function

$$\psi^{(v)} = F^{(v)}(\mathbf{r})\left[\alpha_1^{(v)}u_1(\mathbf{r})e^{ik_z z} + \alpha_2^{(v)}u_2(\mathbf{r})e^{-ik_z z}\right], \quad (19)$$

where $F^{(v)}(\mathbf{r})$ is the envelope wave function corresponding to valley v and $u_{1,2}(\mathbf{r})$ is the lattice-periodic part of the Bloch functions at the conduction band minima at $\pm k_z$. Inhomogeneities such as disorder and interface roughness typically couple the two minima, resulting in eigenstates with $\alpha_1^{(\pm)} = \frac{1}{\sqrt{2}}$ and $\alpha_2^{(\pm)} = \pm\frac{1}{\sqrt{2}}$.

Both SO and electron-phonon interaction can couple opposite valley states [37], and virtual valley excitation can thus cause leakage in a way similar to virtual orbital excitation. The relevant matrix elements, however, depend sensitively on details of the confinement along the z direction that are hard to predict. We thus take a slightly more qualitative approach and start by employing the dipole approximation $e^{-i\mathbf{k}\cdot\mathbf{r}} \approx 1 - i\mathbf{k}\cdot\mathbf{r}$ in the electron-phonon Hamiltonian (3), which amounts to assuming that the emitted phonon has a wavelength much larger than the electronic confinement length [equivalent to the assumption $E_{\mathrm{Z}}^2 \ll (\hbar v_t/\sigma)^2$ used before]. This allows us to write

$$\left\langle 0_j+s; 1_{\mathbf{k},p}\middle|\hat{H}_{\mathrm{e\text{-}ph}}\middle|0_j-s; \mathrm{vac}\right\rangle$$
$$\approx \sqrt{\frac{\hbar}{2\rho_0 v_p k \mathcal{V}}}\left[\Xi_d \mathbf{e}_k^p \cdot \mathbf{k} + \Xi_u\left(\mathbf{e}_k^p\right)_z k_z\right]e^{-ik_x x_j}\mathbf{k}\cdot\mathbf{r}_{+-},$$
$$\quad (20)$$

with $\mathbf{r}_{+-} = \langle 0_j+s|\mathbf{r}|0_j-s\rangle$ being the valley dipole matrix element. If we use again $\hat{\mathbf{p}} = \frac{i}{\hbar}m^*[\hat{H}, \mathbf{r}]$, then we can express the SO Hamiltonian in terms of the same dipole matrix elements. The precise magnitude of these elements depends again on microscopic details, and for simplicity we will use $|z_{+-}| \ll |x_{+-}|, |y_{+-}|$ and assume $x_{+-} = y_{+-} \equiv r_d$ [56,57]. This phenomenological parameter can be related to the magnitude of SO-induced anticrossings in the electronic spectrum between states with different spin and valley indices; for Si metal-oxide-semiconductor-based quantum dots $|r_d| \sim 1$–2 nm has been reported [57].

We can now calculate the leakage rates and find, using again the same assumptions,

$$\Gamma_1 \approx \frac{1}{\pi} \frac{A^2}{v_t^2} \frac{|r_d|^4}{l_Z^4} \frac{E_Z^2}{E_v^2} \frac{\Xi_u^2 E_Z^3}{\hbar^4 v_t^5 \rho_0} f_1^{\mathrm{val}}\left(\frac{dE_Z}{\hbar v_t}\right), \quad (21)$$

$$\Gamma_0 \approx \frac{1}{3\pi} \frac{A^2}{v_t^2} \frac{|r_d|^4}{l_Z^4} \frac{E_Z^2}{E_v^2} \frac{\Xi_u^2 E_Z^3}{\hbar^4 v_t^5 \rho_0} f_0^{\mathrm{val}}\left(\frac{dE_Z}{\hbar v_t}\right), \quad (22)$$

where, for convenience of notation, we introduced the Zeeman length $l_Z = \hbar/\sqrt{m^* E_Z}$ and E_v denotes the splitting between the two valley states. The parameter $A \sim \alpha, \beta$ sets the strength of the SO interaction; we cannot resolve the detailed dependence on the angles ϑ, χ in this case since that would require knowing the exact relative magnitude and phase of x_{+-} and y_{+-} as well. The dimensionless functions $f_{1,0}^{\mathrm{val}}(x)$, given in Appendix A, are again of the order of 1 for $x \gtrsim 1$ and can be expanded in small x when $E_Z^2 \ll (\hbar v_t/d)^2$, giving

$$\Gamma_1 \approx \frac{32}{315\pi} \frac{A^2}{v_t^2} \frac{|r_d|^4}{l_Z^4} \frac{E_Z^2}{E_v^2} \frac{d^2 \Xi_u^2 E_Z^5}{\hbar^6 v_t^7 \rho_0}, \quad (23)$$

$$\Gamma_0 \approx \frac{16}{3465\pi} \frac{A^2}{v_t^2} \frac{|r_d|^4}{l_Z^4} \frac{E_Z^2}{E_v^2} \frac{d^4 \Xi_u^2 E_Z^7}{\hbar^8 v_t^9 \rho_0}. \quad (24)$$

We find again $\Gamma_1 \propto E_Z^9$ and $\Gamma_0 \propto E_Z^{11}$, as well as that Γ_1 is larger than Γ_0 by a factor of $(dE_Z/\hbar v_t)^{-2}$ and that the rates do not depend on tuning parameters, all qualitatively similar to the rates based on virtual orbital excitation. Comparing the rest of the expressions, we find that the valley-assisted rates are smaller than the orbital-assisted ones by a factor of $\sim |r_d|^4 E_{\mathrm{orb}}^4/\sigma^4 E_v^2$, where typically $|r_d| \sim 1$–2 nm and $\sigma \sim$ 10–30 nm, which makes this a very small factor. A significant variation of E_v or $|r_d|$ over the dots would yield relaxation rates that scale as $\Gamma \propto E_Z^7$ in both cases.

In the presence of valley-orbital mixing of the excited states it is also hard to write analytic expressions for the dipole matrix elements needed. In this case Eqs. (21)–(24) are the most useful results, where r_d now describes the dipole matrix element between the ground state and first excited valley-orbital state and E_v should, of course, be replaced by the valley-orbital ground-state gap E_{vo}.

IV. NUMERICAL RESULTS

We corroborate our approximate analytic results with a numerical evaluation of the leakage rates across the whole (1,1,1) charge region. We focus here on the dominating exchange-assisted mechanism of Sec. III A, which is also the only one that shows a dependence on the tuning parameters ϵ and V_m.

We start by diagonalizing the Hamiltonian $\hat{H} + \hat{H}_{\mathrm{SO}}$, disregarding the excited orbital and valley states. We then identify in the spectrum the two qubit states $|1\rangle$, $|0\rangle$ (the spin doublet states with $S_z^{\mathrm{tot}} = -\frac{1}{2}$) and the quadruplet state $|Q_2\rangle$. Using Fermi's golden rule,

$$\Gamma_\alpha = \frac{2\pi}{\hbar} \sum_{\mathbf{k},p} |\langle Q_2; 1_{\mathbf{k},p}|\hat{H}_{\mathrm{e\text{-}ph}}|\alpha; \mathrm{vac}\rangle|^2 \delta(E_f - E_i), \quad (25)$$

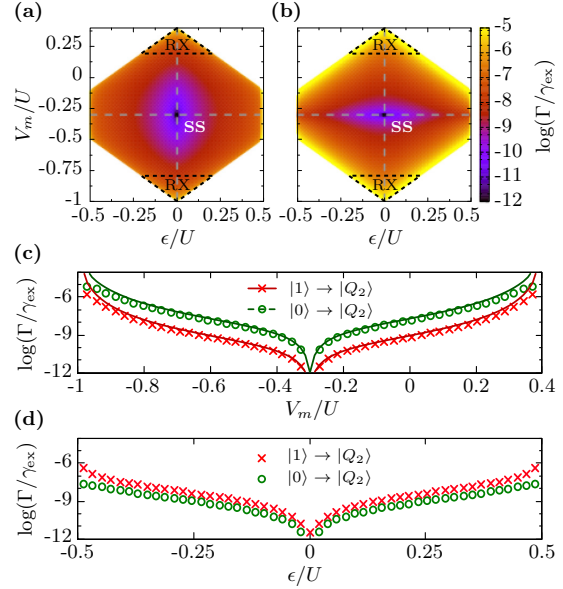we finally calculate the two leakage rates numerically.

FIG. 2. Spin-flip-tunneling-assisted leakage rates out of the qubit space across the whole (1,1,1) charge region, from (a) $|1\rangle$ and (b) $|0\rangle$ to $|Q_2\rangle$ in units of $\gamma_{\mathrm{ex}} = d^2 \Xi_u^2 E_Z^3/l_{\mathrm{so}}^2 \hbar^4 v_t^5 \rho_0$ (see text for the choice of parameters). (c) $\Gamma_{1,0}$ as a function of V_m for $\epsilon = 0$ (circles and crosses), i.e., along the vertical dashed lines in (a) and (b). Solid lines show the analytical results from Eqs. (9) and (10). (d) $\Gamma_{1,0}$ as a function of ϵ for $V_m = -0.3\,U$, i.e., along the horizontal dashed lines in (a) and (b).

The results are shown in Fig. 2, where we plot the leakage rates in units of $\gamma_{\mathrm{ex}} \equiv d^2 \Xi_u^2 E_Z^3/l_{\mathrm{so}}^2 \hbar^4 v_t^5 \rho_0$. We used $t_{12} = t_{23} \equiv \tau = 16$ μeV, $U = 50\tau$, $U_c = 15\tau$, $E_Z = 2\tau$ and set the angles $\vartheta = \chi = 0$. We assumed Si/SiGe quantum dots with $\sigma = 10$ nm and $d = 100$ nm, and we used the material parameters $\alpha = 609$ m/s, $\Xi_d = 5$ eV, $\Xi_u = 9$ eV, $\rho_0 = 2330$ kg/m^3, $v_l = 9150$ m/s, $v_t = 5000$ m/s [30,46,58,59] and the transverse effective mass $m^* = 0.19m_e$ [58,60], for which we find $\gamma_{\mathrm{ex}} = 960$ kHz. The value of β is irrelevant in this case since A_{xx} is independent of β for our choice of angles ϑ and χ. Figure 2(a) shows the rate Γ_1, and Fig. 2(b) shows the rate Γ_0. We see that the magnitude of the rates ranges from $\sim 10^{-12}\,\gamma_{\mathrm{ex}}$ to $\sim 10^{-5}\,\gamma_{\mathrm{ex}}$, which is typically much smaller than the decoherence rates due to other mechanisms, such as phonon-mediated qubit relaxation (transitions from $|1\rangle$ to $|0\rangle$) and dephasing caused by charge noise. Vertical and horizontal dashed lines indicate the line cuts that we show in Figs. 2(c) and 2(d). Here we plot the leakage rates as a function of V_m for $\epsilon = 0$ [Fig. 2(c)] and as a function of ϵ for $V_m = -0.3U$ [Fig. 2(d)]. Circles and crosses present numerical results, and the solid lines in Fig. 2(c) show the analytical results of Eqs. (9) and (10), which indeed agree well with the numerical results.

At the SS the qubit can also be operated electrically by tuning the tunnel barriers, without the need of leaving this point of low decoherence, as has been pointed out before

[18]. Our numerical calculations confirm that at the SS the relaxation rates between any two states in the lowest part of the spectrum (including the qubit relaxation rate Γ_{rel}) are strongly suppressed, not only for $t_{12} = t_{23}$ as in Fig. 2 but for any combination of tunneling energies. The triple-dot spin qubit can thus be operated at the SS via a modulation of the tunneling amplitudes (the always-on exchange-only qubit [15]) while being highly insensitive to charge noise, relaxation, and SO-assisted leakage. The constant contributions of virtual valley and orbital excitation to the leakage rates (see Secs. III B and III C) are estimated to be $\sim 10^{-10} \gamma_{\text{ex}}$ for our choice of parameters and therefore do not affect these conclusions qualitatively.

V. DEPHASING AT THE SS

Dephasing in ^{28}Si-based triple-dot spin qubits is believed to mainly come from electric noise in the qubit's environment [13,24]. As a first approximation, one can understand such dephasing by assuming the noise manifests itself as fluctuations of the gate potentials, $V_i(t) = V_i + \delta V_i(t)$, that are Gaussian and have zero mean. To leading order, the qubit frequency then acquires a time dependence $\omega(t) = \omega + \delta\omega(t)$, with $\delta\omega(t) = \sum_i (\partial\omega/\partial V_i)\delta V_i(t)$, and a qubit prepared in the coherent superposition $|\psi(0)\rangle = |+\rangle = \frac{1}{\sqrt{2}}(|0\rangle + |1\rangle)$ will thus evolve as $|\psi(t)\rangle = \frac{1}{\sqrt{2}}(|0\rangle + e^{i[\phi(t)+\delta\phi(t)]}|1\rangle)$, where $\delta\phi(t) = \int_0^t dt'\,\delta\omega(t')$. The noise-induced dephasing can then be characterized by investigating the expectation value $\langle e^{i\delta\phi(t)}\rangle$: Since the fluctuations $\delta\omega(t)$, and thus the fluctuations $\delta\phi(t)$, are Gaussian, only the second cumulant in the expansion of $\langle e^{i\delta\phi(t)}\rangle$ is nonzero, resulting in low-frequency noise in an exponential decay of the coherent qubit oscillations $\sim e^{-t^2/T_\varphi^2}$, where the exact form of the dephasing time T_φ depends on the detailed noise spectrum [23,24,61,62].

Exactly at the SS, all first-order derivatives $\partial\omega/\partial V_i$ vanish, and therefore this type of dephasing is highly suppressed. To understand the remaining charge-noise-induced dephasing at the SS, one could thus try to use the same approach but now focus on the next order, $\delta\omega(t) = \sum_{i,j} (\partial^2\omega/\partial V_i\partial V_j)\delta V_i(t)\delta V_j(t)$. In this case, however, the fluctuations $\delta\omega(t)$ [and thus $\delta\phi(t)$] are no longer Gaussian, and one would thus have to include all cumulants in the expansion of $\langle e^{i\delta\phi(t)}\rangle$ [63]. Therefore it is more convenient to investigate the explicit time evolution of the qubit [5,7,15,28]. Assuming for simplicity quasistatic fluctuations [23,61,62], we can evaluate the time-dependent probability $P(t) = |\langle+|\psi(t)\rangle|^2$ to find the qubit in the state $|+\rangle$ and average this probability over the fluctuations δV_i [64]. To good approximation we then find (see Appendix B for details)

$$\langle P(t)\rangle = \frac{1}{2} + \frac{\cos(\omega t - \arctan[t/T_\varphi])}{2\sqrt{1 + t^2/T_\varphi^2}}, \quad (26)$$

where $T_\varphi = \hbar(U - U_c)^3/4\tau^2\xi^2$ is the dephasing time, with $\xi^2 = \langle(\delta V_i)^2\rangle$ being the variance of the fluctuations. At the SS the leading-order contribution of the charge noise to dephasing thus results in (i) a time-dependent phase shift in the qubit oscillations, which goes to $-\pi/2$ for $t \gtrsim T_\varphi$, and (ii) a decay of the coherent oscillations with a
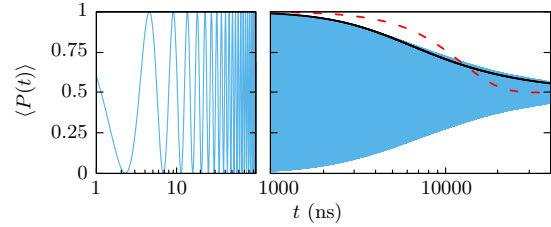

FIG. 3. Numerically calculated time-dependent return probability $|\langle+|\psi(t)\rangle|^2$ after initializing in $|+\rangle$, averaged over 10^5 different sets of $\delta V_{1,2,3}$ taken from a normal distribution with $\xi = 5\,\mu$eV (thin blue line). The thick black line shows the envelope function of the oscillations as predicted by Eq. (26), and the dashed red line shows the best fit obtainable assuming an exponential envelope of the form $\frac{1}{2} + \frac{1}{2}e^{-t^2/\tilde{T}_\varphi^2}$.

power-law behavior, $\sim T_\varphi/t$ for large times, in contrast to the exponential decay $\sim e^{-t^2/T_\varphi^2}$ one finds away from the SS, whenever $\sum_i (\partial\omega/\partial V_i)\delta V_i(t) \gg \sum_{i,j} (\partial^2\omega/\partial V_i\partial V_j)\delta V_i(t)\delta V_j(t)$ [24]. One can also use a detailed cumulant-expansion approach to describe quadratic coupling to Gaussian noise, which leads to the same long-time behavior as we found here [63].

We can also calculate the averaged probability $\langle P(t)\rangle$ numerically, again assuming quasistatic charge noise. Using the same parameters as before, we tune the Hamiltonian (1) to the SS ($\epsilon = 0$, $V_m = -0.3\,U$) but then add random offsets $\delta V_{1,2,3}$, taken from a normal distribution with $\xi = 5\,\mu$eV [14]. We diagonalize the resulting Hamiltonian, identify the two qubit states $|1\rangle$ and $|0\rangle$, and create an initial state $|+\rangle = \frac{1}{\sqrt{2}}(|0\rangle + |1\rangle)$. We then evaluate numerically the time-dependent qubit state $|\psi(t)\rangle = \exp\{-\frac{i}{\hbar}\hat{H}t\}|+\rangle$, and from this we can calculate $P(t)$ for the specific set of δV_i chosen. This procedure is repeated 10^5 times, and the resulting average $\langle P(t)\rangle$ is shown by the blue curve in Fig. 3. As expected, we see an oscillating probability that decays to 1/2 over time. The black solid line shows the envelope function of the decaying oscillations, as given by Eq. (26), where we have $T_\varphi \approx 4\,\mu$s for our choice of parameters. We see that the power-law decay predicted by (26) matches the numerical results very well. For comparison we include a best fit of the form $\frac{1}{2} + \frac{1}{2}e^{-t^2/\tilde{T}_\varphi^2}$ (red dashed line), which yields $\tilde{T}_\varphi \approx 12.4\,\mu$s but indeed shows a much worse agreement with our numerical results than the power-law from (26).

VI. CONCLUSIONS

Leakage out of the qubit subspace in XO qubits hosted in ^{28}Si-based triple quantum dots is caused mainly by SO interaction via virtual spin-flip tunneling. Together with spin-conserving phonon emission, this results in tuning-dependent leakage rates that scale as $\Gamma_1 \propto E_Z^7$ and $\Gamma_0 \propto E_Z^5$ and are strongly reduced at the SS, where the qubit is minimally sensitive to charge noise as well. We found that the other two mechanisms of leakage we investigated, virtual orbital and valley excitation, result in much smaller relaxation rates, scaling as $\Gamma_1 \propto E_Z^9$ and $\Gamma_0 \propto E_Z^{11}$; they are constant

throughout the entire (1,1,1) charge region, thus becoming the most relevant mechanism of leakage only at the SS. Further, we showed that also (spin-conserving) qubit relaxation, enabled by electron-phonon coupling, is minimal at the SS, making this an ideal operation point in many respects.

We also investigated the residual effects of charge noise at the SS, which are most likely the dominating source of pure dephasing at that point. We found that slow electric fluctuations result in dephasing that makes coherent qubit oscillations decay as $\propto 1/t$, in analogy to Refs. [63,64]; this

in contrast to the exponential decay that dominates elsewhere in the (1,1,1) charge region.

APPENDIX A: DETAILED ANALYTIC RESULTS

The dimensionless functions used in the analytic results presented in Sec. II read explicitly

$$f_1^{\text{ex}}(x) = \frac{4}{5} + \frac{1}{16x^5}[128x(x^2 - 9)\cos x - 2(4x^2 - 9)(x\cos 2x + 64\sin x) + (16x^2 - 9)\sin 2x], \tag{A1}$$

$$f_0^{\text{ex}}(x) = \frac{4}{15} + \frac{1}{16x^5}[2x(4x^2 - 9)\cos 2x - (16x^2 - 9)\sin 2x], \tag{A2}$$

$$f_1^{\text{orb}}(x) = \frac{8}{105}\left(a_{xx}^2 + a_{yx}^2\right) + \frac{1}{32x^6}\left[3a_{yx}^2(8x^2 - 15) + 2a_{xx}^2(8x^4 - 78x^2 + 135)\right]\cos 2x$$
$$+ \frac{1}{64x^7}\left[a_{yx}^2(16x^4 - 84x^2 + 45) - 2a_{xx}^2(64x^4 - 258x^2 + 135)\right]\sin 2x, \tag{A3}$$

$$f_0^{\text{orb}}(x) = \frac{8}{35}\left(a_{xx}^2 + a_{yx}^2\right) + \frac{1}{64x^7}\left\{512x\left[3a_{yx}^2(2x^2 - 15) + a_{xx}^2(x^4 - 39x^2 + 270)\right]\cos x\right.$$
$$- 2x\left[3a_{yx}^2(8x^2 - 15) + 2a_{xx}^2(8x^4 - 78x^2 + 135)\right]\cos 2x + 512\left[a_{yx}^2(x^4 - 21x^2 + 45) - a_{xx}^2(8x^4 - 129x^2 + 270)\right]$$
$$\times \sin x - \left[a_{yx}^2(16x^4 - 84x^2 + 45) - 2a_{xx}^2(64x^4 - 258x^2 + 135)\right]\sin 2x\right\}, \tag{A4}$$

$$f_1^{\text{val}}(x) = \frac{16}{105} + \frac{1}{64x^7}[2x(16x^4 - 132x^2 + 225)\cos 2x - (112x^4 - 432x^2 + 225)]\sin 2x, \tag{A5}$$

$$f_0^{\text{val}}(x) = \frac{16}{35} + \frac{8}{x^7}[x(x^4 - 33x^2 + 225)\cos x - (7x^4 - 108x^2 + 225)\sin x]$$
$$- \frac{1}{64x^7}[2x(16x^4 - 132x^2 + 225)\cos 2x - (112x^4 - 432x^2 + 225)\sin 2x], \tag{A6}$$

where the spin-orbit velocities in (A3) and (A4) are rescaled with the transverse phonon velocity, $a_{xx,yx} \equiv A_{xx,yx}/v_t$.

APPENDIX B: CHARGE NOISE AND DEPHASING AT THE SWEET SPOT

In the absence of significant hyperfine interaction, the main source of decoherence for exchange-based spin qubits is believed to be (low-frequency) charge noise on the gate electrodes [14–16]. Such noise results in fluctuations of the on-site potentials as used in the Hamiltonian $\hat{H}$ in Eq. (1),

$$V_i(t) = V_i + \delta V_i(t). \tag{B1}$$

This causes the projected qubit Hamiltonian to fluctuate as well,

$$\hat{H}_{\text{qubit}} = \frac{\hbar}{2}[\omega_0 + \delta\omega_z(t)]\hat{\sigma}_z + \frac{\hbar}{2}\delta\omega_x(t)\hat{\sigma}_x. \tag{B2}$$

We focus on pure dephasing in this qubit basis; that is, we investigate how the phase of the qubit gets randomized through the fluctuations in the qubit splitting $\delta\omega_z(t)$. To this end, we consider the system to be prepared in the state $|+\rangle = \frac{1}{\sqrt{2}}(|0\rangle + |1\rangle)$ at $t = 0$. After some time t, the sys-

tem evolved into the state $|\psi(t)\rangle = \frac{1}{\sqrt{2}}(|0\rangle + e^{i\phi(t)}|1\rangle)$, where $\phi(t) = \omega_0 t + \delta\phi(t)$, the unknown part of the phase being $\delta\phi(t) = \int_0^t \delta\omega_z(t')dt'$.

The expectation value of this random component of the phase can be found by evaluating $\ln\langle e^{i\phi(t)}\rangle$. For simplicity we will assume quasistatic (time independent during each individual time evolution) Gaussian noise in V_i:

$$\delta\phi(t) = t\sum_{i=1}^3 \frac{\partial\omega_z}{\partial V_i}\delta V_i + \frac{t}{2}\sum_{i,j}\frac{\partial^2\omega_z}{\partial V_i \partial V_j}\delta V_i\delta V_j + \mathcal{O}(\delta V^3). \tag{B3}$$

Usually, one then focuses on the leading (first-order) term, which is linear in the fluctuations δV_i. This makes $\delta\omega_z$ also a Gaussian variable, and then one can do a cumulant expansion of the logarithm,

$$\ln\langle e^{i\delta\phi(t)}\rangle = \sum_{n=1}^\infty \kappa_n \frac{(it)^n}{n!}, \tag{B4}$$

with κ_n being the nth cumulant of the distribution of $\delta\omega_z$, and use the fact that for Gaussian variables with zero mean only the second cumulant $\kappa_2 = \sum_i (\partial\omega_z/\partial V_i)^2\langle\delta V_i^2\rangle$ is nonzero.

This yields the familiar result $\ln\langle e^{i\phi(t)}\rangle = -\frac{1}{2}t^2\kappa_2$, from which one can extract an approximate dephasing time.

At the sweet spot, however, where we expect this dephasing time to be maximal, the first derivative of ω_z vanishes (per definition [18,24]), and one has to use the next (second-)order term in the series expansion of the phase (B3). A subtle point, sometimes overlooked, is that, although the fluctuations δV_i are Gaussian, the product $\delta V_i \delta V_j$ of two Gaussian random variables is not Gaussian anymore. This implies that the cumulant expansion has many more nonzero terms that become relevant at long times, causing $\ln\langle e^{i\phi(t)}\rangle \neq -\frac{1}{2}t^2\kappa_2$ [63]. One can use such an equality only as long as $\frac{\partial\omega_z}{\partial V_i} \gg \frac{\partial^2\omega_z}{\partial V_i \partial V_j}$, a condition that is not satisfied at the sweet spot.

To extend the analysis to the sweet spot we focus on the Schrödinger equation resulting from the effective qubit Hamiltonian instead. We will consider only a diagonal Hamiltonian,

$$i\hbar\frac{\partial}{\partial t}\psi(t) = \frac{\hbar}{2}(\omega_z + \delta\omega_z)\sigma^z\psi(t), \quad (B5)$$

and use again the initial condition $|\psi(t=0)\rangle = |+\rangle = \frac{1}{\sqrt{2}}(|0\rangle + |1\rangle)$, with $|0\rangle$ and $|1\rangle$ being two eigenvalues of the qubit Hamiltonian for $\delta\omega_z = 0$. In this case, the probability of finding the qubit in the initial state $|+\rangle$ after time t is

$$P = |\langle +|\psi(t)\rangle|^2 = \cos\left(\frac{t[\omega_z + \delta\omega_z]}{2}\right)^2. \quad (B6)$$

For the exchange-only qubit at the sweet spot, the fluctuation $\delta\omega_z$ is given by the second-order term

$$\delta\omega_z = \frac{\tau^2}{(U-U_c)^3}[(\delta V_2 - \delta V_1)^2 + (\delta V_2 - \delta V_3)^2], \quad (B7)$$

where we again have set $t_{12} = t_{23} \equiv \tau$.

In order to average over the fluctuations, we define two variables, $x_1 = \delta V_2 - \delta V_1$ and $x_2 = \delta V_2 - \delta V_3$, that we will consider independent for simplicity. These variables have mean zero and standard deviation $\sqrt{2}\xi$ (with ξ being the standard deviation of the original variables δV_i) and can be combined into one χ^2-distributed random variable $y = \frac{x_1^2}{2\xi^2} + \frac{x_2^2}{2\xi^2}$. With this the probability becomes

$$P = \frac{1}{2}\int_0^\infty dy\, e^{-y/2}\cos^2\left[\frac{t}{2\hbar}\left(\frac{2\tau^2}{U-U_c} + \frac{2\sigma^2\tau^2}{(U-U_c)^3}y\right)\right]. \quad (B8)$$

This integral can be solved analytically, yielding

$$P = \frac{1}{2} + \frac{\cos\left(t\frac{2\tau^2}{\hbar(U-U_c)} - \arctan\left[t\frac{4\tau^2\xi^2}{\hbar(U-U_c)^3}\right]\right)}{2\sqrt{1 + t^2\frac{16\tau^4\xi^4}{\hbar^2(U-U_c)^6}}}. \quad (B9)$$

We see that, as expected, the probability oscillates with a frequency $2\tau^2/\hbar(U-U_c)$ (while also gradually acquiring a phase shift that goes to $-\pi/2$ for $t \to \infty$). The amplitude of the oscillations decays within the envelope function

$$P_{\text{env}} = \frac{1}{2} + \frac{1}{2\sqrt{1 + t^2\frac{16\tau^4\xi^4}{\hbar^2(U-U_c)^6}}}, \quad (B10)$$

which, for long times, predicts a decay $\propto T_\varphi/t$ with a dephasing time of $T_\varphi = \hbar(U-U_c)^3/4\tau^2\xi^2$. This is in contrast to the exponential decay $\propto e^{-t^2/T_\varphi^2}$ that is predicted by the "cumulant expansion method" [23,24]. A simple simulation of the time evolution of the state $|+\rangle$ under the action of quasistatic random noise at the sweet spot corroborates this result (see Sec. V).

[1] D. Loss and D. P. DiVincenzo, Phys. Rev. A **57**, 120 (1998).

[2] J. R. Petta, A. C. Johnson, J. M. Taylor, E. A. Laird, A. Yacoby, M. D. Lukin, C. M. Marcus, M. P. Hanson, and A. C. Gossard, Science **309**, 2180 (2005).

[3] F. H. L. Koppens, C. Buizert, K. J. Tielrooij, I. T. Vink, K. C. Nowack, T. Meunier, L. P. Kouwenhoven, and L. M. K. Vandersypen, Nature (London) **442**, 766 (2006).

[4] D. P. DiVincenzo, D. Bacon, J. Kempe, G. Burkard, and K. B. Whaley, Nature (London) **408**, 339 (2000).

[5] J. M. Taylor, V. Srinivasa, and J. Medford, Phys. Rev. Lett. **111**, 050502 (2013).

[6] J. Medford, J. Beil, J. M. Taylor, E. I. Rashba, H. Lu, A. C. Gossard, and C. M. Marcus, Phys. Rev. Lett. **111**, 050501 (2013).

[7] F. K. Malinowski, F. Martins, P. D. Nissen, S. Fallahi, G. C. Gardner, M. J. Manfra, C. M. Marcus, and F. Kuemmeth, Phys. Rev. B **96**, 045443 (2017).

[8] J. Medford, J. Beil, J. M. Taylor, S. D. Bartlett, A. C. Doherty, E. I. Rashba, D. P. DiVincenzo, H. Lu, A. C. Gossard, and C. M. Marcus, Nat. Nanotechnol. **8**, 654 (2013).

[9] C. B. Simmons, M. Thalakulam, B. M. Rosemeyer, B. J. Van Bael, E. K. Sackmann, D. E. Savage, M. G. Lagally, R. Joynt, M. Friesen, S. N. Coppersmith, and M. A. Eriksson, Nano Lett. **9**, 3234 (2009).

[10] F. A. Zwanenburg, A. S. Dzurak, A. Morello, M. Y. Simmons, L. C. L. Hollenberg, G. Klimeck, S. Rogge, S. N. Coppersmith, and M. A. Eriksson, Rev. Mod. Phys. **85**, 961 (2013).

[11] M. Veldhorst, J. C. C. Hwang, C. H. Yang, A. W. Leenstra, B. de Ronde, J. P. Dehollain, J. T. Muhonen, F. E. Hudson, K. M. Itoh, A. Morello, and A. S. Dzurak, Nat. Nanotechnol. **9**, 981 (2014).

[12] J. T. Muhonen, J. P. Dehollain, A. Laucht, F. E. Hudson, R. Kalra, T. Sekiguchi, K. M. Itoh, D. N. Jamieson, J. C. McCallum, A. S. Dzurak, and A. Morello, Nat. Nanotechnol. **9**, 986 (2014).

[13] K. Eng, T. D. Ladd, A. Smith, M. G. Borselli, A. A. Kiselev, B. H. Fong, K. S. Holabird, T. M. Hazard, B. Huang, P. W. Deelman, I. Milosavljevic, A. E. Schmitz, R. S. Ross, M. F. Gyure, and A. T. Hunter, Sci. Adv. **1**, e1500214 (2015).

[14] F. Martins, F. K. Malinowski, P. D. Nissen, E. Barnes, S. Fallahi, G. C. Gardner, M. J. Manfra, C. M. Marcus, and F. Kuemmeth, Phys. Rev. Lett. **116**, 116801 (2016).

[15] M. Russ and G. Burkard, J. Phys.: Condens. Matter **29**, 393001 (2017).

[16] C. Zhang, X.-C. Yang, and X. Wang, Phys. Rev. A **97**, 042326 (2018).

[17] R. Hanson, L. P. Kouwenhoven, J. R. Petta, S. Tarucha, and L. M. K. Vandersypen, Rev. Mod. Phys. **79**, 1217 (2007).

[18] Y.-P. Shim and C. Tahan, Phys. Rev. B **93**, 121410 (2016).

[19] V. Srinivasa, J. M. Taylor, and C. Tahan, Phys. Rev. B **94**, 205421 (2016).

[20] N. E. Bonesteel, D. Stepanenko, and D. P. DiVincenzo, Phys. Rev. Lett. **87**, 207901 (2001).

[21] G. Burkard and D. Loss, Phys. Rev. Lett. **88**, 047903 (2002).

[22] M. J. Rančić and G. Burkard, Phys. Rev. B **96**, 201304 (2017).

[23] M. Russ and G. Burkard, Phys. Rev. B **91**, 235411 (2015).

[24] M. Russ, F. Ginzel, and G. Burkard, Phys. Rev. B **94**, 165411 (2016).

[25] S. Das Sarma, X. Wang, and S. Yang, Phys. Rev. B **83**, 235314 (2011).

[26] A. Sala and J. Danon, Phys. Rev. B **95**, 241303 (2017).

[27] Due to microscopic inhomogeneities, the effective phase ϕ_i of the valley ground state can differ between neighboring dots [10]. In general this results in a "redistribution" of tunnel coupling amplitudes over valley-*conserving* tunneling $\sim(t_{ij}/2)[1 + \exp(i\,\delta\phi_{ij})]$ and valley-*flip* tunneling $\sim(t_{ij}/2)[1 - \exp(i\,\delta\phi_{ij})]$, where $\delta\phi_{ij} = \phi_j - \phi_i$. The possibility of valley-flip tunneling has the same effect as the (in principle, always present) tunnel coupling between *orbital* ground and excited states on neighboring dots: Since the associated tunneling to doubly occupied states is no longer spin selective it does not modify exchange effects in the system, but it could contribute to leakage via a spin-flip-tunneling mechanism (see Sec. III A); the resulting rates, however, will be smaller than those for the valley- and orbital-conserving processes due to extra terms $\sim E_v$, E_{orb} in the virtual energies involved.

[28] E. A. Laird, J. M. Taylor, D. P. DiVincenzo, C. M. Marcus, M. P. Hanson, and A. C. Gossard, Phys. Rev. B **82**, 075403 (2010).

[29] Alternatively, one could use the two higher-lying equivalent doublet states with opposite polarity $S_z^{\mathrm{tot}} = \frac{1}{2}$.

[30] P. Huang and X. Hu, Phys. Rev. B **89**, 195302 (2014).

[31] L. Gaudreau, G. Granger, A. Kam, G. C. Aers, S. A. Studenikin, P. Zawadzki, M. Pioro-Ladrière, Z. R. Wasilewski, and A. S. Sachrajda, Nat. Phys. **8**, 54 (2011).

[32] C. G. Péterfalvi and G. Burkard, Phys. Rev. B **96**, 245412 (2017).

[33] A. V. Khaetskii and Y. V. Nazarov, Phys. Rev. B **61**, 12639 (2000).

[34] A. V. Khaetskii and Y. V. Nazarov, Phys. Rev. B **64**, 125316 (2001).

[35] V. F. Maisi, A. Hofmann, M. Röösli, J. Basset, C. Reichl, W. Wegscheider, T. Ihn, and K. Ensslin, Phys. Rev. Lett. **116**, 136803 (2016).

[36] C. Tahan and R. Joynt, Phys. Rev. B **71**, 075315 (2005).

[37] C. Tahan and R. Joynt, Phys. Rev. B **89**, 075302 (2014).

[38] R. M. Jock, N. T. Jacobson, P. Harvey-Collard, A. M. Mounce, V. Srinivasa, D. R. Ward, J. Anderson, R. Manginell, J. R. Wendt, M. Rudolph, T. Pluym, J. K. Gamble, A. D. Baczewski, W. M. Witzel, and M. S. Carroll, Nat. Commun. **9**, 1768 (2018).

[39] G. Dresselhaus, Phys. Rev. **100**, 580 (1955).

[40] M. Prada, G. Klimeck, and R. Joynt, New J. Phys. **13**, 013009 (2011).

[41] L. E. Golub and E. L. Ivchenko, Phys. Rev. B **69**, 115333 (2004).

[42] M. O. Nestoklon, E. L. Ivchenko, J.-M. Jancu, and P. Voisin, Phys. Rev. B **77**, 155328 (2008).

[43] R. Ferdous, K. W. Chan, M. Veldhorst, J. C. C. Hwang, C. H. Yang, H. Sahasrabudhe, G. Klimeck, A. Morello, A. S. Dzurak, and R. Rahman, Phys. Rev. B **97**, 241401 (2018).

[44] T. Tanttu, B. Hensen, K. W. Chan, H. Yang, W. Huang, M. Fogarty, F. Hudson, K. Itoh, D. Culcer, A. Laucht, A. Morello, and A. Dzurak, arXiv:1807.10415.

[45] J. Danon, Phys. Rev. B **88**, 075306 (2013).

[46] O. Malkoc, P. Stano, and D. Loss, Phys. Rev. B **93**, 235413 (2016).

[47] C. Herring and E. Vogt, Phys. Rev. **101**, 944 (1956).

[48] M. Friesen and S. N. Coppersmith, Phys. Rev. B **81**, 115324 (2010).

[49] V. N. Golovach, A. Khaetskii, and D. Loss, Phys. Rev. B **77**, 045328 (2008).

[50] A. Hofmann, V. F. Maisi, T. Krähenmann, C. Reichl, W. Wegscheider, K. Ensslin, and T. Ihn, Phys. Rev. Lett. **119**, 176807 (2017).

[51] M. Raith, P. Stano, F. Baruffa, and J. Fabian, Phys. Rev. Lett. **108**, 246602 (2012).

[52] M. Raith, P. Stano, and J. Fabian, Phys. Rev. B **86**, 205321 (2012).

[53] V. N. Golovach, A. Khaetskii, and D. Loss, Phys. Rev. Lett. **93**, 016601 (2004).

[54] For a more general and thorough analysis of spin relaxation via SO interaction in single QD refer to, e.g., Ref. [49].

[55] Typically, an external magnetic field of ~100 mT is applied, which corresponds to a Zeeman energy of $\sim10\,\mu$eV in Si. The orbital level splitting in a dot with $\sigma = 15$ nm is $E_{\mathrm{orb}} \sim 2$ meV, which makes $(E_Z/E_{\mathrm{orb}})^4 \sim 10^{-9}$.

[56] P. Huang and X. Hu, Phys. Rev. B **90**, 235315 (2014).

[57] C. H. Yang, A. Rossi, R. Ruskov, N. S. Lai, F. A. Mohiyaddin, S. Lee, C. Tahan, G. Klimeck, A. Morello, and A. S. Dzurak, Nat. Commun. **4**, 2069 (2013).

[58] O. Madelung, *Semiconductors: Data Handbook*, 3rd ed. (Springer, Berlin, 2004).

[59] P. Yu and M. Cardona, *Fundamentals of Semiconductors: Physics and Materials Properties*, Graduate Texts in Physics (Springer, Berlin, 2010).

[60] M. Raith, P. Stano, and J. Fabian, Phys. Rev. B **83**, 195318 (2011).

[61] G. Ithier, E. Collin, P. Joyez, P. J. Meeson, D. Vion, D. Esteve, F. Chiarello, A. Shnirman, Y. Makhlin, J. Schriefl, and G. Schön, Phys. Rev. B **72**, 134519 (2005).

[62] Y. Makhlin and A. Shnirman, Phys. Rev. Lett. **92**, 178301 (2004).

[63] Ł. Cywiński, Phys. Rev. A **90**, 042307 (2014).

[64] F. H. L. Koppens, D. Klauser, W. A. Coish, K. C. Nowack, L. P. Kouwenhoven, D. Loss, and L. M. K. Vandersypen, Phys. Rev. Lett. **99**, 106803 (2007).
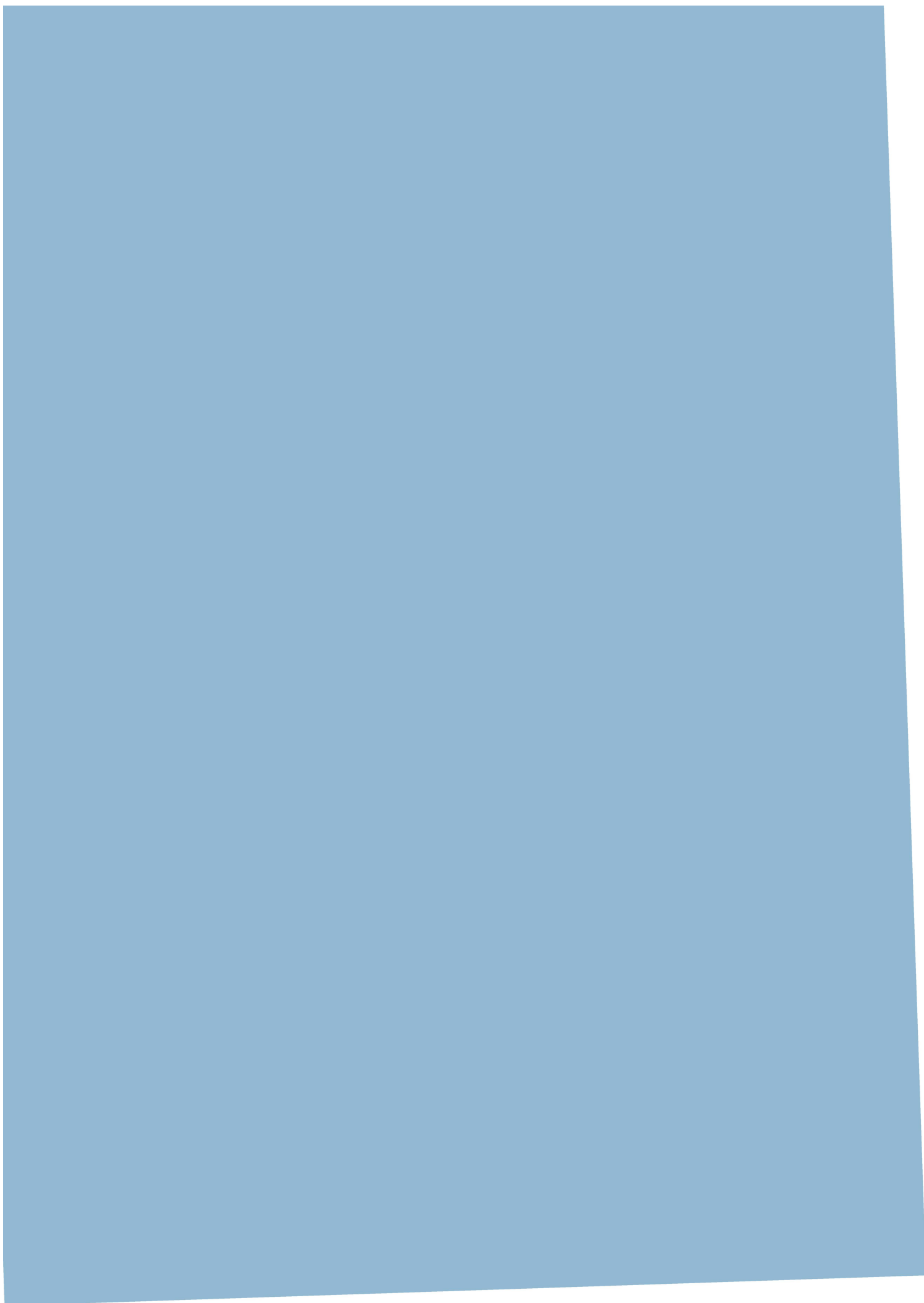
Paper III

Arnau Sala, Jørgen Holme Qvist and Jeroen Danon

Highly tunable exchange-only singlet-only qubit in a GaAs triple quantum dot

Highly tunable exchange-only singlet-only qubit in a GaAs triple quantum dot

Arnau Sala ⬤, Jørgen Holme Qvist ⬤, and Jeroen Danon ⬤

Center for Quantum Spintronics, Department of Physics, Norwegian University of Science and Technology, NO-7491 Trondheim, Norway

We propose an implementation of a singlet-only spin qubit in a GaAs-based triple quantum dot with a (1, 4, 1) charge occupation. In the central multielectron dot, the interplay between Coulomb interaction and an out-of-plane magnetic field creates an energy spectrum with a tunable singlet-triplet splitting, which can be exploited to create a six-particle singlet-only qubit with a qubit splitting that can straightforwardly be tuned over tens of μeV by adjusting the external magnetic field. We confirm the full exchange-based electric control of the qubit and demonstrate its superior coherence properties due to its singlet-only nature.

Introduction. Semiconductor spin qubits are among the most promising candidates for the physical realization of quantum processors [1,2]. Multispin exchange-only (XO) qubits, in particular, have drawn much attention in recent years since they offer fast qubit manipulation and full electric control [3–10]. However, rapid decoherence of the qubit—due to magnetic noise from randomly fluctuating nuclear spins [11,12], electric noise in the qubit's environment [13–15], electron-phonon coupling [16–18], and other spin-mixing mechanisms [19–22]—still causes the usable operation time of most XO qubits to be too short for scaling up. Besides, the typically small qubit splitting [4,8] hinders the long-distance coupling of XO qubits via, e.g, microwave resonators, where a large qubit splitting is required for fast two-qubit gates [23–25].

There have been several proposals put forward to increase the coherence time of quantum-dot-based XO qubits while retaining their conceptual simplicity and ease of manipulation. Of special interest are (i) proposals to suppress the effects of charge noise and electron-phonon interaction, via a symmetric operation of the qubit or operating at a sweet spot (SS) [17,26–28], and (ii) proposals to reduce magnetic noise or suppress its effects, either by isotope purification or by constructing decoherence-free qubit subspaces [9,29–32].

In the exchange-only singlet-only (XOSO) spin qubit proposed in Ref. [31], the leading effects of magnetic noise are suppressed by encoding the qubit states in a four-electron singlet-only subspace, while electric noise can be mitigated by operating the system symmetrically at a SS. However, the exceptionally long coherence time of the qubit comes at the cost of an increase in device complexity (a quadruple quantum dot in a T geometry) and the proposal suffers from the common problem with XO qubits of having a relatively small qubit splitting.

Here, we propose a GaAs-based implementation of the XOSO qubit that overcomes both drawbacks and, furthermore, has a qubit splitting that is straightforwardly tunable over a large range of energies. The reason why the XOSO qubit of Ref. [31] used a fourth quantum dot is that the qubit splitting scales with the singlet-triplet splitting of the "central" two electrons: Implementing the same qubit in a linear triple dot in a (1, 2, 1) charge configuration is in principle possible but results in a qubit with a splitting of the order of the orbital level splitting on the central dot ($\sim$ meV), which is too large for practical purposes. In Ref. [32], it was pointed out that one can implement the same qubit in a Si-based triple dot, where the on-site singlet-triplet splitting is typically set by the valley splitting, which can be 20–200 μeV. The drawback of this proposal is that (i) the magnitude of the valley splitting is hard to control or predict in practice [2] and (ii) uncontrollable phase differences between valley couplings on different dots can severely affect the exchange effects used to define and operate the qubit [33]. Besides, Si can be purified to be almost nuclear spin free, which eradicates the need for a singlet-only qubit [9].

The solution is to tune the triple quantum dot to a (1, 4, 1) charge configuration and apply an out-of-plane magnetic field. On the central dot, the interplay between the magnetic field and the Coulomb interaction between the electrons results in an energy spectrum with many crossings between levels with different total spin and orbital angular momentum. For the case of four electrons, the ground state changes from a triplet to a singlet character, typically at a moderate field of $\approx$ 100 mT [34]. Tuning close to this crossing and adding the singly occupied outer dots to the picture yields a XOSO qubit where the singlet-triplet splitting on the central dot, and thus the qubit splitting, can be tuned by adjusting the external magnetic field. This yields a superior GaAs-based XOSO qubit that is not more complicated to create or operate than existing spin qubits and has a qubit splitting that is straightforwardly tunable from zero to tens of μeV [35]. This high degree of tunability could also be beneficial for a Si-based version of this qubit.

Multielectron dot. The single-particle Hamiltonian of an electron labeled i in a two-dimensional planar quantum dot,

assuming a parabolic confinement and an external magnetic field perpendicular to the plane, is

$$H_0^{(i)} = \frac{[\mathbf{p}_i + e\mathbf{A}(\mathbf{r}_i)]^2}{2m^*} + \frac{1}{2}m^*\omega_0^2 r_i^2 + \frac{1}{2}g\mu_B B\sigma_i^z, \quad (1)$$

where $\mathbf{A}(\mathbf{r}) = \frac{1}{2}B(x\hat{y} - y\hat{x})$ is the vector potential, ω_0 sets the effective radius of the dot in the absence of a magnetic field $\sigma_0 = \sqrt{\hbar/m^*\omega_0}$, g is the g factor of the host material, and σ^z is the third Pauli matrix. The eigenstates of this Hamiltonian are the Fock-Darwin states

$$\psi_{n,l,\eta}(\mathbf{r}) = \sqrt{\frac{n!}{\pi\sigma^2(n+|l|)!}} \rho^{|l|}e^{-\rho^2/2}L_n^{|l|}(\rho^2)e^{-il\theta}, \quad (2)$$

in terms of the dimensionless polar coordinates $\rho = r/\sigma$ and θ. We used $\sigma = \sqrt{\hbar/m^*\Omega}$, with $\Omega = \sqrt{\omega_0^2 + \omega_c^2/4}$ and $\omega_c = eB/m^*$, and $L_a^b(x)$ is the associated Laguerre polynomial. The quantum numbers $n \in \mathbb{N}_0$, $l \in \mathbb{Z}$, and $\eta = \pm 1$ label the radial state, orbital angular momentum, and spin of the electron, respectively. The corresponding eigenenergies are (we will set $\hbar = 1$ from now on)

$$E_{n,l,\eta} = \Omega(2n + |l| + 1) - \frac{1}{2}\omega_c l + \frac{1}{4}g\omega_c \frac{m^*}{m_e}\eta. \quad (3)$$

In order to find the approximate eigenenergies and spin structure of multielectron states in the presence of electron-electron interactions, we follow the method used in Refs. [34,36]; see the Supplemental Material [37] for the details. We create a many-particle basis of antisymmetrized products of single-particle states (2), where we restrict ourselves to the states with $n \leqslant 1$ and $|l| \leqslant 3$, which corresponds to including all single-particle levels up to $\approx 4\,\Omega$ at small fields. In the thusly constructed basis, we evaluate all matrix elements of the interaction Hamiltonian

$$V = \sum_{i<j} \frac{e^2}{4\pi\varepsilon|\mathbf{r}_i - \mathbf{r}_j|}, \quad (4)$$

and the eigenstates and eigenenergies of the full many-particle Hamiltonian $H_1 = \sum_i H_0^{(i)} + V$ can then be found from numerical diagonalization or, in the weak-interaction limit characterized by $\kappa \equiv e^2/4\pi\varepsilon\sigma_0\omega_0 \ll 1$, from perturbation theory in κ. For few particles and not too large κ (we consider up to five electrons and $\kappa \leqslant 1.5$), the low-energy part of the spectrum of H_1 will resemble the exact many-particle spectrum fairly accurately [34,44].

In Fig. 1(a), we present typical results for the lowest few levels for the case of four electrons, where we set $\kappa = 0.5$ and $g = -0.4$. The dots show the numerically calculated lowest five eigenenergies, where green (blue) dots indicate a state with a four-particle spin singlet (triplet) structure. The three triplet states are labeled $|T_\beta\rangle$ and have the largest weight in the orbital configuration $(0,0)^2(0,1)^1(0,-1)^1$, where $(n,l)^m$ means m electrons in the orbital state (n,l) [34]. The three lowest singlet states, labeled $|S_{\alpha,\beta,\gamma}\rangle$, live mostly in the orbital configurations $(0,0)^2(0,1)^2$, $(0,0)^2(0,1)^1(0,-1)^1$, and $(0,0)^2(0,-1)^2$, respectively.

For small κ, these lowest eigenenergies can also be approximated through perturbation theory in the interaction Hamiltonian V. Up to second order in κ, this yields for the

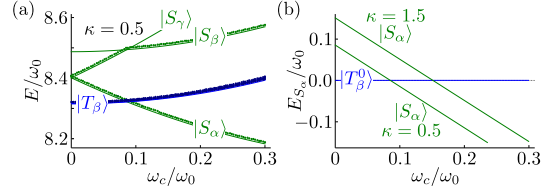
FIG. 1. (a) Field-dependent low-energy part of the spectrum of a four-electron quantum dot with $\kappa = 0.5$ and $g = -0.4$. Dots present numerical results and solid lines show the perturbative results of (5). (b) The numerically evaluated energy of the state $|S_\alpha\rangle$ (green lines) relative to $|T_\beta^0\rangle$ for two values of κ.

lowest six states the generic expression

$$E_\nu = 6\Omega - \frac{L}{2}\omega_c + \frac{S}{2}g\omega_c\frac{m^*}{m_e} + c_1^{(\nu)}\kappa\sqrt{\Omega\omega_0} + c_2^{(\nu)}\kappa^2\omega_0, \quad (5)$$

where L and S denote the total orbital and spin angular momentum along $\hat{z}$ of the four electrons. The coefficients $c_{1,2}^{(\nu)} \sim 1$ differ per state $|\nu\rangle$ but can be found explicitly; see Ref. [37] for their exact values. The resulting energies E_ν are plotted in Fig. 1(a) as solid lines and show good agreement with the numerics. For larger κ, the perturbation theory breaks down, but the low-energy part of the spectrum is qualitatively the same. This suggests that one can use Eq. (5) to describe the E_ν if one treats the coefficients $c_{1,2}^{(\nu)}$ as fit parameters to the numerical data. As illustrated in Ref. [37] for the case $\kappa = 1.5$, this still leads to excellent agreement. In Fig. 1(b), we show the numerically evaluated energy of the state $|S_\alpha\rangle$ relative to $|T_\beta^0\rangle$ as a function of ω_c, for $\kappa = 0.5$ and $\kappa = 1.5$. In both cases, the splitting between $|S_\alpha\rangle$ and $|T_\beta^0\rangle$ is to good approximation linear in ω_c in the regime of interest, and the ground state changes from a spin triplet to a singlet around $\omega_c/\omega_0 \sim 0.1$. These two generic features are the key ingredients for our qubit proposal.

Triple-dot six-electron states. We will construct our qubit in two *six*-electron states hosted in a linear arrangement of three quantum dots with a perpendicular magnetic field applied, such as sketched in Fig. 2(a), where the effective on-site potentials V_i and the interdot tunnel couplings t_{ij} can be controlled through nearby gate electrodes, as schematically
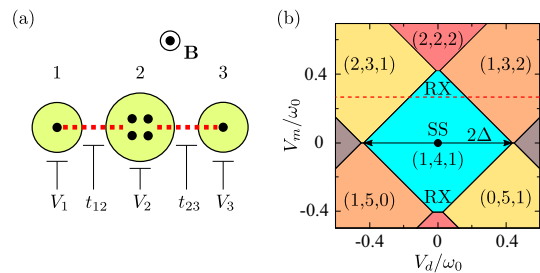

FIG. 2. (a) Sketch of the linear triple-dot setup in a $(1, 4, 1)$ charge configuration with a perpendicular magnetic field applied. (b) Six-electron charge stability diagram around the $(1, 4, 1)$ ground state, as a function of V_m and V_d.

indicated. We describe this system using a simple Hubbard-like Hamiltonian [16,31,45],

$$H = \sum_{i=1}^{3} \left(H_1^{(i)} - V_i n_i \right) + \sum_{\langle i,j \rangle} U_c n_i n_j - \sum_{\langle i,j \rangle, \eta} \frac{t_{ij}}{\sqrt{2}} c_{i\eta}^\dagger c_{j\eta}, \quad (6)$$

where $n_i = \sum_\eta c_{i\eta}^\dagger c_{i\eta}$ is the number operator for dot i, $c_{i\eta}$ annihilates an electron on dot i with spin η, U_c accounts for the cross capacitance between neighboring dots, and $H_1^{(i)}$ is the single-dot many-particle Hamiltonian for dot i as described above. We thus made several simplifying assumptions: (i) The gate-induced potentials are smooth enough so that they affect all electronic orbitals in the same way. (ii) The separation between the dots is large enough to allow us to treat the *inter*dot electrostatic energy as being dependent only on the n_i and not on the exact orbital configuration of the electrons on the neighboring dots. (iii) All tunneling processes we will consider below mostly involve a (0, 0) orbital on a lateral dot and a $(0, \pm 1)$ orbital on the central dot; since all $(0, \pm 1)$ orbitals have the same radial structure, we assume that this allows us to use tunneling coefficients t_{ij} that are independent of the exact electronic orbitals involved.

We first study the electrostatic properties of H by diagonalizing the first two terms in Eq. (6). The charge stability diagram in Fig. 2(b) shows the resulting six-electron ground-state charge configuration (n_1, n_2, n_3), where n_i is the number of electrons on dot i, as a function of the detuning parameters $V_d = \frac{1}{2}(V_3 - V_1)$ and $V_m = \frac{1}{2}(V_1 + V_3) - V_2$. We fixed $V_1 + 4V_2 + V_3$ and focused on the regime around the (1, 4, 1) state. As indicated in Fig. 2(a), we assumed different dot sizes, $\sigma_0 = 30$ nm for the central dot and $\sigma_0 = 20$ nm for the lateral dots, which results in a good ratio between the orbital splitting on the outer dots and the splitting of the many-electron states in the middle dot [46]. Furthermore, we used $U_c = 0.2\,\omega_0$ (where ω_0 is the bare level splitting on the *central* dot) and set $\omega_c/\omega_0 = 0.1$, $\kappa = 0.5$, and $m^*/m_e = 0.067$.

In the (1, 4, 1) region, the four lowest-energy six-particle states with $S^2 = 0$ can be written as

$$|0\rangle = |S_\alpha S_{(13)}\rangle, \quad (7)$$

$$|1\rangle = \frac{1}{\sqrt{3}} \left[|T_\beta^0 T_{(13)}^0\rangle - |T_\beta^- T_{(13)}^+\rangle - |T_\beta^+ T_{(13)}^-\rangle \right], \quad (8)$$

$$|2\rangle = |S_\beta S_{(13)}\rangle, \quad (9)$$

$$|3\rangle = |S_\gamma S_{(13)}\rangle, \quad (10)$$

where $|S_{(13)}\rangle$ and $|T_{(13)}\rangle$ indicate pairing in a singlet or triplet state of the two electrons in the outer dots, and $|S_{\alpha,\beta,\gamma}\rangle$ and $|T_\beta\rangle$ are the lowest four-particle singlets and triplet on the central dot, see above.

The qubit. We propose to tune close to the degeneracy of $|S_\alpha\rangle$ and $|T_\beta\rangle$ on the central dot, which for $\sigma_0 = 30$ nm happens at $B \approx 75$ mT. The two lowest-energy singlet states $|0\rangle$ and $|1\rangle$ can then be used as qubit basis, and the singlets $|2\rangle$ and $|3\rangle$ will be split off by an energy much larger than the qubit splitting.

We assume that $t/\Delta \ll 1$, with t the magnitude of the tunnel couplings (typically $t \sim 10\ \mu$eV) and 2Δ the width of the (1, 4, 1) region; see its definition in Fig. 2(b). Then we can

treat the tunnel coupling perturbatively for most of the (1, 4, 1) region, and we thus project the full Hamiltonian (6) onto the qubit subspace by means of a Schrieffer-Wolff transformation [37], yielding to order t^2

$$H_{\text{qb}} = \frac{1}{2}(E_{ST} + J_z)\sigma_z + J_x \sigma_x, \quad (11)$$

where $\sigma_{x,z}$ are Pauli matrices. The qubit splitting is dominated by the singlet-triplet splitting on the central dot $E_{ST} = E_{T_\beta^0} - E_{S_\alpha}$ [see Fig. 1(b)], which follows to good approximation from the expressions given in Eq. (5),

$$E_{ST} \approx \gamma_0 \omega_0 + \omega_c, \quad (12)$$

with $\gamma_0 = -0.235\,\kappa + 0.128\,\kappa^2$, accurate for $\kappa \lesssim 0.5$ (see Ref. [37] for all derivations and an explicit expression for γ_0). We wrote E_{ST} here up to linear order in ω_c/ω_0; the next correction is smaller by a factor $\approx 10^{-2}\kappa\omega_c/\omega_0$. Through $\omega_c \propto B$, this term, and thus the qubit splitting, can be easily tuned over tens of μeV. We emphasize that this magnetic field dependence arises through coupling of the field to the *orbital* degrees of freedom of the electrons; the (singlet-only) qubit subspace is insensitive to the coupling of magnetic fields to the *spin* of the electrons.

Close to the line where $V_d = 0$ and assuming approximately symmetric tunnel couplings $t_{12} \approx t_{23}$, the two exchange terms read as [37]

$$J_z \approx -t^2 \left[\frac{\Delta}{\Delta^2 - V_m^2} + \frac{3(\Delta + \omega_c)}{(\Delta + \omega_c)^2 - V_m^2} \right], \quad (13)$$

$$J_x \approx \frac{\sqrt{6}t\Delta}{\Delta^2 - V_m^2} \left[\delta t + \frac{2tV_m}{\Delta^2 - V_m^2} V_d \right], \quad (14)$$

for Δ as defined in Fig. 2(b) and with $t = \frac{1}{2}(t_{12} + t_{23})$ and $\delta t = t_{12} - t_{23}$. We see that J_z in general presents a small tuning-dependent correction to the qubit splitting, which is dominated by E_{ST}, whereas J_x provides a coupling to σ_x linear in δt and/or V_d (depending on tuning), which can be used to drive Rabi oscillations.

We now discuss two regimes of special interest in the charge stability diagram shown in Fig. 2(b): (i) In the resonant-exchange (RX) regime, close to the top and bottom of the (1, 4, 1) region, the strong coupling to the other charge states offers fast qubit control through V_d [8]. In Fig. 3(a), we show the lowest-lying states as a function of V_d along the horizontal dashed line in Fig. 2(b) ($V_m/\omega_0 = 0.27$) calculated from the Hamiltonian as given in (6), where we ignored the Zeeman splitting for clarity. We used the same parameters as in Fig. 2(b) and further set $t = 25\ \mu$eV and $\delta t = 0$. We labeled the two qubit states $|0\rangle$ and $|1\rangle$, three spin triplets $|T_{1,2,3}\rangle$, and a spin quintuplet $|Q\rangle$; including the Zeeman effect, a triplet (quintuplet) acquires an additional threefold (fivefold) splitting of 1.7 μeV for $\omega_c/\omega_0 = 0.1$. (ii) In the center of the (1, 4, 1) region, we find a SS where the qubit is to linear order insensitive to fluctuations of the potentials V_i, offering some protection against charge noise. In Fig. 3(b), we show the spectrum at the SS for the same parameters as in Fig. 3(a), now as a function of δt while setting $V_d = 0$. At the SS exchange effects are much smaller and thus the qubit splitting is closer to E_{ST} ($\approx 18.3\ \mu$eV for $\omega_c/\omega_0 = 0.1$), but apart from that the spectrum looks similar to the RX regime.
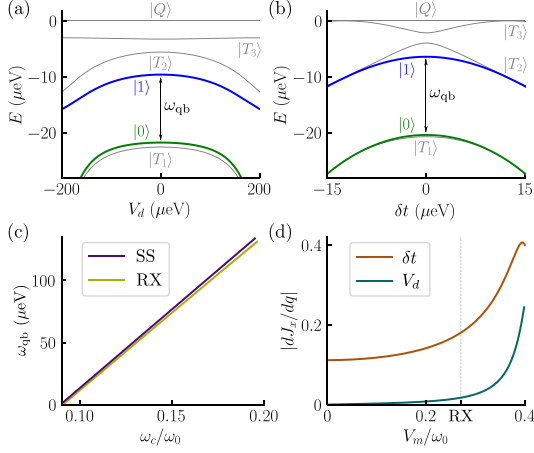
FIG. 3. Low-energy part of the spectrum of the Hamiltonian (6) (a) as a function of V_d at $V_m/\omega_0 = 0.27$ and (b) as a function of δt at the SS, $V_d = V_m = 0$. The green and blue lines show the spin-singlet qubit states $|0\rangle$ and $|1\rangle$ respectively; the gray lines show the spin triplet and quintuplet states. (c) The qubit splitting as a function of the magnetic field, where $\omega_c/\omega_0 = 0.1$ corresponds to $B \approx 75$ mT. (d) The derivative dJ_x/dq for $q \in \{\delta t, V_d\}$ as a function of V_m and at $V_d = 0$.

In Fig. 3(c), we plot the qubit splitting ω_{qb} as a function of the magnetic field, in the RX regime ($V_m = 0.27$, $V_d = 0$, yellow line) and at the SS (purple line). This confirms the high degree of tunability of our qubit. We further note how the spectra in Figs. 3(a) and 3(b) strongly resemble those in the XOSO spin-qubit proposals of Refs. [31,32], the main difference being the large and straightforwardly tunable qubit splitting $\omega_{qb} \propto B$ in our proposal. This permits an efficient and adaptable coupling to other systems such as microwave cavities which can be used to couple distant qubits [47–50].

Qubit operation. Single-qubit rotations can be performed via resonant Rabi driving, using a sinusoidal modulation of a tuning parameter $q = \{V_d, V_m, t, \delta t\}$ with a small amplitude $\tilde{q}$ and frequency ω, i.e., $q(t) = q_0 + \tilde{q}\sin(\omega t)$. For small enough $\tilde{q}$, the qubit Hamiltonian (11) can be approximated as

$$H_{qb} = \tfrac{1}{2}\omega_{qb}\sigma_z + A_q \sin(\omega t)\sigma_x, \quad (15)$$

where $A_q = \tilde{q}(dJ_x/dq)_{q=q_0}$. Driving the qubit resonantly, $\omega = \omega_{qb}$, then induces Rabi oscillations with a frequency A_q. At the RX regime, where we can use V_d as the driving parameter, an amplitude of $\tilde{V}_d = 5$–10 μeV gives a Rabi period of $T_{Rabi} \approx 20$–40 ns. At the SS, Rabi rotations are much more efficient via a driving of δt, which gives a period of $T_{Rabi} \approx 20$ ns for an amplitude $\tilde{\delta t} = 2$ μeV. Fast qubit rotations can therefore be achieved both in the RX regime and at the SS. In Fig. 3(d), we plot the "efficiency" dJ_x/dq of the two driving parameters $q \in \{\delta t, V_d\}$ as a function of V_m, along the line $V_{d,0} = 0$. We see that at the SS the sensitivity to V_d vanishes, in accordance with Eq. (14), whereas driving of δt stays effective all the way down to $V_m = 0$.

Qubit initialization and readout can be accomplished by standard spin-to-charge conversion, i.e., pulsing the qubit to one of the neighboring charge configurations that has only one low-lying six-particle singlet state. For example, when tuning into the $(1, 3, 2)/(2, 3, 1)$ charge regions, only the qubit state $|0\rangle$ is adiabatically connected to the new ground-state charge configuration. This allows for initialization in $|0\rangle$ as well as readout of the qubit by means of charge detection.

Decoherence. In most GaAs-based spin qubits, the main source of decoherence is the fluctuating bath of nuclear spins that couples to the electron spins via contact hyperfine interaction. On a mean-field level, the effect of this interaction can be described by the Hamiltonian $H_{hf} = \tfrac{1}{2}g\mu_B \sum_i \mathbf{K}_i \cdot \boldsymbol{\sigma}_i$, with $\mathbf{K}_i$ being a random effective nuclear field acting on electron i, typically of the order of a few mT. In the device we propose in this paper, both qubit states are singlets and therefore the qubit splitting is not directly influenced by any intrinsic or external (gradient) of Zeeman fields acting on the electrons, thereby reducing the hyperfine-induced decoherence dramatically [31,32]. We estimate the coupling between the nuclear magnetic moments and the *orbital* degrees of freedom of the electrons to be negligible and dominated by hyperfine coupling of the qubit states to nearby triplet states, which leads to random higher order shifts of the qubit levels [31]. The timescale of this residual hyperfine-induced dephasing can be estimated as $T_2^* \sim A_q \hbar(\delta\varepsilon)^2/\sigma_K^4$, where $\delta\varepsilon$ is the energy splitting between $|0\rangle$ and $|T_1\rangle$; see Figs. 3(a) and 3(b) [37]. For the range of parameters considered here, we find $T_2^* \sim 0.5$–5 μs [37], giving a number of visible, coherent Rabi oscillations of $n_{coh} = T_2^*/T_{Rabi} \sim 25$–$250$.

Another source of decoherence for exchange-based qubits are low-frequency fluctuations in the electrostatic environment of the system. A common way to mitigate such charge noise is to operate the qubit at the SS [Fig. 3(b)], where the qubit splitting is insensitive to fluctuations in the potentials V_i to leading order; there we find a dephasing time of $T_2^* \gg 10$ μs. Away from the SS, the effects of charge noise are larger. At the RX regime [Fig. 3(a)], far away from the SS, the contribution from charge noise to dephasing becomes similar to that of nuclear noise, with a dephasing time of $T_2^* \sim 0.5$ μs [37].

Finally, qubit relaxation via electron-phonon coupling causes qubit decoherence. The relaxation rate can be estimated using Fermi's golden rule and depends on the qubit splitting and on the strength of the exchange interaction [31]. In the RX regime, where the qubit splitting can be extensively tuned through ω_c, we estimate relaxation rates from $\Gamma_{rel} \sim 1$ GHz for $\omega_{qb} \sim 50$ μeV to $\Gamma_{rel} \sim 1$ MHz for $\omega_{qb} \sim 10$ μeV. And, as is common in exchange-based qubits [18,31], the relaxation rate is strongly suppressed as we approach the SS.

Conclusions. We propose a six-electron exchange-only singlet-only spin qubit hosted in a GaAs linear triple quantum dot. Its singlet-only nature makes the qubit intrinsically insensitive to randomly fluctuating nuclear fields. The qubit can be operated fully electrically, either in an RX regime which enables fast qubit operations or at a SS where the qubit is better protected against charge noise. Furthermore, the fact that the qubit splitting is highly tunable over a large range of energies allows for efficient and adaptable coupling

to microwave resonators, enabling coupling of distant qubits. The only ingredient on which this tunability relies is the appearance of a ground-state singlet-triplet transition at finite magnetic field in the multiparticle spectrum of the central dot. This is a very commonly observed feature in quantum dots of various shapes and sizes.

[1] R. Hanson, L. P. Kouwenhoven, J. R. Petta, S. Tarucha, and L. M. K. Vandersypen, Rev. Mod. Phys. **79**, 1217 (2007).

[2] F. A. Zwanenburg, A. S. Dzurak, A. Morello, M. Y. Simmons, L. C. L. Hollenberg, G. Klimeck, S. Rogge, S. N. Coppersmith, and M. A. Eriksson, Rev. Mod. Phys. **85**, 961 (2013).

[3] D. P. DiVincenzo, D. Bacon, J. Kempe, G. Burkard, and K. B. Whaley, Nature (London) **408**, 339 (2000).

[4] M. Russ and G. Burkard, J. Phys.: Condens. Matter **29**, 393001 (2017).

[5] E. A. Laird, J. M. Taylor, D. P. DiVincenzo, C. M. Marcus, M. P. Hanson, and A. C. Gossard, Phys. Rev. B **82**, 075403 (2010).

[6] L. Gaudreau, G. Granger, A. Kam, G. C. Aers, S. A. Studenikin, P. Zawadzki, M. Pioro-Ladrière, Z. R. Wasilewski, and A. S. Sachrajda, Nat. Phys. **8**, 54 (2011).

[7] J. Medford, J. Beil, J. M. Taylor, S. D. Bartlett, A. C. Doherty, E. I. Rashba, D. P. DiVincenzo, H. Lu, A. C. Gossard, and C. M. Marcus, Nat. Nanotechnol. **8**, 654 (2013).

[8] J. Medford, J. Beil, J. M. Taylor, E. I. Rashba, H. Lu, A. C. Gossard, and C. M. Marcus, Phys. Rev. Lett. **111**, 050501 (2013).

[9] K. Eng, T. D. Ladd, A. Smith, M. G. Borselli, A. A. Kiselev, B. H. Fong, K. S. Holabird, T. M. Hazard, B. Huang, P. W. Deelman, I. Milosavljevic, A. E. Schmitz, R. S. Ross, M. F. Gyure, and A. T. Hunter, Sci. Adv. **1**, e1500214 (2015).

[10] R. W. Andrews, C. Jones, M. D. Reed, A. M. Jones, S. D. Ha, M. P. Jura, J. Kerckhoff, M. Levendorf, S. Meenehan, S. T. Merkel, A. Smith, B. Sun, A. J. Weinstein, M. T. Rakher, T. D. Ladd, and M. G. Borselli, Nat. Nanotechnol. **14**, 747 (2019).

[11] J.-T. Hung, J. Fei, M. Friesen, and X. Hu, Phys. Rev. B **90**, 045308 (2014).

[12] C. G. Péterfalvi and G. Burkard, Phys. Rev. B **96**, 245412 (2017).

[13] M. Russ and G. Burkard, Phys. Rev. B **91**, 235411 (2015).

[14] F. Martins, F. K. Malinowski, P. D. Nissen, E. Barnes, S. Fallahi, G. C. Gardner, M. J. Manfra, C. M. Marcus, and F. Kuemmeth, Phys. Rev. Lett. **116**, 116801 (2016).

[15] J. Yoneda, K. Takeda, T. Otsuka, T. Nakajima, M. R. Delbecq, G. Allison, T. Honda, T. Kodera, S. Oda, Y. Hoshi, N. Usami, K. M. Itoh, and S. Tarucha, Nat. Nanotechnol. **13**, 102 (2018).

[16] J. M. Taylor, V. Srinivasa, and J. Medford, Phys. Rev. Lett. **111**, 050502 (2013).

[17] C. Zhang, X. C. Yang, and X. Wang, Phys. Rev. A **97**, 042326 (2018).

[18] A. Sala and J. Danon, Phys. Rev. B **98**, 245409 (2018).

[19] V. N. Golovach, A. Khaetskii, and D. Loss, Phys. Rev. Lett. **93**, 016601 (2004).

[20] M. Raith, P. Stano, F. Baruffa, and J. Fabian, Phys. Rev. Lett. **108**, 246602 (2012).

[21] M. Raith, P. Stano, and J. Fabian, Phys. Rev. B **86**, 205321 (2012).

[22] A. Hofmann, V. F. Maisi, T. Krähenmann, C. Reichl, W. Wegscheider, K. Ensslin, and T. Ihn, Phys. Rev. Lett. **119**, 176807 (2017).

[23] V. Srinivasa, J. M. Taylor, and C. Tahan, Phys. Rev. B **94**, 205421 (2016).

[24] A. J. Landig, J. V. Koski, P. Scarlino, U. C. Mendes, A. Blais, C. Reichl, W. Wegscheider, A. Wallraff, K. Ensslin, and T. Ihn, Nature (London) **560**, 179 (2018).

[25] S. P. Harvey, C. G. L. Bøttcher, L. A. Orona, S. D. Bartlett, A. C. Doherty, and A. Yacoby, Phys. Rev. B **97**, 235409 (2018).

[26] M. D. Reed, B. M. Maune, R. W. Andrews, M. G. Borselli, K. Eng, M. P. Jura, A. A. Kiselev, T. D. Ladd, S. T. Merkel, I. Milosavljevic, E. J. Pritchett, M. T. Rakher, R. S. Ross, A. E. Schmitz, A. Smith, J. A. Wright, M. F. Gyure, and A. T. Hunter, Phys. Rev. Lett. **116**, 110402 (2016).

[27] Y.-P. Shim and C. Tahan, Phys. Rev. B **93**, 121410(R) (2016).

[28] F. K. Malinowski, F. Martins, P. D. Nissen, S. Fallahi, G. C. Gardner, M. J. Manfra, C. M. Marcus, and F. Kuemmeth, Phys. Rev. B **96**, 045443 (2017).

[29] D. Bacon, J. Kempe, D. A. Lidar, and K. B. Whaley, Phys. Rev. Lett. **85**, 1758 (2000).

[30] M. Friesen, J. Ghosh, M. A. Eriksson, and S. N. Coppersmith, Nat. Commun. **8**, 15923 (2017).

[31] A. Sala and J. Danon, Phys. Rev. B **95**, 241303(R) (2017).

[32] M. Russ, J. R. Petta, and G. Burkard, Phys. Rev. Lett. **121**, 177701 (2018).

[33] D. Culcer, X. Hu, and S. Das Sarma, Phys. Rev. B **82**, 205315 (2010).

[34] M. Eto, J. Phys. Soc. Jpn. **66**, 2244 (1997).

[35] An in-plane magnetic field would also induce crossings between singlet and triplet many-particle states, but due to the strong confinement of the electrons along one of the axes perpendicular to the field, a much larger magnetic field would be required to achieve the same effect.

[36] M. Rontani, F. Rossi, F. Manghi, and E. Molinari, Phys. Rev. B **59**, 10165 (1999).

[37] See Supplemental Material at http://link.aps.org/supplemental/10.1103/PhysRevResearch.2.012062 which includes Refs. [38–43], for more detailed discussions and derivations of the equations presented in the main text.

[38] V. N. Golovach, A. Khaetskii, and D. Loss, Phys. Rev. B **77**, 045328 (2008).

[39] L. P. Kouwenhoven, T. H. Oosterkamp, M. W. S. Danoesastro, M. Eto, D. G. Austing, T. Honda, and S. Tarucha, Science **278**, 1788 (1997).

[40] M. Rontani, Electronic states in semiconductor quantum dots, Ph.D. thesis, Università degli Studi di Modena e Reggio Emilia, Modena, Italy, 1999.

[41] F. C. Zhang and S. Das Sarma, Phys. Rev. B **33**, 2903 (1986).

[42] L. Jacak, J. Krasnyj, D. Jacak, W. Salejda, and A. Mituś, Acta Phys. Pol. A **99**, 277 (2001).

[43] V. Srinivasa, H. Xu, and J. M. Taylor, Phys. Rev. Lett. **114**, 226803 (2015).

[44] S. M. Reimann and M. Manninen, Rev. Mod. Phys. **74**, 1283 (2002).

[45] G. Burkard, D. Loss, and D. P. DiVincenzo, Phys. Rev. B **59**, 2070 (1999).

[46] The dependence of the orbital spacing on the dot size allows us to design a device with an orbital splitting on the outer dots larger than the level splittings in the central multielectron dot,

which enables full spin blockade in the regime where the qubit is operated.

[47] M. Russ and G. Burkard, Phys. Rev. B **92**, 205412 (2015).

[48] M. Russ, F. Ginzel, and G. Burkard, Phys. Rev. B **94**, 165411 (2016).

[49] A. J. Landig, J. V. Koski, P. Scarlino, C. Müller, J. C. Abadillo-Uriel, B. Kratochwil, C. Reichl, W. Wegscheider, S. N. Coppersmith, M. Friesen, A. Wallraff, T. Ihn, and K. Ensslin, Nat. Commun. **10**, 5037 (2019).

[50] G. Burkard, M. J. Gullans, X. Mi, and J. R. Petta, Nat. Rev. Phys. **2**, 129 (2020).